Earth Abundant Catalysts For Alkaline Hydrogen And Oxygen Electrochemistry

by

Rituja Bhagwant Patil

Bachelor of Chemical Engineering, Institute of Chemical Technology, 2016

Submitted to the Graduate Faculty of

the Swanson School of Engineering in partial fulfillment

of the requirements for the degree of

Doctor of Philosophy

University of Pittsburgh

2021

UNIVERSITY OF PITTSBURGH

SWANSON SCHOOL OF ENGINEERING

This dissertation was presented

by

Rituja Bhagwant Patil

It was defended on

October 14, 2021

and approved by

Dr. Götz Veser, PhD, Professor, Department of Chemical and Petroleum Engineering

Dr. Giannis Mpourmpakis, PhD, Associate Professor, Department of Chemical and Petroleum Engineering

Dr. Raúl Hernández Sánchez, PhD, Assistant Professor, Department of Chemistry

Dissertation Director: Dr. James R. McKone, PhD, Assistant Professor, Department of Chemical and Petroleum Engineering

Earth Abundant Catalysts For Alkaline Hydrogen And Oxygen Electrochemistry

Rituja Bhagwant Patil, PhD

University of Pittsburgh, 2021

The worldwide chemical industry makes extensive use of H_2 as a fuel and feedstock. However, most hydrogen production occurs through natural gas, fossil fuels, or coal as a primary source. For the environmental sustainability of hydrogen production, it is necessary to replace these sources with new approaches based on renewable resources, such as solar-driven water electrolysis. Alkaline anion exchange membrane electrolyzers are an attractive technological target to meet the cost target of \$2/kgH_2 set by the U.S. Department of Energy (DOE). These electrolyzers facilitate the use of non-precious catalysts for the hydrogen evolution and oxygen evolution half-reactions, resulting in significant reductions in capital cost. This dissertation focuses on using Ni–Mo alloy catalysts for hydrogen evolution and oxidation reactions and $NiFeO_x$ catalyst for oxygen evolution.

We have clarified the nanoscale composition of a previously reported Ni–Mo alloy nanocatalyst by showing that it consists of a core@shell structure where the core is rich in Ni and the shell is predominantly Mo-rich oxides. The structural evolution of core@shell geometry was monitored using *in-situ* transmission electron microscopy, and methodologies were developed to study the metal/metal-oxide interfaces. Based on this compositional insight, we have also determined that unsupported Ni–Mo catalysts suffer from significant conductivity (i.e., electronic transport) limitations, which we have successfully mitigated via the use of carbon supports. The intrinsic activity of these catalysts obtained after carbon incorporation for hydrogen evolution and oxidation reactions was also analyzed. The results suggest that the catalytic activity exhibited by them is within an order of magnitude of the benchmark catalysts but are thousand times cheaper and are therefore very promising. We have extended these studies to $NiFeO_x$ catalysts for the oxygen evolution reaction and generated core@shell morphologies by electrochemical activation of binary Ni–Fe alloy nanoparticles supported on oxidized Vulcan carbon. Interestingly, we observed that the activity of these composites systematically increased when the catalyst spent more time in the solution comprising Nafion and isopropyl alcohol. Overall, we have reduced the gap in activity and stability between non-precious and precious metal catalysts for alkaline hydrogen and oxygen electrochemistry.

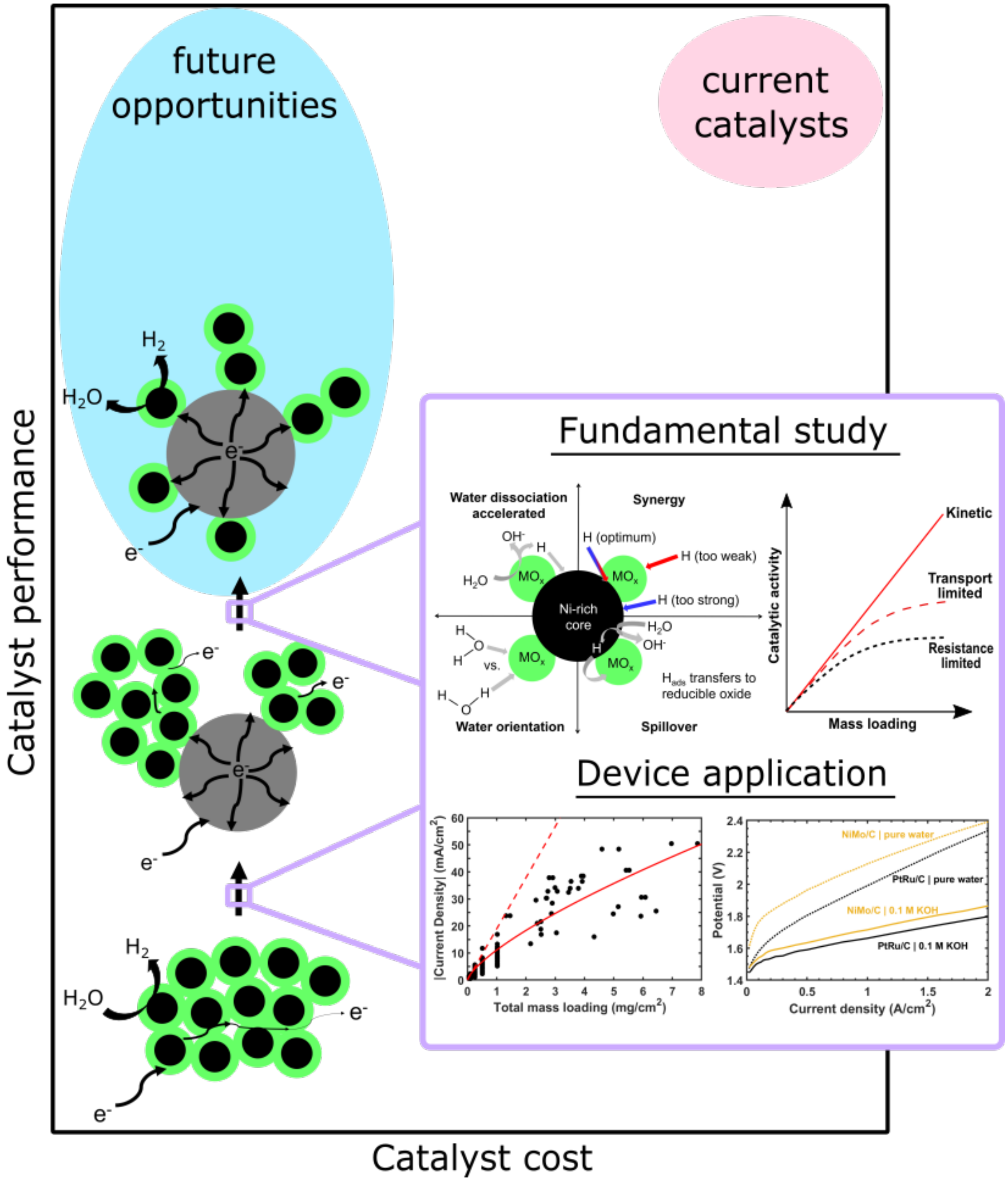
future opportunities
current catalysts
Catalyst performance
Catalyst cost
H_2
H_2O
e^-
Fundamental study
Water dissociation accelerated
Synergy
H (optimum)
H (too weak)
H (too strong)
Ni-rich core
MO_x
OH^-
H_2O
vs.
Water orientation
Spillover
H_{ads} transfers to reducible oxide
Catalytic activity
Mass loading
Kinetic
Transport limited
Resistance limited
Device application
|Current Density| (mA/cm^2)
Total mass loading (mg/cm^2)
0
10
20
30
40
50
60
1
2
3
4
5
6
7
8
Potential (V)
Current density (A/cm^2)
1.4
1.6
1.8
2
2.2
2.4
0.5
1.5
NiMo/C | pure water
PtRu/C | pure water
NiMo/C | 0.1 M KOH
PtRu/C | 0.1 M KOH

Table of Contents

List of Figures

Preface

I am very grateful to my advisor, Dr. James R. McKone, for giving me an opportunity to work with him over the last five years. His passion for science and engineering and excellent knowledgebase for literally everything under the sun has been phenomenal for shaping me into the way I am today. I will always cherish his constant encouragement, mentorship, and patience in guiding me throughout my journey and desire to be more like him. He has been an amazing advisor and a great friend who has left in me in awe after every interaction. I consider myself privileged to have worked with such a great scientist and shall forever be thankful to him. Special thanks also to Matilda and Eleanor who sometimes made special appearances in our meetings to make them more fun.

I also want to express gratitude towards my committee members Dr. Götz Veser, Dr. Giannis Mpourmpakis, and Dr. Raúl Hernández Sánchez for their valuable feedback and wonderful insights on my work to help broaden the horizons. Huge gratitude also towards Prof. Stephen House for conducting all the fascinating but exhausting TEM analysis throughout this work. Further, I would like to acknowledge all the undergraduate and graduate students, and post doc in McKone lab who have made working in lab an enjoyable experience. I would particularly like to thank Jeffrey Hoffmann and Margaret Orr for contributing to the work on oxygen evolution reaction catalysts and special thanks to Jeff for being very persistent on this project. Thanks also to Evan Miu and Dr. Manjodh Kaur for insightful discussions and providing critical assessment of my work. The list of acknowledgements is incomplete without my friends – Dr. Tejal Sawant, Shubham Awate, Sanjana Karpe, Ritesh Pawar, Riddhesh Patel, Nikhil Budhkar, Dr. Rishabh Shah, Chinmay Mhatre, Dnyanesh Sarawate and Dr. Pooja Mapara. They have made my PhD journey memorable and exciting.

Finally, my deepest appreciation to my parents, Bhagwant Patil and Madhuri Patil, for always being very supportive and motivating. Their blessings and love have allowed me to peacefully sail through this tortuous PhD journey. Gratitude also towards my brother, Shalin Patil, for being my strength and helping me maintain a "healthy" balance between my work and food. I would also like to acknowledge my cousin, Mukesh Bauskar, sister-in-law Shweta and their kids Parinaya and Sanidhya for their affection. I would not have completed my journey without all these people.

1.0 Introduction

1.1 Purpose and Scope

This dissertation document summarizes my research efforts in electrocatalysis accomplished since the fall of 2016. The primary purpose of this work was to develop electrocatalysts to improve the efficiency of water electrolyzers and fuel cells, particularly for hydrogen evolution/oxidation and oxygen evolution reactions. This dissertation is intended to be helpful for researchers who would like to expand on my work to reach the ultimate aim of utilizing carbon-neutral technologies for making and using hydrogen with low carbon intensity.

The remainder of this chapter will motivate the use of low-carbon emission technologies and lay out some of the challenges for practical implementation. Chapter 2 will provide an overview of the alkaline anion exchange membrane systems that we believe are promising to enable such technologies. Chapter 3 provides a detailed analysis of typical hydrogen evolution/oxidation reaction experiments executed in electrocatalysis. The chapter also describes the different mechanisms by which unsupported Pt nanoparticles can degrade under acidic and alkaline conditions. A combination of voltammetric analysis and identical location transmission electron microscopy (IL-TEM) allowed us to elucidate the degradation pathways under experimental conditions commonly employed in most research laboratories. Chapters 4 and 5 encompass our work on Ni–Mo composites for reversible hydrogen evolution/oxidation reactions. Chapter 4 provides a detailed compositional analysis of Ni–Mo composites. The revelation of core@shell Ni–Mo metal@oxides led us to explore the growth of the oxide shell and significance of such metal/metal-oxide interfaces for hydrogen catalysis.

Chapter 5 discusses the practical outlook of Ni–Mo composites for reversible hydrogen electrochemistry. Due to promising hydrogen evolution reaction performance, we progressed towards establishing an industry collaboration for their implementation in alkaline anion exchange membrane electrolyzers. We further expanded the scope of Ni–Mo composites for the alkaline hydrogen oxidation reaction and demonstrated the ability to reversibly generate and oxidize hydrogen using our nonprecious catalyst.

Chapter 6 compiles our work on Ni–Fe composites for the oxygen evolution reaction. The compositional insights obtained from Ni–Mo composites, particularly related to its metal@oxide core-shell geometry, were extended to Ni–Fe catalysts. Additional insights about the activity and stability of these composites under the oxidizing conditions associated with oxygen evolution reaction are provided.

I hope the readers find this dissertation insightful and encouraging about the potential for utilization of carbon-neutral technologies, especially for hydrogen production and electricity generation. I wish that continued laboratory advances of this type will ultimately enable a civilization that is 100 % free of harmful carbon emissions.

1.2 Renewable resource-based devices for hydrogen production and energy storage

Hydrogen is an industrially relevant fuel and chemical feedstock, and it will only grow in importance as we adopt low- and zero-carbon technologies. This section provides an overview of the production routes and applicability of green hydrogen. It also presents the motivations of our lab to work on technologies related to hydrogen production and utilization. With hydrogen as a green fuel source, we envision to substantially minimize carbon-based emissions for a sustainable future.

1.2.1 Hydrogen economy

A total of 80 million metric tons of hydrogen is produced per year, out of which about 40% is used in ammonia synthesis, 30% is employed to refine petroleum; 20% is used in methanol synthesis; and the remaining 10% is used in other applications such as iron, steel or glass making.[1](figure 1.1) Hydrogen is used in the ammonia synthesis to react with nitrogen in a 3:1 ratio to produce ammonia gas, which serves as a precursor for various nitrogen-based fertilizers. [11] In petroleum refining, hydrogen is primarily used to reduce the sulfur content of the diesel fuel.[12] With the historical increase in demand for fertilizers, transportation, long-term energy storage, and the need to refine heavy crude oils, the demand for hydrogen has increased commensurately.[1, 2]

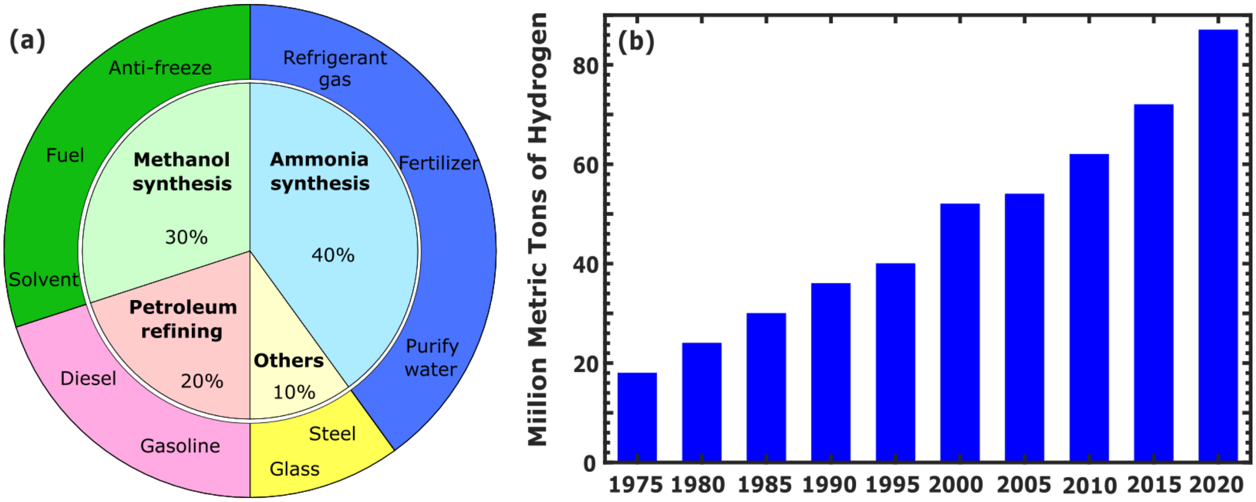

Figure 1.1: (a) Application of hydrogen as a fuel and chemical feedstock with the outer circle denoting the end user applications. (b) Global annual demand for hydrogen gas over the last four decades.The data is compiled from prior International Energy Agency (IEA) reports.[1, 2]

Figure 1.2 summarizes the carbon dioxide emissions and cost required to produce 1 kg of H_2 using various non-renewable and renewable resources.[3] Most hydrogen production relies on steam methane reforming (SMR) or coal gasification, as these are the cheapest sources.[3] About 75% of the hydrogen is generated from steam methane reforming, termed gray hydrogen. Moreover, hydrogen produced from steam methane reforming consists of a mixture of hydrogen and carbon monoxide (also known as syngas). To improve the hydrogen yield, additional processing steps such as water gas shift reactions or pressure swing adsorption reactions are needed. However, these processes increase the carbon dioxide emissions that result from hydrogen production. Hydrogen generation from coal gasification, termed brown hydrogen, is responsible for only about 25% of hydrogen production. However, since coal contains a greater ratio of carbon to hydrogen, coal gasification releases more carbon dioxide and other harmful emissions.

Based on global reserves and the current rate of consumption of natural gas and coal, it is estimated that these non-renewable resources will last for 5–10 decades, but it is reasonable to expect continued exploration to support a fossil resource base that could last for centuries.[13, 14] However, the carbon emissions from these sources are a serious threat to the climate change. It is therefore

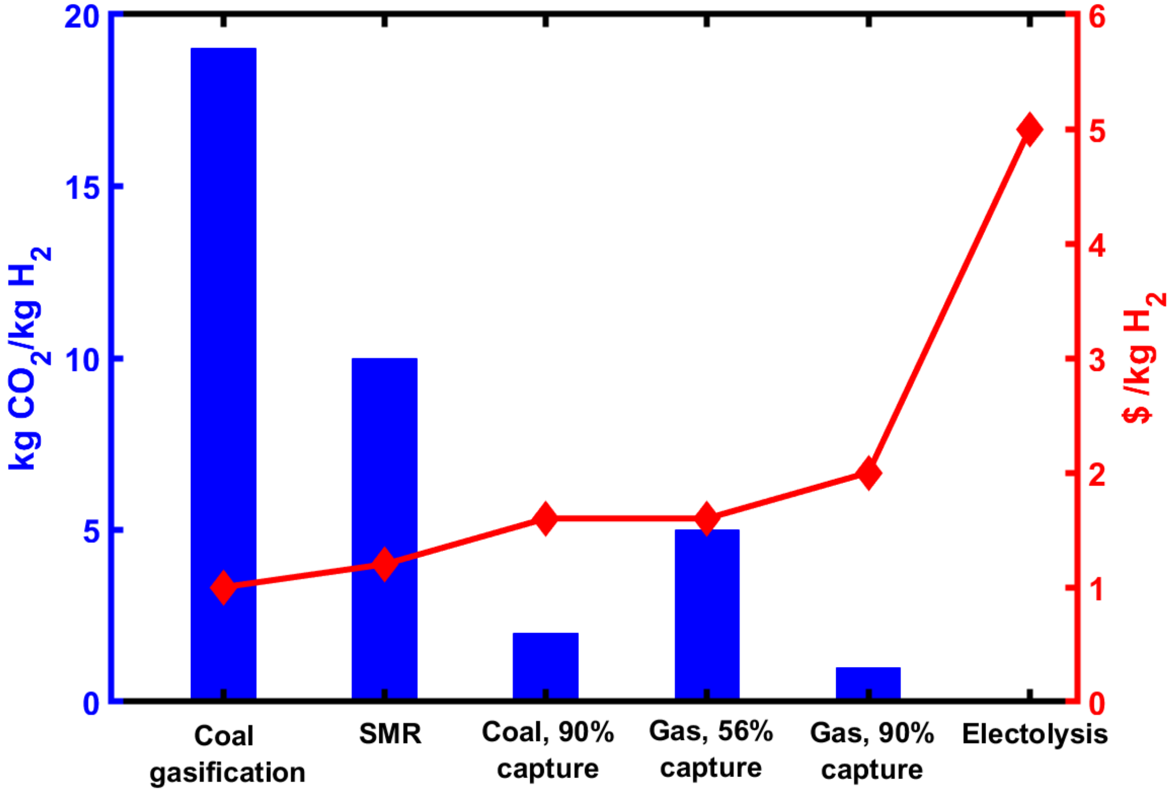

Figure 1.2: Carbon dioxide emissions per kg of H_2 and cost of production of 1 kg of H_2 for various non-renewable and renewable resources. (SMR denotes Steam Methane Reforming). The data is compiled from prior report from Resources for the Future.[3]

imperative to mitigate carbon-based emissions and limit the net increase in the global temperature. For example, the Paris Climate Agreement stipulates that global temperature should not be allowed to increase more than 1.5 ^{o}C.[15]

Carbon capture, utilization, and storage (CCUS) techniques can mitigate the carbon dioxide emission from natural gas- and coal-based hydrogen production. With CCUS, about 90% of the carbon capture can be achieved, and the hydrogen produced this way is referred to as blue hydrogen. Nonetheless, the production of clean hydrogen in cost-effective way using these technologies remains a challenge. Moreover, while natural gas and coal have the potential to meet the current hydrogen demand with lower average carbon dioxide emissions, they will not suffice for an indefinite time.

Thus to meet long-term climate goals, while continuing to produce important fuels and chemicals, there is a need to find an alternative renewable resource-based technique with lower carbon dioxide emission for hydrogen production.

1.2.2 Water electrolyzers

The main focus of my doctoral research was on water electrolysis, which offers the potential for a near-zero carbon emission route for hydrogen production. Water electrolysis is the process by which electricity is used to split water into hydrogen and oxygen gases (equation 1.1).

$$2\,\mathrm{H_2O_{(aq)}} \longrightarrow 2\,\mathrm{H_{2(g)}} + \mathrm{O_{2\ (g)}} \qquad \Delta E = 1.23 V vs..RHE \tag{1.1}$$

The potential difference between the two half reactions of water splitting—hydrogen and oxygen evolution—is 1.23 V, but in practice, at least 1.5–1.6 V is required at modest temperatures due to sluggish reaction kinetics. Because renewable electricity remains considerably more expensive than the commodity cost of fossil fuels on a cost/energy basis, the cost associated with renewable hydrogen production from electrolysis at the current stage is high. *Therefore, the overarching objective of my dissertation research has been to reduce the cost associated with electrolysis to less than $2/kg for hydrogen production.*[16]

A detailed accounting of the technological viability of renewable hydrogen production depends on the cost and carbon emissions associated with the source of electricity. A cost-effective and carbon neutral electricity source is therefore needed. Currently, 60% of the global electricity is produced from non-renewable resources such as coal and natural gas.[17] The carbon-based emissions arising from these sources can be significantly reduced if the electricity is generated via renewable sources such as solar and wind. The intermittent nature of these renewable resources, however, demands efficient electric grid management to maintain a balance between the supply and demand for electricity. Energy storage thus plays a critical role to reduce the gap between electricity supply and demand.

1.2.3 Fuel cells

To enable efficient energy storage, various options can be considered, including: mechanical (pumped hydrogen systems and compressed air); electrical (supercapacitors); electrochemical (batteries, flow batteries); and chemical (hydrogen and other fuels); as shown in figure 1.3.[18] Hydrogen is attractive as a carbon-free store of energy due to its very high gravimetric energy density of 145 MJ/kg, which is three times greater than gasoline and ∼100 times greater than solid-state batteries.[19] Thus the use of hydrogen for energy storage is promising and *a secondary focus of my dissertation research was on the development of catalysts for hydrogen fuel cells.*

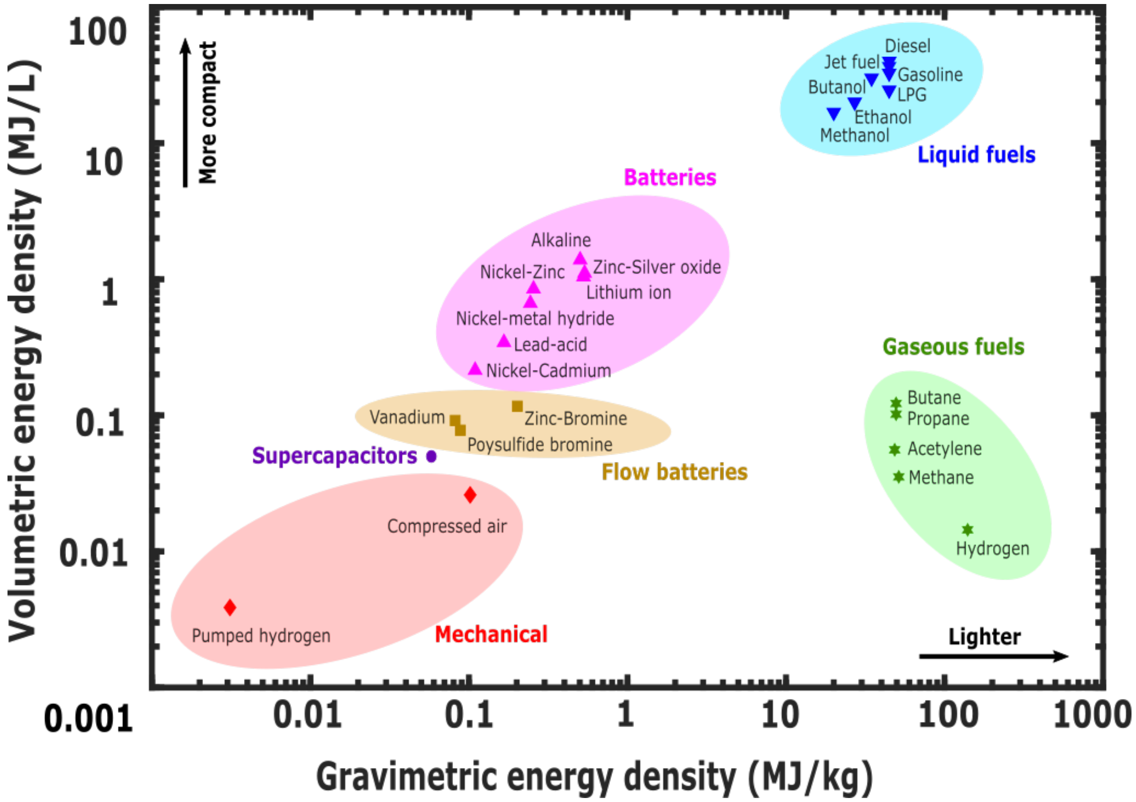

Figure 1.3: Comparison of gravimetric and volumetric energy densities of various energy conversion and energy storage technologies. The data is compiled from prior work by Rajasegar et al. and Sabihuddin et al.[4, 5]

Hydrogen fuel cells combine hydrogen and oxygen gases to generate water and electricity (equation 1.2).

$$\mathrm{H}_{2(\mathrm{g})} + \frac{1}{2}\,\mathrm{O}_{2\ (\mathrm{g})} \longrightarrow \mathrm{H}_2\mathrm{O}_{(\mathrm{aq})} \qquad \Delta E = 1.23 V vs..RHE \tag{1.2}$$

The theoretical voltage extracted from a hydrogen fuel cell is 1.23 V at standard state, but in practice, the potential lower than 1.23 V is obtained again due to sluggish kinetics.

Some types of hydrogen fuel cell systems can already be considered mature technologies. Fuel cells have been in commercial operation in space craft for 7 decades.[20] NASA first employed fuel cells in the Gemini mission and later in the Apollo mission. Fuel cells have been the primary source of electrical power on human spaceflight systems and efforts are also underway, by Airbus, to operate an airplane on fuel cells.[21] To minimize carbon emissions and for a sustainable future, Lancaster, a city in California, has become the first city in the United States to operate with hydrogen power.[22] Amongst the automobiles, Toyota Mirai, a hydrogen fuel cell-operated mid-size car has been on market for the last 7 years.[23] More recently, Hyundai Nexo was commercialized as a fuel cell SUV that runs a total of 551.5 miles in one fuel tank.[24]

In comparison to established battery vehicles, the fuel cell vehicles offer lower greenhouse gas emissions (provided the hydrogen fuel was generated using low- and zero-carbon resources) and require less fueling time, but they still suffer from high capital costs.[25] The cost of energy storage (battery vs. hydrogen) depends on system size and storage times. Based on the cost comparisons for batteries and hydrogen, it was observed that batteries are advantageous for short-term storage whereas compressed hydrogen is most effective for storage time exceeding three days. Thus, fuel cell vehicles are particularly explored for heavy duty vehicles including buses and trucks. However, the volumetric energy density of hydrogen is low, causing difficulties in its storage compared to conventional liquid fuel.[26]

1.2.4 Regenerative fuel cells

A significant research effort is underway to develop strategies for efficient hydrogen storage, including liquid hydrogen, compressed gas, solid-state storage in metal and chemical hydrides, and liquid-state storage in organic hydrides.[27, 28, 29, 30, 31] Another strategy to minimize the hazards associated with storage and transportation of hydrogen is to *use hydrogen at the same location where it is generated in regenerative fuel cells (RFC).* A regenerative fuel cell is a type of fuel cell which operates in a reversible mode, wherein the hydrogen generated from an electrolyzer is used directly in a fuel cell for electricity generation. Thus, RFCs are similar to batteries but with the added advantage of decoupled energy and power.[32] Unlike conventional batteries, fuels are stored outside the electrochemical stack, and thus the energy stored in RFC is unaffected by time, temperature, and the number of charge/discharge cycles. Moreover, RFCs benefit from the very high gravimetric energy density hydrogen fuel.[33] RCS are therefore especially useful for applications where a large amount of energy must be stored for long periods, such as remote off-grid power sources, emergency or backup power generation. Additional applications include continued development as energy storage/propulsion systems for space crafts, and long endurance high altitude aircraft. The first practical demonstration of RFC was by the General Electric Company in 1961, and they argued in favor of the technology as especially promising for space application.[34]

1.3 Research challenges

Electrochemical technologies related to generating and using hydrogen gas, such as water electrolyzers, fuel cells, and regenerative fuel cells, have been developed for many decades and have reached various stages of technological maturity. This section will dive deeper into those technologies to understand the key research challenges.

Regenerative fuel cells (RFCs) are divided into two configurations – discrete (DRFC) and unitized (URFC); schematics shown in figure 1.4.[6] DRFC consists of two separate units for energy generation (fuel cells) and energy storage (electrolyzers). On the contrary, URFCs use a single unit that can operate as either a fuel cell or an electrolyzer. Compared to DRFC, URFCs offer lower capital cost, simpler structure, higher specific energy, and no need for auxiliary heating.[6] Such a reversible system also uses catalysts that are either a mixture of catalysts for electrolyzer and fuel cell reactions, or they comprise a single catalyst that is reversible for each reaction.

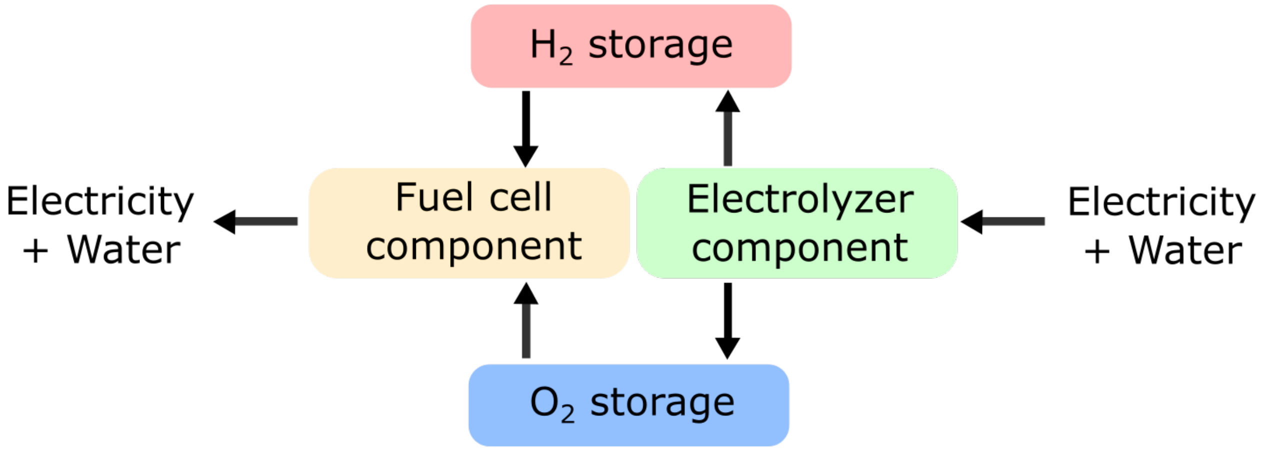
(a) Discrete regenerative fuel cell (DRFC)

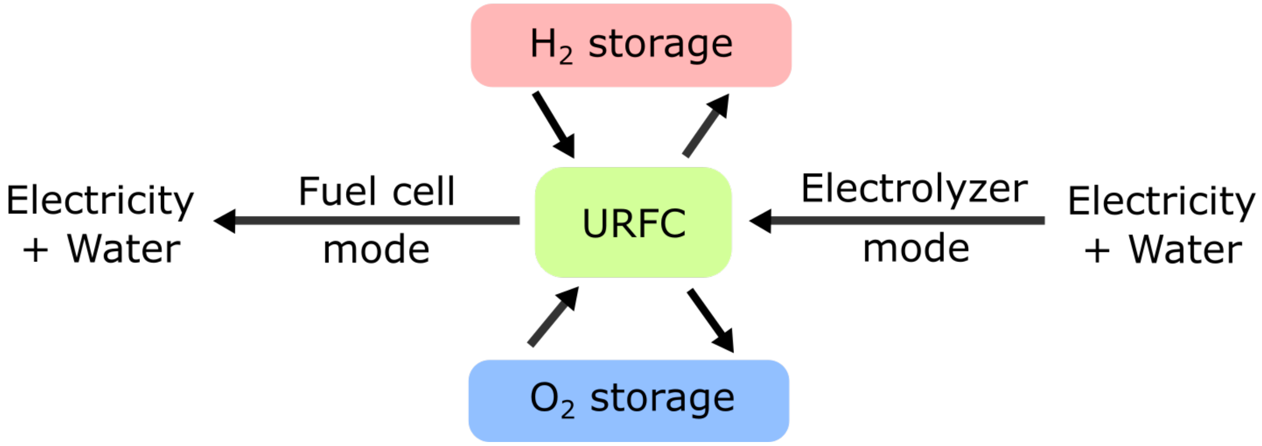
(b) Unitized regenerative fuel cell (URFC)

Figure 1.4: Schematic of (a) discrete (DRFC) and (b) unitized (URFC) regenerative fuel cells [6]

These devices are further divided into two categories depending on the type of electrolyte used—acidic or alkaline. Schematics for several configurations are shown in figure 1.5. A subgroup of alkaline systems is the alkaline anion exchange membrane (AAEM) configuration, which uses an anion-conducting polymer membrane to neutralize charge across the negative electrode (which catalyzes the reactions involving hydrogen) and the positive electrode (for reactions involving oxygen).

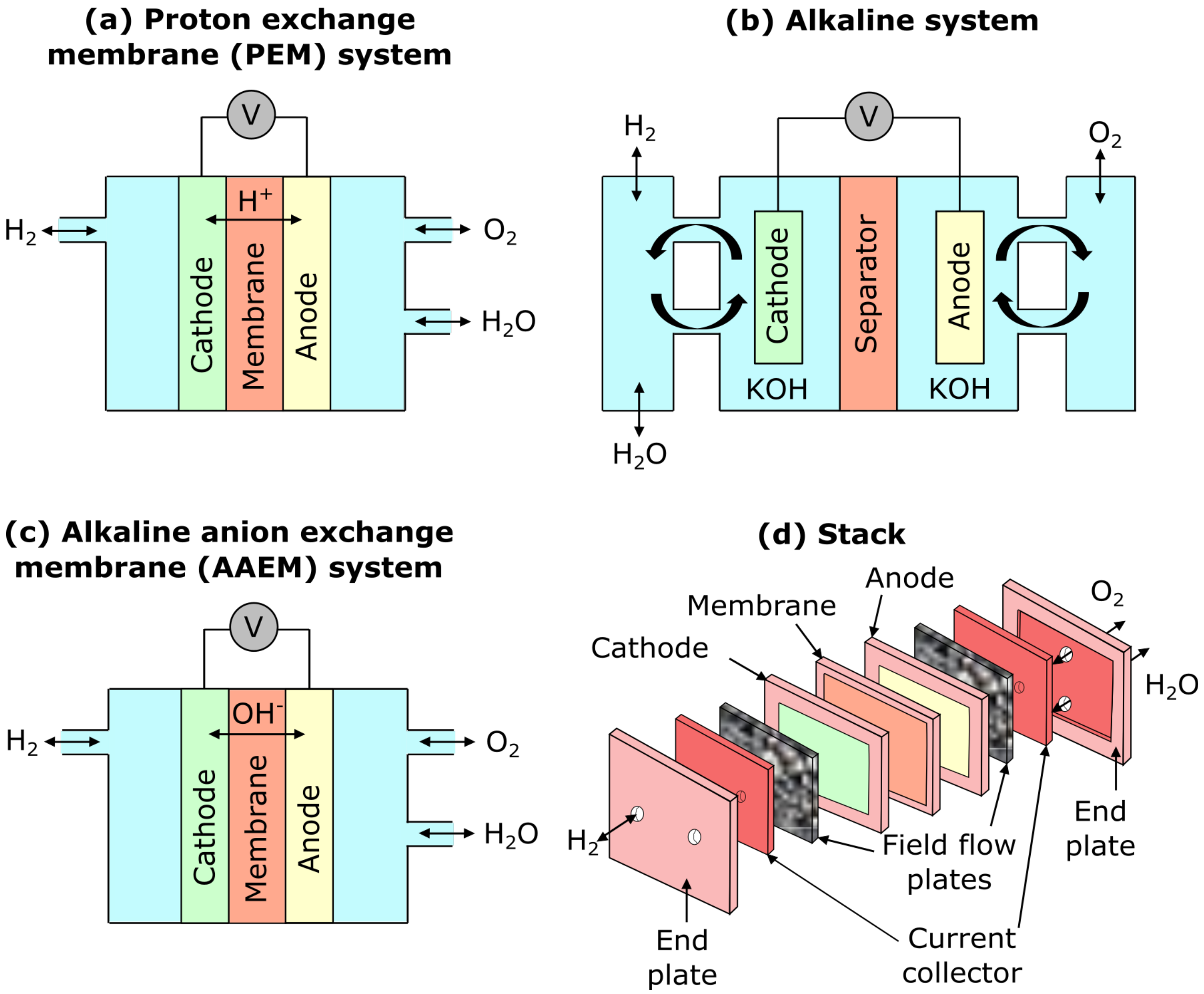

Figure 1.5: Schematic of electrolyzer and fuel cell systems in (a) Proton exchange membrane (PEM), (b) liquid Alkaline, and (c) Alkaline anion exchange membrane (AAEM) configurations. (d) Typical stack of membrane electrode assembly in an electrolyzer or a fuel cell.

The main characteristics of electrolyzers and fuel cells are described in table 1.6.[7, 8, 9, 10] Proton-exchange membrane (PEM) electrolyzers and fuel cells are compact systems and are also commercialized but require precious metal catalysts as electrodes and ancillary components due to the corrosive acidic environment. Liquid alkaline systems, on the other hand facilitate the use of non-precious catalysts and ancillary components, which results in significantly lower capital cost. These systems, however, are significantly bulkier than PEM systems and suffer from higher electrolyte resistance and gas crossover. AAEM configurations are technologically less mature than alkaline systems but are advantageous to overcome their limitations and ultimately decrease the operating cost.[35, 36, 37] Thus, AAEM systems are promising to meet the DOE cost target of \$2/kg hydrogen production and for cost-effective carbon neutral electricity generation using hydrogen. However, significant research needs to be directed towards investigating efficient membranes and catalysts for AAEM configurations.

Our research group is working to develop non-precious catalysts that enable the efficient and cost-effective interconversion between electricity and energy stored in fuels and chemicals. Various non-precious catalyst candidates are promising for use in AAEM electrolyzers and fuel cells. However, the activity demonstrated by non-precious catalysts is lower than precious counterparts, and their long-term stability is relatively unexplored. The mechanism for activity enhancement in non-precious transition metal catalysts is also not very clear. Various hypotheses have been put forward, many of which implicate cooperative reactivity between multiple chemically distinct surface sites. Despite significant research in the field of fuel cell and electrolyzer catalysis, the dual research challenges of low activity and poor stability remain.

In that regard, my doctoral dissertation focuses on improving the performance of Ni-based catalysts for hydrogen evolution, hydrogen oxidation and oxygen evolution reactions with an intention to ameliorate the technological viability of AAEM electrolyzers and fuel cells. The specific research aims of this work include:

1. Elucidate the nanoscale composition of several high performing Ni-based catalysts

The composition of Ni-based catalysts was studied using various characterization techniques, including transmission electron microscopy (TEM) and X-ray photoelectron spectroscopy (XPS). The structural evolution of these catalyst composites was also monitored using *in situ* TEM analysis. This work is described in detail in Chapter 4.

2. Develop methodologies to understand the influence of metal/metal-oxide interfaces on hydrogen evolution/oxidation catalysis

The significance of the compositional analysis on Ni-based catalysts towards their practical performance for hydrogen reactions was speculated. Novel synthetic and analytical techniques were also developed to understand how the elementary steps of hydrogen evolution/oxidation are accelerated at metal/metal-oxide interface sites. These techniques are also discussed in Chapter 4.

	Electrolyzer			**Fuel cell**		
	PEM systems	**Alkaline systems**	**AAEM systems**	**PEM systems**	**Alkaline systems**	**AAEM systems**
Electrolyte	PEM (e.g., Nafion)	Aqueous KOH (20 – 40 wt%)	Anion exchange membrane	PEM (e.g., Nafion)	Aqueous KOH (30 – 40 wt%)	Anion exchange membrane
Cathode	Pt-based	Ni-based	Ni and its alloys	Pt	Pt, Pd, Ag, MnO_2	Mn, Co oxides or heteroatom doped C
Anode	Ir-oxide based	Ni-based	Ni, Fe, Co oxides	Pt	Pt, Pd, Raney Ni	Ni and its alloys
Separation	Nafion 117 (e.g., 180 µm)	Diaphragm (Zirfon Perl 500 µm)	(under active research)	Nafion 117	Aqueous KOH (30 – 40 wt%)	(under active research)
Current density (A/cm^2)	0.6 – 2	0.2 – 0.4	0.2 – 1	1	0.1 – 0.3	0.3 – 10
Cell voltage (V)	1.8 – 2.2	1.8 – 2.4	1.8 – 2.2	0.6 – 0.7	0.6 – 0.7	0.6 – 0.7
Temperature (^{o}C)	50 – 80	60 – 80	50 – 60	60 – 80	40 – 75	50 – 90
Pressure (bar)	30 – 76	1 – 30	1 – 30	3 – 4	1 – 3	1 – 3
Production rate (m^3/h)	< 40	< 760	< 1	-	-	-
Gas purity (vol %)	> 99.9999	> 99.5	-	-	-	-
Peak power density (mW/cm^2)	-	-	-	700 – 1500	50 – 300	100 – 3500
Stack lifetime (h)	20 – 60k	60 – 100k	-	5 – 20k	> 5000	-
Technology status	Commercial	Mature	Laboratory scale	Commercial	Mature	Laboratory scale
Capital cost (\$/kW$_{el}$)	2300 – 3000	1200 – 1500	-	2300 – 3000	3000 – 4000	-

Figure 1.6: Comparison between different configurations for electrolyzers and fuel cells. This data is obtained from several prior reports on electrolyzer and fuel cell technologies. [7, 8, 9, 10]

3. Formulate highly active and stable Ni-based catalysts for alkaline hydrogen and oxygen electrochemistry

Based on the nanoscale compositional insights, the activity of Ni-based catalysts was improved by developing different synthetic and processing techniques. An assessment of the durability and practical device performance of the best catalyst compositions was also completed. A detailed narrative of these studies is presented in Chapters 5 and 6.

We are ultimately interested in developing catalysts that can accomplish reversible hydrogen and oxygen electrochemistry for applications in regenerative fuel cells. Successful completion of these objectives will provide insights into the composition-activity relationships of non-precious electrocatalysts. Better catalysts can then be developed by either modifying the existing catalysts or synthesizing new ones based on these insights.

2.0 Scientific and Technological Background

Alkaline anion exchange membrane (AAEM) electrolyzers and fuel cells are promising for cost-effective and green hydrogen production and energy storage. This chapter will elaborate on their key components, particularly membranes and catalysts. The primary motive of this chapter is to explain the functioning of alkaline anion exchange membranes and catalysts and thus describe the critical performance parameters. Our focus is particularly on Ni-based electrocatalyst materials and therefore current challenges towards their practical implementation are presented. The interest in AAEM electrolyzers and fuel cells is spurred because they facilitate cost reduction. Brief economic estimates, adopted from limited sources, are also provided to envision their commercialization.[38, 39, 40]

2.1 Cost analysis

The complete cost analysis of AAEM electrolyzers and fuel cells has not been executed due to lack of commercial operations, but accurate estimates have been made. We will focus this economic discussion only on AAEM electrolyzers, but the results are likely to be similar for AAEM fuel cells. The total cost of hydrogen production consists of capital expenditure (CAPEX) and operational expenditure (OPEX). CAPEX includes the cost of an electrolyzer, compression plant (to increase the pressure of hydrogen for storage), storage system, direct and indirect depreciable capital cost.[39] OPEX includes the cost of material, labor, upstream products such as deionized water, KOH, steam, and nitrogen.

The cost of catalysts, membranes and other electrolyzer stack components are considered as capital expenditures. AAEM systems facilitate the use of Ni-based non-precious catalysts compared to Pt-based precious metals in PEM systems. And because catalysts contribute significantly to the cost of the electrode, AAEM electrodes are markedly cheaper than the PEM systems.[40]

Additional components in AAEM electrolyzer stacks comprise gas diffusion layers, bipolar plates, and current collectors, and these can be fabricated from carbon cloth, stainless steel, or Ni. Although the material of construction for the gas diffusion layer in PEM electrolyzer stacks is the same as that of AAEMs, the bipolar plate and current collector are derived from expensive Pt coated stainless steel or Ti. Thus, the total stack cost of AAEMs is about half of that of PEM systems.[38] It is therefore predicted that with non-precious catalysts and ancillary components in AAEM electrolyzers, the DOE cost target of $2/kg can be attained.[40, 16]

2.2 Membranes

The choice of a membrane is critical for an efficient AAEM electrolyzer and fuel cells. The primary role of AAEMs is to be able to transfer hydroxide ions through them. Alkaline anion exchange membranes are polymer electrolytes with cationic (positively charged) groups covalently bounded to a polymer backbone. These cationic groups can either be incorporated in the backbone or bound through side chains (via alkyl or aromatic groups). The most common polymer backbones are poly(arylene) ethers, poly(ether ketones), poly(ether imides), poly(ether oxadizoles), poly (phenylene oxides), perfluorinated, polyethylenes, polystyrenes, poly(vinlybenzyl chloride) and poly(vinyl alcohol). The most studied cationic head-group chemistries include quaternary ammoniums, heterocyclic systems, guanidinium systems, phosphonium types, sulfonium types, and metal-based systems.[41]

They have lower conductivity and oxidative stability than well-renowned proton exchange membranes.[32] Significant research is therefore underway to reduce this performance gap. Moreover, AAEMs react with carbon dioxide in the air to form carbonates and thus require a closed system to operate. The parameters of a membrane that are important for their effective performance are hydroxide conductivity, ion-exchange capacity, swelling, and stability.

Hydroxide conductivity is the measure of the ability of the membrane to conduct hydroxide ions. It is inversely proportional to the voltage drop across the membrane. Most AAEMs report hydroxide conductivities between 5–20 mS/cm, while commercialized proton-conducting membrane, Nafion 117, exhibits proton conductivity of 78 mS/cm.[42] The advancement in hydroxide conductivity is especially challenging because the mobility of hydroxide in aqueous media is considerably lower than proton mobility.[41] With advancements in polymer chemistry and improved conductivity measurement techniques, membranes with very high hydroxide conductivity (hundreds of mS/cm) are also reported.[43] The hydroxide conductivities of 100 mS/cm are considered to be optimum, which are expected to give a voltage drop of 1 mV in an electrolyzer operating at 1 A/cm^2 with a 100 μm thick membrane.

Ion exchange capacity (IEC) is another important parameter to assess the effectiveness of a membrane. It represents the number of functional groups per unit polymer mass. Thus, a high ion exchange capacity of the membrane is desirable to increase the hydroxide conductivity. However, with an increase in ion exchange capacity, the water uptake and membrane swelling also increase. Strategies such as synthesis of self cross-linking polymers or self aggregating polymers are executed to mitigate membrane swelling without affecting the IEC.[44] It is believed that the proton conduction in Nafion occurs through a hopping mechanism via phase segregation of the hydrophilic and hydrophobic domains.[45] The IEC of Nafion is about 0.92 mmol/g and is expected that the local IEC is significantly higher.[41] In AAEMs, the hydroxide conduction is hypothesized to proceed via the same hoping mechanism but the phase segregation of the hydrophilic and hydrohphobic domains is expected to assist ion conduction.[46] The highest IEC reported to date for AAEMs is therefore about 2 mmol/g.[47]

Stability of AAEMs in alkaline conditions is significantly lower than those of PEMs in acidic conditions. The degradation of AAEMs can occur at the backbone as well as at the functional groups. The degradation of the polymer backbone decreases the mechanical stability of the membranes while degradation of the functional groups reduces the ionic conductivity. There are various mechanisms by which membrane degradation is plausible. The most common cause is nucleophilic substitution in which hydroxide reacts with the methyl group to form methanol or with methylene group to form free trimethyl amine.[48] Hofmann elimination of the β hydrogen atoms to form free amine groups is another possibility. The loss of amine groups from the polymeric chain perturbs the cross-linking ability of the membrane and also affects the ionic conductivity. AAEMs also tend to undergo chemical degradation on contamination with transition metal ions (such as Ni or Fe) to form reactive oxygen species (such as hydroxyl or hydroperoxyl radicals) in the membrane. In general, degradation of a membrane is proportional to the number of hydroxide ions in the membrane.

Despite significant progress on alkaline anion exchange membranes, a research challenge to make conductive and stable membranes remains. Our research group does not develop new AAEM materials, but we have established a collaboration with a start-up company that has shown a promising membrane performance. The details of the analysis are presented in Chapter 5.

2.3 Electrocatalysts

As noted previously, the focus of my thesis research was to study non-precious Ni-based catalysts for alkaline hydrogen and oxygen electrochemistry. Alkaline systems offer non-corrosive environments and facilitate the use of these types of non-precious catalysts, which is expected to translate into a significant reductions in capital cost. This section presents an overview of the typical characteristics of the catalysts studied for the hydrogen evolution reaction (HER), the hydrogen oxidation reaction (HOR), and the oxygen evolution reaction (OER).

2.3.1 Hydrogen evolution

The hydrogen evolution reaction (HER) is the cathodic reaction in an electrolyzer where water consumes electrons to form hydrogen gas and hydroxide ions are passed through the membrane. The hydrogen evolution reaction in alkaline conditions is given by equation 2.1.

$$2\,\mathrm{H_2O} + 2\,\mathrm{e^-} \longrightarrow \mathrm{H_2}_{\,(g)} + 2\,\mathrm{OH^-_{(aq)}} \tag{2.1}$$

This reaction occurs via a series of elementary steps as shown in equations 2.2- 2.4.

$$Volmer : \mathrm{H_2O} + * + \mathrm{e^-} \longrightarrow \mathrm{H^*} + \mathrm{OH^-} \tag{2.2}$$

$$Heyrovsky : \mathrm{H^*} + \mathrm{H_2O} + \mathrm{e^-} \longrightarrow \mathrm{H_2} + \mathrm{OH^-} + * \tag{2.3}$$

$$Tafel : 2\,\mathrm{H^*} \longrightarrow \mathrm{H_2} + 2\,* \tag{2.4}$$

The overall reaction is understood to proceed either via a Volmer–Heyrovsky or Volmer–Tafel mechanism. In either route, hydrogen adsorption also requires dissociation of a water molecule, and this process is also considered to be critical for efficient alkaline hydrogen evolution.

A major concern in hydrogen evolution reactions is the ability of a catalyst to bind hydrogen. The propensity is described by the Sabatier principle, where HER catalytic activity can be expressed as a function of metal-hydrogen bond strength. The metals that bind hydrogen too strongly or too weakly each display low activity. An ideal catalyst should display an optimum intermediate binding energy for hydrogen, such that both the hydrogen adsorption and desorption processes are kinetically fast.

Ni-based catalysts have been extensively studied for the HER due to their relatively moderate affinity for hydrogen among non-precious transition metals. However, Ni is still understood to bind hydrogen too strongly and therefore the formation of dihydrogen becomes rate-determining. To solve this problem, efforts have been directed to make a solid solution of Ni with metals that poorly bind hydrogen with an intention to optimize the binding energy on Ni. These advances led to the discovery of various Ni-based alloys including Ni–Co, Ni–Cu, Ni–Mo, and Ni–W.[49, 50, 51, 52, 53] Among the full library of catalysts studied, Ni–Mo is one of the most active for hydrogen evolution reaction, and it also displays promising long term stability.[51] Nonetheless, the alkaline HER performance of these Ni-based catalysts is considerably lower than benchmark precious transition metal-based catalysts, which are typically based on Pt.

Focusing now specifically on Ni–Mo composites, the mechanism by which these catalysts give higher HER activity than other non-precious counterparts is still not clear. Various theories have been put forward to explain the enhanced activity in Ni–Mo composites. Incorporation of Mo may affect the electronic state or oxidation state of Ni, so that the binding energy of hydrogen is weaker on Ni–Mo compared to Ni.[54, 55, 56, 57, 58, 59] To this effect, increasing the Mo content of Ni–Mo alloys has been shown to increase the HER activity.[60, 51] Many Ni–Mo catalyst also contain Ni- and Mo-based oxides, which have also been implicated as important for HER catalysis.[61, 62] However, the specific influence these oxides on catalysis is not clear. Several researchers support the claim that the oxides accelerate the water dissociation step, while others argue that oxides dissolve in the electrolyte and do not participate in the HER.[63, 64, 65]

2.3.2 Hydrogen oxidation

The hydrogen oxidation reaction (HOR) is the anodic reaction in fuel cells wherein gaseous hydrogen in combination with hydroxide ions generate water and electricity (equation 2.5).

$$\mathrm{H_2}_{\,(g)} + 2\,\mathrm{OH}^-_{(aq)} \longrightarrow 2\,\mathrm{H_2O} + 2\,\mathrm{e}^- \tag{2.5}$$

This is however not a single step reaction and the detailed reaction mechanism is shown in equations 2.6- 2.8.

$$Tafel : \mathrm{H_2} + 2\,{*} \longrightarrow 2\,\mathrm{H}^* \tag{2.6}$$

$$Heyrovsky : \mathrm{H_2} + \mathrm{OH}^- + {*} \longrightarrow \mathrm{H}^* + \mathrm{H_2O} + \mathrm{e}^- \tag{2.7}$$

$$Volmer : \mathrm{H}^* + \mathrm{OH}^- \longrightarrow \mathrm{H_2O} + {*} + \mathrm{e}^- \tag{2.8}$$

The reaction proceeds either via Tafel-Volmer or Heyrovsky-Volmer pathway. In either route, dissociation of hydrogen molecule and recombination with hydroxide are critical parameters for HOR.

A major concern in the hydrogen oxidation reaction at non-precious catalysts is the stability of the electrodes under oxidizing conditions. According to the Pourbaix diagram, most non-precious transition metals exist as oxides or hydroxides in alkaline pH at applied potentials associated with hydrogen oxidation.[66] A small proportion of oxides/hydroxides on metal surfaces are believed to enhance HOR by accelerating the hydroxide adsorption step in the HOR reaction mechanism[67]. A study focused on dissolution dynamics of transition metals under HOR conditions showed that Mo-oxides tend to readily dissolve in solution even under open circuit potential (no current flow), whereas the dissolution of Cu-oxides is potential dependent.[68] In the same study, Ni, Co, and Fe oxides were least prone to dissolution.

Historically, Raney Ni derivatives were used as catalysts for HOR in liquid alkaline fuel cell systems owing to their high surface area.[69, 70, 71, 72, 73, 74, 75] However, the long term stability of these catalysts is affected due to poor catalyst pore wetting and changes in catalyst morphology.[76] With advances in catalysts, promising alternative candidates include Ni–Mo, Ni–Ti and Ni–Cu composites.[77, 78, 79, 80, 81, 82, 83, 84, 85, 86, 87, 88] Tertiary alloys comprising Co, Ni, and Mo and Ni-based catalysts supported on functionalized carbon are also gaining interest.[89, 90, 91, 92]

Similar to the hydrogen evolution reaction, the overarching design principles for active HOR catalysts follow the Sabatier principle: they must have binding energy for hydrogen intermediates that is neither too strong nor too weak. Kabir et al. hypothesized that incorporation of Mo in Ni lattice decreases the binding energy of hydrogen on Ni. [82] The possibility of accelerating the Volmer step of the reaction because of the presence of Mo-oxides was also mentioned. However, after long-term stability experiments in a membrane electrode assembly (MEA), they observed complete dissolution of the Mo-oxides, while the surface of the catalyst became enriched in Ni-hydroxides and a smaller proportion of mixed nickel-molybdenum oxides. More recently, Duan et al. synthesized Ni_4Mo alloy catalyst using a microwave synthesis approach and showed excellent activity and stability for the HOR, comparable to benchmark Pt catalyst.[88] Roy et al. claimed that Ni–Cu alloys are better than Ni–Mo alloys due to improved dewetting behavior associated with the use of less oxophilic Cu. A ternary system consisting of CoNiMo alloy was also studied by Sheng et al., who claimed this mixture exhibits an improved hydrogen binding energy relative to binary Ni–Mo.[93] Despite these practical advances, the exact mechanism(s) for enhanced HOR activity in all of these Ni-based alloys is still unclear.

2.3.3 Oxygen evolution

The oxygen evolution reaction is the anodic reaction in an electrolyzer where water and electrons are produced as by-products. The oxygen evolution reaction in alkaline conditions is given by equation 2.9.

$$4\,\mathrm{OH}^-_{(aq)} \longrightarrow 2\,\mathrm{H_2O} + 4\,\mathrm{e}^- + \mathrm{O}_{2\ (g)} \tag{2.9}$$

Multiple reaction pathways for this process have been put forward with oxides, peroxides or both as reaction intermediates.[94, 95, 96, 97] This reaction requires the transfer of 4 electrons, which results in sluggish kinetics, while the possibilities of various adsorbed intermediates (O^*,OH^*,OOH^*) makes the identification of a single "descriptor" (analogous to hydrogen binding energy for the HER) more difficult.

Metal catalysts generally undergo structural and chemical changes to metal oxides or soluble species during the operating conditions of OER.[66] The aqueous reaction environment also means that thermodynamically stable (oxy)hydroxides are more relevant for OER than crystalline oxides. Iridium and ruthenium oxides are the most active precious metal OER catalysts in alkaline conditions.[98, 99] A comparative benchmarking study of non-precious nickel and cobalt-based catalysts for OER in alkaline conditions showed that Ni–Fe catalysts display especially promising activity and stability, better than even precious metal catalysts.[98] Ni–Fe catalysts were first discovered, however, in the 1980s when Corrigan et al. were working on nickel-based batteries and found Fe impurities to catalyze the parasitic oxygen evolution during the charging phase.[100]

Various types of Ni–Fe composites in the form of mixed oxides, hydroxides, oxyhydroxides, spinels, alloys, and layered double-hydroxides have all been reported to exhibit alkaline OER performance that rivals the precious metal catalysts.[101, 102, 103, 104, 105, 106, 107] Despite this broad range of chemical compositions, it is plausible that the surface chemistry of many of these catalysts are similar under OER conditions. It is established that the NiO layer is instantaneously formed when Ni encounters aqueous alkaline solution, which then gets converted to α–Ni(OH)$_2$ under oxidizing conditions.[95] Moreover, in the presence of Fe, Ni(OH)$_2$ converts to a layered double hydroxide. Ni-based (hydr)oxides are also known to “age” in alkaline solutions, causing the transformation of α–Ni(OH)$_2$/γ–NiOOH to more compact and ordered β–Ni(OH)$_2$/β–NiOOH.[102] The effect of Fe incorporation into these materials has also been studied, and it is believed that up to 30 mol% Fe can be incorporated in the Ni lattice before it begins to phase segregate.[108, 109] Nonetheless, all known OER catalysts exhibit a relatively large onset overpotential of about 200–300 mV near room temperature, which constitutes an efficiency loss of 15–20% relative to the free energy stored in H_2 and O_2 at room temperature.

Long term stability of Ni-based OER catalysts is generally a major concern for these materials. Corrosion or degradation of the catalyst under oxidizing conditions often limits the choices for catalysts and catalyst supports. The conductivity of these catalysts is also a crucial factor, as metal oxides and hydroxides often exhibit semiconducting or insulating behavior. Incorporation of graphitized conductive carbon supports is the most convenient solution to deal with this electronic conductivity concern, but graphitic carbon is thermodynamically unstable under OER conditions. Nontheless, NiFe layered double hydroxides (LDH) synthesized by direct nucleation and growth on oxidized multiwalled carbon nanotubes (CNT) displayed high activity and stability for at least 1 hour.[104] No oxidative etching was reported and the charge transfer was associated with the strong bonding between LDH and CNTs. A sandwich Ni–Fe/C assembly was also proposed as stable OER catalyst which displayed excellent stability for 40 hours.[106] However, in practice there have not yet been credible reports of Ni–Fe catalysts with high stability toward the alkaline OER for thousands of hours, as would be required for AAEM operation.

3.0 Unsupported Pt nanoparticles for electrochemical applications

This chapter is reproduced from a manuscript posted on the ChemRxiv preprint server titled “Unsupported Pt Nanoparticles: Synthesis, Deactivation, and Hydrogen Electrocatalysis in Unpurified Electrolytes." A version of this manuscript is also under consideration for publication in a peer-reviewed research journal.

3.1 Introduction

Platinum is one of the most widely studied transition metals for applications in thermal and electrochemical catalysis.[110, 111, 112, 113, 114] The many thermocatalytic applications of Pt include automotive exhaust treatment [115, 116, 117, 118] as well as the production of nitric acid[119, 120], silicones [121, 122], and petrochemical feedstocks[123, 124]. Pt is also used ubiquitously in analytical and industrial electrochemistry, and many of these applications revolve around its high catalytic activity toward reactions involving hydrogen.[125, 126, 127, 128, 129, 130, 131, 132, 133, 134] For example, carbon-supported Pt catalysts (Pt/C) are used for the hydrogen evolution reaction (HER) in proton-exchange membrane electrolyzers and the hydrogen oxidation reaction (HOR) in low and intermediate temperature fuel cells.[135] Despite its very high catalytic activity, Pt is susceptible to deactivation under electrochemical conditions; thus, the dynamics and mechanisms of Pt deactivation have also been studied extensively.[136, 137, 138, 139, 140] The most prevalent deactivation processes generally fall in one of several categories: catalyst poisoning, particle growth, particle detachment, and dissolution. Ultimately, the dynamics of these deactivation processes dictate the practical lifetime of Pt catalysts. Thus, a major research focus on Pt has been on evaluating and minimizing the impact of catalyst deactivation in analytical and practical applications.[141, 142, 143, 144]

Owing to its very high catalytic activity for hydrogen evolution/oxidation electrocatalysis, Pt is used as a benchmark against which novel HER/HOR catalysts are measured. It is also used to calibrate voltage measurements in aqueous electrocatalysis via the determination of the reversible hydrogen electrode (RHE) potential in the electrolyte of interest. The propensity of Pt electrocatalysts to deactivate under reaction conditions makes these key measurements considerably more challenging.[145, 146, 147] Whereas prior studies have generally addressed this challenge by maintaining scrupulously clean experimental conditions,[141, 140, 142] routine measurements of novel electrocatalysts (and associated comparisons to Pt) are often carried out in unpurified, reagent-grade electrolytes. This motivates the question of whether control experiments using Pt electrodes can be properly executed.

Herein, we describe a straightforward preparation of unsupported Pt nanoparticles (NPs) as well as their use as a laboratory standard for hydrogen evolution/oxidation studies. We have focused on experimental conditions that are not scrupulously clean but are nevertheless representative of the methods and materials used for routine measurements in applied electrocatalysis research laboratories. Accordingly, we also studied the deactivation of Pt NPs, as reflected in the progressive loss of electrochemically active surface area. When cycled continuously between oxidizing and reducing conditions in unpurified aqueous acidic and alkaline electrolytes, our Pt NPs lost 25–40 % of their active surface area over tens of minutes. We also deployed identical location transmission electron microscopy (IL-TEM)[148, 149] to differentiate deactivation processes involving changes in catalyst morphology from those that do not. At positive potential limits below 1 V vs. RHE, we observed minimal changes in particle size/shape, implying the dominant mode of deactivation is catalyst poisoning rather than particle dissolution or growth. These observations were found to be consistent across acid and base conditions, but the relative rate of deactivation were modestly slower in base than in acid. By contrast, when the positive potential limit was increased to 1.5 V vs. RHE, the Pt NPs were found to grow in size, leading to irreversible loss in surface area.

3.2 Experimental

The synthesis protocol for Pt nanoparticles was developed from several prior literature reports.[150, 151, 152] A representative procedure is as follows. Aqueous stock solutions of 12 mM H_2PtCl_6 (99.5% Alfa Aesar) precursor and 100 mM sodium polyacrylate (average molecular weight $\sim$1200, 45 wt% in water, 99.5%, Alfa Aesar), respectively, were prepared by dissolution with ultrasonic agitation for at least 5 minutes. These solutions were prepared in bulk quantities and used for several synthetic runs. A fresh solution of 100 mM L-ascorbic acid reducing agent was prepared immediately before the synthesis by adding 0.0195 g of anhydrous L-$C_6H_8O_6$ (99.5%, Alfa Aesar) to 1 mL deionized water and mixed by sonication. In a 20 mL scintiallation vial, 0.833 g of 12 mM H_2PtCl_6 and 0.1 g of 100 mM sodium polyacrylate were added to 1 mL ascorbic acid solution. deionized water ($\geq$18 MΩ cm resistivity, Millipore) was then added to increase the solution volume to 10 ml. The final concentrations of the reagents in the precursor solution were 1 mM each of H_2PtCl_6 and sodium polyacrylate and 10 mM ascorbic acid. The precursor mixture was initially transparent with a slight yellow color.

The vial was placed in a preheated bath of silicone oil (Fluke 5010, Type 200.05) at 90 °C. The contents were stirred at 600 rpm for 60 minutes using a magnetic stir bar. The temperature was monitored using an alcohol thermometer to ensure that the variation was within $\pm$3 °C. Within 15 minutes, the solution became black and opaque. The reaction was allowed to continue for 60 minutes, and successive additions of deionized water were made every 20 minutes to maintain a constant total volume of solution. The vial was then removed from the bath and allowed to cool at room temperature. After cooling, 0.4 g NaOH (98%, Alfa Aesar) was added to the suspension to alkalize the solution to pH$\sim$14. The vial was then capped and left to stand at room temperature for 14 days, during which the black suspended solids settled to the bottom of the vial. Note that this settling process was sometimes found to proceed over a shorter timescale, but a 14-day incubation period was always found to be sufficient for particles to settle.

The clear solution above the settled layer was decanted using a pipette and the particles were extracted by centrifugation at 6000 rpm for 15 minutes. The supernatant was again decanted and the particles were re-suspended and centrifuged using 1 M aqueous NaOH solution a total of 3 times. Finally, the particles were suspended in 1.5 ml of deoinized water; this suspension was found to remain stable for several days. The colloidal solution was either used as-is or further diluted with pure deionized water as appropriate prior to subsequent analysis.

The NP yield was measured by depositing a known volume of the final colloid on a pre-weighed borosilicate glass microscope slide. The particles were dried under an infrared heat lamp (McMaster Carr, 125 watt, BR40 type bulb) for ~45 minutes. The mass of the glass slide with the dried film of Pt nanoparticles was again recorded. The particle yield was thus calculated by subtracting the mass of the initial uncoated slide from the Pt-coated slide. The average yield obtained after the centrifugation process from 6 synthetic runs was 1.48 ± 0.03 mg, which is 76 ± 1 % of the 1.95 mg theoretical yield. Note that this error bound, and all others unless otherwise noted, represent 1.96 times the standard error of the mean, which we interpret as a 95 % confidence interval.

The final, purified Pt NPs were characterized with respect to composition and morphology using Fourier-transform infrared spectroscopy (FTIR), X-ray diffraction (XRD), and transmission electron microscopy (TEM). FTIR spectra were collected on Bruker VERTEX-70LS instrument using an attenuated total reflection (ATR) accessory at a resolution of 4 cm^{-1}. Deionized water was used as a blank solution, with aqueous Pt NP suspension as the experimental sample. A Bruker D8 system with Cu Kα radiation (λ=1.54 Å) was used for XRD analysis. Diffraction patterns were collected from 30° to 90° 2θ with 0.02° steps. The data collection time per step was optimized empirically to yield diffraction peaks that were well resolved from the noise floor.

Transmission electron microscopy (TEM) imaging was executed using a Hitachi H-9500 environmental transmission electron microscope at an accelerating voltage of 300 kV. For IL-TEM analysis, the nanoparticles were deposited on center-marked 400 mesh Au TEM grids (Ted Pella). A perforation was made manually near the edge of the grid using sharp tweezers (Ted Pella). Approximately 5 μL of the Pt nanoparticle suspension was dropcast on the grid and dried under an infrared heat lamp. The dried grid was then immersed in water to remove soluble impurities and poorly adhered NPs. Finally, a hooked gold wire (0.5 mm, 99.999%, Fisher Scientific) was inserted through the perforation to make electrical contact for electrochemical measurements.

A Gamry Reference 600+ Potentiostat was used to characterized the electrochemical properties of the Pt nanoparticles. For non-TEM based studies, 10 μL of a known loading of platinum suspension was dropcast onto a 3 mm diameter (0.071 cm^2 surface area) glassy carbon electrode and dried under infrared. The counter electrode was a Pt wire in acidic electrolyte and Ni foil in alkaline conditions;

the reference electrode was Ag/AgCl (1 M KCl). The potential from the Ag/AgCl reference electrode was later converted to the reversible hydrogen electrode (RHE) potential by measuring the open circuit potential value of a clean Pt NP film in H_2-saturated electrolyte at 1 atm. Electrolytes used for electrochemical analysis were 0.5 M H_2SO_4 (Certified ACS Plus grade, Fisher Scientific) and 0.5 M KOH (ACS Reagent grade, Sigma Aldrich). Note that the specifications of these reagents allow them to contain transition metal and anionic (e.g., chloride, sulfate, phosphate) impurities in the ppm to tens of ppm range. The electrolytes were used as obtained from the supplier and did not undergo additional purification steps.

To qualitatively assess surface cleanliness and quantitatively estimate the electrochemically active surface area (ECSA), electrolytes were purged with N_2 gas (Zero grade, Matheson gas). Cyclic voltammograms were then collected at a fixed negative potential limit of 0 V vs. RHE while the positive potential limit was varied from 0.5 V to 1.5 V vs. RHE at a scan rate of 100 mV/s.

RHE potential calibration and hydrogen evolution/oxidation catalysis measurements were performed on a rotating disk electrode (RDE) in a sealed Teflon cell (Pine Research). For RDE experiments, a known volume of Pt suspension was dropcast on a 5 mm diameter glassy carbon electrode for measurements in acid and on 5 mm Au for analysis in alkaline conditions. The Au substrate in alkaline electrolyte was found to yield improved adhesion, whereas Pt NPs were found to re-suspend when deposited onto glassy carbon. The electrolytes were purged with H_2 and the potential was scanned in the range of -0.15 V to +0.1 V vs. RHE in acid and -0.2 V to +0.2 V vs. RHE in base at 10 mV/s. Commercial 10 wt% Pt/C (Alfa Aesar) and a polycrystalline Pt disk electrode (Pine Research) were used as controls.

3.3 Catalyst synthesis and decapping

Our synthesis of platinum nanoparticles relies on the reduction of H_2PtCl_6 using ascorbic acid and sodium polyacrylate as the capping agent. The synthesis procedure is adopted from prior literature reports, where Pt(IV) salts have been shown to undergo reduction to metallic Pt with two equivalents of ascorbic acid.[153, 154, 155, 156, 157, 158] Sodium polyacrylate polymer as a capping agent offers narrow particle size distribution and has been reported previously for Pt synthesis.[159, 160, 161, 162, 163, 164, 165] Alkalizing the reaction mixture with sodium hydroxide destabilizes the colloid and facilitates removal of the polyacrylate from the nanoparticle.[166, 165, 167, 168] The main advantage of this approach (over the use of commercial Pt/C catalyst, for example) is that it offers a route to synthesize catalytically active Pt NPs that can be deposited on any substrate and analyzed without the confounding effects of supports or polymer binders. Our synthetic approach also makes use of low-cost reagents (other than the Pt precursor itself) and equipment that is readily available in many wet chemistry laboratories.

We executed TEM, XRD, and FTIR measurements to verify the composition and crystallinity of the Pt NPs before and after removal of the polyacrylate capping agent. Figures 3.1a,b show representative TEM images of capped and uncapped Pt NPs. The particles in panel a clearly remain encapsulated in a matrix of polymer several nm in diameter. In some cases the polymer encapsulates a single Pt particle and in others several distinct particles are visible, which suggests that the polyacrylate arrests Pt NP growth by encapsulating individual particles, and these core–shell assemblies further aggregate in solution or upon deposition on the TEM grid. By contrast, particles that have been uncapped with alkaline solution aggregate significantly on the TEM grid. Manual analysis of the particle size distribution (see Supporting Information) shows a normal distribution with a mean diameter of 3.1 ± 0.05 nm and circularity index of 0.906. D-spacings extracted from high resolution TEM imaging (insets of Figures 3.1a,b) further confirm the particle as face-centered cubic (fcc) Pt.

Figures 3.1c,d depict representative XRD and ATR-FTIR data of capped and uncapped Pt NPs. XRD results further confirm fcc Pt as the only crystalline component in the reaction mixture before and after purification. ATR-FTIR data from capped Pt exhibit absorbance features at 1640 cm^{-1} and 1723 cm^{-1}, which we attribute to carboxylic and/or alcoholic peaks that are blue-shifted relative to the aqueous sodium polyacrylate control. This shift has been previously attributed to the interaction between the particle and the polymer.[169, 170, 171] The uncapped Pt NPs also exhibited absorbance in this range, but at a considerably lower intensity and without clear evidence for a blue shift relative to aqueous polyacrylate. This further suggests that the base treament substantially removes polyacrylate from the NPs, but we cannot rule out the possibility that some polymer remains in solution or bound to Pt.

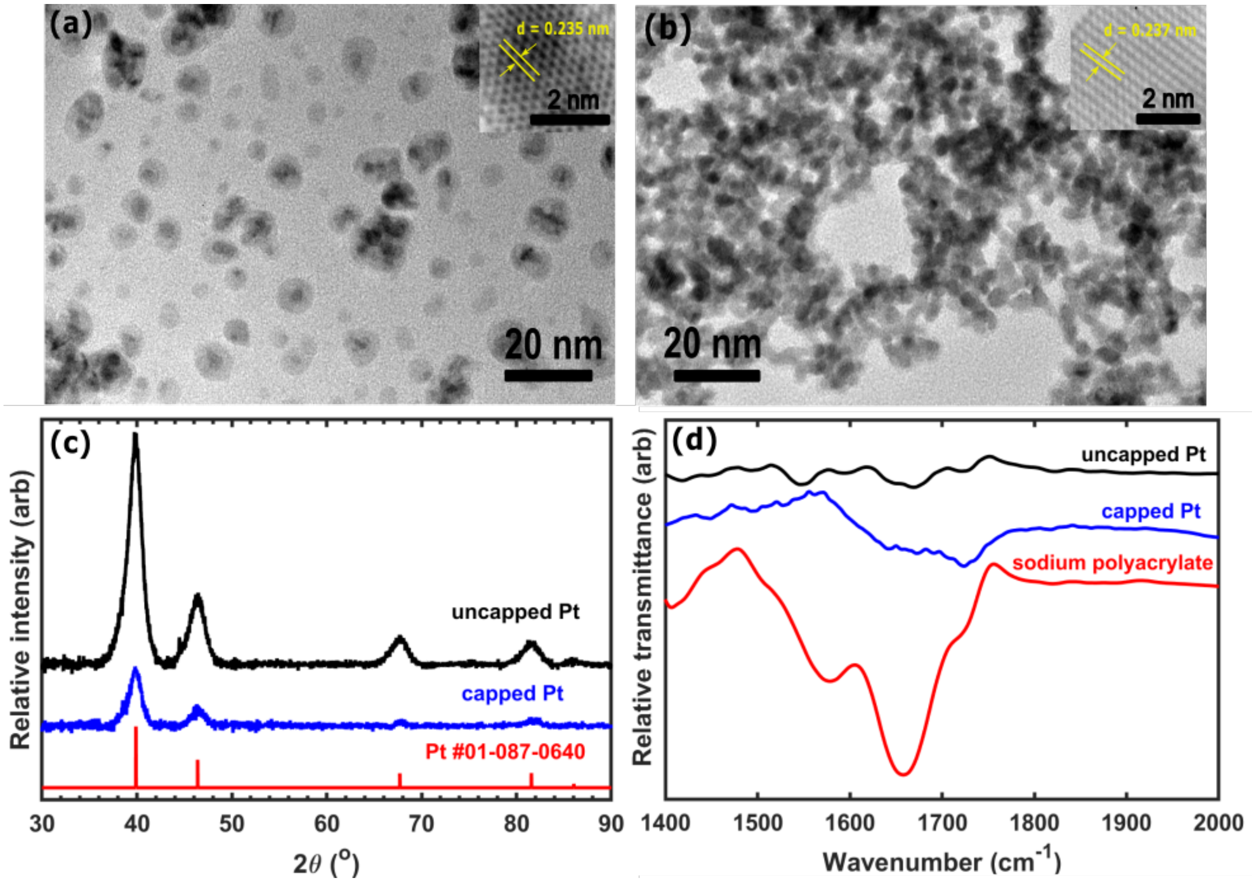

Figure 3.1: Compiled compositional analysis of Pt nanoparticles via (a,b) TEM, (c) XRD, and (d) ATR-FTIR. The standard XRD pattern of Pt was obtained from the ICDD database via the numerical index indicated in panel (c).

To further characterize the uncapped NPs, we used surface voltammetry to assess the accessibility of Pt surface sites to hydrogen via hydrogen underpotential deposition (HUPD). We evaluated the initial cleanliness of Pt nanoparticles (i.e., the proportion of Pt surface atoms that are electrochemically accessible) by using HUPD to determine the electrochemically active surface area (ECSA).[128] We also used changes in the ECSA under continuous voltammetric cycling to assess the rate and extent of catalyst deactivation over time. Figure 3.2 shows representative surface voltammograms of uncapped Pt nanoparticles in 0.5 M H_2SO_4 and in 0.5 M KOH. Using the generally accepted HUPD surface charge density of 210 μC/cm^2,[172] the ECSA-based specific surface area for uncapped Pt was found to be 16.2 and 12.6 m^2/g in acid and alkaline electrolytes, respectively. These values can be compared to the expected ECSA of 16.1 ± 0.3 m^2/g using the mean particle size obtained from TEM images as $A_{\text{TEM}} = 1/\rho d$ where ρ is the bulk density of Pt and d is the mean particle diameter. Accordingly, despite the tendency for uncapped Pt particles to aggregate—as is clearly evident from TEM imaging—the observed initial ECSA in acid agrees with the value calculated directly from individual particle geometries, implying the particle surface is free of capping agent and other poisons. Moreover, we found similar results for particles deposited from fresh colloids and those that were re-suspended after being allowed to settle, suggesting aggregation does not lead to particle growth at room temperature over timescales of hours to days.

By contrast, the ECSA values extracted from voltammetry in base were consistently lower than those in acid. We tentatively attribute the difference not to residual surface contamination, but instead to a combination of poor adhesion of the unsupported NPs to the electrode surface and a systematic underestimation of the HUPD charge that we attribute to the proximity of the oxygen desorption peak to the HUPD features (see Supporting Information). Nonetheless, these voltammetry results broadly agree with prior literature reports that NaOH(aq) treatment substantially removes polyacrylate without inducing a significant increase in particle size.[152]

3.4 Quantifying rates of deactivation in unpurified electrolytes

Prior literature reports have emphasized the susceptibility of Pt electrocatalysts to deactivation, which negatively impacts activity and lifetime.[173, 174, 175] We were interested in understanding the mechanism or mechanisms by which our unsupported Pt NPs degrade. To do so, we quantified ECSA decay under continuous voltammetric cycling. Figure 3.3 presents the results as ECSA versus cycle number in acid and alkaline electrolytes. For this analysis, 0.2 mg/cm^2 of Pt NPs were swept at 100 mV/s over the potential range from 0 V to one of three positive potential limits: 0.5, 1.0, and 1.5 V vs.. RHE for a total of 50 cycles. A different Pt film was used for each potential window and 15 such films obtained from 5 different synthesis batches were tested for the analysis.

In acid, the initial ECSA showed a pronounced increase with increasing positive potential, which suggests that the cleaning effect of the first cycle involves oxidative removal of contaminants. A

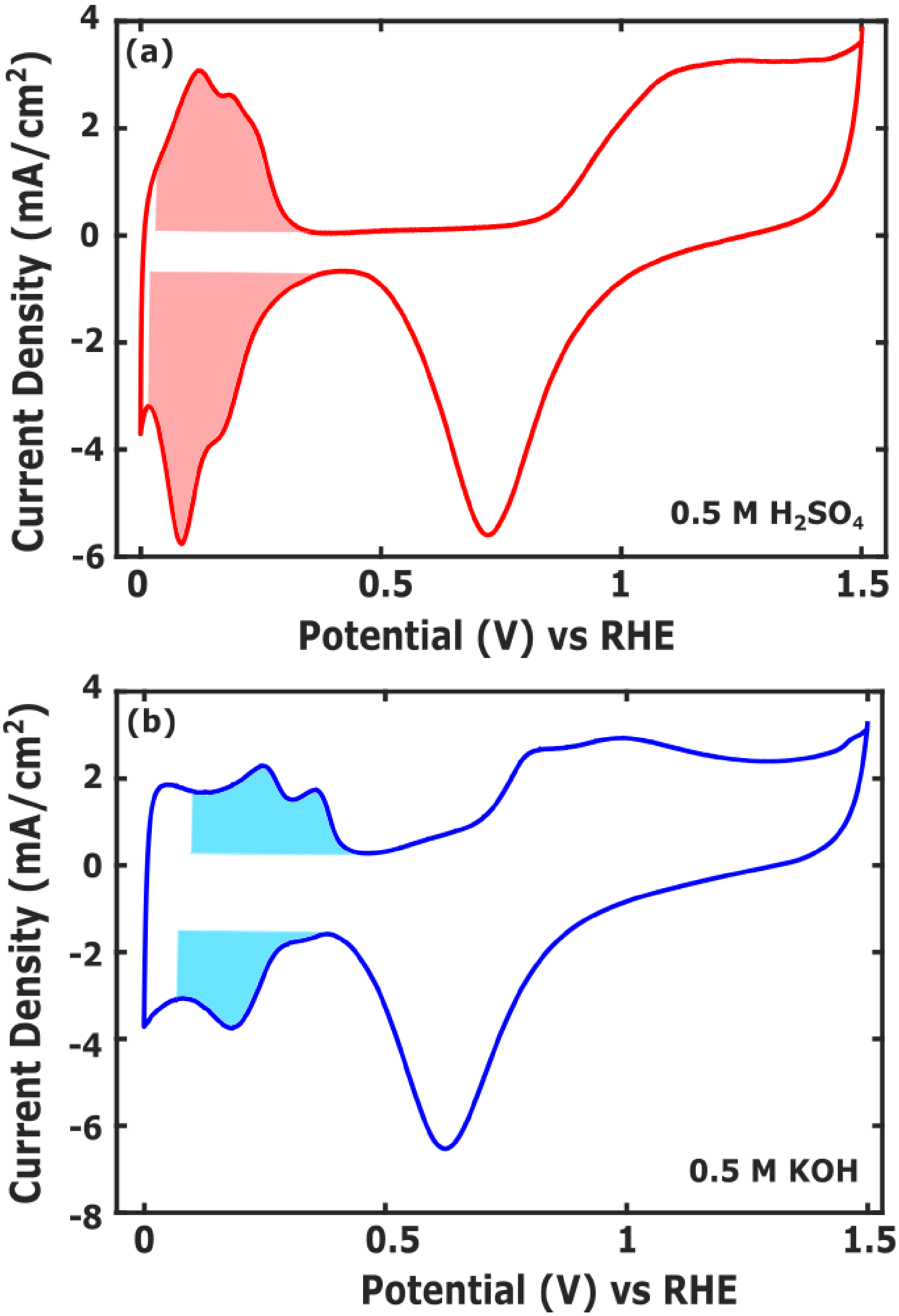

Figure 3.2: Cyclic voltammogram of Pt nanoparticles in (a) 0.5 M H_2SO_4 and (b) 0.5 M KOH under nitrogen atmosphere at 100 mV/s. The shaded region represents the area used for ECSA calculation.

monotonic decrease in ECSA was observed in all cases over 50 cycles. Moreover, we observed that the relative (normalized to initial ECSA) rate of ECSA loss per cycle was nearly identical when Pt nanoparticles were scanned at 0.5 V and 1 V vs. RHE, suggesting similarity in their deactivation mechanisms. When scanned to 1.5 V vs. RHE, the rate of deactivation was initially lower, but accelerated after several cycles such that the total fractional loss in surface area was $\sim$40 % in all cases.

ECSA values also decreased monotonically with cycle number in alkaline electrolyte across all positive potential limits. However, the relationship between initial ECSA and potential limit was reversed relative to the acid case, with the least positive potential limit resulting in the highest initial ECSA. We believe this difference again is attributable to the proximity of the oxygen desorption feature to the HUPD region, which results in a systematic underestimate of the ECSA when significant surface coverages of PtO_x are generated in the positive-going sweep (see Supporting Information). The relative rates of deactivation in base were also found to be similar at 1 V and 1.5 V vs. RHE, whereas the less positive potential limit resulted in marginally slower ECSA loss. These observations are consistent with the ability of aqueous base to remove residual capping agent from the Pt NP surface (which negates the benefit of positive potential cycling) and suggests the presence of a second deactivation mechanism that dominates at positive potentials.

We consider it significant that these Pt NPs lost 25–40 % of their initial ECSA over just 50 voltammetric cycles, which required as little as $\sim$10 minutes. This extent of ECSA loss is large enough to conclude that the Pt particles are no longer pristine, thereby calling into question their use as experimental controls or activity benchmarks. Hence, it is reasonable to adopt as a general guideline that unsupported Pt NPs of this type should be freshly deposited onto a clean electrode at relatively short time intervals (every few minutes or perhaps between each individual measurement) if they are to be used to good effect in unpurified electrolytes.

3.5 Differentiating between several modes of deactivation

Several deactivation mechanisms are understood to proceed for Pt catalysts under electrochemical conditions. These include catalyst poisoning via surface adsorption or electrodeposition of impurities;

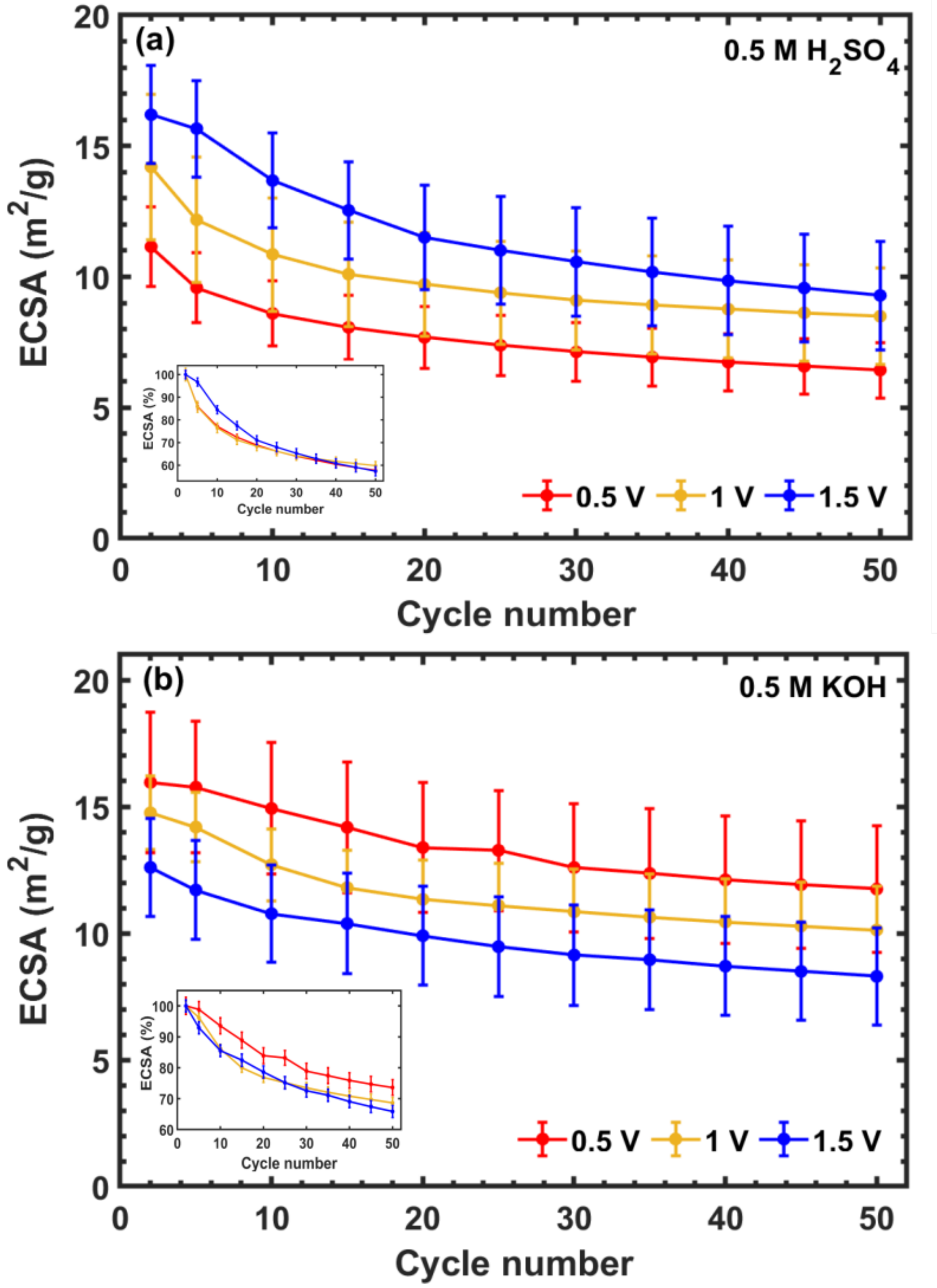

Figure 3.3: Variation of Pt NP ECSA as a function of cycle number when cycled between a fixed negative scan limit of 0 V vs. RHE and the noted positive scan limits over 50 cycles in (a) 0.5 M H_2SO_4 and (b) 0.5 M KOH. Experimental conditions were otherwise identical to that in Figure 2. Error bars represent 95% confidence intervals from 15 distinct films. The inset shows the relate rate of ECSA decay versus cycle number by normalizing to that of the first full cycle.

oxidative dissolution, which could be chemically or electrochemically induced; particle growth resulting from Ostwald ripening or similar processes; and particle detachment from the electrode substrate. In acidic electrolyte, unsupported Pt nanoparticles are known to undergo dissolution by repeated cycling across the potential range required to generate and reduce Pt-oxides.[176, 177, 178, 174, 175] The dissolution proceeds primarily during the reductive scan when platinum oxide is nominally reduced back to metallic Pt; this reaction proceeds in parallel with dissolution of Pt^{2+} ions. Under continuous cycling, these ions may remain in the electrolyte or they may be redeposited as the electrode potential is swept further negative. This dissolution-redeposition process may then induce particle growth via electrochemically accelerated Ostwald ripening.[179, 180] Nevertheless, it is difficult to entirely eliminate oxidative cycling in practice, as this treatment is also highly effective at removing organic and/or inorganic contaminants from the Pt surface, either through catalytic oxidation or as a direct result of the dissolution of Pt surface layers.[181]

The deactivation of Pt nanoparticles has not been as thoroughly characterized in alkaline conditions as in acid. Deposition of transition metal impurities on the electrode surface and analogous dissolution processes have each been implicated as the root causes of reduced catalytic activity.[129] Our ECSA variation versus cycle number data in figure 3.3 yield puzzling results where the initial ECSA values and the potential window are not consistent across acid and base conditions. Moreover, the relative rates of deactivation (20–40% over 50 cycles) are similar across nearly all conditions studied. These observations leave open the question of whether the dominant mechanism of ECSA loss is similar or different across all potential windows and pH conditions.

Figure 3.4 compiles the results of an experiment directed at differentiating between reversible catalyst poisoning and irreversible loss of surface area, wherein Pt NP films were first subjected to 50 cycles to a positive limit of 0.5 V vs. RHE, followed by 50 cycles to 1.5 V vs. RHE, and then a third set of 50 cycles to 0.5 V. The ECSA decay on scanning at 0.5 V vs. RHE for the first 50 cycles in acid and alkaline solutions again resulted in a 20–40% loss in ECSA. When the positive potential was shifted to 1.5 V vs. RHE, ECSA values in acid recovered over $\sim$5 cycles and in some cases even exceeded the initial values. This indicates that the Pt surface was renewed after scanning at oxidizing potential, which strongly suggests catalyst poisoning dominates at 0.5 V vs. RHE. Nonetheless, after the initial recovery at 1.5 V vs. RHE, the ECSA decayed again by nearly the same amount as in the initial set of 50 cycles. Returning the potential window to a 0.5 V positive limit had little further impact on the ECSA, which continued to diminish slowly through a final set of 50 cycles. These data suggest the mechanism by which ECSA diminishes when cycling to a more positive potential limit is irreversible—dissolution, particle growth, or detachment.

By contrast to the results in acid, when cycled in alkaline electrolyte, the ECSA did not recover when the voltage range was modulated from 0.5 to 1.5 V and back to 0.5 V. Instead we observed a nearly continuous decrease in surface area over 150 cycles, with a systematic offset for data collected to 1.5 V vs. RHE again attributable to systematic errors resulting from the Pt surface oxide reduction feature in the voltammogram.

Our observations in acid agree with prior reports that electrochemical oxidation is highly effective at removing catalyst poisons from Pt in acid.[181] Many organic (e.g., hydrocarbons) and inorganic (e.g., sulfate, chloride) species from the synthesis mixture, the electrolyte, or the atmosphere may adsorb to the Pt surface and can be removed by cycling to positive potentials.[181, 182, 183] By contrast, oxidative electrochemical cleaning did not renew the catalyst surface in base. There are at least three possible explanations for this observation. First, the catalyst surface may become contaminated with a non-oxidizable poison over all potential windows. A second explanation is that alkaline conditions facilitate detachment of nanoparticles from the electrode surface, and this may proceed at some relatively constant rate regardless of cycling conditions. A third explanation is that the Pt NPs undergo continuous particle growth in alkaline conditions under potential cycling that again depends weakly, if at all, on cycling conditions.

To further differentiate between loss of surface area via particle growth, dissolution, and detachment, we performed identical location transmission electron microscopy (IL-TEM) experiments on catalyst thin films before and after they were subjected to CV cycling over a range of potential windows for 50 cycles at 100 mV/s. Figure 3.5 compiles the results of these experiments in acid electrolyte. At 0.5 V vs. RHE, the TEM images before and after cycling do not show significant changes in the particle morphology. The overall particle size distribution also did not significantly change before and after cycling. Similar results were observed when Pt NPs were scanned to 1 V vs. RHE in acid. However, a stark difference was observed when the particles were cycled to 1.5 V vs. RHE, where the TEM images clearly show particle growth. The particle size distribution data confirmed that the mean particle diameter increases by slightly more than two-fold. A similar analysis was also performed in alkaline solution, where scanning at 0.5 V and 1 V vs. RHE did not

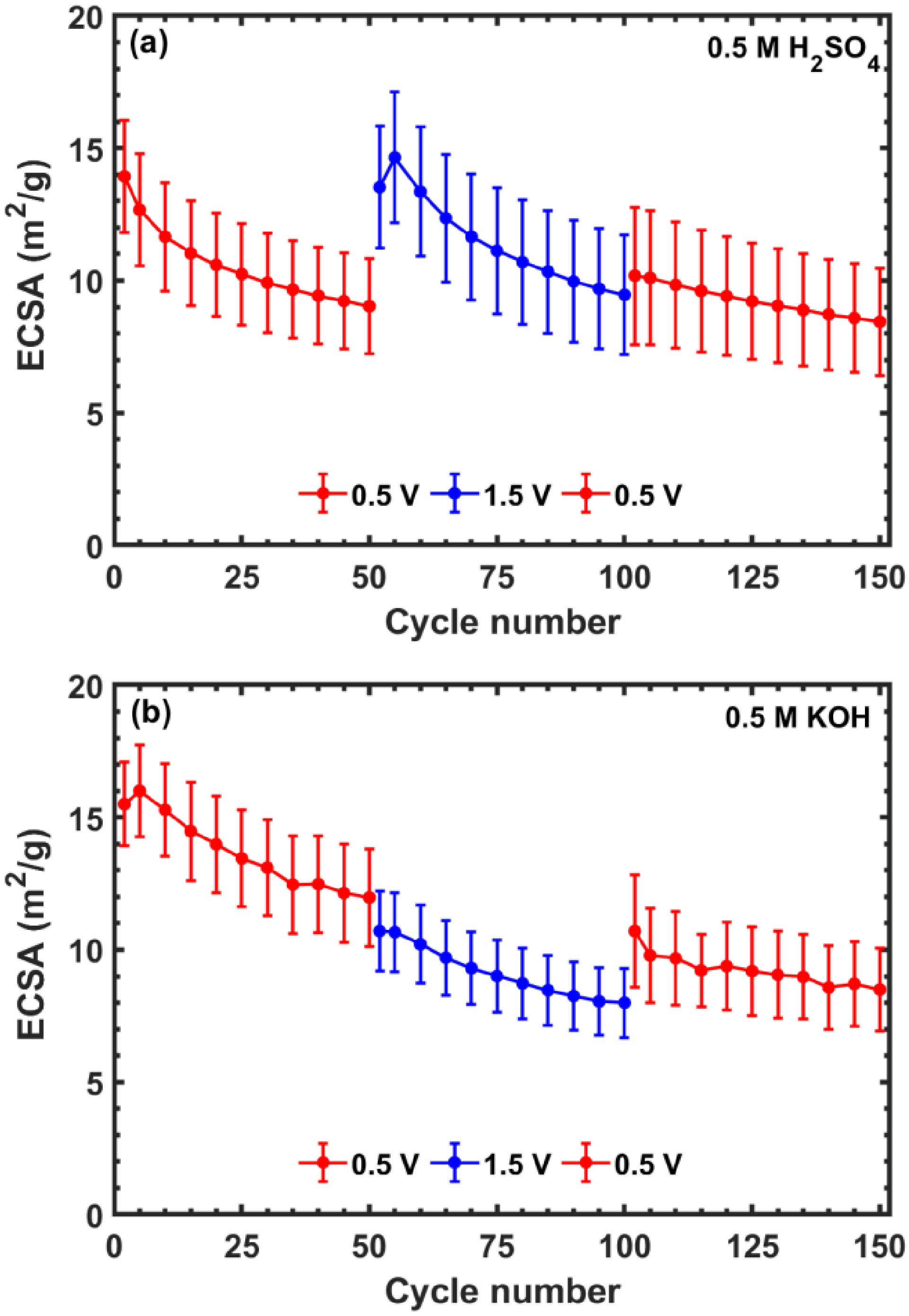

Figure 3.4: ECSA versus cycle number for Pt NP films scanned to narrow potential of 0.5 V for 50 cycles, followed by positive potential limit of 1.5 V for 50 cycles and again followed by 0.5 V for 50 cycles in (a) 0.5 M H_2SO_4 and (b) 0.5 M KOH. Experimental conditions and error bounds were otherwise identical to those in Figures 2 and 3.

result in a significant increase in particle size but cycling at 1.5 V vs. RHE resulted in a ~30 % increase in mean particle diameter (see Supporting Info).

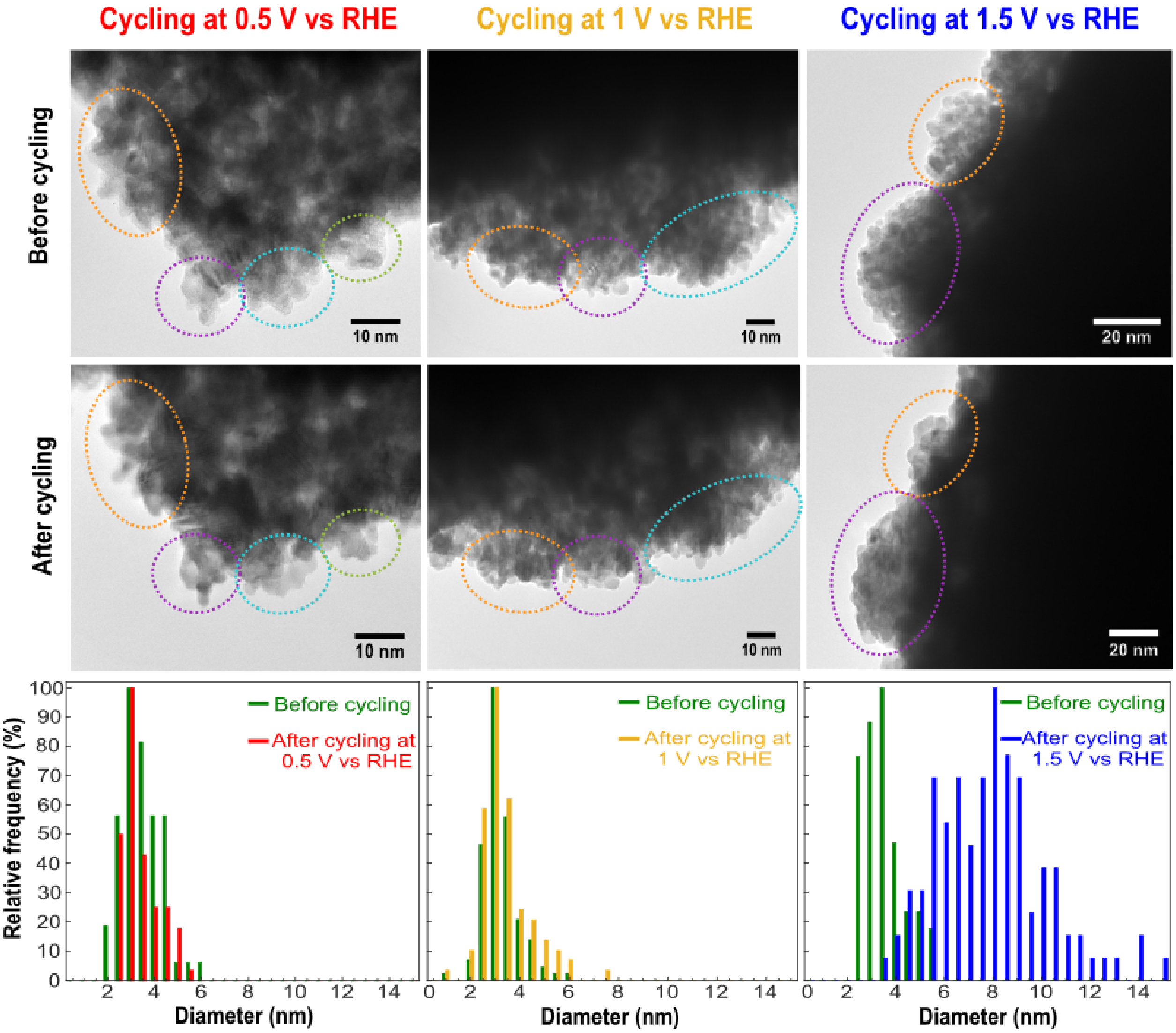

Figure 3.5: Identical location TEM images and particle size distributions of Pt nanoparticles before and after cycling at three different positive limit potentials in 0.5 M H_2SO_4.

Combining the ECSA and IL-TEM analysis, it is evident that when the potential is cycled at least as positive as 1 V vs. RHE, catalyst poisoning is the dominant mechanism by which ECSA diminishes. This is evidenced by the fact that we saw no changes in particle size before and after cycling. But when samples were cycled to 1.5 V vs. RHE, the particle size increased significantly in acid and base. We therefore attribute the growth of Pt nanoparticles to Ostwald ripening, which may be facilitated by transient Pt dissolution and redeposition during cycling.[142] The observed decrease in ECSA in base at 1.5 V vs. RHE can be fully attributed to the increase in particle size. By contrast, the observed loss in ECSA in acid was smaller than that predicted from increase in particle size. We speculate that this discrepancy may result from a modest increase in atomic scale roughness (i.e., increased surface disorder) for Pt NPs in acid that also results from continuous formation and reduction of Pt-oxides.

It is striking that, despite evidence that at least two different potential and pH-dependent mechanisms are involved, the observed rate of Pt NP deactivation was remarkably consistent—tens of percent loss in ECSA over tens of minutes—across all conditions studied. Absent evidence to the contrary, we conclude that this consistent rate of ECSA loss is coincidental, and in fact the comparative rates of catalyst poisoning and particle growth would likely be different in more highly purified or severely contaminated electrolytes. Indeed, prior work on Pt NPs under scrupulously clean conditions showed that stable cycling can be achieved when the potential is maintained negative of 1 V vs. RHE.[163, 152] However, it is challenging and costly to obtain this level of cleanliness; hence, it may be preferable in many cases to simply refresh the Pt NP film by removing "spent" particles from the electrode substrate and replacing with a fresh NP film. This approach is directly analogous to the ubiquitous use of abrasive polishing to clean polycrystalline Pt electrodes between experiments, with the added benefit of the ability to control the Pt loading, and hence the areal density of active sites.

3.6 The effect of Pt deactivation on benchmark measurements

Upon determination that our Pt NPs initially exhibit high accessibility to adsorbed hydrogen, we endeavored to assess their ability to perform routine measurements associated with HER/HOR catalyst benchmarking. Specifically, we sought to identify experimental timescales over which our Pt NPs exhibit reduced catalytic activity toward hydrogen evolution/oxidation in reagent-grade electrolytes.

Figure 3.6 shows representative HER/HOR polarization curves of Pt nanoparticles in comparison with a commercial Pt/C catalyst at Pt mass loading of 0.2 mg/cm^2. Note that, based on ECSA measurements and known particle sizes, these electrodes exhibit roughness factors (electractive surface area normalized to project area of the electrode) of $\sim$30. We also included a simulated concentration overpotential curve (simulation details can be found in the Supporting Information), which represents the current-overpotential response of an ideal nonpolarizable electrode whose activity is limited only by mass transfer. In acid, the HER activity of Pt/C and our unsupported Pt NPs are nominally identical and overlay with the concentration overpotential curve. This means that the hydrogen evolution/oxidation reaction on Pt is purely transport limited, and the true kinetics of the catalyst are not directly measurable. We then cycled the unsupported Pt NPs in the HER/HOR region for $\sim$30 minutes from -0.15 to +0.1 V vs. RHE at 100 mV/s and measured the HER/HOR performance again. No change was observed in the current-overpotential data after cycling, which suggests that any loss in catalytic activity was not sufficient to induce a kinetic limitation.

This result illustrates several important properties of Pt catalysts when used for hydrogen evolution/oxidation measurements in acid. First, a clean, high surface area Pt catalyst film should generally yield transport-limited activity for the HER/HOR in aqueous acid unless steps are taken to greatly increase the mass transfer coefficient beyond what is achievable using conventional techniques like RDE voltammetry.[184, 185] This means the activity should be indistinguishable from that of a catalyst with a heterogeneous electron transfer of infinity. Such a nanostructured Pt catalyst will continue to exhibit transport-limited activity even after it becomes poisoned or otherwise deactivated, provided the remaining areal site density remains sufficiently high. A recent report showed that areal loadings of unsupported 3.8 nm Pt NPs needed to be reduced to <1 μg/cm^2 to observe kinetically limited behavior.[131] This would be roughly equivalent to a $>$99.5 % loss in ECSA at the 0.2 mg/cm^2 loading we used here. Accordingly, unsupported Pt NPs and commercial Pt/C catalysts can certainly be used to benchmark the activity of a new HER/HOR catalyst, even in unpurified reagent-grade electrolyte. However, if a novel catalyst is found to exhibit higher activity toward the HER or HOR than a Pt control in acid solution, it is in fact very unlikely that the catalyst of interest is “better than Pt,” but rather the Pt control has likely been severely contaminated by electrolyte impurities or another source.

We also performed HER/HOR measurements in alkaline electrolyte, which gave considerably different results. The activity of Pt/C and Pt nanoparticles was similar, and both were lower than the simulated concentration overpotential. This is consistent with numerous prior reports showing that Pt is less active toward hydrogen evolution/oxidation under alkaline conditions than in acid.[185, 128] Cycling of Pt nanoparticles in the HER region from -0.2 V to +0.2 V vs. RHE for $\sim$ 30 minutes also resulted in $\sim$30% reduction in current density. This agrees well with our ECSA data showing that accessible Pt surface sites decreased by tens of % over tens of minutes of continuous cycling. It is also consistent with the expectation that Pt HER/HOR electrocatalysis is kinetically limited in base, even for electrodes with relatively high Pt surface areas; hence, catalyst deactivation manifests as a proportional decrease in activity. These results collective suggest that Pt-based control measurements in alkaline electrolytes are considerably more sensitive to the cleanliness and sample history than those in acid. Comparisons between Pt and novel HER/HOR catalysts in alkaline conditions are also more relevant, since Pt remains limited by reaction kinetics over a wide range of catalyst loadings and it is indeed possible to obtain catalytic activities exceeding that of pure Pt.[186, 187, 188]

As a final assessment of the utility of our Pt NPs for catalyst benchmarking, we used open-circuit potential (OCP) measurements in hydrogen-purged electrolytes to calibrate our Ag/AgCl reference electrode to the reversible hydrogen electrode (RHE) potential. This procedure is crucial in characterizing catalysts for reactions involving proton-electron transfer because it enables accurate determination of catalyst overpotentials relative to an empirically measured, pH-dependent thermodynamic equilibrium potential. Figure 3.7 depicts representative RHE calibrations using our Pt NPs alongside polycrystalline Pt disk electrodes in acid and base. For consistency, these measurements were initiated in electrolytes that were first purged with atmospheric air for several minutes ($\sim$1000 seconds) until a stable potential was attained. The purge gas was then switched to hydrogen at the same flow rate. The open-circuit potential was found to decrease over several minutes as dissolved oxygen was replaced with hydrogen until it asymptotically approached a stable potential in the expected range for a reversible hydrogen electrode (near -0.25 V vs.. Ag/AgCl in 0.5 M H_2SO_4 and -1.0 V in 0.5 M KOH). Figures 3.7c and d show detailed views of a narrow range of potentials in the asymptotic region. In acid, OCP values for the Pt disk electrode and unsupported Pt nanoparticles remained stable within $\pm$2 mV over the last 10 minutes of the measurement. The minimum OCP values, which can be interpreted as an estimate of 0 V vs. RHE, were -0.266 and -0.270 V vs. Ag/AgCl; the modest difference between these values constitutes uncertainty in the RHE calibration attributable to, e.g., reference electrode drift or incomplete exclusion of atmospheric air during the hydrogen purge. These data show that clean Pt electrodes of varying surface roughness remain

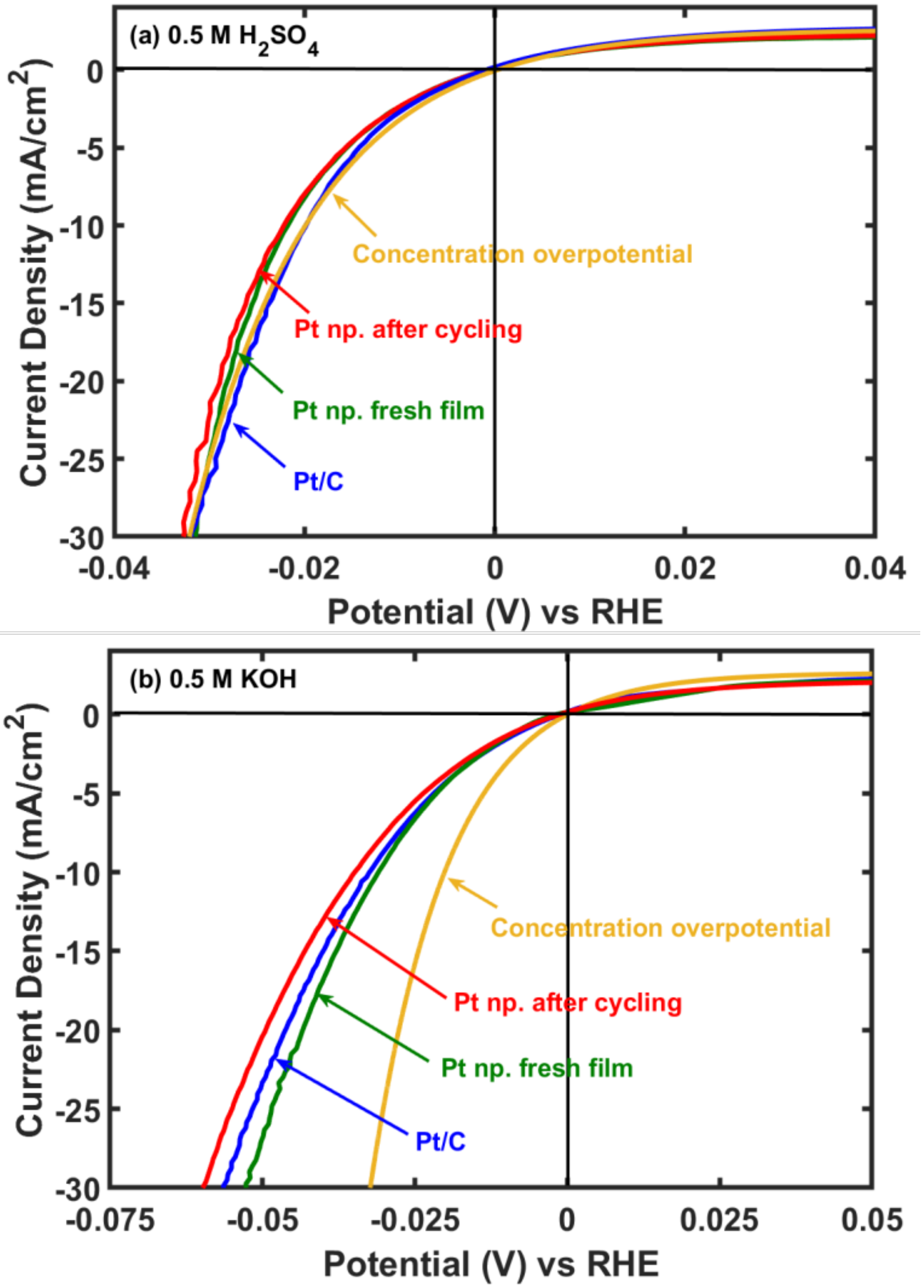

Figure 3.6: HER/HOR polarization curve of fresh film of Pt nanoparticles and after cycling in the HER potential range for 30 minutes (i.e.at 100 mV/s for 300 cycles)in comparison with commercial 10 wt% Pt/C and simulated diffusion overpotential curve under hydrogen gas purge at 1600 rpm in (a) 0.5 M H_2SO_4 and (b) in 0.5 M KOH. The Pt mass loading was kept constant at 0.2 mg/cm^2.

sufficiently catalytic over the measurement interval to obtain a stable equilibrium between hydrogen and protons.

In alkaline solution, Pt nanoparticles gave a similarly stable final OCP value, but the Pt disk was found to drift positive by $\sim$30 mV over several minutes. This indicates that this relatively low surface-area electrode becomes sufficiently deactivated on the timescale of the RHE calibration to exhibit a mixed potential likely involving equilibration to the HER/HOR equilibrium and one or more additional equilibria associated with impurities in solution or adsorbed on the electrode.[189] These data again exemplify the greater sensitivity of Pt to deactivation in base, which results from its lower catalytic activity toward hydrogen evolution/oxidation and can be ameliorated by increasing the areal density of Pt surface sites.

3.7 Summary

In summary, we synthesized uniform, 3 nm unsupported Pt nanoparticles via a straightforward aqueous route involving ascorbic acid and polyacrylate as reductant and capping agent, respectively. The resulting Pt NP colloidal suspension can be purified by simply basifying the reaction mixture, which substantially removes the polyacrylate capping agent. The purified particles remain stably suspended in pure water, which lends well to their use as a laboratory standard for electrochemical hydrogen evolution/oxidation and potentially in numerous other applications. We further showed that these catalyst particles lose considerable active surface area over a span of tens of minutes during continuous electrochemical cycling in unpurified, reagent grade aqueous acid and base. We contextualized these results in terms of the utility of these Pt NPs for benchmarking novel HER/HOR catalysts. We further demonstrated that Pt deactivation has a much greater negative impact on these measurements in base than in acid.

Considering together all the results reported here, we conclude that it is indeed possible to collect accurate Pt HER/HOR activity benchmark data and to calibrate reference electrodes relative to the RHE without the need to rigorously purify electrolytes or otherwise maintain scrupulously clean conditions. To do so consistently, we recommend adopting the following practices:

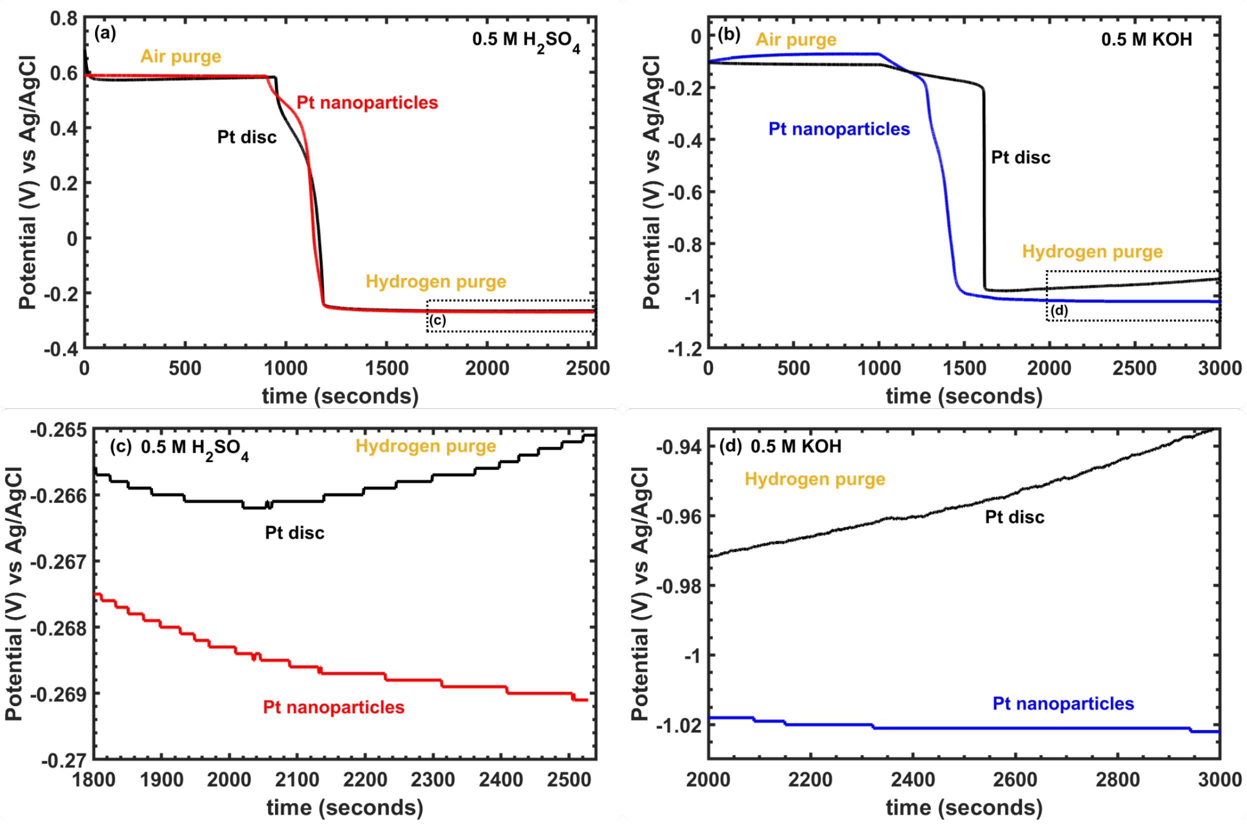

Figure 3.7: Open circuit potential measurements of Pt nanoparticles and Pt disk electrodes under air purge followed by H_2 purge in (a) 0.5 M H_2SO_4 and (b) 0.5 M KOH. Panels (c) and (d) are details of the potential vs. time data in (a) and (b), respectively, over a narrower range of potentials after the solution became saturated with H_2.

1. When possible, maximize the areal density of Pt active sites by using Pt NPs with mass loading $\geq$0.1 mg/cm^2 or platinized Pt electrodes.

2. When using Pt NPs, compare the results of ECSA measurements against the surface area expected from independently measured particle size/shape to determine whether they are free of surface site-blocking impurities.

3. When operating in an acidic environment, Pt catalysts may be further cleaned by scanning to oxidizing potentials on the order of 1.5 V vs. RHE. However, these treatments should be limited to a short duration (no more than a few minutes), after which particle films should simply be

removed from the electrode substrate and a fresh film deposited.

4. Do not use potential cycling to clean Pt catalysts in alkaline electrolytes, as is has no beneficial effect. Instead, measurements should be limited to a few tens of minutes or less, between which catalyst films should be removed and refreshed. Experiments that require longer durations will likely require electrolyte purification.
5. Regularly execute internal checks for catalyst deactivation. These include hydrogen evolution/oxidation measurements in acid, which should give mass-transfer limited activity, and RHE calibrations, which should yield little to no potential drift over at least several minutes.

4.0 Compositional Analysis of Ni–Mo Catalysts

Nickel Molybdenum (Ni–Mo) alloy composites are used to catalyze redox reactions involving surface-bound hydrogen intermediates. The water gas shift reaction[190], hydrotreating reactions[191], CO_2 methanation[192] and electrochemical water splitting [193, 194, 195, 196] are some of the examples of chemical processes where Ni–Mo catalysts are used. Ni–Mo catalysts have been synthesized by various synthetic approaches, including sol-gel, hydrothermal, co-precipitation, precipitation-reduction and electrodeposition.[197, 60, 51, 198, 199, 200, 201] In most of these synthesis routes, the final catalyst is derived from the thermal reduction of the nickel molybdenum-based oxide intermediate. However, the details of intermediate oxide synthesis and its thermal reduction have been shown to influence the activity of the final catalyst.[202, 203, 204, 205, 206] Nonetheless, to date there have been few studies directed at characterizing the precise composition of these Ni–Mo composites, and how this composition changes as a function of processing conditions. This chapter summarizes our work to understand the composition of Ni–Mo catalysts in reference to their application in alkaline hydrogen electrochemistry. It was carried out in close collaboration with Profs. Stephen House and Judith Yang, who performed the transmission electron microscopy (TEM) analysis. Shubham Awate, from Prof. Susan Fullerton's research group, also executed the atomic force microscopy (AFM) analysis.

4.1 Composition of Ni–Mo catalyst revealed

Numerous prior studies have already clearly demonstrated that Ni–Mo alloy catalysts exhibit high activity for the alkaline hydrogen evolution reaction.[207, 208, 209, 210, 211, 212, 213, 214, 215, 216, 217, 218, 219, 220, 221, 222, 223, 224, 225] Our work is based on a set of previous studies in which Ni–Mo alloys were synthesized using a precipitation-reduction approach. This approach allows for easy variation of the alloy composition, support material, and deposition substrate. This section compiles complete details on the synthesis and compositional analysis of high perfoming Ni–Mo composite catalysts, adapted with permission from Rituja B. Patil, Aayush Mantri, Stephen

D. House, Judith C. Yang and James R. McKone; ACS Applied Energy Materials, 2019, 2, 4, 2524–2533. Copyright 2019 American Chemical Society.

A synthetic procedure for the Ni–Mo was adopted from prior report by McKone et al.[60]. A representative procedure is described here. A Corning PC-420D hotplate was preheated to 400 °C for 30 minutes. 1.5 g (5.2 mmol) of nickel nitrate hexahydrate and 0.6 g (3.4 mmol) of ammonium molybdate tetrahydrate were dissolved in a mixture of 5 ml deionized water and 2 ml ammonium hydroxide in a 100 mL beaker to give a deeply blue solution. 45 ml diethylene glycol was then added to this solution. The solution was then placed on the preheated hotplate and stirred using a PTFE-coated stirbar (Fisher Scientific) at 500 rpm. An alcohol thermometer was used to monitor the temperature. The mixture was heated until the temperature reached 110 °C, which we found to require 5–7 minutes. Upon heating, a green precipitate formed; part of this precipitate remained suspended in the parent solution and part became entrained on the bottom and sidewalls of the beaker and stir bar. After reaching the target temperature, the beaker was removed from the hotplate and allowed to cool slightly. The still-warm reaction mixture was then transferred to a 50 mL polyethylene centrifugation vial and centrifuged (Thermo Scientific Sorvall ST 8) at 3000 rpm for 10 minutes. A pale blue supernatant remained and was decanted, followed by repeated washing and centrifugation steps using pure water until the supernatant became colorless. A final rinse and centrifugation step was carried out using acetone instead of water, and then the final precipitate was collected by suspending in a minimum of methanol and dried in a drying oven (Fisher Scientific Isotemp) at 60 °C for several hours. The final yield of green powder ranged from 17–21% relative to the total mass of precursors. A Thermo-Scientific Mini Mite tube furnace was used to reduce the oxides. The oxides were then transferred to a crucible, and thermally reduced in a tube furnace under a flow of forming gas (5% H_2 and 95% N_2) at a rate of 15 sccm. The furnace temperature was first increased to 200 °C and held for 30 minutes, followed by increasing to 450 °C for 1 hour. The forming gas flow was discontinued and the furnace was allowed to cool naturally to room temperature. The product (still a black powder) was then removed and weighed again.

Figure 4.1 shows XRD results for Ni–Mo oxides and catalysts synthesized by the precipitation-reduction approach. The oxide precipitate exhibited broad diffraction features at $2\theta = 25$, 35, and 61°, which we were unable to index to a known compound containing Ni and/or Mo.

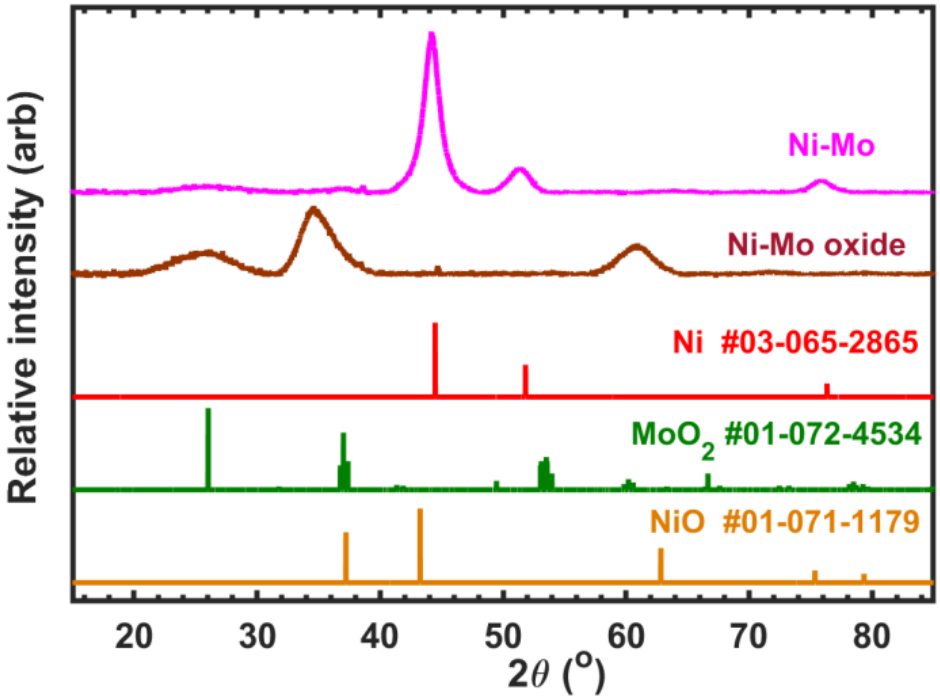

Figure 4.1: X-ray diffraction patterns of intermediates and products associated with ammonia-based nanopowders. Standard diffraction patterns corresponding to the indexed compounds are also included and labeled with card numbers corresponding to entries in the ICDD PDF database.

Upon reduction, Ni–Mo nanopowders with and without carbon supports gave diffraction features consistent with face-centered cubic (fcc) Ni. The carbon-containing samples also showed a broad feature at $2\theta \sim 24°$, matching that of Vulcan carbon black alone. Peak positions were shifted slightly to lower 2θ values than in pure Ni, which is attributable to lattice expansion arising from the incorporation of Mo into the Ni lattice, as has been reported previously.[219] By application of Bragg's law to the fcc peaks, we extracted a lattice constant of 3.56 ± 0.017 Å, implying Mo content of 9.3 ± 0.4 mol% in the alloy. Scherrer analysis indicated a crystallite size of 5.48 ± 0.54 nm for the crystalline fcc component. Careful inspection of the ammonia-based Ni–Mo XRD pattern baseline also showed broad peaks corresponding to MoO_2 and NiO (see Supporting Information). Based on these results, we conclude that the ammonia-based synthesis gave rise to products comprising a Ni-rich alloy phase along with residual Ni and Mo oxides.

Figure 4.2 depicts scanning electron micrographs of Ni–Mo oxides and Ni–Mo nanopowder composites without carbon supports. EDS analysis gave 70–75 mol% Ni and 25–30 mol% Mo, indicating Mo loss during the precipitation or oxide purification steps. Additional elemental analysis using inductively-coupled plasma optical emission spectroscopy (ICP-OES) agreed with the EDS results. This is consistent with the trend observed in prior work on Ni–Mo Nanopowder synthesis.[60] The final nanopowders were irregular agglomerates that were several hundred nm in diameter in the oxide and the reduced product.

TEM analysis was used to probe the nanoscale composition and morphology of a representative sample of unsupported Ni–Mo nanopowder. This examination revealed that the Ni–Mo agglomerates in fact consisted of Ni-rich nanoparticles encased in a Mo-rich oxide matrix. Examples of the predominant morphology are shown in Figure 4.3a, where one such Ni-rich nanoparticle is indicated by a white arrow, and the oxide surrounding it by a black arrow. The Ni-rich nanoparticles were convex and few tens of nm in size. Most of these Ni-rich nanoparticles came in close contact with at least one other nanoparticle, effectively forming connected chains, though nanoparticles on the periphery of these aggregates were more likely to be isolated by an oxide layer. Consistent with XRD results, electron diffraction showed that the Ni-rich nanoparticles were crystalline with the fcc structure and the Mo-rich oxide was nanocrystalline with ultra-fine grains (Figure 4.3b). The Mo-rich oxide coating also varied in thickness from near zero to several nm, but appeared to fully enclose the Ni-rich phase in nearly all areas (Figure 4.3c and d). The elemental identity and distribution of the nanoparticles and oxide were verified via EDS mapping, as shown in Figure 4.4. The maps confirm that the interior nanoparticles were strongly Ni-rich, while the co-localization of the Mo and O—but not Ni—confirm a Mo-rich oxide matrix into which metallic nanoparticles were embedded.

The core@shell catalyst geometry was found to be independent of the ratio of Ni and Mo precursors and the precursor salts of Ni and Mo (Ni nitrates versus chlorides or ammonium versus sodium salt of Mo).[226, 227] Attempts were also undertaken to remove the Mo-oxide layer by immersing the catalyst in different concentrations of KOH solutions (1–5 M) for different intervals of time (minutes to days), but the results were inconsistent. Nonetheless, the presence of an oxide shell around a nominally metallic catalyst was not explicitly known before, and this motivated our subsequent work to understand the structural evolution of the core@shell structure.

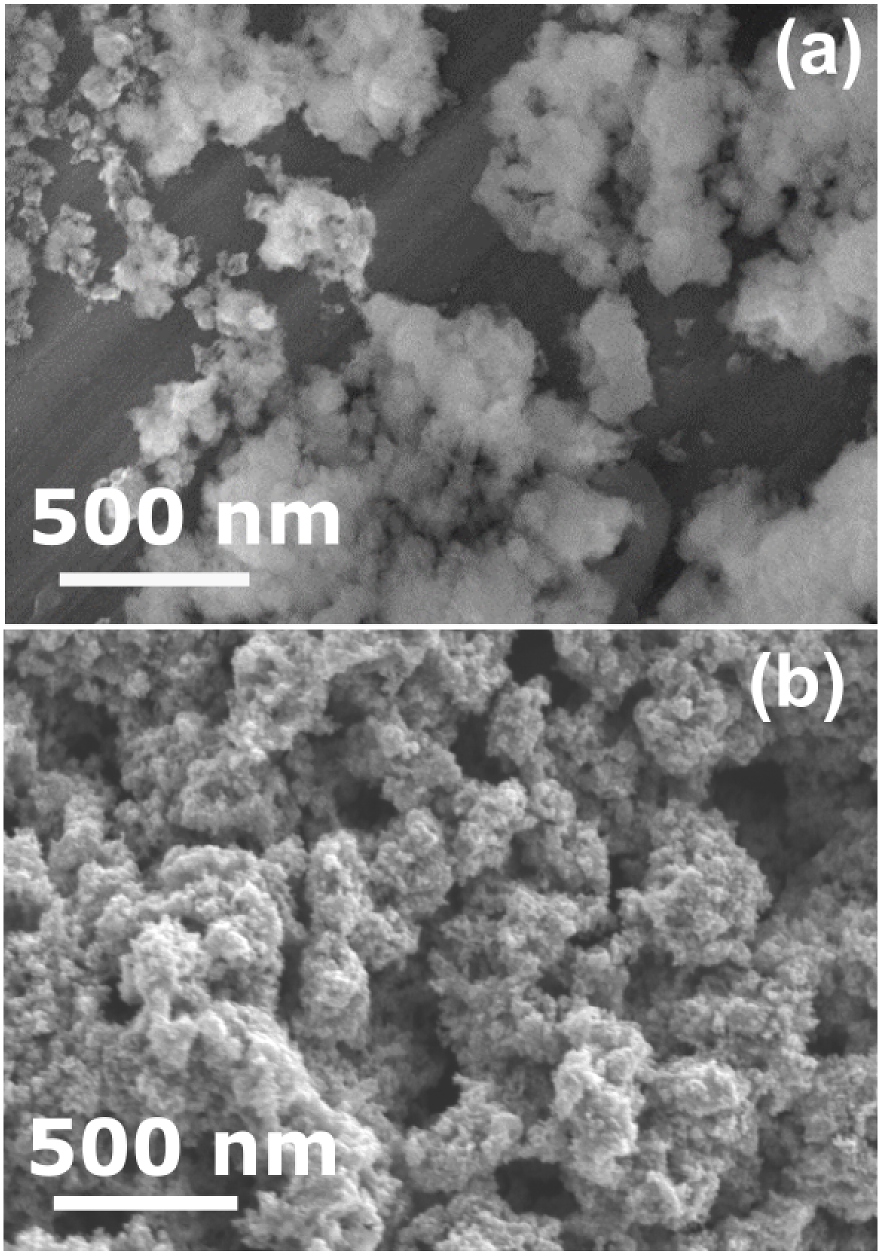

Figure 4.2: Representative SEM images of (a) oxide precipitates and (b) reduced powders without carbon supports.

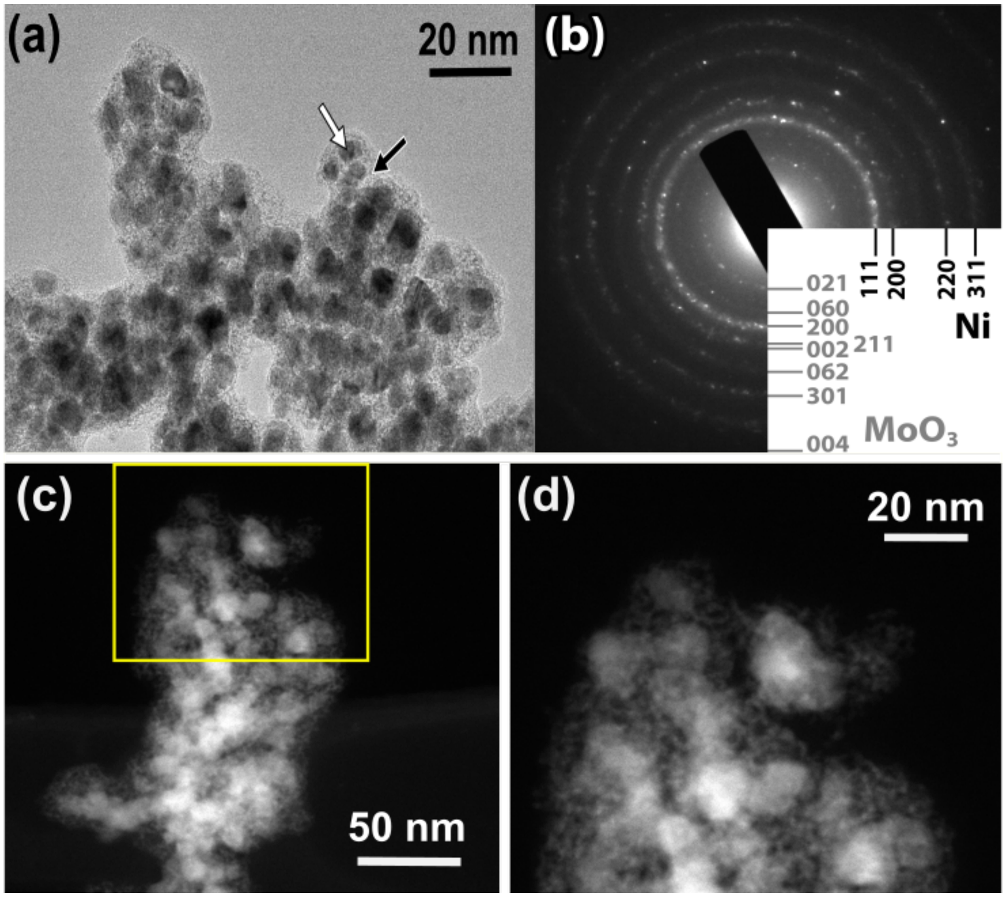

Figure 4.3: (a) Bright-field TEM image of unsupported Ni–Mo, showing Ni-rich particles (white arrow) surrounded by Mo-rich oxide (black arrow). (b) Selected area electron diffraction (SAED) pattern showing crystalline Ni and MoO_3 phases. (c) Dark-field STEM image from the same ammonia-based Ni–Mo sample, and (d) detail of the region highlighted in (c).

4.2 Direct observation of core@shell structure in Ni–Mo

We saw in the previous section that Ni–Mo alloys consist of Ni-rich core, coated by a Mo-rich oxide phase. It was unclear, however, how a pure phase oxide catalyst precursor evolves into a mixed-phase core@shell structure upon reduction. We therefore performed a series of in-situ environmental TEM (ETEM) experiments to directly observe the thermal reduction of $NiMoO_4$ to Ni–Mo composite under hydrogen. This study is published and is reproduced here with permission

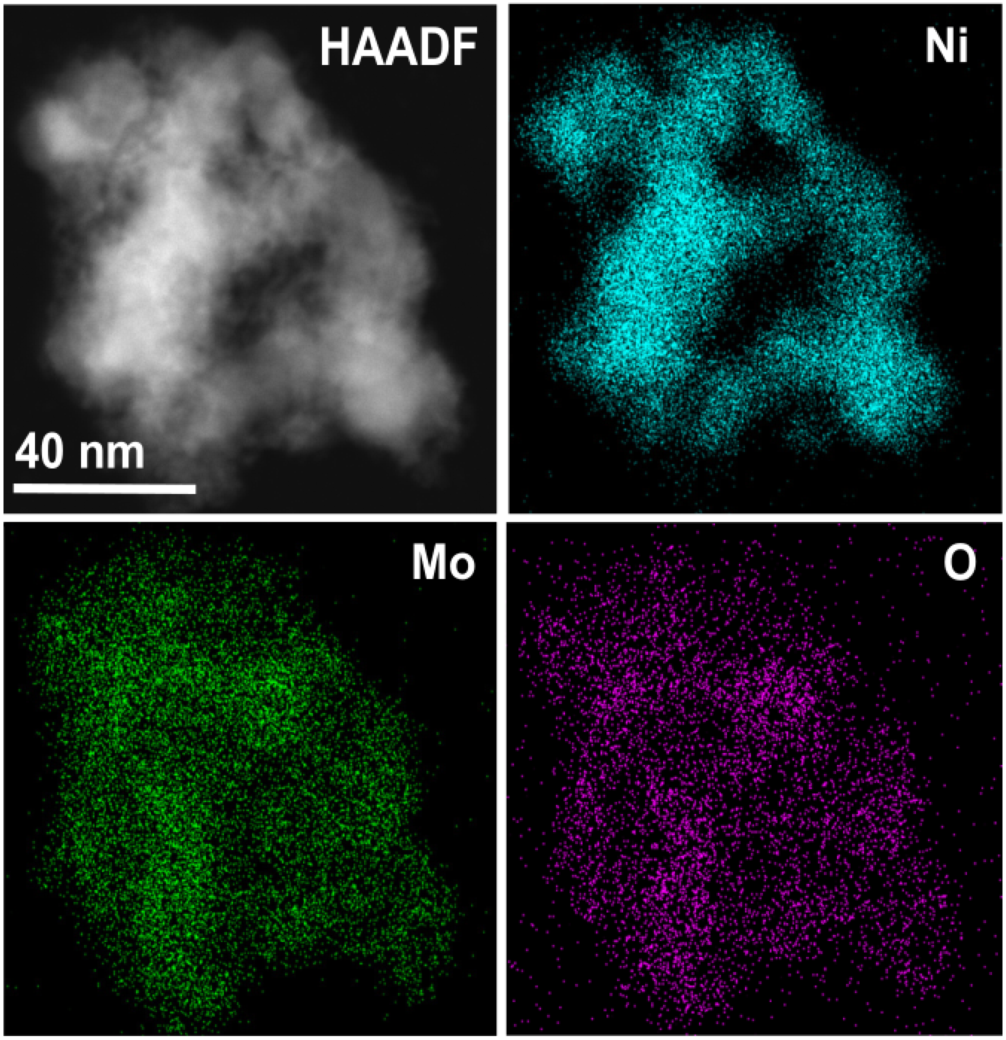

Figure 4.4: HAADF STEM image of single ammonia-based Ni–Mo agglomerate along with corresponding EDS elemental maps of the spatial distribution of Ni, Mo and O.

from Rituja B. Patil, Stephen D. House, Aayush Mantri, Judith C. Yang, James R. McKone; ACS Catalysis, 2020, 10, 18, 10390–10398. Copyright 2020 American Chemical Society.

4.2.1 Experimental

Nickel molybdate nanorods were synthesized via a hydrothermal reaction between aqueous Ni and Mo salts, following several prior reports.[228, 229, 230, 197, 231, 232, 233, 234, 235, 236] In a representative synthesis, 0.15 g of nickel nitrate hexahydrate (98%, Alfa Aesar) and 0.12 g of sodium molybdate dihydrate (99.5%, Alfa Aesar) were added to 15 mL of deionized water (purified using a Millipore Advantage A10 system) and dissolved by sonication in an ultrasonic bath (Branson M1800). Ni gauze (Alfa Aesar, 100 mesh, 100 mm dia wire) was cut into several 3x8 cm strips and cleaned by ultrasonication for 5-10 minutes in 2 M hydrochloric acid (99.5%, Fisher Scientific), followed by rinsing in ethanol (99.5%, Decon laboratories) and deionized water. Several strips were then vertically oriented against the interior walls of a polytetrafluoroethylene (PTFE) lined acid digestion reactor (Parr 4744). The reactor was finally loaded with the aqueous Ni+Mo precursor mixture, sealed, and placed in a preheated muffle furnace (Lindberg/Blue M Moldatherm) at 160°C for 6 hours. The reactor was allowed to cool to room temperature passively for several hours prior to opening. The Ni gauze, which had become matte green in color, was then removed from the reactor and sonicated for 30 minutes to remove the green solid. The resulting suspension was dried at 60 °C overnight.

Reduced Ni–Mo composites were generated by heating the $NiMoO_4$-coated Ni gauze samples in a tube furnace (Lindberg/Blue M Mini Mite) under an atmosphere containing 5% H_2 and 95% Ar or N_2 (Matheson). The reduction temperatures were varied from 200 to 600 °C for a total of 1 hour. After reduction, the mesh was sonicated in isopropanol to suspend the Ni–Mo catalyst composite. The mass of catalyst in the suspension was obtained by dropcasting a known volume of the solution on a borosilicate glass microscope slide and weighing it on an ultramicrobalance. A final suspension was then prepared with 1 mg/mL of Ni–Mo in isopropanol along with 1 mg/mL of 20 wt% Nafion solution.

4.2.2 *Ex-situ* analysis

Initially we focused on *ex situ* characterization of the $NiMoO_4$ nanorods before and after thermal reduction by combining temperature-programmed reaction experiments with SEM, TEM and XRD measurements. The structural and compositional analysis of as-synthesized oxide are compiled in Figure 4.5. The prominent phases identified by XRD were α– and β–$NiMoO_4$ with the possible addition of residual $NaNO_3$ from the synthesis mixture. EDS analysis in the SEM gave a 3:2 ratio of Ni to Mo, indicating unequal incorporation of the metals in the hydrothermal reaction. We attribute the presence of a minor fraction of metastable β–$NiMoO_4$ to the excess Ni, as has been reported elsewhere.[203, 204, 205, 237, 238] The particles were predominately rod-shaped up to a few hundred nm in diameter and several μm in length (Figure 4.5b). A small fraction of spherical particles were also observed (see Supporting Information), and exclusion of Ni mesh from the synthesis mixture gave a much larger proportion of isotropic nanoparticles. TEM examination (Figure 4.5c–e) confirmed the nanorods to be crystalline $NiMoO_4$ with a high density of planar faults running parallel to the rod axis.

Figure 4.6 depicts representative diffraction, SEM, and TPR data for thermally reduced $NiMoO_4$ nanorods. On reduction at 200 °C, the catalyst composition resembled the as-synthesized oxide. Reduction at 300 °C resulted in a marked decrease in long-range crystalline order, as evidenced by the loss of discernible XRD features associated with $NiMoO_4$. After reduction at 400 °C, the XRD showed peaks corresponding to unreduced $NiMoO_4$ and comparatively broad features at 2θ = 44, 52, and 76° (Figure 4.6a), which we assigned to a Ni-rich fcc Ni_xMo_{1-x} alloy. A lattice constant of 3.56 ± 0.01 Å was extracted from these peaks. The Mo content in the reduced alloy was calculated from the shift relative to that of pure Ni and found to be 9.86 ± 1.99 mol%.[219] Increasing the reduction temperature to 500 °C resulted in a significant decrease in the intensity of the fcc peaks relative to several new features below $2\theta = 25°$; some of these correspond to mixed Ni–Mo nitride phases, but several others we were unable to index to any known phase containing Ni and/or Mo.

SEM imaging of the Ni–Mo composite after reduction at 400 °C (Figure 4.6b) shows that the rod structure remained intact alongside a modest population of isotropic particles. The TPR data in Figure 4.6c indicate a monotonic decrease in mass with increased temperature under H_2, consistent with thermal reduction of $NiMoO_4$ to metallic and/or suboxide products.[227] The first-derivative of the weight loss curve gives three minima at 240, 340, and 460 °C. This suggests multiple distinct chemical transformations occur over the temperature range from 25 to 600 °C.

Figure 4.7 compiles XPS data for as-synthesized $NiMoO_4$ and the composite obtained after reduction at 400 °C. Prominent peaks identified in the survey spectra were Mo 3d, C 1s, N 1s, O 1s, Ni 2p and Na 1s. We attribute the presence of Na and N to $NaNO_3$, the water soluble product of the salt metathesis reaction that may remain entrained within $NiMoO_4$. High resolution XP spectra for the Ni 2p and Mo 3d regions were also collected. Nickel peaks in the oxide are consistent with Ni^{2+}, and upon reduction there emerged evidence for metallic Ni. The relatively low intensity of this

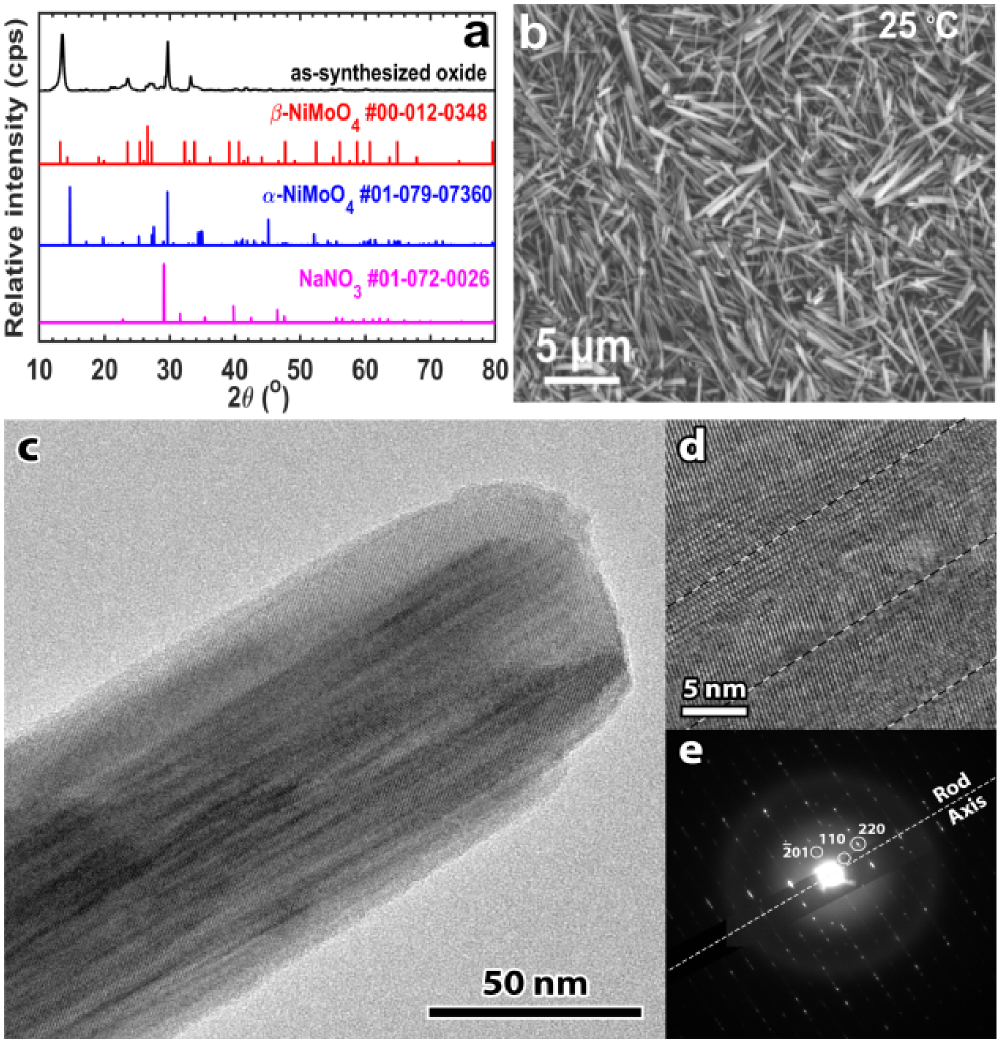

Figure 4.5: (a) XRD pattern of as-synthesized Ni–Mo oxide nanorod with the corresponding standard diffraction patterns obtained from the ICDD database. (b) SEM image of the as-synthesized oxide. (c) TEM micrograph of a representative nanorod. (d) HRTEM of a representative nanorod showing planar faults running parallel to the rod axis, as seen in the lattice shifts (examples indicated with dashed lines). These faults also manifest as the stripes in the contrast of (c). (e) Representative SAED pattern of the nanorod in (c) indexed to α-NiMoO$_4$; the pattern also displays characteristic streaking (perpendicular to the rod axis) and extra spots associated with planar faults.

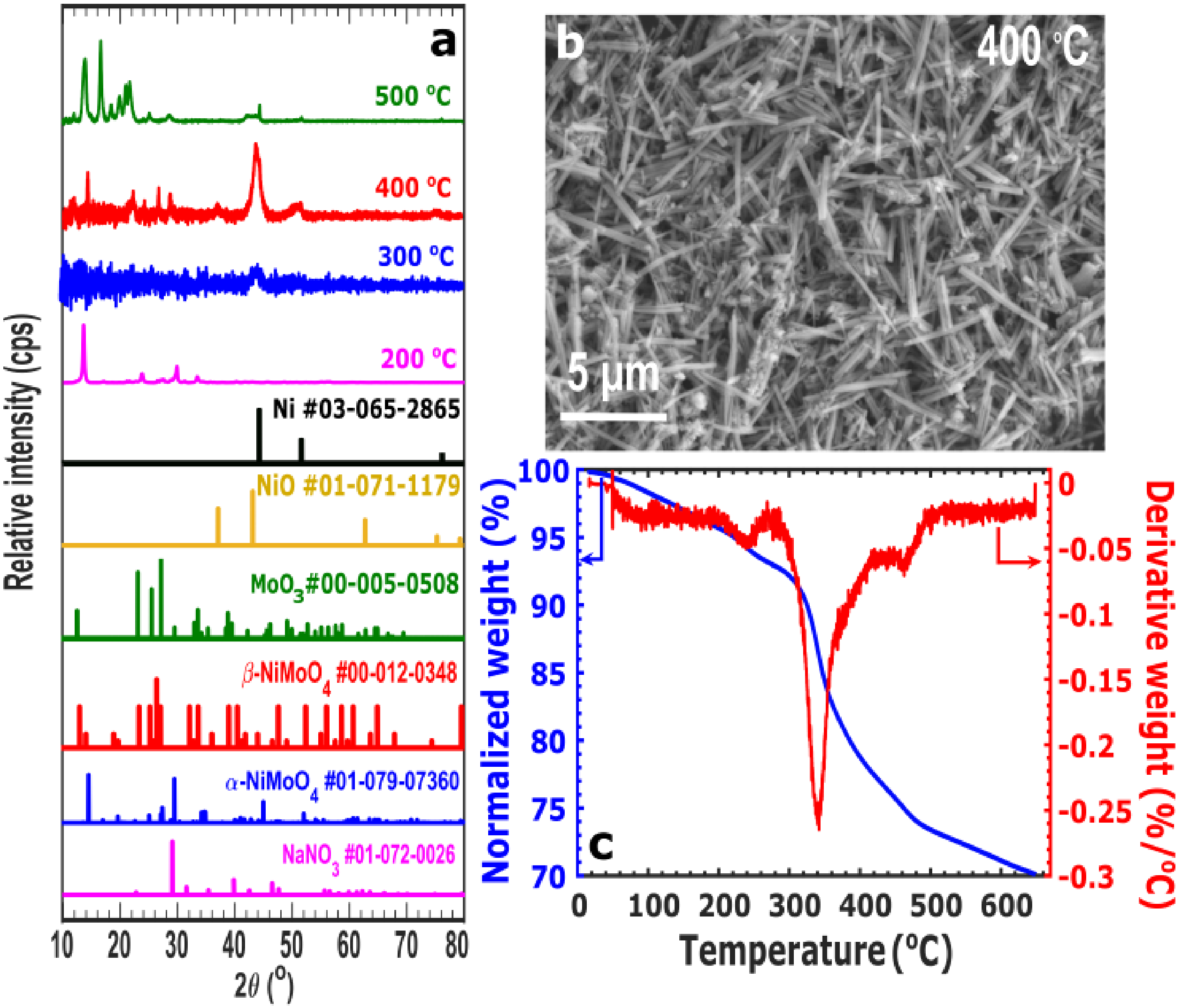

Figure 4.6: Characterization of NiMoO$_4$ nanorods after thermal reduction: (a) Empirical XRD patterns at 200, 300, 400, and 500 °C along with standard patterns obtained from the ICDD database. (b) Representative SEM image of the product upon reduction at 400 °C. (c) TPR data showing percent weight loss and the first derivative of the weight loss over the temperature range of interest.

metallic feature is consistent with oxidized Ni on the surface of the catalyst composite, which may result from incomplete reduction or re-oxidation of Ni in the alloy phase after handling the sample in air. Similarly, the Mo region in the oxide phase shows only features corresponding to Mo^{6+}, while the final product shows a clear evidence for partially reduced Mo^{5+} and Mo^{4+} and tentative evidence for Mo^0.

The observed changes in composition and morphology can be directly correlated with catalytic activity toward the alkaline hydrogen evolution reaction. Figure 4.8 collects representative polarization data (normalized to macroscopic electrode area) and cathodic current densities at 200 mV overpotential as a function of reduction temperature in 0.1 M KOH. A catalyst mass loading of 50 μg/cm^2 was used throughout these measurements to minimize the confounding effects of electrical resistance associated with thicker films containing significant residual oxide.[227] The catalytic activity increased initially up to 400 °C and then decreased significantly at higher reduction temperatures. This trend is consistent with the TPR measurements, where two distinct chemical transformations were observed below and above 400 °C.

These activity measurements, combined with the characterization results, suggest that $NiMoO_4$ reduction is a multi-step process, and the product obtained at moderate reduction temperatures exhibits the greatest HER catalytic activity. The as-synthesized oxide and the products obtained on heating at $\leq$200 °C display activity that is not significantly greater than the glassy carbon background (see Supporting Information). At 240 °C, a slight mass loss in the TPR data does not result in any apparent change in composition (see Supporting Information); hence, we attribute this feature to be loss of adsorbed water. The HER activity begins to increase discernibly at 300 °C, which also coincides with initial XRD evidence for formation of the fcc Ni–Mo alloy, suggesting initial formation of the active catalyst. At 400 °C, the XRD data clearly indicate the formation of an alloy phase, but the high XPS intensities for Ni and Mo oxides suggest incomplete reduction. Nonetheless, the HER activity is maximized at this treatment temperature, which suggests that the active catalyst may require metallic and oxidized components.

The decrease in activity at 450 °C corresponds well to the TPR data showing the onset of a second major chemical transformation near this temperature. However, additional analysis by XRD and *ex situ* TEM (see Supporting Information) do not give a clear indication of the nature of this chemical transformation. While increased temperature would be expected to decrease surface

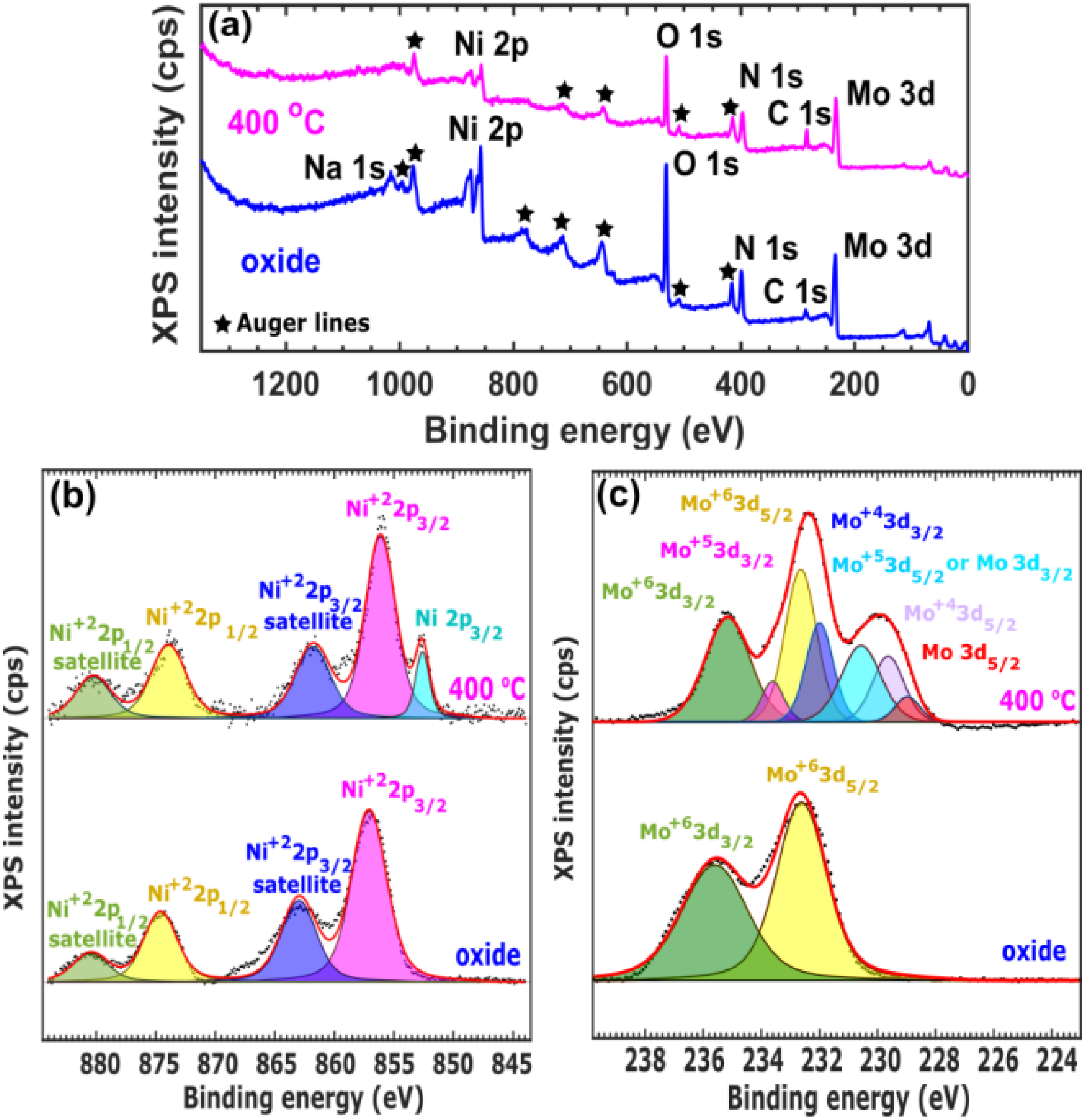

Figure 4.7: Representative XP spectra and fits for $NiMoO_4$ oxide before and after reduction at 400 °C: (a) survey scans; (b) Ni 2p region; (c) Mo 3d region.

area through particle coarsening, electrochemical impedance spectroscopy and HRTEM data (see Supporting Information) suggest that the activity maximum around 400 °C cannot be attributed to

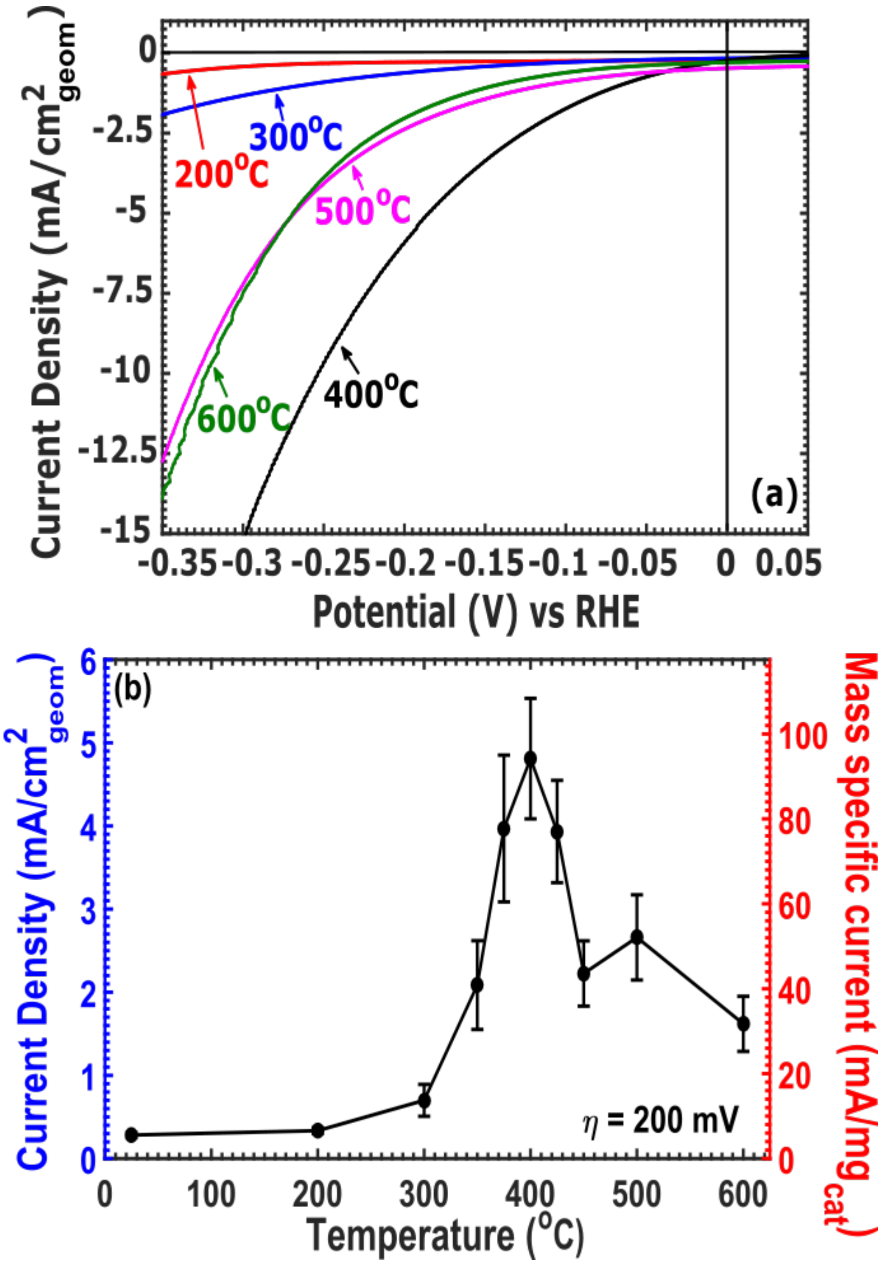

Figure 4.8: Representative polarization curves (a) along with absolute values of geometric and mass activity (b) for $NiMoO_4$ nanorods that were thermally reduced for 1 hour at the noted temperatures. Measurements were performed in H_2-saturated 0.1 M KOH using a catalyst mass loading of 50 μg/cm^2 at 10 mV/s scan rate. The error bars in (b) represent 95% confidence intervals about the mean calculated from at least 10 samples at each temperature.

surface area alone. Nonetheless, all of the materials analysis presented up to this point leave open the question of what is the nanoscale composition and morphology of the active form of the catalyst obtained around 400 °C.

4.2.3 *In-situ* analysis

To provide further insight into the nanoscale structural changes occurring during the catalyst nucleation and growth processes, we performed TEM characterization *in situ* during thermal reduction using an ETEM system along with *ex situ* HRTEM imaging and elemental analysis of the reduced products. $NiMoO_4$ nanorod specimens were heated under 1.1 x 10^{-2} Pa of H_2 from 25 to 500 °C. Heating was performed in 25 °C steps, with the temperature held steady at each step until no further structural changes were observed. In addition to the nanorods followed continuously throughout this process, additional nanorods that were not continuously exposed to the electron beam were also briefly examined after each major transformation (see Supporting Information). The morphological changes we observed were consistent across all examined nanorods, confirming that these changes were not merely the result of interactions with the electron beam.

Real-time ETEM data were collected during thermal reduction as continuous videos, which are included as Supporting Information. Representative bright-field still images as well as selected-area electron diffraction (SAED) data over a range of temperatures (after cessation of the associated structural changes) are collected in Figure 4.9. Extensive additional imaging and SAED data have also been included in the Supporting Information. Consistent with the TEM data in Figure 4.5, the as-synthesized $NiMoO_4$ rods (Figure 4.9a,g,k) were highly crystalline with planar faults running parallel to the rod axis. This morphology remained unchanged until reaching 350 °C (Figure 4.9b,h,l), when small Ni-rich nanoparticles (mean of 4.5 $\pm$ 1.5 nm, Figure 4.10) were observed to nucleate in and on a porous Mo-rich oxide “skin.” The nanoparticles were evenly dispersed and, once nucleated, remained in place, evidently growing via diffusion of Ni from the surrounding $NiMoO_4$ as it continued to react. As seen in the image, as well as by the continued presence of the strong planar-faulted single-crystal diffraction pattern in Figure 4.9j, the core of the nanorods remained mostly intact.

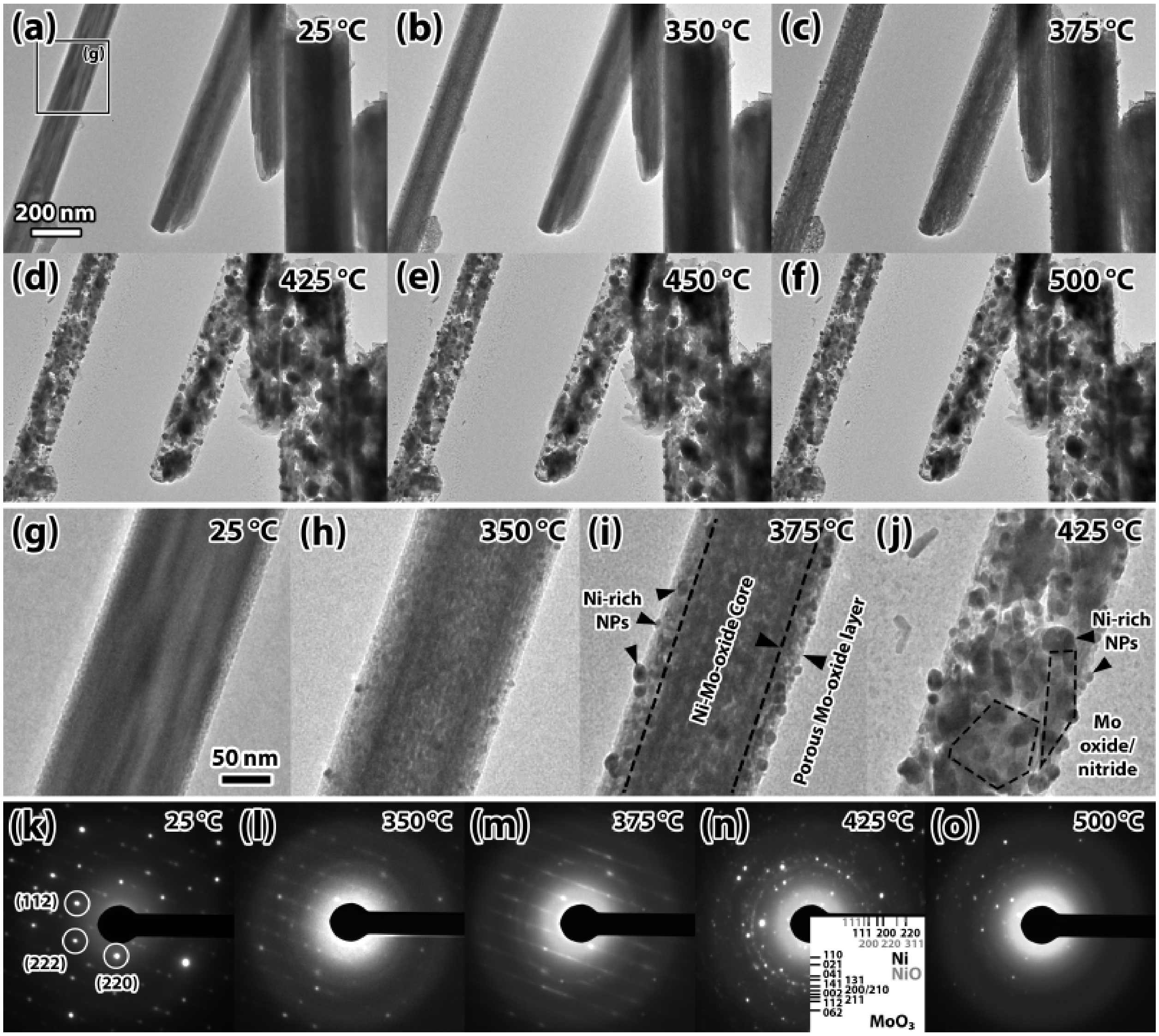

Figure 4.9: TEM micrographs and SAED patterns for $NiMoO_4$ nanorods that were thermally reduced in the ETEM at selected temperatures. Images were collected after cessation of observable structural changes. (a-f) Images of the full region continuously followed during reduction. (g-j) Close-ups of a region of the thin nanorod indicated by the box in (a) at the indicated temperatures. The dashed lines in (i) delineate the boundary between a porous, Mo-rich outer oxide layer and a solid nanorod core. Dashed oulines in (j) indicate Mo-rich oxide and/or nitride flakes. (k-o) SAED patterns of the thin (leftmost in a-f) nanorod at each of the indicated temperatures. The pre-reduction diffraction pattern (k) indexes as α-$NiMoO_4$ (Miller indices are annotated). The polycrystalline pattern in (n) is consistent with fcc Ni and one or more Mo-rich oxides/nitrides.

Increasing the temperature to 375 °C (Figure 4.9c,i,m) produced more Ni-rich nanoparticles along with a coarsening of their overall size to 9.4 ± 3.1 nm (Figure 4.10) as the porous outer layer progressed deeper into the nanorods. Upon equilibration, the outer layer of each nanorod had transformed into a porous Mo-rich oxide network, into and onto which was embedded metallic nanoparticles. Electron diffraction indicated these particles showed the Ni fcc crystal structure; hence, they agree well with the XRD observations indicating formation of a Ni–Mo alloy containing ∼90 mol% Ni. For all the rods examined, this structural change halted at a depth of 20-30 nm below the original nanorod surface, leaving the core largely intact (Figure 4.9i,m).

Upon heating to 425 °C, the second major reductive transformation began to occur. The previously intact core of the nanorod completely reacted, leading to a dramatic phase segregation into isotropic Ni-rich nanoparticles and large, angular Mo-rich oxide crystals (Figure 4.9d,j,n). The number and average size of the Ni-rich nanoparticles notably increased (14.1 ± 7.4 nm, Figure 4.10), and the size distribution also increased markedly, with the largest particles growing to nearly 100 nm in diameter. The coarsening of existing nanoparticles combined with a transition to a strongly lognormal overall distribution (see Supporting Information) indicates that both Ostwald ripening and particle migration and coalescence were active at this stage. The Mo-rich oxide particles—with a mean diameter of 72 ± 38 nm and an observed range from 20 to 200 nm—formed by the reduction of the core were predominantly flake- or rod-like, highly faceted crystals, as confirmed via HRTEM (see Supporting Information). The porous outer layer that had formed at 350-375 °C was also partially consumed into these crystals as they reacted further.

The overall process of $NiMoO_4$ chemical transformation and phase segregation was largely complete after equilibration at 425 °C, but slight coarsening and particle movement continued until 500 °C (Figure 4.9f,o), where the experiment was terminated. The trends were consistent in all rods observed, regardless of initial diameter or whether they were actively imaged during reduction (see Supporting Information). In fact, particle coarsening and phase separation were actually more pronounced in some rods that were only exposed to the electron beam before and after heating. This suggests that although interaction with the 100-kV electron beam may change some specific details of the morphology change (e.g., the exact size, number, and/or distribution of nucleated Ni-rich particles), the general trajectory of oxide reduction is not significantly influenced by the beam.

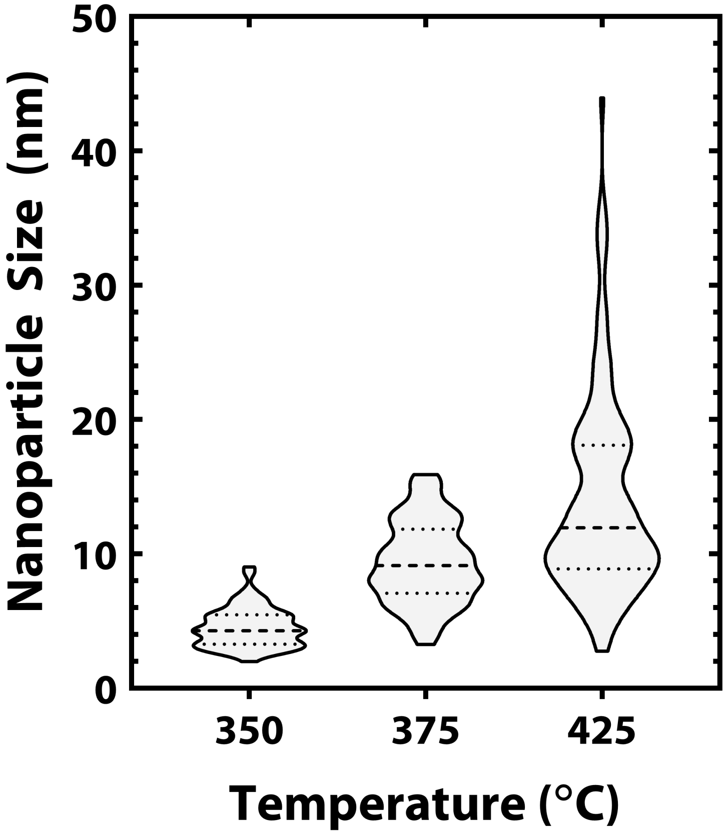

Figure 4.10: Size distribution violin plots of the Ni-rich nanoparticles in the Ni–Mo composite after thermal reduction at 350, 375, and 425 °C. The nanoparticle populations were taken from the same region of the same nanorod at the given temperatures. The dashed lines indicate the median and the dotted lines indicate the quartiles. Total population sizes were N = 64, 90, 125 particles, respectively. Only particles that were clearly resolvable were counted.

Attempts to quantitatively identify the crystalline phases present in the fully reacted product via SAED were hindered by the near-equivalent plane spacings in several Mo-rich oxides as well as fcc Ni. Thus, for each of the observed diffraction rings we identified at least two possible phases. Nonetheless, the measured diffraction rings/spots are consistent with a Ni-rich fcc alloy and the expected Mo-rich oxides. Major diffraction peaks present in the SAED pattern (Figure 4.9n) corresponding to the dominant phases observed by XRD have been indicated. There was also some evidence for Mo nitride in the final product; we speculate that this results from thermal reduction of residual nitrate from the synthesis mixture.

The phase segregation of the fcc Ni-rich alloy from the Mo-rich oxide was confirmed via HAADF-STEM imaging and EDS elemental mapping of the fully reduced nanorods (Figure 4.11). These data show that Ni is localized almost entirely to the isotropic nanoparticles (brighter in the HAADF image), while the rods' outer shell and large interior crystals are comprised primarily of Mo, O, and N. Additional HAADF-STEM images and EDS maps from nanorods in the primary cluster and from a nanorod that had not been imaged at all before or during the *in situ* reduction are included in the Supporting Information. These observations indicate that all of the Ni in the $NiMoO_4$ precursors that is accessible to the gas-phase H_2 reactant is fully reduced at $\leq$500 °C, and the oxidized Ni observed by XPS likely results from post-synthetic exposure to atmospheric oxygen. By contrast, the vast majority of the Mo content of the precursor remains oxidized, which is consistent with prior reports showing that Mo-oxides are highly resistant to complete reduction under H_2 at temperatures below 600 °C.[239, 240, 241]

4.2.4 Combining *ex-situ* and *in-situ* analysis

Upon consideration of the *in situ* and *ex situ* data together, the increase in alkaline HER activity beginning at 300 °C is consistent with the formation of catalytically active Ni-rich nanoparticles surrounded by porous Mo-rich oxide network. The highest activity is then achieved upon formation of a substantial number of sub-10 nm Ni-rich nanoparticles that remain embedded in and on the oxide matrix. This leaves at least two plausible explanations regarding active sites for the alkaline HER in this catalyst. The first is that metallic $Ni_{0.9}Mo_{0.1}$ nanoparticles are the only catalytically competent species, and the narrow activity maximum at $\sim$400 °C corresponds to point at which the exposed surface area of these particles is maximized. The activity decrease above 400 °C then results from loss of surface area and inter-particle connectivity due to nanorod pulverization. However, the total number (and apparent surface area, see Supporting Info.) of Ni-rich particles actually increased at temperatures above 400 °C, which makes it difficult to implicate surface-area effects alone.

Another possibility is that the catalytic performance of these materials depends on the interaction between the metallic alloy particles and the remaining oxide. This interpretation agrees

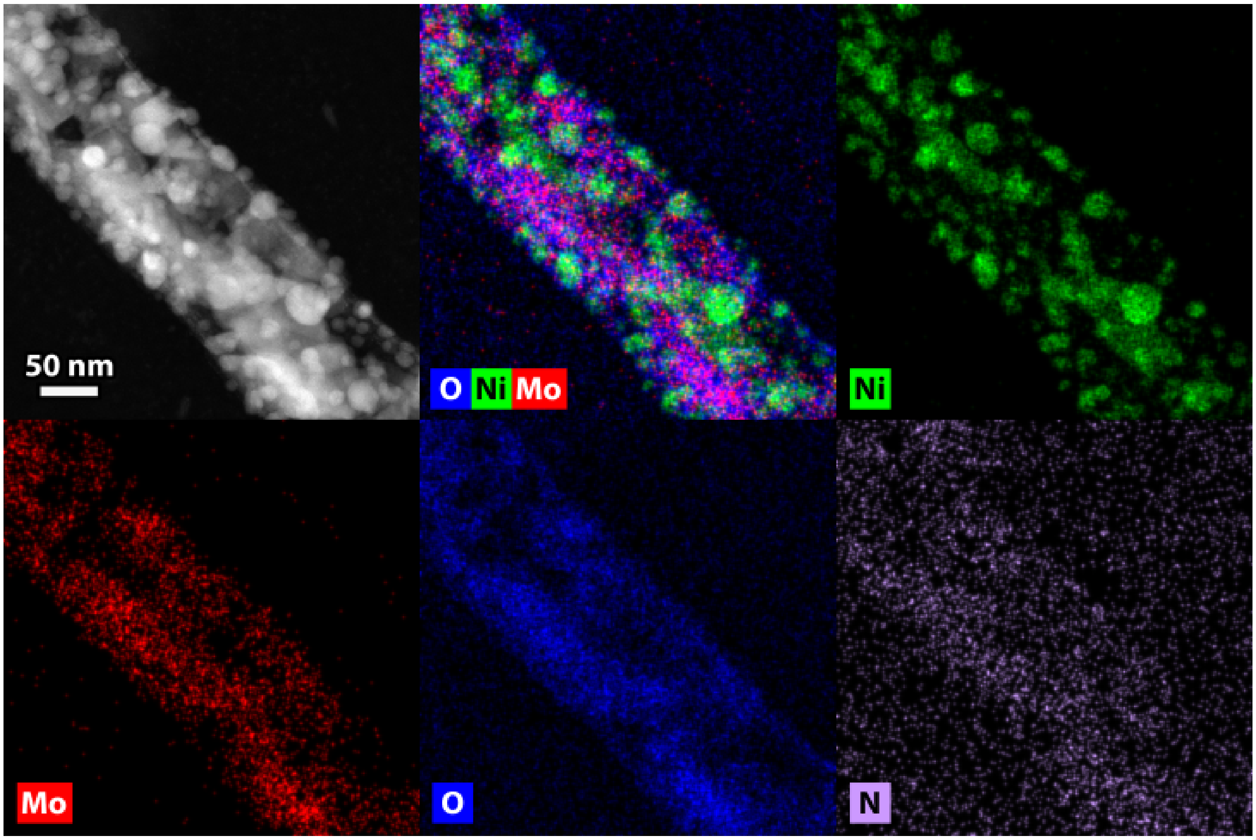

Figure 4.11: HAADF-STEM image (upper left) and the corresponding EDS elemental maps from a region of the thinnest (leftmost) rod in Figure 4.9 after thermal reduction at 500 °C.

with numerous recent reports indicating that alkaline HER electrocatalysts based on precious and nonprecious metals benefit from synergistic interactions between metallic and oxidized surface sites.[64, 65, 242, 63, 243] We speculate that the active catalytic unit in these Ni–Mo composites comprises interfacial sites where Ni, MoO_x (or $NiMoO_x$), and aqueous electrolyte coexist under HER reaction conditions. Accordingly, the decrease in activity at reduction temperatures above 400 °C would then be attributable to a significant decrease in metal–oxide contact area that results from restructuring of the Mo-rich oxide matrix.

Galvanostatic stability analysis performed on the highest performing catalyst (see Supporting Information) showed a significant decrease in HER activity within tens of minutes. This loss in activity was also accompanied by significant restructuring of the catalyst into large isotropic aggregates. This further suggests that the oxide phase is relevant to the HER mechanism.

Ultimately these data show that the synthesis of catalytically active Ni–Mo composites from Ni–Mo oxides is a kinetically controlled process that requires intercepting a partially reduced product containing metallic and oxidized components in intimate contact. While these studies were directed at electrocatalytic hydrogen evolution, it is plausible that very similar catalyst compositions are generated spontaneously in thermal hydrogenation reactors.[244, 245, 246, 247, 248, 190, 192] While it is possible to follow these chemical transformations using *ex situ* measurements alone, *in situ* ETEM enables direct observations that can be used to further inform synthetic strategies to improve kinetic control. For example, the chemical and structural transformations associated with each temperature step in the ETEM were complete within a few minutes. Hence, it would be intriguing to pursue improved control over catalyst microstructure using rapid thermal processing techniques, which are routinely deploying in the semiconductor industry.[249, 250] Nonetheless, the multiphase and morphologically irregular nature of this catalyst makes it difficult to implicate a specific active site or reaction mechanism. Further work would also be warranted to pursue alternative synthetic routes for Ni–Mo metal/oxide composites with improved control over the composition and morphology of each component.

Thus, using *in situ* ETEM alongside extensive *ex situ* characterization, we showed that the thermal reduction of $NiMoO_4$ nanorods proceeds via a series of distinct chemical and structural transformations. The reaction initiates with Ni-centered nucleation events and ultimately leads to phase segregation between Ni-rich alloy nanoparticles and Mo-rich oxides. The catalytic activity of this composite toward the HER is maximized over a narrow range of reduction temperatures that coincide with the formation of small Ni-rich nanoparticles embedded in a Mo-rich oxide matrix. These data suggest that the active catalyst requires metallic and oxidized species in intimate contact, but the multiphase nature of the catalyst makes it difficult to identify the precise composition of the active site or sites. Further work would be warranted to synthesize phase-pure, monodisperse Ni–Mo alloys and metal/oxide composites to further assess the active sites for hydrogen evolution and thermochemical hydrogenation reactions in these materials.

4.3 Metal/metal-oxide interfaces for hydrogen electrochemistry

We have now seen that Ni–Mo alloys consist of an oxide shell and that it is formed due to incomplete reduction of a mixed $NiMoO_4$ starting material. But there remains a question of whether these metal/metal-oxide interfaces are important for HER catalysis. A thorough literature review suggests that there are four mechanisms by which metal/metal-oxide composites may cooperate to improve catalytic activity. These four are schematized in figure 4.12. In all cases, it is broadly hypothesized that the water dissociation step associated with the Volmer or Heyrovsky steps in HER catalysis is rate-determining. One hypothesis is that metal/oxide cooperatively causes directly accelerates water dissociation at oxide sites proximal to the metallic H-binding sites. Another similar possibility is that dipolar surface interactions at the metal oxide favorably influence the orientation of water molecules as they approach the metallic active site. A third possibility involves electronic synergy, in which unique sites at or near the metal/metal-oxide interface exhibit uniquely favorable binding energies for H intermediates. Finally, the HER mechanism at metal/metal-oxide interfaces may involve H-spillover——that is, the physical migration of H-intermediates between the metallic and oxidized surfaces.

Metal/metal-oxide interfaces are ubiquitous in thermal catalysis, but they have been considerably less studied in electrocatalysis since most oxide supports are not sufficiently conductive to enable facile electron transfer to a metallic active site. Nonetheless, we broadly hypothesize that many metal/metal-oxide interfaces are beneficial for hydrogen evolution/oxidation electrocatalysis.

4.3.1 Wire catalysts

Motivated by a key finding from Liang et al.,[63], we were motivated to explore whether every experimentally accessible transition metal surface would exhibit enhanced HER when it was partially oxidized electrochemically. Specifically, we tested Ni, Co, Cu, Ag, and Fe metals in the form of wires that were 99.995% pure from Alfa Aesar. These metals were chosen in part because they are readily commercially available and span a wide range of HER activities. The metal oxides were generated electrochemically by varying the potential range over which the samples were cycled electrochemically. The synergy of underlying metal with its oxide on the HER activity was

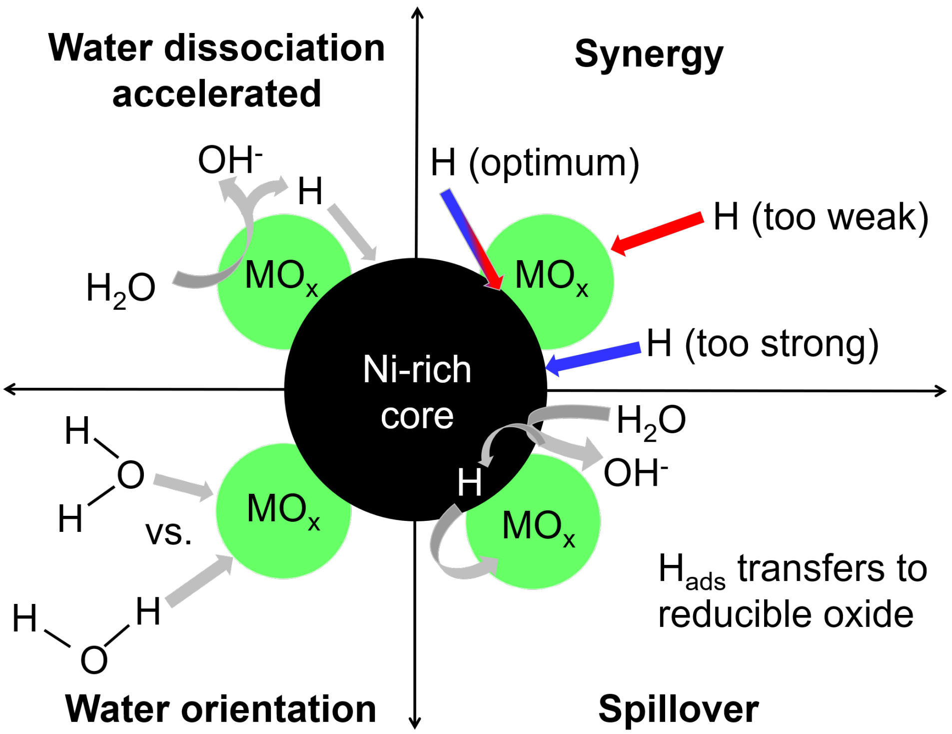

Figure 4.12: Possible mechanisms for enhancement in HER activity due to metal/oxide

monitored by measuring the activity at a fixed HER potential as a function of positive potential limit (figure 4.13), where less positive potential limits corresponded to nominally un-oxidized material and more positive limits gave rise to progressively greater sample oxidation.

The HER activity of Ni and Co wires increased when dicationic oxides were formed. This suggests that Ni^{2+} and Co^{2+} oxide (or hydoxide) facilitate HER on Ni and Co metals, respectively, as also reported by several others.[63, 188, 65] The +3 oxidation state of Co continued to promote HER while Ni^{+3} suppressed the HER activity. The oxides of Fe, Ag, and Cu had no discernible beneficial effect on the HER activity of the respective metals, and Cu oxidation lead to a decrease in performance. Accordingly, this analysis showed that alkaline HER activity is not simply enhanced by the presence of any transition metal oxide. Rather, only certain oxides appear to behave as effective co-catalysts; or, alternatively, only certain transition metals benefit from the presence of an oxide co-catalyst.

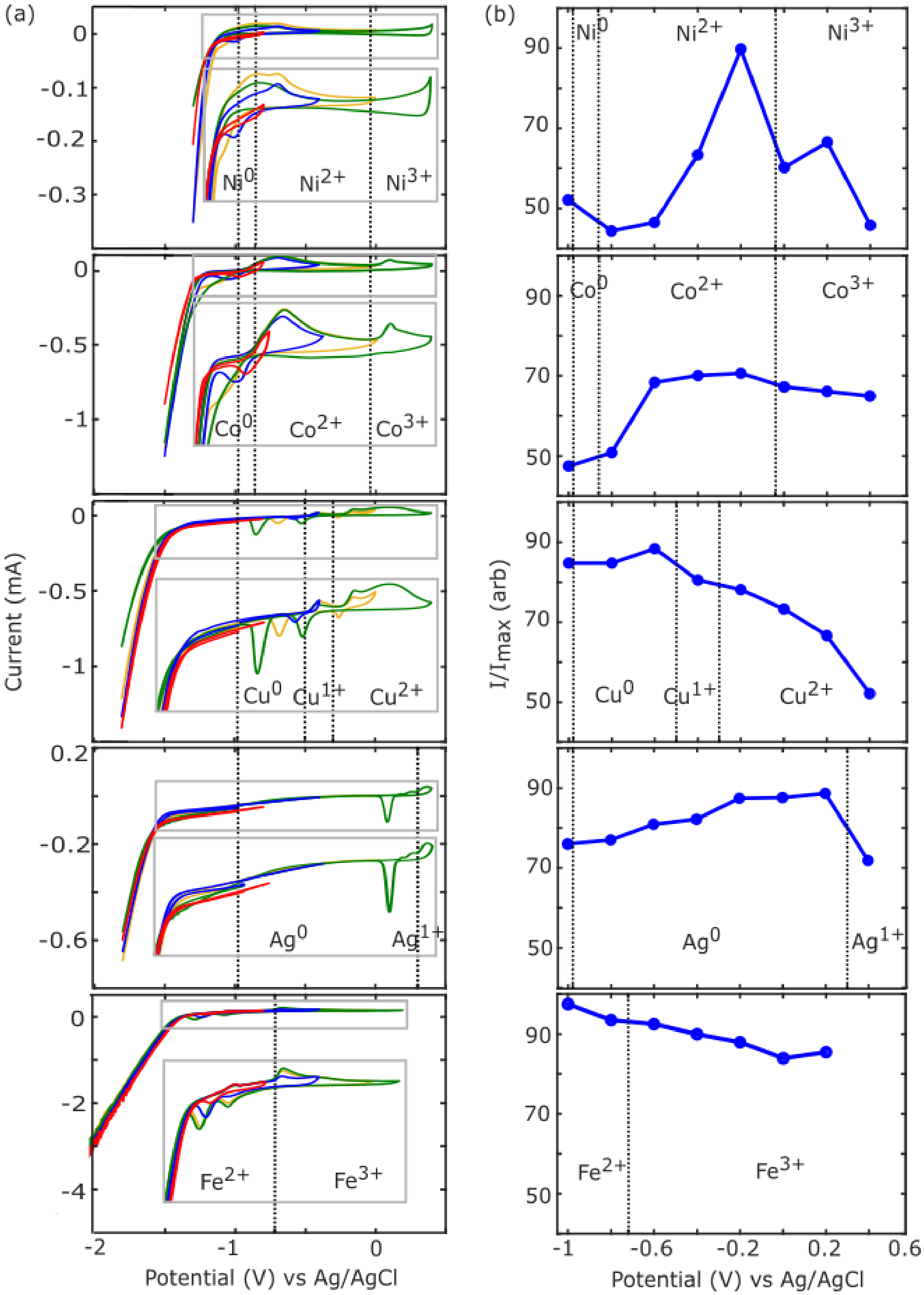

Figure 4.13: Influence of oxidation of metals on their HER activity. (a) shows representative cyclic voltammograms for respective metals at different potentials at 50 mV/s under N_2 purge in 0.1 M KOH and (b) shows HER activity normalized to the maximum observed current as a function of different positive limit potentials (-1 to 0.4 V vs. Ag/AgCl). The HER activity was measured at that potential where there was no influence of the redox peaks.

4.3.2 Thin film catalysts

The research literature contains several prominent examples of metal/metal-oxide interfacial synergy that was revealed through a detailed study of composite thin films. For example, it was shown recently that $Ni(OH)_2$ islands enhance the alkaline HER activity of a wide range of transition metals.[65, 64] Deposition of discontinuous RuO_x layers on Pt also showed enhanced activity for the methanol oxidation reaction.[251, 252] Many of these studies employed single-crystal surfaces, which enable highly precise experimentation at the expense of high financial and temporal costs. To address this constraint, we have adopted a technique called "template stripping" to study thin-film metal/metal-oxide interfaces. The surfaces generated by template stripping are ultra-flat (RMS roughness values are routinely sub-nm) and polycrystalline. The polycrystalline nature of the surfaces allow us to study the influence of metal/oxide interfaces on different crystal facets, at the expense of site specificity. However, surface probe techniques can be used to directly correlate the composition and two-dimensional density of metal/metal-oxide interfaces to the observed catalytic activity.

The template stripping process involve depositing the metal of choice on a freshly oxidized prime-grade single crystal silicon wafer with a surface roughness in the sub-nm regime. A microscope slide is then coated with an adhesive (e.g., two-part epoxy) and placed on the wafer with glue side touching the metal (figure 4.14). The glue is cured by heating, after which the microscope slide is manually separated the wafer, which also strips the metal film from the Si wafer. The metal-deposited glass slide can now serve as the working electrode in electrochemical analysis, and the morphology of the metal film exhibit similar roughness as the parent Si wafer.

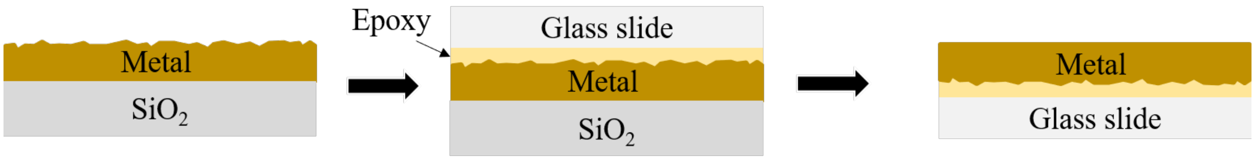

Figure 4.14: Procedure to fabricate template stripped surfaces

Figure 4.15 depicts the topography of a representative Pt surface as well as cyclic voltammograms of 3 different metals that we tested, which confirms that the template stripping method works for these metals. The RMS roughness of each metal surface was found to be sub-nanometer, with peak-to-trough vertical displacements of the same order as a single metal-metal bond length over micron-scale distances. The identity and chemical cleanliness of the metals were confirmed from their characteristic CV patterns when Pt displayed its typical hydrogen underpotential deposition peaks in the potential range from 0 to 0.2 V vs. RHE, while Au and Ni exhibited their oxidation/reduction peaks in 0.8–1.4 V vs. RHE. The absence of peaks other than these characteristic peaks further indicated that the surfaces were free of electrochemically active contaminants. This degree of dimensional control is helpful for increasing the resolution of surface characterization techniques, especially atomic force microscopy (AFM), to correlate surface topology with chemical composition and, ultimately, interfacial catalytic activity.

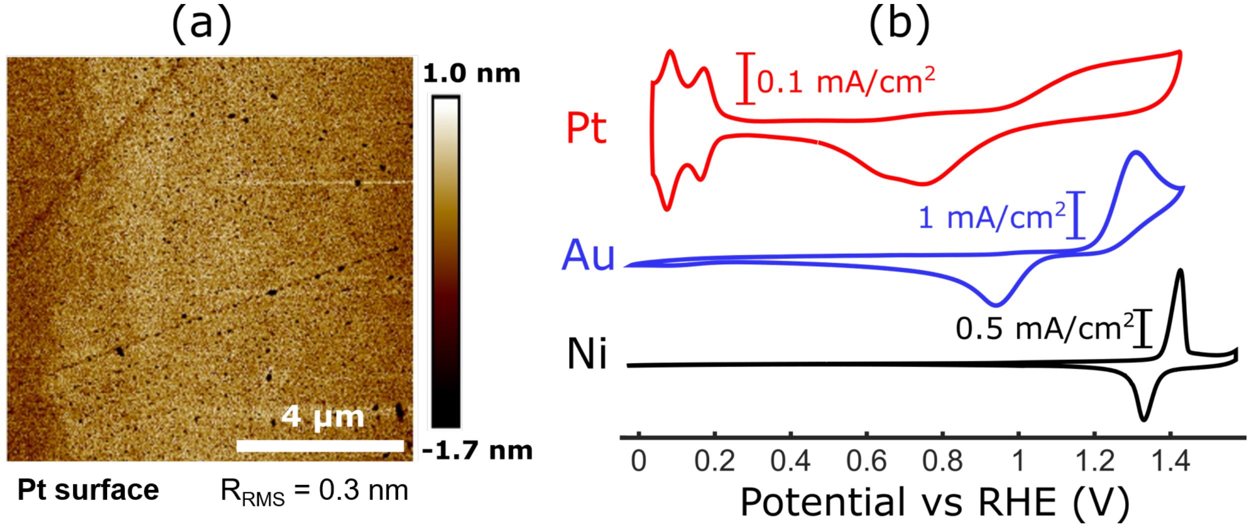

Figure 4.15: (a) AFM image of a representative Pt surface; (b) cyclic voltammograms of template-stripped Pt, Au and Ni surfaces.

Encouraged by these preliminary results, we proceeded to assess the influence of metal/metal-oxide interfaces on the hydrogen evolution reaction. The aim of these experiments was to correlate the areal density of interfacial edge sites at the boundary between Pt and $Ni(OH)_2$ to the observed catalytic activity of the composite. We hypothesize that the observed HER activity would increase linearly with the interfacial edge length, and not the overall surface area of the metal and hydroxide components. To assess this hypothesis, we created metal/metal-oxide interfaces where a template stripped Pt surface was decorated with $Ni(OH)_2$ in the form of a discontinuous film. Note that this experimental method closely resembles those used by Danilovic et al. to study Pt/$Ni(OH)_2$ interfaces using single-crystal Pt substrates.[65]

A typical deposition of discontinuous oxide film began by immersing a template stripped Pt surface in $NiCl_2$ solution so that the metal chlorides from the solution strongly adsorb on the Pt. The chloride ions are then replaced with hydroxide ions by removing and rinsing the sample with pure water and then immersing it in aqueous KOH solution. The concentration of $NiCl_2$ and the time of deposition were varied to vary the surface coverage of $Ni(OH)_2$. The AFM data shown in Figure 4.16 (inset on right-hand side) shows that samples in which $Ni(OH)_2$ had been deposited exhibited notable increased RMS roughness, which is consistent with the formation of discontinuous islands of $Ni(OH)_x$. The partial coverage of the Pt surface was confirmed by calculating the electrochemically accessible surface area (ECSA) of pristine Pt versus the Pt|$Ni(OH)_2$ composite. Importantly, the HER activity of the oxide decorated surface was found to be 2–3 times higher than the pristine Pt surface, despite a 40 % decrease in the number of exposed Pt surface sites.

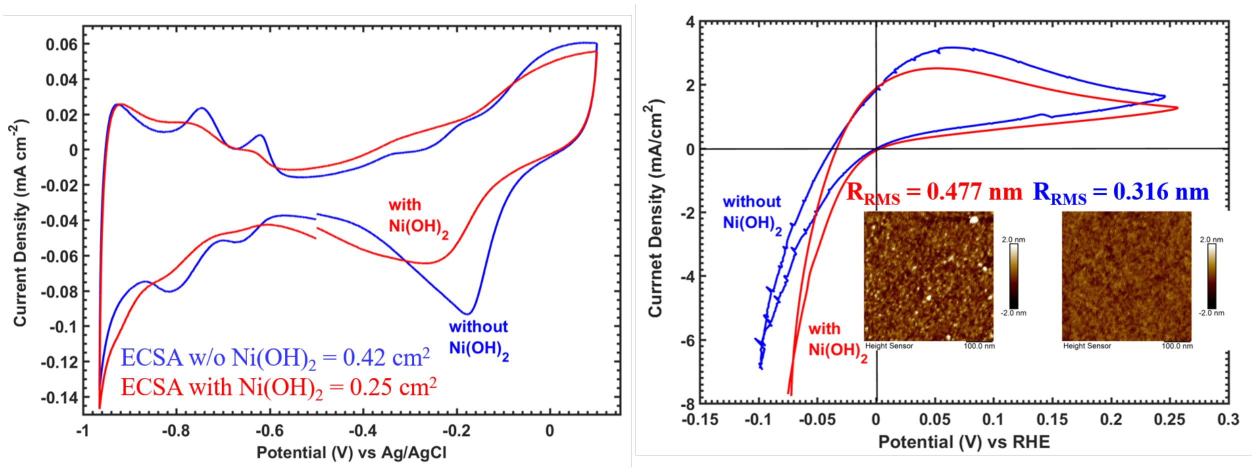

Figure 4.16: Enhancement in HER performance due to Pt-$Ni(OH)_x$ synergy

To differentiate between Pt and $Ni(OH)_2$ on the sample surface, we performed Peak Force Tunneling Current AFM (PF-TUNA) analysis. The conductivity of Pt is 9.4×10^6 S/m while that of $Ni(OH)_2$(aq) is 1×10^{-2} S/m, which is significantly lower than Pt and thus was expected to yield a clear difference in current flow as a function of AFM tip position on a discontinuous

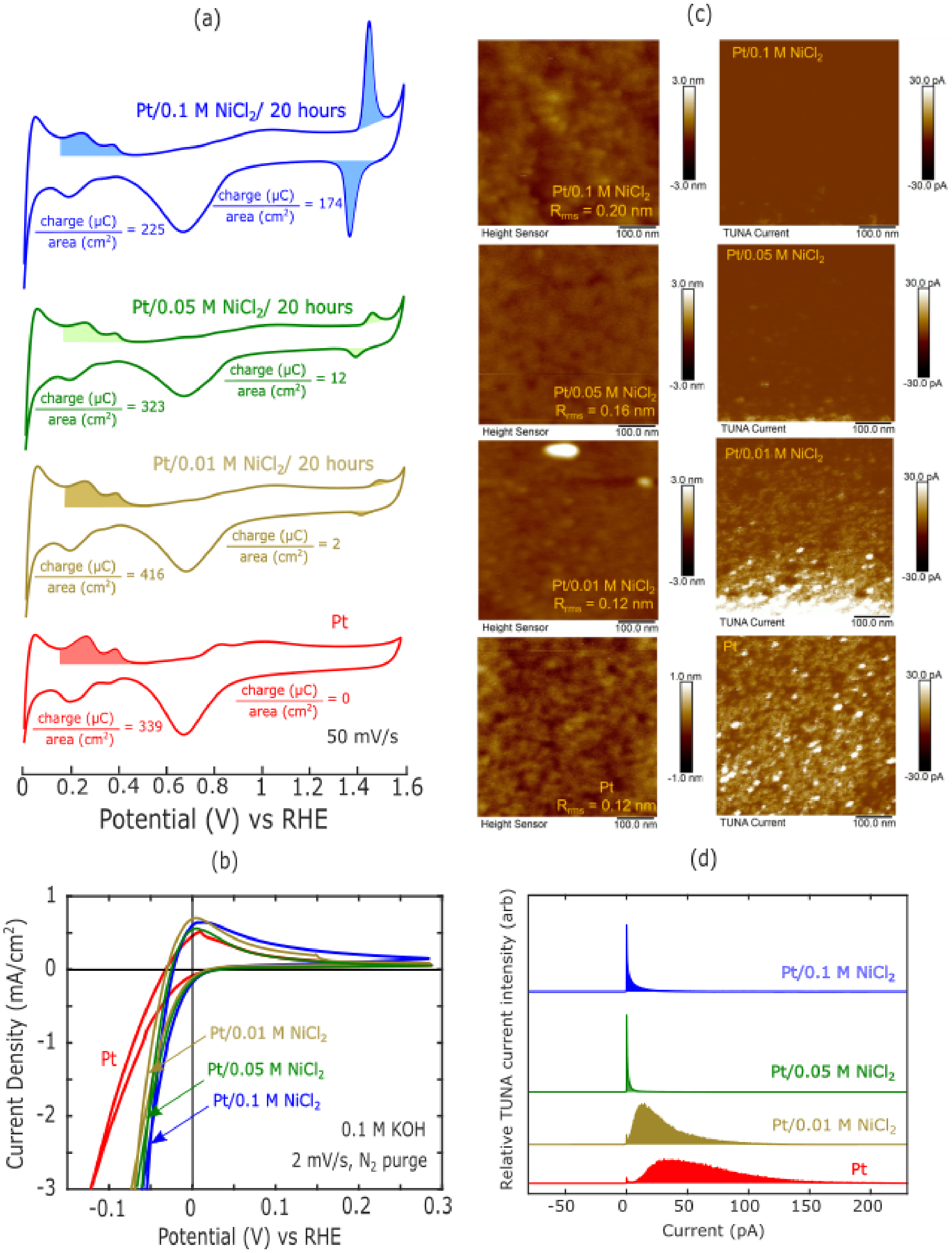

Figure 4.17: Electrochemcial and AFM analysis on Pt/Ni(OH)$_x$ systems prepared by immersing template stripped Pt surfaces in different concentrations of NiCl$_2$ precursor. (a) The voltammetric data collected by scanning the potential from 0–1.6 V vs. RHE encompassing the hydrogen underpotential region (HUPD) of Pt (0.2–0.4 V vs. RHE) and Ni$^{2+/3+}$ redox couple (1.2–1.55 V vs. RHE) in 0.1 M KOH at 50 mV/s under nitrogen gas purge. (b) HER polarization curves collected by scanning the potential from -0.3 to 0.3 V vs. RHE at 2 mV/s in 0.1 M KOH and N$_2$ gas purge. (c,d) PF-TUNA analysis was done using SCM-PIT tip at 200–500 mV applied DC bias.

interface.[253, 254] We prepared 4 different metal/metal-oxide films by systematically varying the concentration of $NiCl_2$ solution with an expectation to observe changes in the number and/or size of $Ni(OH)_x$ islands on Pt. Freshly prepared template stripped Pt films were immersed in $NiCl_2$ solution concentrations of 0.01 M, 0.05 M, and 0.1 M each for 20 hours and compared with pure Pt film. Figure 4.17 summarizes the electrochemical and AFM analysis performed on these films. The charge densities of the HUPD and the Ni-redox peaks, calculated from the voltammetric curves, indicate the exposed sites of Pt and Ni respectively after the deposition. With an increase in precursor concentration, the intensity of $Ni^{2+/3+}$ peak increased systematically indicating formation of more Ni-based species on Pt surface. The electrochemically active surface area (ECSA) of Pt also decreased monotonically by up to a factor of 2 with an increase in the precursor concentration, suggesting that the exposed surface of Pt decreased continuously. The pure Pt film, however, did not comport with this trend, and additional experiments will be needed to address this unexplained result. Moreover, the HER activity of all $Pt/Ni(OH)_x$ films was uniform and consistently higher than pure Pt. This result was also unexpected, but suggests that a synergistic mechanism between Pt and $Ni(OH)_x$ is operative but largely independent of the total amount of Ni-based species on the surface.

The AFM analysis comprising height and peak force tunneling (PF-TUNA) current images of all $Pt/Ni(OH)_x$ films were collected after the electrochemical analysis. The root mean square roughness obtained from the height image increased with an increase in $NiCl_2$ precursor concentration, indicating a systematic change in the surface roughness that we tentatively attribute to increased $Ni(OH)_2$ coverage. On the contrary, the PF-TUNA analysis gave neglibly low tunneling currents on samples immersed in 0.05 M and 0.1 M $NiCl_2$ solution. This suggests that the surface is either fully covered with $Ni(OH)_x$ at $NiCl_2$ concentrations higher than 0.05 M, or that islands are sufficiently densly packed that the AFM probe tip is unable to extend sufficiently close to the exposed Pt surface to observe tunneling current.

High-resolution conductive AFM imaging was also performed on template stripped Pt films immersed in 0.1 and 0.01 M $NiCl_2$ solutions in an effort to more clearly distinguish between Pt and Ni regions. Figure 4.18 depicts the height and TUNA current measurements on these films. The high-resolution AFM height image shows regions with different heights that correlates with the TUNA current images showing different currents in those regions. However, the boundary of

(a) 0.1 M $NiCl_2$

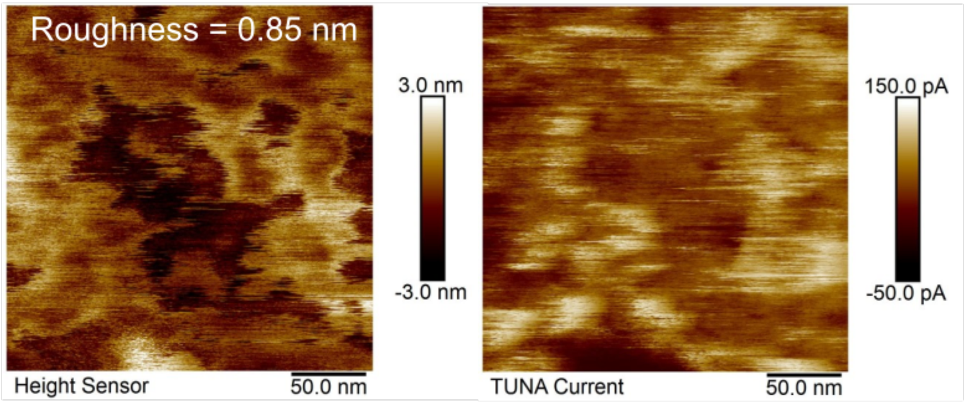

(b) 0.01 M $NiCl_2$

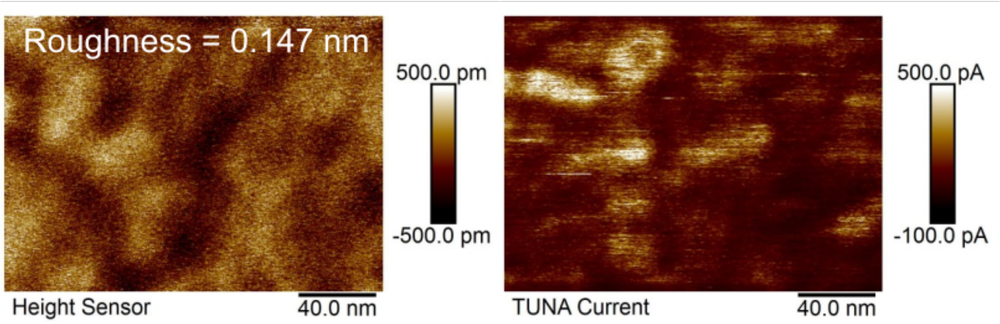

Figure 4.18: High resolution PF-TUNA AFM imaging to differentiate between $Ni(OH)_x$ and Pt regions

those patterns is not very clear, making it difficult to distinguish between Pt and $Ni(OH)_x$ regions. This analysis, therefore, indicates that conductive AFM is not a sufficient technique to differentiate between regions of Pt and $Ni(OH)_x$ on the surface.

4.4 Summary, Impact and Recommended Future work

This chapter discussed our efforts to understand the composition of Ni-based composite HER catalysts. We found that Ni–Mo catalysts comprised metal@oxides core-shell structure and also investigated the evolution of the oxide shell. Based on various literature reports and our results, we believe that the Mo-rich oxide shell is necessary for hydrogen evolution reaction and that the interface between the metallic core and the oxide is active for catalysis. To determine the influence of the metal/metal-oxide interfaces on HER catalysis, we developed a template stripping methodology to make thin films of Pt and deposited discontinuous islands of Ni(OH)$_x$. We observed an increase in the HER catalytic activity on the deposition of Ni(OH)$_x$ islands on Pt, as also shown by several others.[63, 188, 65] Moreover, efforts were made to distinguish between the Pt and Ni(OH)$_x$ regions on the surface using peak force tunneling current (PF-TUNA) AFM.

The compositional insights of Ni–Mo catalysts obtained from this work are essential to determine their mechanism for electrochemical reactions involving hydrogen. The finding that the formation of core@shell structures in these catalysts is due to an incomplete reduction of oxides is crucial. This study can be generalized to state that many catalysts synthesized as nanomaterials from oxide precursors might possess an oxide shell due to air oxidation or incomplete oxide reduction. Moreover, the template stripping methodology developed to determine the influence of metal/metal-oxide interfaces on catalytic activity may be useful as a generalizable analytical strategy. Overall, this work lays a solid foundation for yet more insights into the compositions of metal/metal-oxide structures.

Clearly more work still needs to be done to generalize the effect of metal/metal-oxide interfaces on HER catalysis. The efforts made to understand the influence of the interface on thin-film catalyst geometry using PF-TUNA AFM do not provide a complete understanding of the interface. In the future, scanning tunneling microscopy (STM) is recommended to be used to obtain atomistic insights and thus to determine the regions of different chemical compositions on the surface. Additional surface characterization techniques, including X-ray photoelectron spectroscopy (XPS) and energy-dispersive X-ray spectroscopy (EDS), can also provide insights into the composition on the surface. This compositional analysis can then be correlated to the HER/HOR activity measurements to determine the influence of metal/metal-oxide interfaces. However, the synergy of the metal/metal-oxide interface may not directly affect the catalysis. This would imply that HER/HOR catalysis on metal/metal-oxide catalysts enhances by a different mechanism. In this case, a separate series of hypotheses focused on electronic modifications that result in enhanced water dissociation or hydrogen binding energies will need to be pursued.

Another possibility is that the deposition process employed to make discontinuous oxide films on an atomically flat surface always forms a thin porous layer of oxides on the entire surface and thus a clear distinction between Pt and Ni(OH)$_x$ can never be attained. To avoid this possibility, the recommended future work is to use photolithography techniques to fabricate well-defined patterns of Pt and Ni metals. The Ni region can then be selectively oxidized by thermal or electrochemical treatment. Although some extent of interfacial mixing is still unavoidable in this case, better control over the individual regions can be attained which might also make it easier to characterize them.

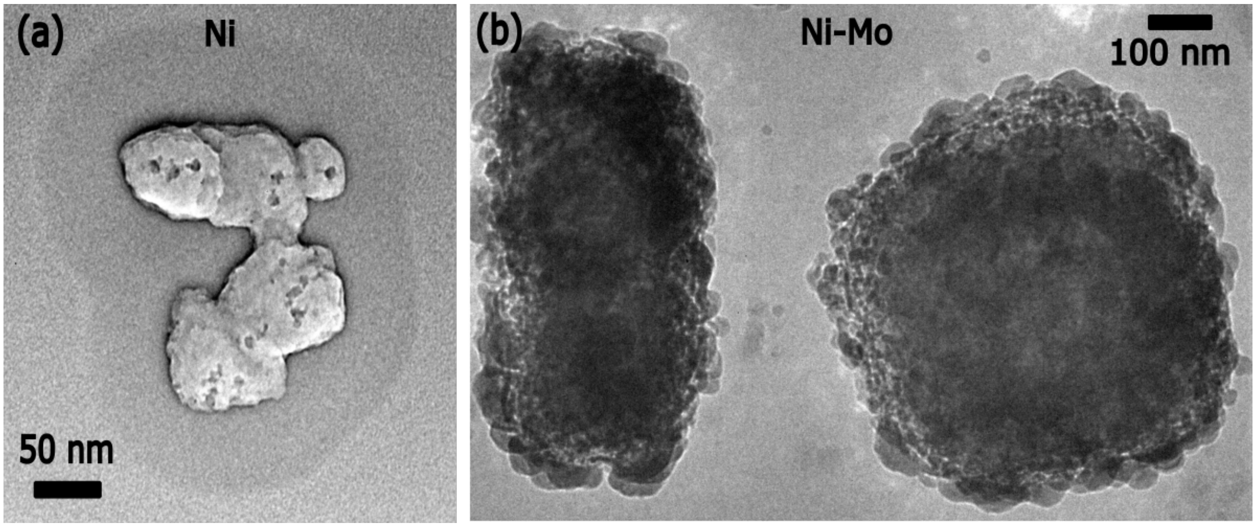

Figure 4.19: Representative TEM data from as-synthesized nonprecious catalysts using the salt-encapsulation approach

With insights obtained from the thin-film catalysts on metal/metal-oxide interfaces, the horizons of the work can be expanded towards metal or alloy nanoparticles. A way to verify the influence of the oxide is to simply synthesize a catalyst without the oxide shell and measure its HER activity before and after subsequent surface oxidation measurements. From the compositional analysis on Ni–Mo systems, it is clear that to prepare oxide-free nanoparticles, the synthesis must be done in an air-free atmosphere using a technique that can directly make the alloys without any oxide intermediate. Chen et al. reported a procedure that allows the synthesis of compositionally homogeneous metallic nanoparticles encapsulated in a KCl salt matrix.[255] This synthesis is performed in an inert gas environment to avoid the interaction of air with the powerful reducing agent. The matrix can later be removed by dissolving in a solvent. This approach of synthesizing catalysts is advantageous because it does not involve oxide intermediates or any air exposure, both of which lead to oxide shell formation in Ni–Mo catalysts. This synthesis procedure should also allow us to control the amount of oxidation on the catalyst surface through post-synthetic chemical or electrochemical oxidation treatments to directly study the impact on catalytic activity.

However this approach was shown before only for precious metal Pt and Pd-based alloys. Our preliminary results in collaboration with Dr. Thomas Allen from Prof. Raúl Hernández Sánchez's group at the Chemistry Department, University of Pittsburgh, suggests that this synthesis is also applicable to non-precious catalysts, where we have shown that 5-10 nm Ni nanoparticles encapsulated in KCl matrix and encapsulated Ni–Mo nanoparticles can be synthesized (figure 4.19). Having synthesized oxide-free Ni and Ni–Mo nanoparticles, they can be oxidized using a series of thermal and/or electrochemical treatments to oxidize their surfaces in a controlled fashion. This analysis could even be performed *in situ* in a transmission electron microscope with an electrochemical holder to continuously monitor the HER activity of the oxidized catalyst. Successful completion of these studies will provide a detailed understanding of the importance of the oxide shells around metal nanoparticles for hydrogen electrocatalysis.

5.0 Ni–Mo Composites for hydrogen Electrochemistry

The focus of this chapter is on the application of Ni–Mo catalysts for alkaline hydrogen electrochemistry by leveraging the compositional insights obtained from Chapter 4. From the compositional analysis, we speculate that the core@shell structure of Ni–Mo composites is beneficial for accelerating electrochemical hydrogen reactions. But there are a few practical challenges associated with metal@oxide Ni–Mo catalysts that suppresses their activity. This chapter presents these concerns and provides our approach to improve their hydrogen evolution/oxidation reaction activity.

5.1 Carbon incorporation

The presence of an oxide shell around a nominally metallic catalyst was interesting because it led us to hypothesize that the oxide shell may be limiting the overall catalytic activity of the composite. Specifically, we postulated that the oxide shell restricts the electronic transport to the core of the catalyst. Thus, the HER activity of such core@shell Ni–Mo alloys might in fact reflect these electronic transport limitations in excess of any kinetic limitations. A complete discussion these conductivity limitations and the efforts we undertook to solve this problem by using carbon supports was published as Patil et al., ACS Appl. Energy Mater. 2019, 2, 4, 2524–2533. The following sections are adapted from that manuscript with permission from the American Chemical Society.

To address the possibility of electrical resistivity as the predominant limiting factor in Ni–Mo nanopowder, we developed a mathematical model that describes how resistive interfaces between nanoparticles can decrease practical HER catalytic activity. This model simplifies the catalyst film into a one-dimensionsal string of nanoparticles attached on one side to a conductive substrate and extending into an electrolyte. The particles are comprised of a metallic core that is catalytically active and a shell that is catalytically inactive and electrically resistive (with a defined bulk resisitivity, ρ) while allowing facile migration of reactants to the core. Thus, upon injection of electrons from the substrate into the particle chain, they may either go on to reduce water to H_2 and OH^- or migrate from one particle to the next through a thin resistive interface. Neglecting losses associated with solution-phase mass transfer, the HER overpotential for particle n in the string can be approximated as the sum of its kinetic (via the Tafel equation) and resistive (via Ohms's law) components:

$$\eta_n = \eta_{n,kinetic} + \eta_{n,resistive} = b\log(i_n/i_0) + i(n \times R_{particle}) \tag{5.1}$$

where η is overpotential, b is Tafel slope, i_0 is exchange current density, i_n is catalytic current through particle n, and $R_{particle}$ is the interfacial resistance between each pair of particles. This equation can be solved numerically for total current by specifying the particle geometry and string length along with the relevant kinetic and resistive parameters. Additional discussion of the model parameters and software code are included as Supporting Information.

Using this model, we simulated HER polarization data (in terms of mass-specific current vs. overpotential) for a chain of 100 Ni particles, each 6 nm in diameter and surrounded by a 2 nm oxide shell (Figure 5.1a). For simplicity, the model relied on reported kinetic values for bulk Ni.[256] We then systematically varied the oxide resistivity to observe the effect on the mass activity of individual particles and the entire catalyst string. Figure 5.1b shows representative results for the particles nearest and furthest from the substrate ($n = 1$ and $n = 100$, respectively) as well as the overall performance of the catalyst chain when the oxide shell had a resistivity of 10^8 Ω-cm. Using these parameters, the activity of the first particle was not significantly diminished by resistive losses, but that of the 100th particle and the overall catalyst performance were both diminished due to the cumulative effects of many resistive interfaces that need to be traversed to access the full catalyst surface area.

Figure 5.1c compiles simulated performance of the same catalyst chain using a range of oxide resistivity values. For these physical dimensions, resistivity values exceeding 10^6 Ω-cm were necessary to observe significant losses, while values above 10^9 Ω-cm were found to completely shut down catalytic activity at overpotentials below 300 mV. Importantly, this range of resistivity values is consistent with reported values for Ni and Mo oxides[257, 258], which our microscopy results showed indeed encapsulate sub-10 nm alloy nanoparticles in our Ni–Mo nanopowders. These simulations also show that catalyst activity can be decreased due to interfacial resistance even without obviously exhibiting linear current-voltage behavior that is often characteristic of series resistance losses in an electrochemical experiment.

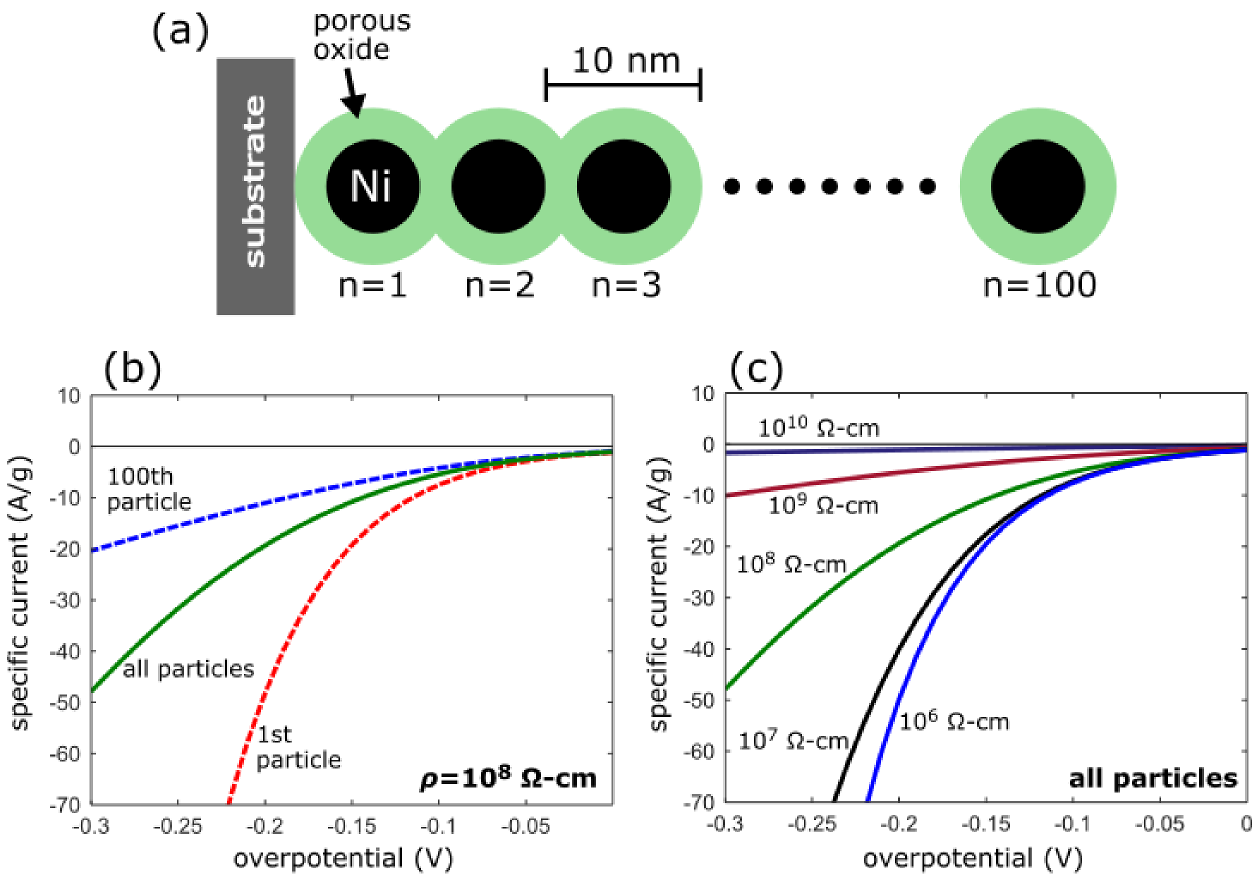

Figure 5.1: (a) Schematic of a 1-dimensional array of 100 Ni particles, each 6 nm in diameter with a 2 nm oxide coating; (b) simulated mass-specific activity of the 1st, 100th and all particles using catalyst parameters approximating that of bulk Ni and an oxide resistivity of 10^8 Ω-cm; (c) simulated mass-specific activity of 100 particles at resistivity values ranging from 10^6 to 10^{10} Ω-cm.

Solid-state electronic conductivity limitations have been identified and addressed for semiconducting catalyst materials,[259, 260, 261] and they are also well-known for non-precious oxide OER catalysts.[262, 99, 263] Nonetheless, it is not intuitive that analogous conductivity limitations would exist in Ni–Mo nanopowder since the XRD results indicate that the predominant crystalline product is a metallic alloy. However, our model results clearly show that even few nm-thin resistive interfacial layers can have a major influence on practical activity, especially for catalysts comprised of very small nanoparticles where electric current will necessarily traverse many such interfaces. In the present case, the oxides apparently result from incomplete reduction of the oxide precursors, but similar interfaces could easily result from incomplete removal of the capping agents during colloidal nanoparticle synthesis, or from aerobic oxidation of non-noble nanoparticles when they are processed in air.

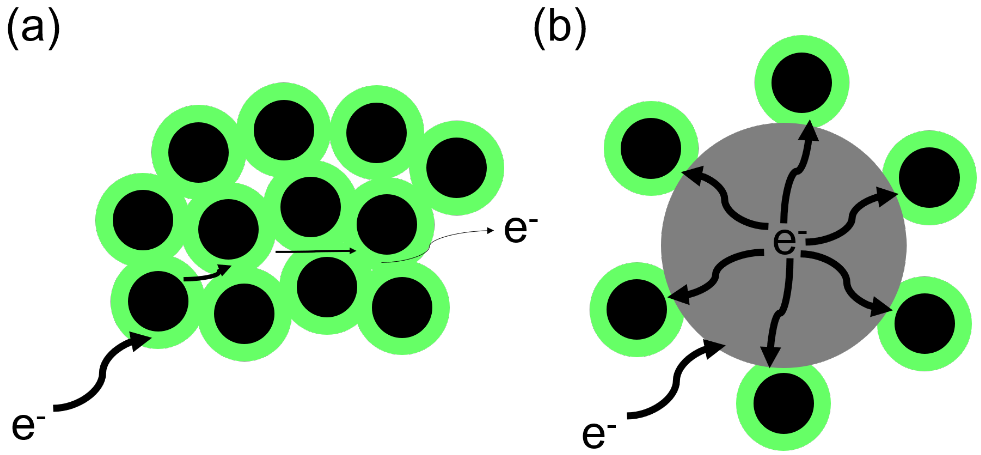

Figure 5.2: Effect of carbon to minimize the resistivity limitations in Ni-Mo alloys. (a) Unsupported Ni-Mo alloys are coated with resistive oxides which decreases the rate of electron transfer through them. (b) The use of carbon supports minimizes the need to conduct electrons through multiple resistive oxide shells.

Based on our observations that thin surface oxides inhibit electronic transport, we postulated that depositing Ni–Mo catalysts on conductive carbon supports would address these conductivity limitations. Vulcan carbon is a commonly used support in fuel cells and electrolyzers owing to its high surface area, high conductivity, and good processability. Dispersing the catalyst onto a percolating network of carbon particles will minimize the interfacial resistance imposed by the oxide shell (figure 5.2).

Carbon was incorporated into Ni–Mo composites using three different methods: (1) the "paste" method, where the Ni–Mo oxide intermediate and Vulcan carbon were physically mixed (referred to hereafter as Ni–Mo/C paste); (2) co-precipitation with Vulcan carbon, where Ni–Mo oxides were precipitated in the presence of Vulcan carbon (Ni–Mo/C); and (3) co-precipitation with oxidized-Vulcan carbon, which is the same as (2) except that the Vulcan carbon was first oxidized using a thermal treatment in air (Ni–Mo/o-C). Subsequent TEM analysis, shown in figure 5.3, clearly indicates that as the synthetic method progressed from (1)-(3), the overall dispersion of the Ni–Mo nanoparticles increased. More specifically, increased dispersion means smaller Ni–Mo agglomerates and higher uniformity of coating on the carbon supports. The next section will detail the influence of type and amount of carbon support in Ni–Mo alloys for the hydrogen evolution reaction.

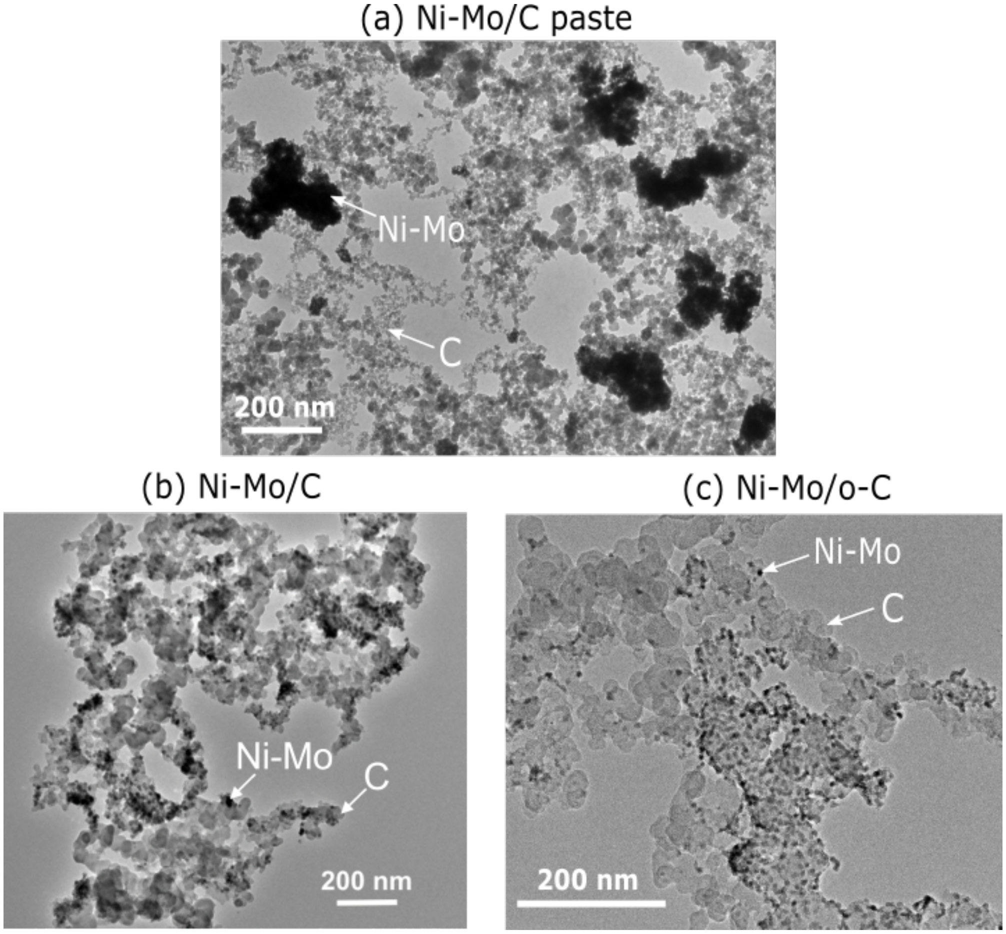

Figure 5.3: TEM images of Ni–Mo composites supported on carbon and prepared by paste method (Ni–Mo/C paste), co-precipitation with Vulcan carbon (Ni–Mo/C) and co-precipitation with oxidized Vulcan carbon (Ni–Mo/o-C)

5.2 Hydrogen evolution reaction performance

Carbon supports were first added to Ni–Mo composite via physical mixture. These composites demonstrated improved HER activity in comparison to unsupported Ni–Mo catalysts. This suggest that the HER activity in unsupported catalysts was indeed inhibited by the interfacial resisitivity. We therefore extended the study to improve the electronic conductivity further using co-precipitated Ni–Mo/C composites and indeed found higher HER activity compared to Ni–Mo/C paste composites. Finally the highest catalytic activity was obtained with Ni–Mo/o-C composites. The HER activity and the relevant analysis on Ni–Mo/C paste and Ni–Mo/C catalysts was published and adapted here with permission from Patil et al., ACS Appl. Energy Mater. 2019, 2, 4, 2524–2533. Copyright 2019 American Chemical Society.

5.2.1 Ni–Mo/C paste composites

Figure 5.4 compares the geometric and mass-specific current vs. overpotential performance of several representative Ni–Mo films, along with pure Ni and Pt/C controls, toward hydrogen evolution in 0.1 M aqueous KOH electrolyte. Carbon-supported Pt exhibited similar geometric activity to pure Ni–Mo in spite of the fact that the metal loading was 50-fold lower. The mass-specific current of the Pt/C catalyst was therefore much greater than Ni–Mo, which agrees with prior reports showing Pt is considerably more active than any known non-precious HER catalyst even though it is less active in base than it is in acid.[264] Pure Ni gave the lowest activity by a considerable margin. We attribute this to its relatively low intrinsic activity along with the fact that our Ni synthesis resulted in much larger particle sizes than for Ni–Mo or Pt.

The as-synthesized Ni–Mo nanopowder films (Ni–Mo not annealed) gave rather low catalytic activity. By contrast, the Ni–Mo films that were hydrogen annealed were comparable to values that have been reported previously—nearly 10 mA/cm^2 at 100 mV overpotential when using a catalyst loading of 1 mg/cm^2.[60] This suggest that the hydrogen annealing is activating the catalyst towards HER, which we believe is due to fusing of the oxide shells such that interfacial resistance decreases. Remarkably, Ni–Mo/C paste films yielded similar geometric activities to annealed Ni–Mo films even though they contained only 25% of the Ni–Mo mass. The implied mass-specific activity was also several times larger for Ni–Mo/C paste. We are primarily interested in improving the mass normalized activity of the catalyst as it closely associates with its intrinsic activity. The area-normalized activity is relevant for practical implementation but is independent of the mass of the catalyst.

To further assess the effect of carbon incorporation, we systematically varied the metal loading over the range from 10 to 100 wt%. Results are shown in Figure 5.5 as geometric polarization data and activity at 100 mV overpotential. The observed geometric activity first increased with metal incorporation up to a maximum at 50 wt% metal, and then decreased at 10 and 25 wt%. Upon normalization to Ni–Mo mass, the 25 wt% carbon sample exhibited the highest apparent activity—25±6 mA/mg at 100 mV overpotential.

We observed substantial variability in catalyst activity in these experiments, as exemplified by the large error bars (up to 50% of the mean current densities) in Figure 5.5b. We attribute this variability to the relatively poor dispersion of Ni–Mo on the Vulcan carbon support material as well as the use of un-optimized catalyst ink formulations for film deposition on glassy carbon rotating-disk electrodes. Both of these have been shown to result in increased sample-to-sample variability in oxygen reduction electrocatalysis.[265, 266, 267] Thus, within the limits of experimental error, the geometric activities of Ni–Mo/C paste films with 25–100 wt% metal loading were essentially indistinguishable. However, after accounting for the differences in catalyst mass in these samples, it is clear that the mass-specific activity increased with carbon loading.

As a compliment to polarization measurements, we performed electrochemical impedance spectroscopy (EIS) on Ni–Mo/C paste films as a function of carbon loading. Figure 5.6 shows representative Nyquist plots and the associated charge-transfer resistance values from EIS measurements collected at 150 mV overpotential over a frequency range from 0.2 Hz to 100 kHz. The impedance data generally exhibited semicircular behavior that was well-described by the parallel combination of a charge-transfer resistance and a constant-phase element.[268] However, as carbon loading was increased, the same frequency range sampled a progressively smaller proportion of the semicircle, which is consistent with the increasing effect of double-layer capacitance from the carbon support. The charge-transfer resistance results broadly agree with the observed geometric activity from polarization data, where the 10 and 100 wt% metal films exhibited larger resistance than the films containing 25–90 wt% carbon.

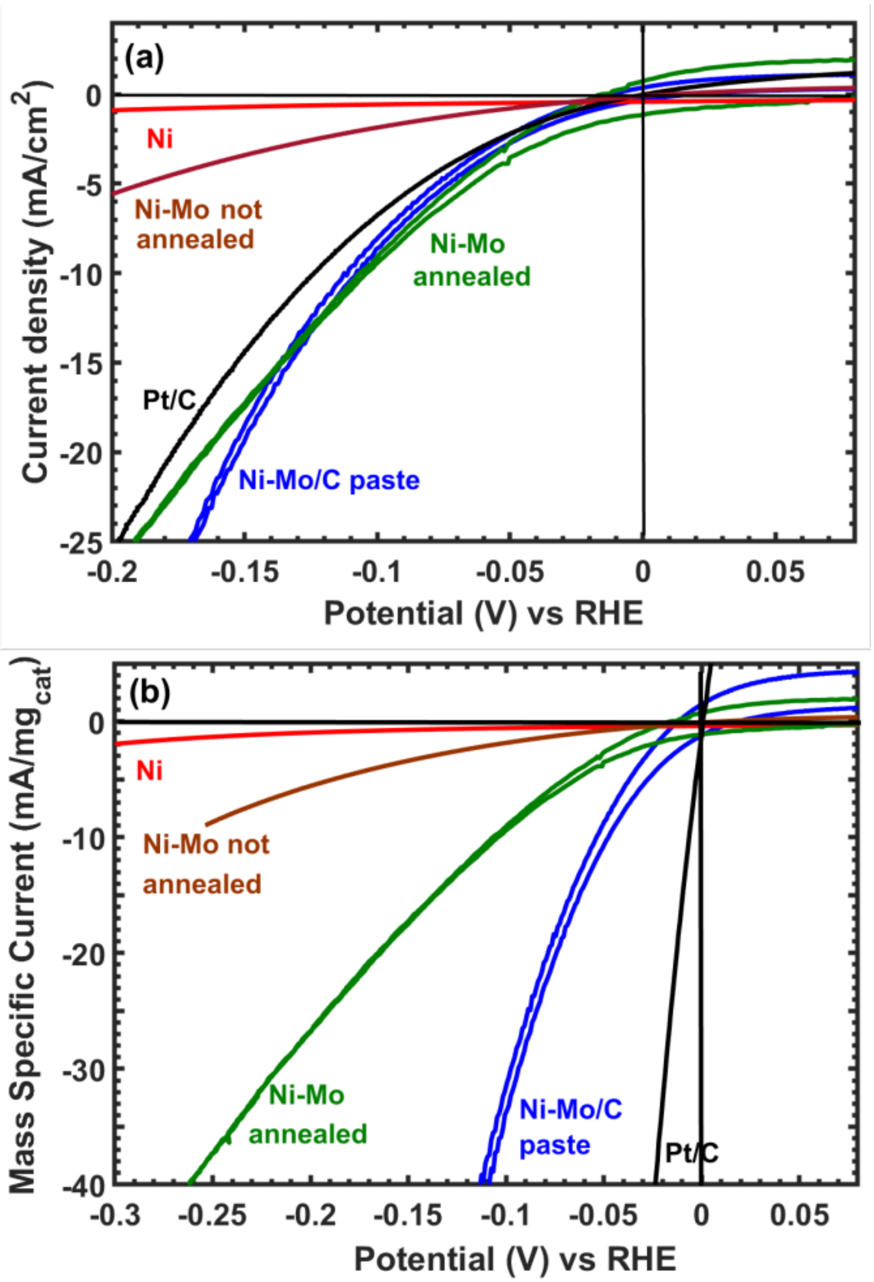

Figure 5.4: Polarization data normalized to (a) geometric area and (b) catalyst mass (total mass less the carbon component) for various Ni–Mo films along with Ni and Pt/C (10 wt% Pt) controls. All curves were collected in 0.1 M KOH solution using a scan rate of 10 mV/s and corrected for solution resistance. Total mass loadings were 1 mg/cm^2 in all cases except for Pt/C, which was 0.2 mg/cm^2. For the Ni–Mo/C paste data, the metal loading was 25 wt% relative to total catalyst mass.

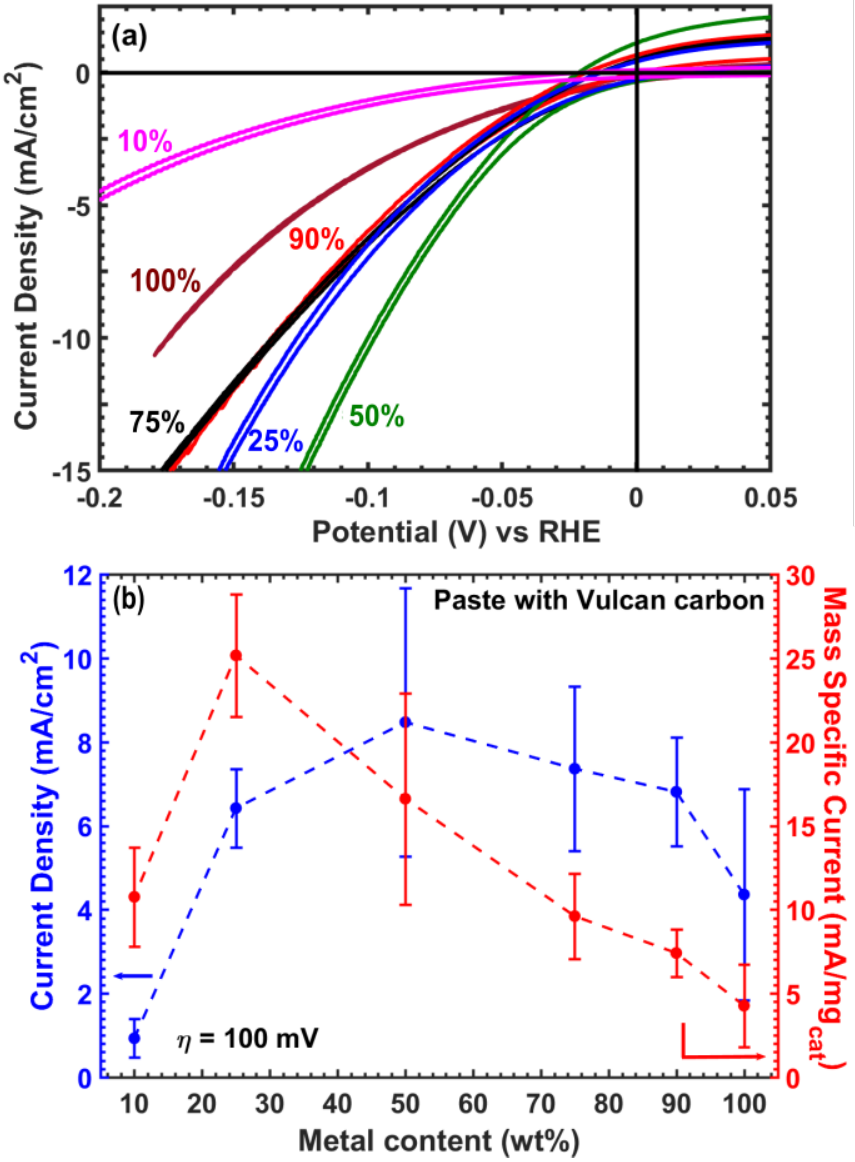

Figure 5.5: HER activity of Ni–Mo/C paste films as a function of metal loading: (a) polarization data normalized to geometric surface area, collected under the same conditions as in Figure 5.4; (b) geometric current density (left axis) and Ni–Mo mass-specific current (right axis) at 100 mV overpotential as a function of carbon content. Error bars in (b) represent standard error with 95% confidence interval of 9 samples each, comprising 3 replicates from 3 separate syntheses.

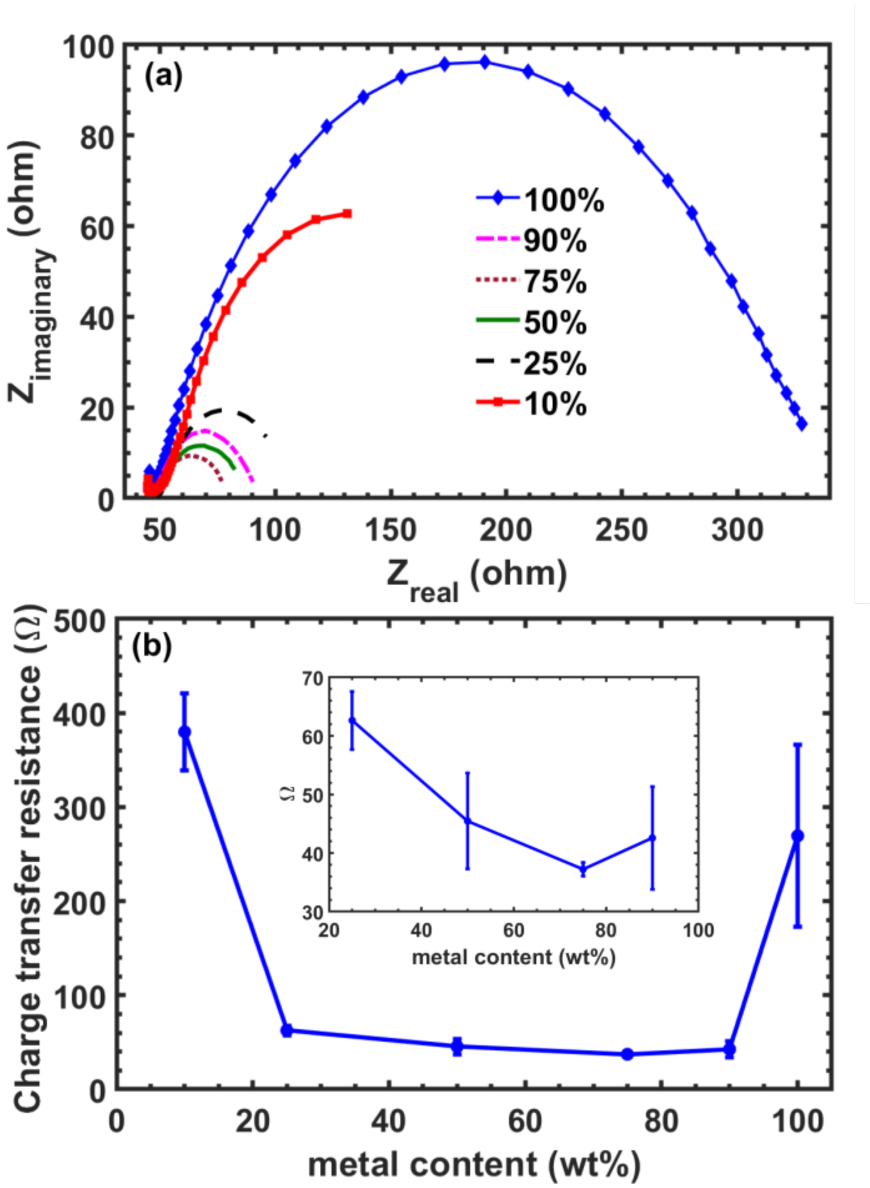

Figure 5.6: (a) Nyquist plot depicting EIS data for Ni–Mo/C paste nanopowders containing different metal loadings. (b) Charge transfer resistance extracted from fits of the semicircular components of the impedance data. The error bars in (b) represent standard error with 95% confidence interval of 3 samples. Data were collected in H_2-saturated 0.1 M KOH electrolyte at 150 mV overpotential over the frequency range from 0.2 Hz to 100 KHz.

The electrochemistry data suggest that the HER activity of unsupported Ni–Mo nanopowders is not limited by electrochemical kinetics. The clearest evidence for this conclusion are the data in Fig 5.5a, which show that replacing up to 50 wt% of the Ni–Mo catalyst with carbon black (while keeping total mass loading constant) increased the observed geometric HER activity. This is not plausible in a kinetically limited regime, where decreasing catalyst loading on the electrode should always lead to lower geometric activity. Moreover, the catalyst mass activity was found to increase with carbon loading as high as 75 wt%. We postulate that the catalyst is in fact limited by solid-state transport of electrons through the Mo-rich oxide shells that coat the Ni–Mo alloy nanoparticles. The carbon support thus provides percolative pathways for electron conduction, thereby decreasing the total electrical resistance attributable to these thin oxide layers.

Another possible explanation for these observations—one that does not invoke transport limitations—is that the carbon support itself contributes significantly to the observed HER activity. However, we found that Vulcan carbon alone exhibits negligible activity toward alkaline hydrogen evolution at overpotentials below 300 mV (see Supporting Information). If the co-deposition of Ni–Mo with carbon black instead served to increase the intrinsic activity of Ni–Mo toward the HER, then we would expect to observe a monotonic increase in mass activity with carbon loading. Thus, the observed decrease at 90 wt% carbon is not consistent with activation of Ni–Mo by Vulcan carbon. Instead we attribute this decrease to saturation of the solid-state conductivity enhancement accompanied by the onset of diffusion limitations or physical blocking of the Ni–Mo particles by excessive carbon.

We undertook further experiments to assess the practical performance of Ni–Mo/C paste containing 25 wt% metal. Figure 5.7 compares the observed geometric HER activity at 100 mV overpotential as a function of total catalyst loading. For mass loadings ≤ 1 mg/cm^2, we used glassy carbon substrates, whereas the substrate was changed to Ni mesh for higher loadings due to poor adhesion of thick Ni–Mo/C paste films on glassy carbon. Considerable spread was again observed in the data, particularly for samples with high mass loadings, which we attribute to inhomogeneous coating thicknesses and variable loss of catalyst from thick films during handling. Nonetheless, these data are reasonably well described by a power law relationship, $J = 11m^{0.73}$, where J is geometric current density and m is total mass loading. If the catalyst were limited only by reaction kinetics at all mass loadings, this relationship would be purely linear. Deviations from linearity are expected due to emergent transport limitations, which result in “diminishing returns” in mass activity as the catalyst layer thickness and current density increase. However, in this case the deviations from linearity become significant even at catalyst loadings well below 1 mg/cm^2 and current densities below 10 mA/cm^2. These values are lower than the expected onset of solution-phase transport limitations, providing evidence that these Ni–Mo/C paste films still exhibit electrical resisitive losses despite the incorporation of carbon black. The dotted line in Figure 5.7 corresponds to a linear fit between the origin and the mean of the observed Ni–Mo/C paste current density at the lowest mass loading we tested, which was 50 μg/cm^2. The slope of this line is 19 mA/mg (i.e., 76 mA/mg on the basis of Ni–Mo alone), which we took as an estimate of the achievable mass-activity of the catalyst even at higher mass loadings if resistive limitations could be entirely eliminated.

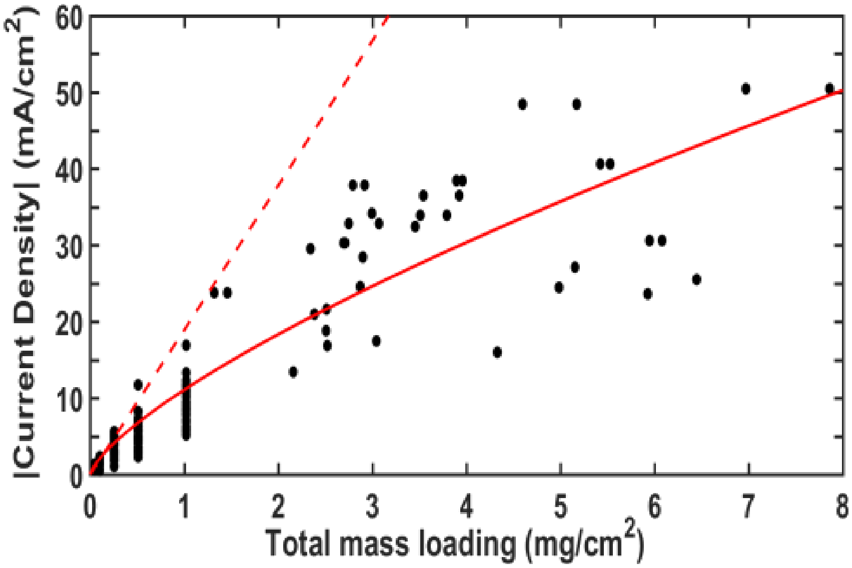

Figure 5.7: Geometric HER activity of ammonia-based Ni–Mo/C paste containing 25 wt% metal at 100 mV overpotential as a function of total mass loading of the composite. The solid red line corresponds to the best-fit equation: $J = 11.07m^{0.73}$, and the dotted line is a linear extrapolation between the origin and the mean of the activity data collected at 0.05 mg/cm^2. Glassy carbon substrates were used for loadings ≤ 1 mg/cm^2 and Ni mesh substrates were used for higher loadings.

5.2.2 Ni–Mo/C composites

Motivated by the results of Ni–Mo/C paste composites, we worked to increase the dispersion of Ni–Mo on the carbon support to further improve inter-particle conductivity. Results are shown in Figure 5.8, which depicts polarization data and mass-activity for Ni–Mo/C films at 1 mg/cm^2 total mass loading in which Vulcan carbon was included in the precipitation mixture rather than composited with Ni–Mo oxide by physical grinding. The geometric activity data in Figure 5.8b also show a non-monotonic trend in which 35 wt% metal loading gave somewhat higher average current densities than 53 wt% carbon. However, the difference is considerably smaller than the associated standard deviations, which leads us to conclude that the geometric activities are in fact essentially the same at these two carbon loadings within our ability to measure them reproducibly.

Remarkably, as the metal loading increased from 20 to 91 wt%, the geometric activity at 100 mV overpotential decreased only by a factor of $\sim$2. The mass activities normalized to Ni–Mo content were as high as 60 mA/mg$_{cat}$, which is $\sim$6 times higher than prior results involving post-deposition annealing and over twice that observed for Ni–Mo/C prepared by physical grinding. We expect that these observations still represent a lower bound estimate of the true HER mass activity of Ni–Mo nanopowders prepared in this way.

Prior work on Ni–Mo nanopowders has shown that they are stable under constant cathodic polarization in alkaline electrolytes for at least several hundred hours.[60] However, it is less clear how well these catalysts can withstand polarization at positive potentials. Thus, we assessed the stability of the highest performing Ni–Mo/C composites (co-precipitated with 80 wt% carbon) via accelerated degradation tests that comprised extended voltammetric cycling over a range of positive potential limits from 0.2 to 1.2 V vs. RHE. The results are shown in Figure C.8. Unsurprisingly, the catalytic activity was found to decrease with increasing positive potential limit. Cycling to 0.2 V vs. RHE resulted in a minimal decrease in activity over 200 cycles and a $\sim$40% decrease after 1000 cycles. Interestingly, we observed a similar $\sim$90% decrease in activity for positive scan limits from 0.8–1.2 V vs. RHE. Based on prior results and the established Pourbaix diagrams for the respective components, we speculate that these large positive potentials substantially oxidize the Ni and Mo components, resulting in dissolution of Mo oxides and deactivation of the Ni component via formation of Ni^{3+} oxyhydroxides.[269, 63]

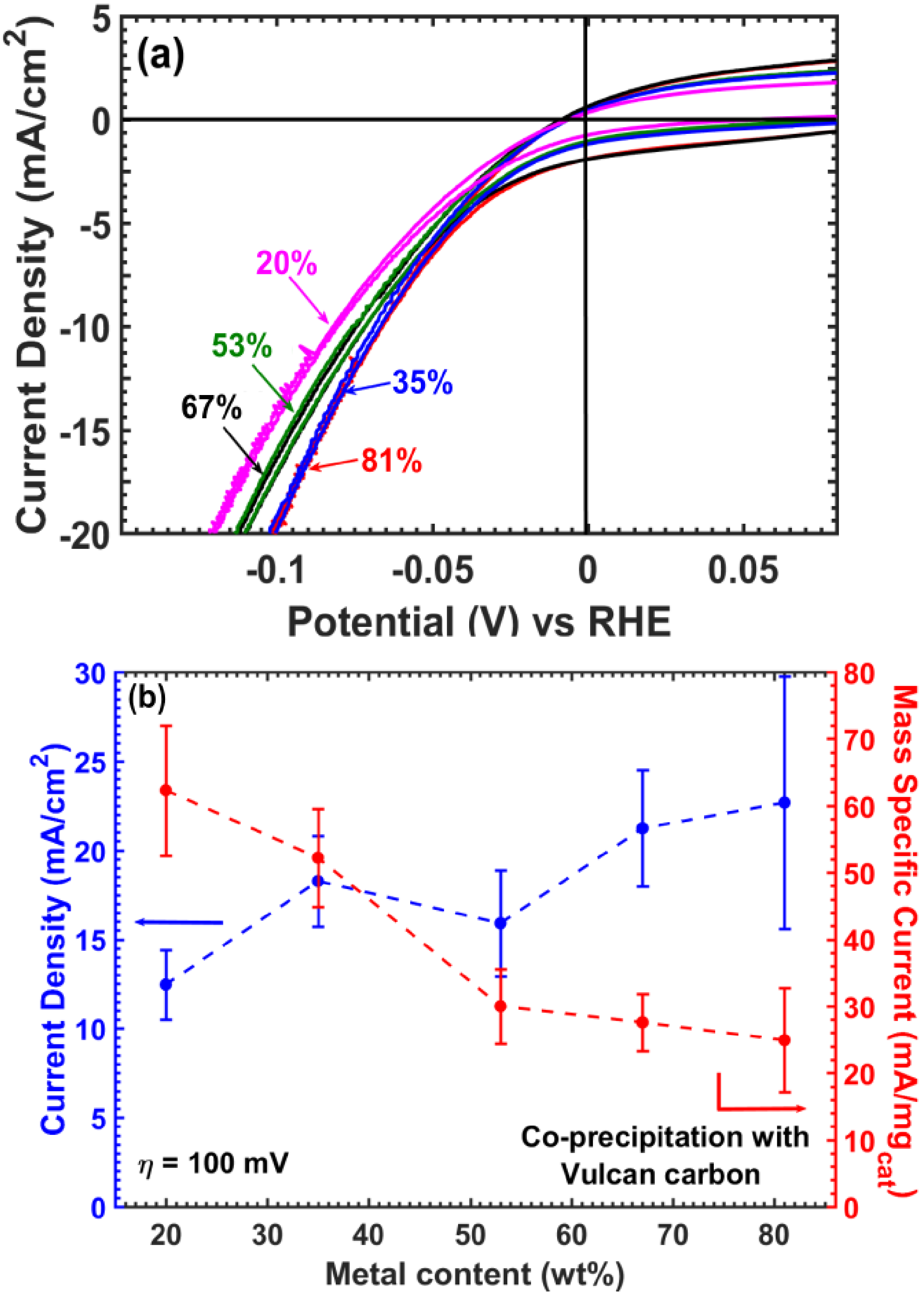

Figure 5.8: HER activity of Ni–Mo/C films prepared by co-precipitation with Vulcan carbon as a function of metal loading: (a) polarization data normalized to geometric surface area, collected under the same conditions as in Figure 5.4; (b) geometric current density (left axis) and mass-specific current (right axis) at 100 mV overpotential as a function of catalyst mass. Error bars in (b) represent standard error with 95% confidence interval of 3–7 samples.

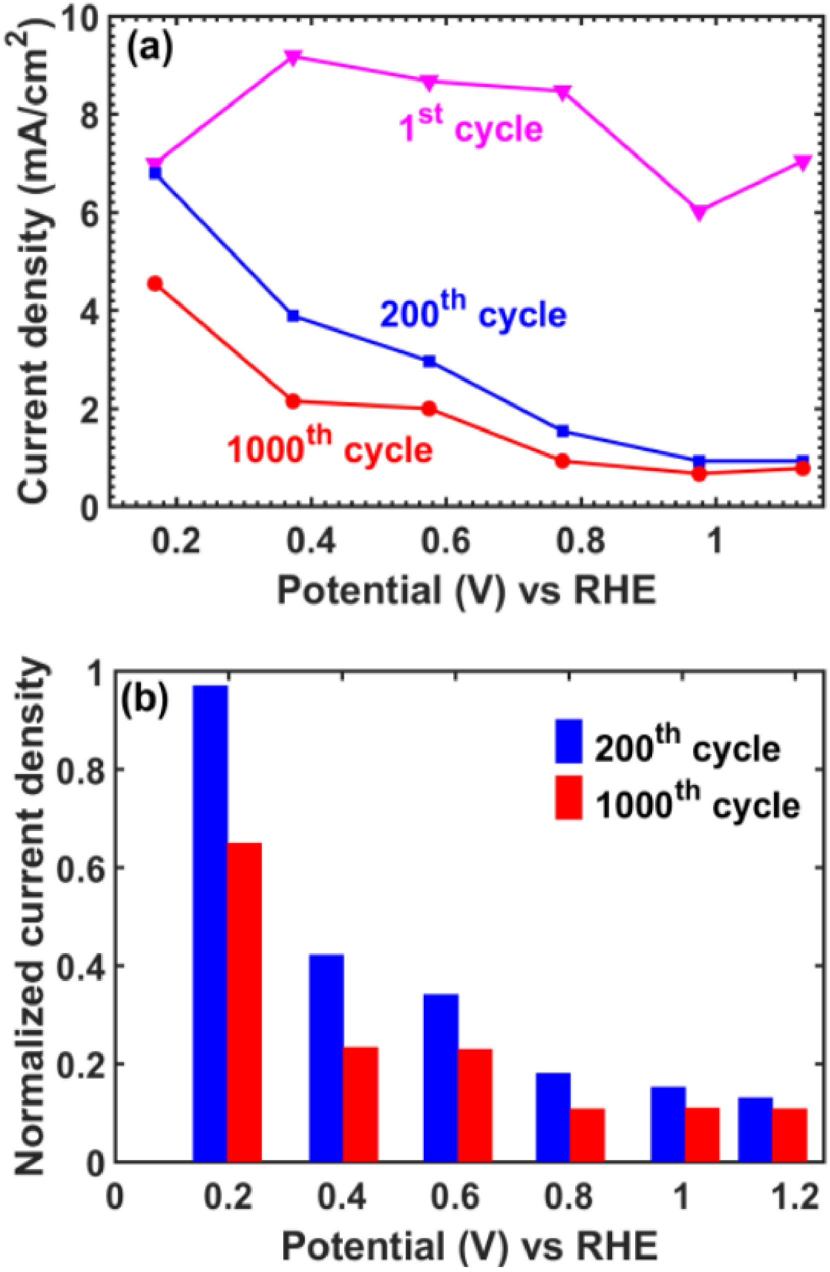

Figure 5.9: Results of accelerated degradation test of 20 wt% Ni-Mo/C composite by extended CV cycling at various positive potential limits: (a) geometric current density at 100 mV overpotential for cycles 1, 200, and 1000; (b) bar chart showing the geometric current density of cycles 200 and 1000 normalized to the initial performance. Experiments were carried out in 0.1 M KOH using a 50 mV/s scan rate.

Further, we looked at the influence of the amount of polymer binder on the mass-specific HER activity of 20 wt% Ni–Mo/C catalyst. For all the studies in this dissertation, we used Nafion cation exchange polymer as binder. Nafion is very often used for electrochemical analysis in both acidic and alkaline conditions, owing to its high stability and ionic conductivity. Figure 5.10 shows the variation of HER activity at 100 mV overpotential of Ni–Mo/C composite with different amounts of Nafion. The maximum HER activity was attained with 15–25 wt% Nafion relative to the total Ni–Mo/C mass. The decrease in activity at low Nafion content can be attributed to poor adhesion of the catalyst on the electrode surface, while decreases in activity at high Nafion loading is likely due to physical blocking of catalyst active sites.

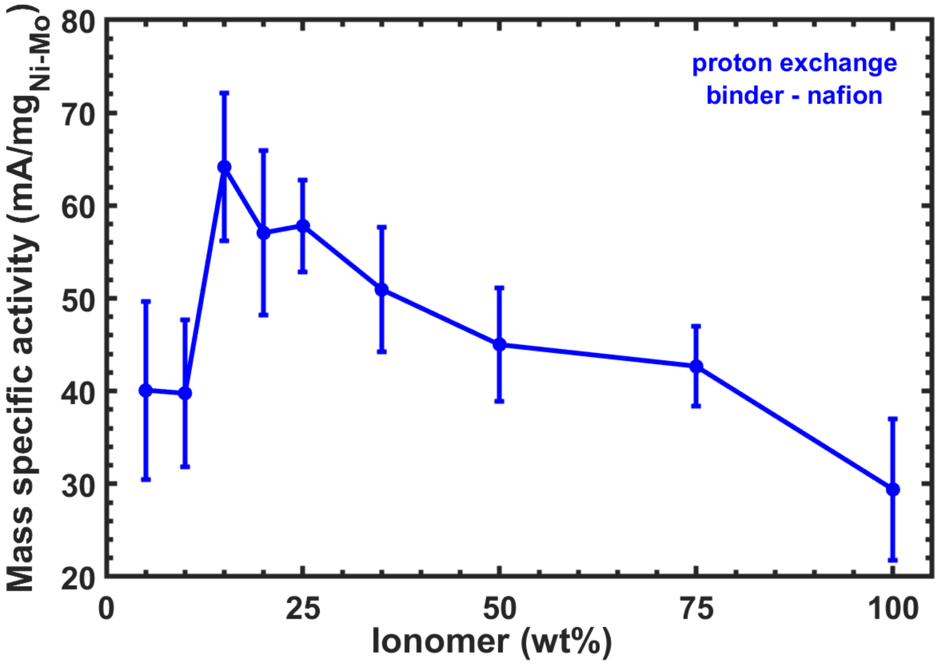

Figure 5.10: Influence of binder content relative to total Ni–Mo/C catalyst mass, on the HER activity at 100 mV overpotential in 0.1 M KOH at 1600 rpm under H_2 gas purge. The error bar represents standard error with 95% confidence interval.

5.2.3 Ni–Mo/o-C composites

Our rationale to incorporate oxidized Vulcan carbon as the support is from several prior reports suggesting that oxidized form of Vulcan carbon results in greater adherence of the transition metal catalysts on the support, and an increase in the hydrophilicity of the catalyst.[270, 271, 272, 273, 274] Building on our prior work, we varied the metal loading of Ni–Mo composites supported on oxidized Vulcan carbon. Figure 5.11 shows that the highest mass specific activity of Ni–Mo/o-C composites was achieved at 25 wt% Ni–Mo. Figure 5.12 shows SEM images, XRD data, and XP spectra of Ni–Mo/o-C catalyst in its intermediate oxide form and of the final reduced catalyst. SEM imaging with a backscatter detector was also used to characterize catalyst dispersion. The bright white spots correspond to Ni–Mo composite while the grey regions belong to carbon support. EDS analysis gave a 70:30 ratio of Ni:Mo in the final reduced catalyst. XRD data shows that the intermediate oxide form of Ni–Mo/o-C catalyst is amorphous and is a mixture of Ni and Mo oxides along with a prominent peak at 2Θ of 25 ^{o} corresponding to oxidized Vulcan carbon. The final reduced Ni–Mo/o-C catalyst displays peaks corresponding to fcc Ni along with oxides of Ni and Mo and oxidized Vulcan carbon. The Mo content in the Ni–Mo alloy was calculated from the shift in fcc Ni peaks and found to be 10.12 ± 1.31 mol%.[219] The crystallite size, calculated from the Scherrer analysis, was 3.6 ± 0.2 nm.

Figure 5.13 shows representative bright and dark field TEM images and EDS mapping of Ni–Mo/o-C catalyst. The dispersion of Ni–Mo on oxidized Vulcan carbon can be seen from the bright field image. The black particles, with an average diameter of 7.7 ± 0.5 nm, correspond to Ni–Mo catalyst while the grey particles of the order of 50 nm are of Vulcan carbon support. From the EDS maps, each Ni-rich particle is surrounded by Mo and O, suggesting the core-shell nature of Ni–Mo/o-C. The characterization data together suggest that Ni–Mo/o-C catalyst again comprises an alloy core surrounded by a mixed oxide shell, which further suggests that pre-oxidiation of the carbon has little to no effect on the composition of the active catalyst.

The performance of Ni–Mo/o-C composite for the hydrogen evolution reaction in alkaline media is shown in figure 5.14. The mass-specific activity of Ni–Mo/o-C normalized to Ni–Mo mass at 100 mV overpotential collected over 50 different films was found to be 82.4 ± 5.8 mA/mg$_{cat}$ where the error represents standard error with 95% confidence interval. This activity is $\sim$8 times higher than the unsupported Ni–Mo catalyst and $\sim$80 times higher than Ni nanoparticles under mutually similar experimental conditions in alkaline media. Compared to commercial 10 wt% Pt/C with 0.2 mg$_{total}$/cm^2 of catalyst loading, the activity of Ni–Mo/o-C is still 4 times lower. However, Ni–Mo/o-C catalysts are 3–4 orders of magnitude cheaper than Pt/C.[275] Hence, three orders of

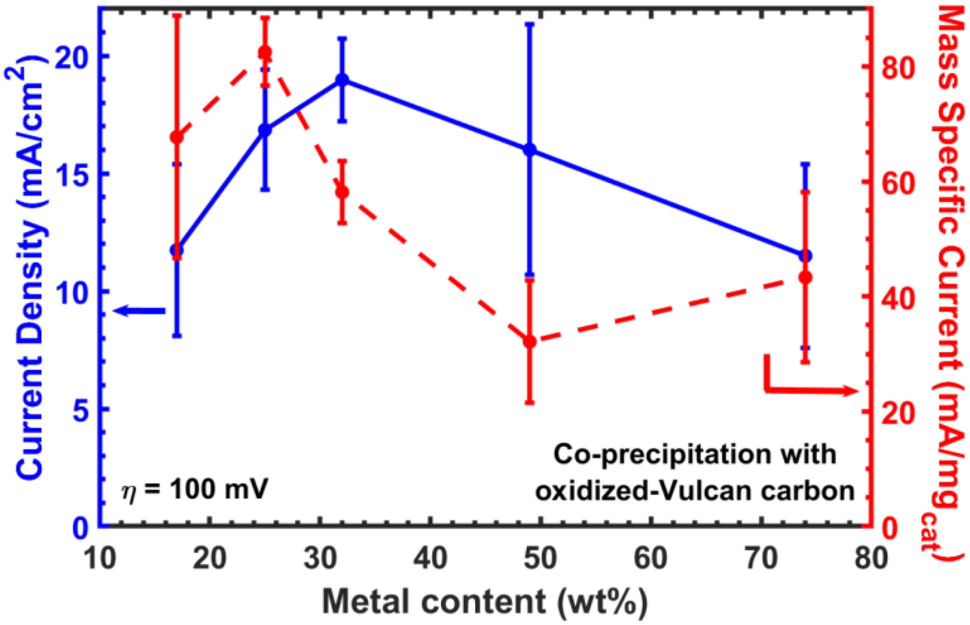

Figure 5.11: HER activity of Ni–Mo/o-C catalysts in terms of geometric current density (left axis) and mass-specific current (right axis) at 100 mV overpotential as a function of metal loading in 0.1 M KOH. Error bars represent standard error with 95% confidence interval for ∼15 different films.

magnitude decrease in cost but only one order of magnitude decrease in HER activity makes these catalysts promising for hydrogen evolution reaction.

We further varied the mass loading of the catalyst on the electrode surface and plotted it against the observed current density at 100 mV overpotential to better estimate the intrinsic activity of these catalysts (figure 5.15), under the assumption that mass transfer at least partially inhibits catalytic activity at catalyst loadings > 0.1 mg/cm^2. A line was fit to the data collected at low total catalyst mass loadings ($<$ 0.15 mg$_{total}$/cm^2) to extract the intrinsic activity from its slope. The predicted intrinsic activity based on this analysis at 100 mV overpotential is ∼90 mA/mg$_{cat}$. This value is in the same range as the observed activity at 1 mg$_{total}$/cm^2, suggesting that the performance of this catalyst in fact diminishes very little with increased loading. A handful of prior reports have also reported mass-specific activity in this range for Ni–Mo composites.[208, 196, 187] Nonetheless, our catalyst has the advantage of using carbon supports, which enables them to be processed in exactly

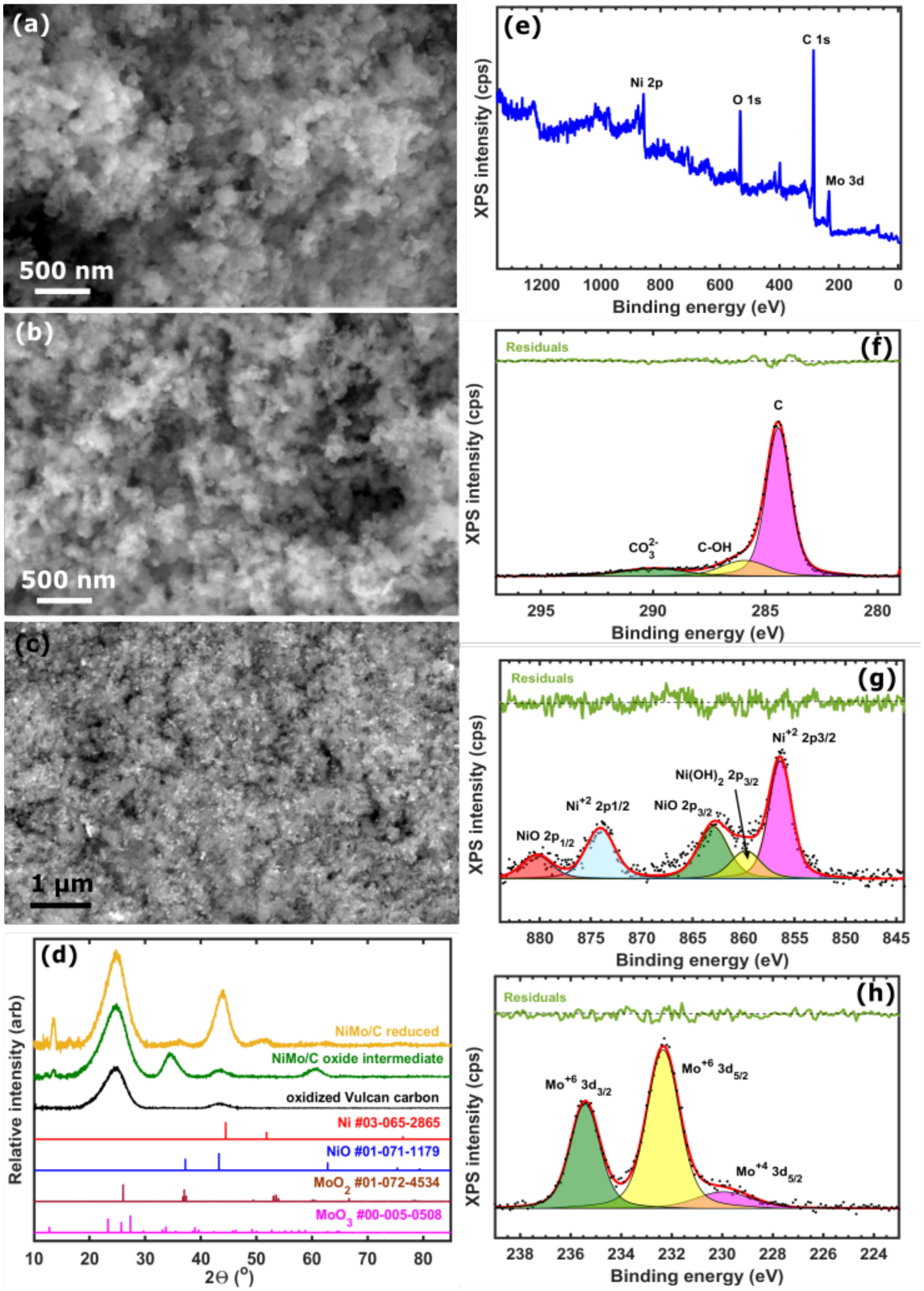

Figure 5.12: SEM image of Ni–Mo/o-C in (a) intermediate oxide and (b) reduced form collected with secondary electron detector. (c) Backscatter SEM image of reduced Ni–Mo/o-C catalyst representing bright white spots for Ni–Mo composite and grey region for carbon support. (d) XRD analysis of Ni-Mo/o-C in its intermediate oxide and the reduced form in comparison with oxidized Vulcan carbon and standard patterns obtained from ICDD database.

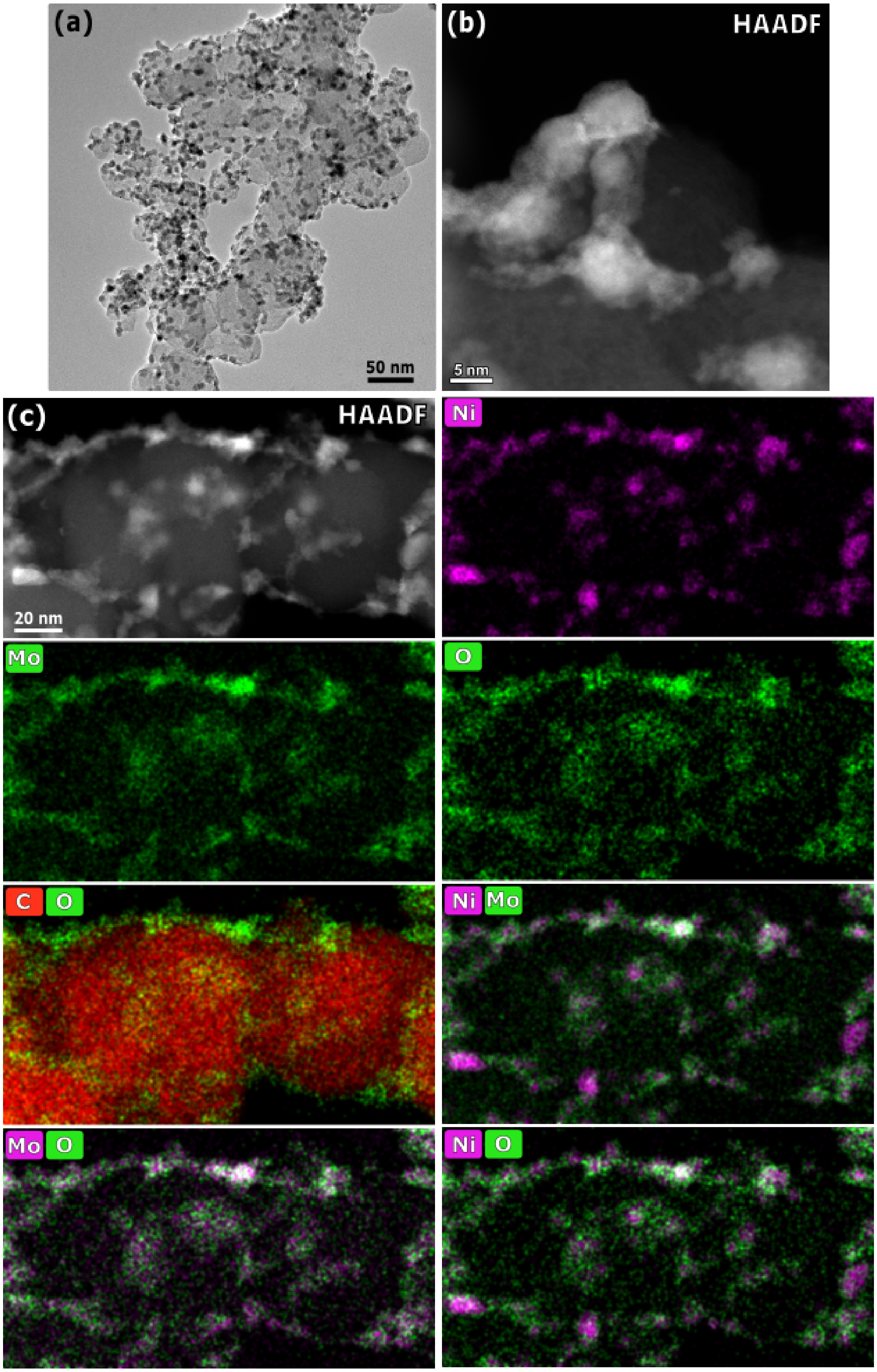

Figure 5.13: TEM analysis of Ni-Mo/o-C with bright and dark field images and EDS mapping

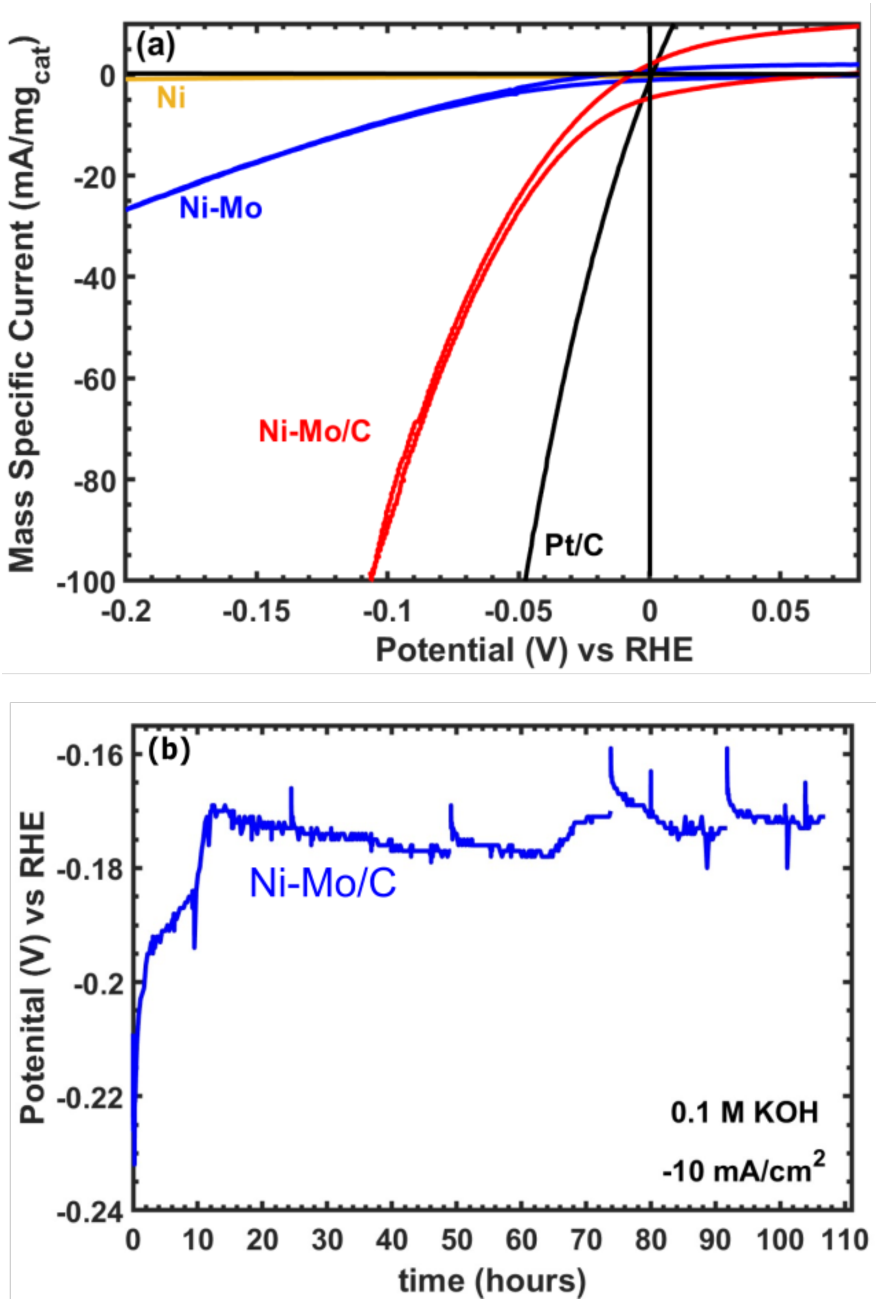

Figure 5.14: (a) Hydrogen evolution reaction activity of 25 wt% Ni–Mo/o-C in comparison with unsupported Ni-Mo, Ni nanoparticles and Pt/C. The total catalyst loading of Ni-based catalysts is 1 mg/cm^2 and that of Pt/C is 0.2 mg/cm^2. (b) Chronopotentiometry data of 1.5 mg$_{total}$/cm^2 Ni–Mo/o-C at 10 mA/cm^2 HER current density. The catalyst was deposited on a 5 mm glassy carbon substrate that was made rough by polishing on 240 grit SiC grinding paper (with pressure sensitive backing, Pace Technology)

the same way as industry standard Pt/C catalysts. The synthesis of Ni–Mo/o-C catalyst can also be easily scaled up for large-scale production. Ni–Mo catalysts are currently synthesized for industrial hydrodesulfurization application using a similar precipitation-reduction approach.[203] Carbon is also routinely employed at industrial scale as a support for battery materials.[276] Moreover, we observed that the incorporation of carbon in Ni–Mo composites suppressed their pyrophoric tendency, thus facilitating safer operations.

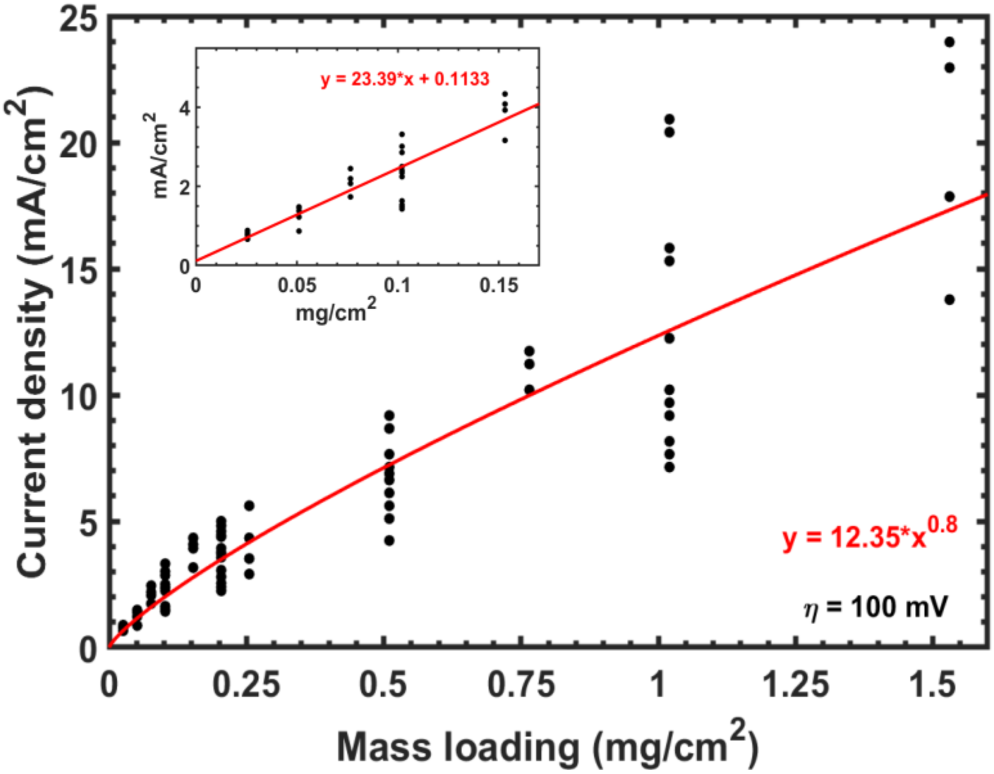

Figure 5.15: Current density as a function of total mass loading of 25 wt% Ni–Mo/C catalyst at -100 mV vs. RHE. A power law model fitted to the data had equation of $J_{-100mV} = 12.35 * m^{0.8}$. Inset shows the linear fit to the data at mass loadings < 0.2 mg$_{total}$/cm^2.

We further analyzed the stability of Ni–Mo/o-C catalyst by performing a chronopotentiometry experiment by holding a constant current density of -10 mA/cm^2 for about 100 hrs as shown in figure 5.14b. The potential required to maintain this current density fluctuated over a range of 20 mV (which may be attributable to local site blocking and convection due to bubble formation), but the overall trend was toward *smaller* overpotentials during this time span, implying increased catalytic activity. This modest improvement over time has been observed previously and attributed to dissolution of undesired Mo-oxides.[51, 225] In any case, stable performance of Ni–Mo/o-C composites over several days is promising for practical applications.

5.2.4 Performance in AAEM electrolyzer

The promising activity and stability of Ni–Mo/o-C composites motivated us to evaluate its activity in practical alkaline anion exchange membrane (AAEM) electrolyzers. In that regard, we have established an industry collaboration with Giner Inc., New York, led by Dr. Judith Lattimer. Figure 5.16 shows the performance of Ni–Mo/o-C catalyst in comparison with PtRu/C in a membrane electrode assembly (MEA) with an alkaline anion exchange membrane (AAEM). The AAEMs were provided by Dr. Keda Hu and Prof. Yushan Yan from Versogen, Delaware, and device tests were completed by Dr. Shirley Zhong. The total voltage required to electrolyze water was $\sim$70 mV higher with a Ni–Mo/o-C cathode catalyst in comparison to a Pt–Ru/C cathode, and this difference persisted over the entire range of current densities measured. This remarkable small difference agrees well with our laboratory experiments suggesting that our Ni–Mo/o-C catalyst is less than 10-fold lower in intrinsic HER activity than the best precious metal catalysts available. By contrast, under a feed of pure water, the potential difference between Pt–Ru/C and Ni–Mo/o-C was markedly larger. This difference is tentatively attributable to mass transfer limitations associated with hydroxide ion conduction through the device, which are likely to be exacerbated by the use of Ni–Mo/o-C at higher mass loading than Pt–Ru/C. Nonetheless, the potential achieved by Ni–Mo/o-C at 1 A/cm^2 under pure water feed, is $\sim$2.1 V, which is comparable to the highest performing AAEM electrolyzer devices observed to date.[35, 277]

5.3 Hydrogen oxidation reaction performance

Considering the promising results with respect to HER performance, we continued to explore applications of Ni–Mo/o-C composites as catalysts for the hydrogen oxidation reaction (HOR). Prior work on Ni–Mo catalysts supported on Ketjen Black have shown promising HOR activity.[82]

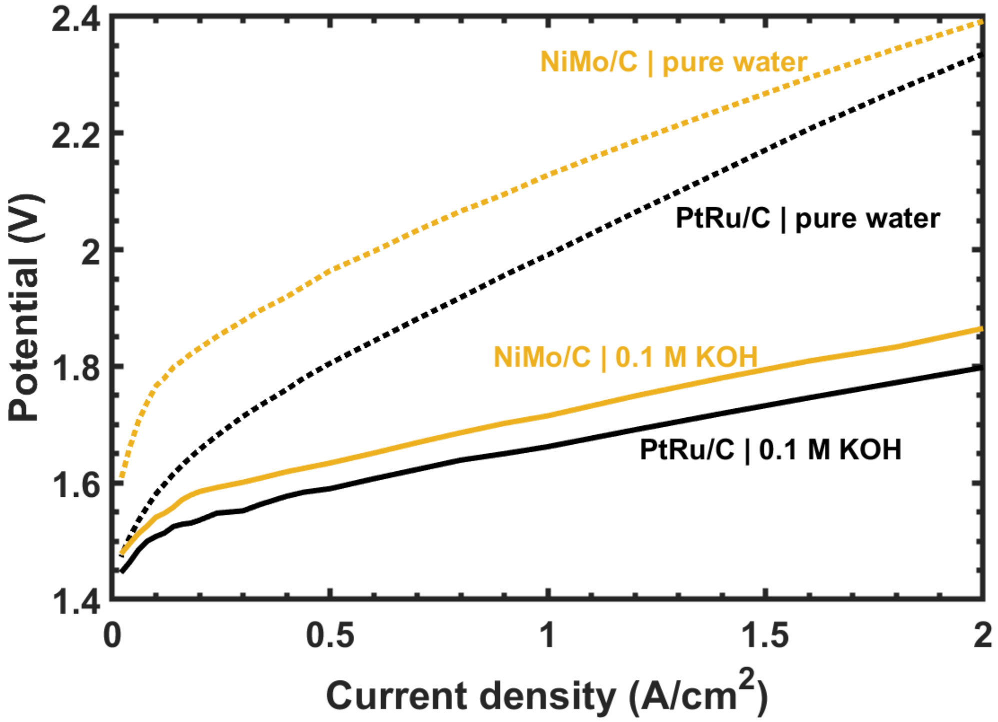

Figure 5.16: Full cell performance of Ni–Mo/C in comparison wit 50%Pt-25%Ru/C in AAEM electrolyzer set up with TP-85 membrane and IrO_x anode catalyst. The total catalyst loading of Ni–Mo/C is 4 mg/cm^2 and of Pt–Ru/C is 0.2 mg/cm^2 on the cathode side while that of IrO_x on the anode is 3mg/cm^2.

However, the synthesis technique employed did not give adequate control over the composition of the catalyst.[278] We hypothesized that our Ni–Mo/o-C catalysts (supported on oxidized Vulcan carbon) would display similar activity towards hydrogen oxidation as it does toward hydrogen evolution——that is, approaching the catalytic activity of pure Pt. If this is true, we believe that Ni–Mo/o-C catalysts have the potential to function well in AAEM reversible fuel cell devices.

The hydrogen oxidation reaction environment requires the application of positive potentials and thus imposes an additional challenge where nonprecious catalysts may be unstable toward oxidation. The HOR is also broadly limited in analytical experiments by external mass transfer of dissolved H_2(aq) to the electrode surface. Thus, a limiting current is attained, which limits the range of potentials over which kinetic data can be collected.

To test our hypothesis that Ni–Mo/o-C can catalyze HOR, we undertook 3 specific research directions. The first was to assess the potential window for the stability of this catalyst. The second was to clarify that any anodic current observed is due to HOR and not surface redox reactions. The third was to assess the influence of internal and external mass transfer limitations on the activity of these catalysts. Our approach towards these directions is further detailed below.

We observed that Ni–Mo/o-C catalysts are stable up to $\sim$200 mV anodic overpotential by monitoring the ratio of HOR to HER activity as a function of the applied potential (figure 5.17). After establishing a desired potential window, we clarified the distinction between HOR activity and the surface reaction using constant potential measurements under N_2 and H_2 environments to monitor the steady-state current flow. When the electrolyte was purged with pure N_2, there was no reactant supply for hydrogen oxidation and, thus, the current monitored over time was near zero. The slight negative current indicated a persistent surface reaction. By contrast, under hydrogen gas purge we observed a continuous positive current flow over several minutes. The magnitude and duration of this positive current flow, as well as the lack of current observed under N_2, provide strong evidence that Ni–Mo catalyzes hyrdogen oxidation and is not oxidatively degraded at 0.1 V vs RHE.

For more detailed experiments of HOR activity, we discovered that the interfacial capacitance of Mo-oxides dominates the electrochemical behavior under conditions of transient voltage; this behavior makes it difficult to directly quantify HOR activity.[213] To minimize the influence of capacitance on the HOR activity, we performed chronoamperometry (constant potential) analysis over a range of applied potentials, each for 120 seconds, and analyzed the results with respect to the total experimental time (figure 5.17c). A voltammogram (current versus potential curve) was then plotted from the chronoamperometry data using the nearly steady-state current flow observed 120 seconds after each potential step (figure 5.17d). When measured in this way, Ni–Mo/o-C catalysts under hydrogen purge exhibited HOR limiting current densities of about 2 mA/cm^2 which is 30% lower than that of Pt/C which is 2.6 mA/cm^2. The dotted line is the concentration overpotential curve depicting the expected HOR behavior of a catalyst that exhibits infinitely fast reaction kinetics, but a well-defined mass transfer limitation. Notably, this model clearly predicts a mass transfer limited current density of 2.6 mA/cm^2 at 1600 rpm in 0.1 M KOH, in close agreement ot the high-overpotential data collected for a Pt/C catalyst. Indeed, for an externally transport limited process, such as HOR at large positive applied potentials, any catalyst should display a limiting current density of about 2.6 mA/cm^2 under these conditions.[125, 128] The fact that Ni–Mo/o-C catalysts did not reach 2.6 mA/cm^2 suggests that additional factors—such as internal mass transfer and/or reversible catalyst poisoning—negatively impact HOR activity. Moreover, Ni–Mo/o-C composites exhibited hysteresis in the chronoamperometry-derived cyclic voltammogram despite discharging the capacitance. However, from these data it is not clear as to why Ni–Mo/o-C catalyst does not reach the expected limiting current density for the hydrogen oxidation reaction.

Unexpectedly low limiting anodic current densities have previously been observed for Ni–Mo catalysts, but these results were not explored in detail.[82] To better understand the kinetic limitations in this system, we systematically varied the total amount of catalyst on the electrode and observed the effect on HOR activity. Specifically, we varied the total mass loading of 25 wt% Ni–Mo/o-C catalyst and also varied Ni–Mo content in the catalyst at a fixed total mass loading of 1.5 mg$_{total}$/cm^2 on the electrode surface. Figure 5.18a shows chronoamperometry derived CV plots of 25 wt% Ni–Mo/o-C catalysts at different catalyst mass loadings. The limiting current density increased with an increase in the mass loading, which further suggests that the HOR activity becomes increasingly kinetically limited as mass loading is decreased.

Thus, figure 5.19 depicts the relationship between total mass loading and HOR current density at a fixed HOR overpotential of 50 mV. Notably, these data follow a clear non-linear trend over the range from 0 to 1.5 mg$_{total}$/cm^2, which strongly suggests mass transfer limitations dominate at higher loadings. However, even the highest mass loading we tested was unsufficient to achieve the expected external mass transfer limited current of 2.6 mA/cm^2. Moreover, the data at the lowest range of catalyst mass loadings below 0.2 mg$_{total}$/cm^2 show an increasingly linear trend, as expected for kinetically limited behavior. Together, these data suggest that Ni–Mo/o-C transitions from kinetic to internal mass transfer limited activity at 50 mV overpotential.

Figure 5.18b shows chronoamperometry derived voltammetric plots at Ni–Mo content varying from 25 wt% to 100 wt% at 1.5 mg$_{total}$/cm^2. Irrespective of the metal content on the electrode surface, the catalyst did not attain the expected HOR limiting current density. We also observed that this catalyst does not follow the Koutecký-Levich relationship (Figure 5.18c), where current

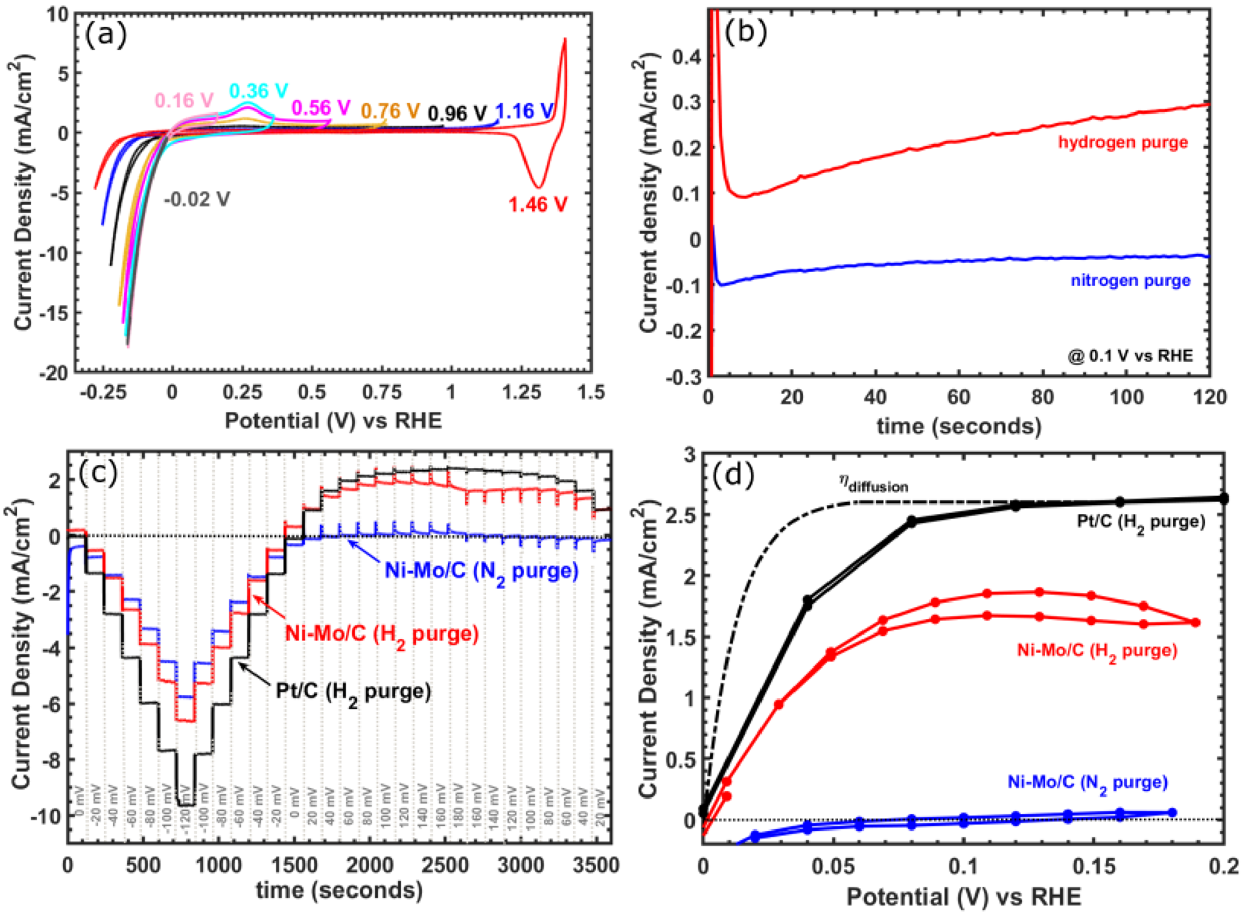

Figure 5.17: (a) Voltammetric curves of Ni–Mo/o-C catalyst collected at 10 mV/s depicting the effect of HOR potentials on the HER activity. (b) Chronoamperometry data of Ni–Mo/o-C at a constant potential of 100 mV vs. RHE under H_2 and N_2 gas purge. (c) Chronoamperometry plots at different potentials for 120 seconds and (d) Chronoamperometry derived cyclic voltammogram at 120^{th} second of Ni–Mo/o-C catalyst under hydrogen and nitrogen purge in comparison with 60 wt% Pt/C and simulated diffusion overpotential.

densities at a fixed overptential increases with the square root of electrode rotation rate. Although the capacitance in these composites likely plays a role here, the current density should demonstrate some increase as a function of rotation rate.

Based on these cumulative results, we are confident that Ni–Mo/o-C catalysts exhibit internal mass transfer limited behavior at modest HOR overpotentials when deposited with high mass loading

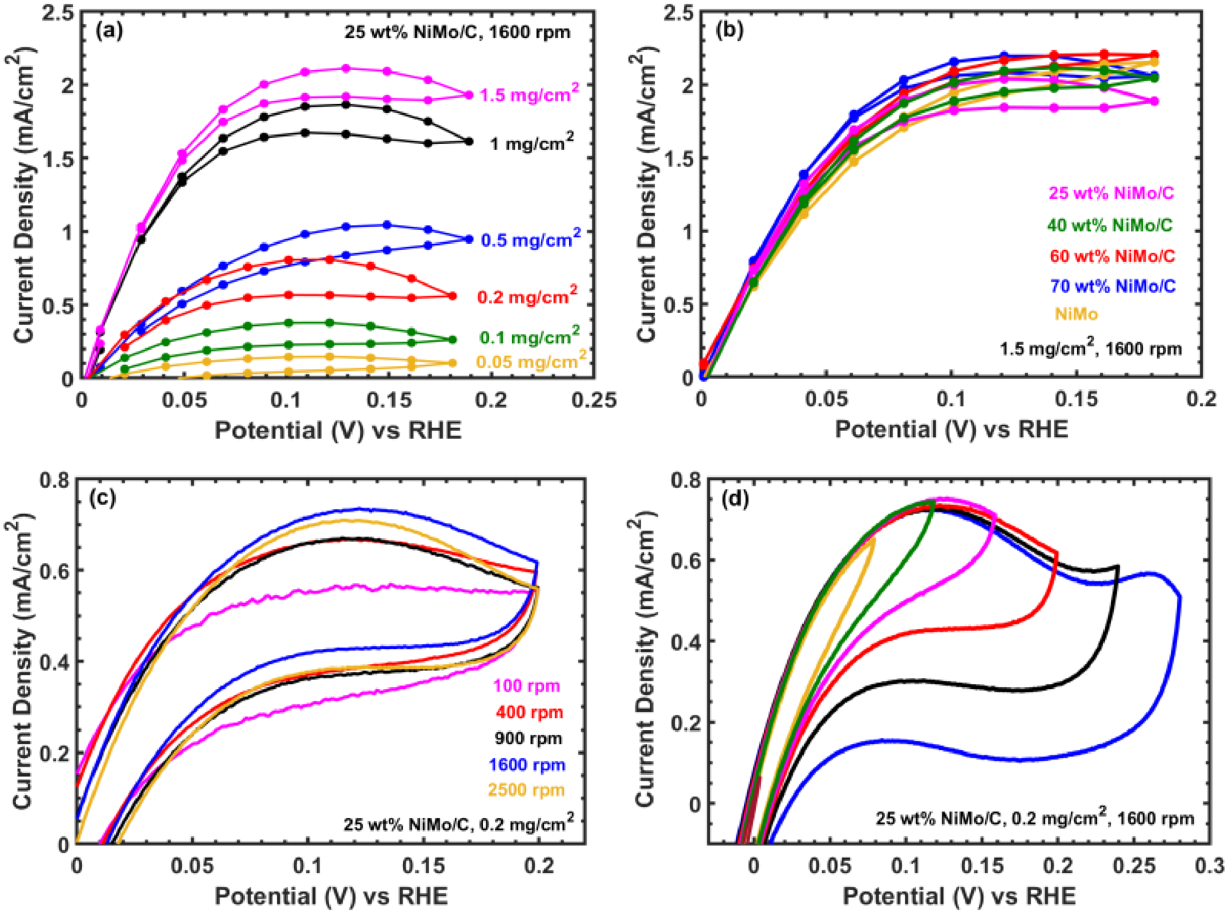

Figure 5.18: Chronoamperometry derived cyclic voltammogram depicting HOR limiting current density of (a) 25 wt% Ni–Mo/o-C for mass loadings varying from 0.05 mg/cm2 to 1.5 mg/cm^2 and (b) Ni–Mo/o-C catalyst with different Ni–Mo content at 1.5 mg/cm^2. (c) Polarization curve depicting rotation rate dependence of 25 wt% Ni–Mo/o-C at 0.2 mg/cm^2 loading and (d) shows the effect of different oxidizing potential limits on Ni–Mo/o-C. Cyclic voltammograms in (d) were collected by conditioning the catalyst at -300 mV vs. RHE for 2 minutes before the analysis at each potential and the cycling was performed from -300 mV vs. RHE to the positive potential limits and back to -300 mV vs. RHE at 2 mV/s.

on electrode substrates. However, this does not explain the inability to achieve an external mass transfer limit at large positive overpotentials. To explain this observation, we hypythesized that the

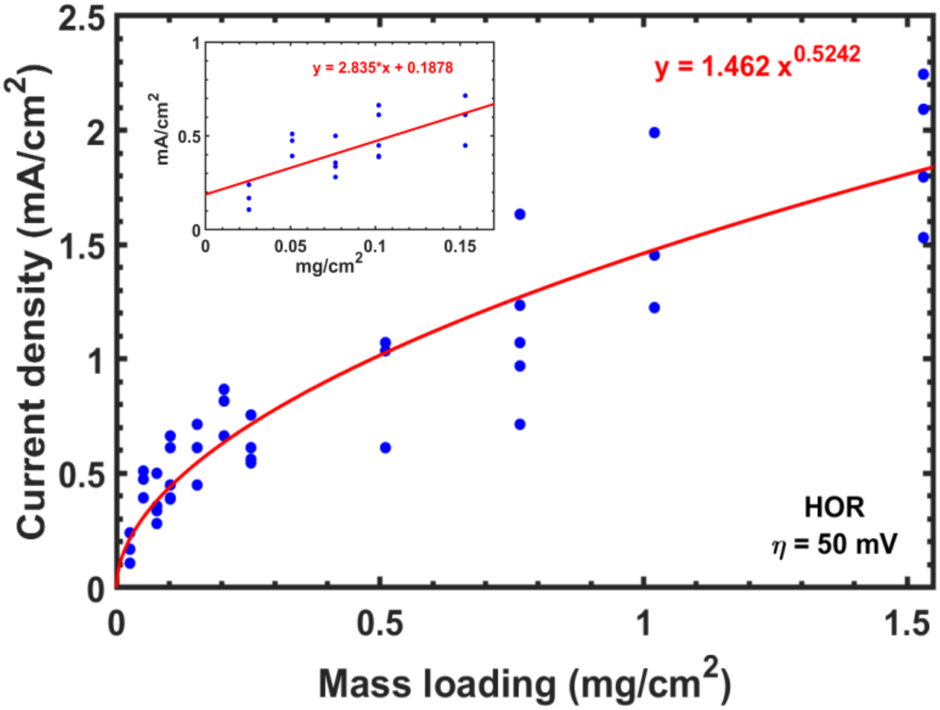

Figure 5.19: Current density as a function of total mass loading of 25 wt% Ni–Mo/o-C catalyst at +50 mV vs. RHE. A power law model fitted to the data had equation of $J_{+50mV} = 1.46 * m^{0.52}$. Inset shows the linear fit to the data at mass loadings < 0.2 mg/cm^2.

catalyst is further limited by instability toward oxidative catalyst deactivation. Thermodynamically, the most stable forms of Ni and Mo are as oxides at modest HOR potentials.[66] To determine the influence of catalyst oxidation on the HOR limiting current density, we ran cyclic voltammetry experiments while progressively increasing the positive potential limit from 80 to 280 mV vs. RHE (shown in figure 5.18d). At first, increasing the positive potential limit from 80 mV to 120 mV vs. RHE increased the anodic current density. However, a further increase in the positive potential limit did not increase the observed anodic current density further, but instead increased the hysteresis of the curve. Finally, CV data obtained by scanning to 280 mV vs. RHE clearly showed the onset of an additional oxidation feature, which we attribute to irreversible catalyst oxidation. Notably, at least some of the catalyst oxidation appears to be reversible, as is evident from the modest recover in anodic current density that we observed in the potential range from 0.2 to 0.05 V vs. RHE in the negative-going return sweeps.

These results enable us to construct a more complete picture of HOR limitations in Ni–Mo/o-C catalyst composites: reaction kinetics dominate at modest overpotentials and low catalyst loadings. Increased catalyst loadings result in internal mass transfer limitations at overpotentials over which the catalyst remains stable ($<$150 mV vs. RHE), and partially reversible catalyst oxidation takes over at HOR overpotentials exceeding 150 mV. Accordingly, these results also show clearly that oxidative instability is the primary challenge that remains to be addressed for this catalyst.

Prior literature has suggested ways to suppress catalyst oxidation by incorporating a third transition metal such as Cr or Cu to shift the d-band of Ni (111) away from the Fermi level.[78, 80] Another way to circumvent the inability to maximize HOR catalytic activity in an oxidatively unstable catalyst is to increase the system temperature, as has been shown for CoNiMo catalysts.[89] More recently, the formation of a metallic Ni–Mo alloy with 20 mol% Mo has been shown to achieve a clear external mass transfer limited current density at HOR overpotentials well below 200 mV.[88, 187] This result suggests that Ni–Mo alloys with higher Mo content are intrinsically more HOR activity, and they may also be more stable toward oxidation. These results provide promising potential future avenues to improve our carbon-supported nanocatalysts.

5.4 Reversibility of Ni–Mo/o-C for hydrogen electrochemistry

Now that we have looked at the activity and stability of Ni–Mo/o-C composites for both hydrogen evolution as well as the hydrogen oxidation reaction, we saught to explicitly confirm that they can be used to catalyze reversible hydrogen evolution/oxidation in sequence. Figure 5.20 shows reversibility of Ni–Mo/o-C and Pt/C for HER and HOR reactions. To demonstrate the ability of 25 wt% Ni–Mo/o-C composites to switch between HER and HOR region, we performed stability analysis wherein the potential was varied from -100 mV to +100 mV vs. RHE after every 10 minutes and compared directly to 60 wt% Pt/C (figure 5.20a). In both cases, catalysts were deposited with total mass loadings that were optimized with respect to maximizing geometric activity with a minimum quantity of active catalyst. 60 wt% Pt/C composites with 0.2 $\text{mg}_{total}/\text{cm}^2$ are routinely employed in fuel cell tests while 1.5 $\text{mg}_{total}/\text{cm}^2$ is the highest amount of Ni–Mo/o-C composites that we were able to deposit on the electrode surface without delamination.

Interestingly, the HER activity of Pt/C clearly decreased beginning after the 3^{rd} or 4^{th} cycle, and the HOR activity started to decrease at 14^{th} cycle. The decrease in the HER activity is attributed to the stability limitations discussed in Chapter 3. The HER and HOR activity of Ni–Mo/o-C, on the other hand, increased slightly over the course of the experiment, which is again consistent with prior results attributed to dissolution of inactive oxides. Nonetheless, the ability of Ni–Mo/o-C to effectively switch between HER and HOR with their performance only 10–30% lower than Pt/C is very promising.

With assurance that Ni–Mo/o-C composites can undergo reversible hydrogen reactions. We further quantified their performance for reversibility by a term denoted as exchange activity (figure 5.20b). The exchange activity was obtained from the potential regions where both the HER and the HOR displayed purely kinetic activity. This region, termed as micropolarization region, was from -10 mV to +10 mV for Ni–Mo/o-C and ± 5 mV for Pt/C. The exchange activity (j_o) was then calculated using the formula $j_o = (RT/F) * (j/V)$ where R is the universal gas constant (8.314 J/mol.K), T is temperature (298 K), F is Faraday's constant (96485 C/mol) and j/V is the slope of a cyclic voltammogram obtained from the micropolarization region. This exchange activity is plotted as a mass-specific activity calculated based on the metal content as a function of total catalyst mass loading.

The exchange activity of Pt/C and Ni–Mo/o-C decreased continuously with an increase in the mass loading and attained a constant value at loadings > 0.25 $\text{mg}_{total}/\text{cm}^2$, which likely reflects the onset of transport-dominated activity. The reported exchange activities for Ni–Mo catalyst supported on Ketjen black at a loading of 0.1 $\text{mg}_{total}/\text{cm}^2$ is 4.5 ± 0.2 mA/mg_{cat}, which is about 3 times lower than the exchange activity of Ni–Mo/o-C.[82] More recently, an exchange activity of 14.1 mA/mg_{cat} is also reported, which is same as that of Ni–Mo/o-C (14 ± 1.35 mA/mg_{cat}, with standard error for 3 independent samples).[187] Moreover, in the low mass loading range (<0.15 $\text{mg}_t otal/\text{cm}^2$), the intrinsic activity of Ni–Mo/o-C was only 5–8 times lower than Pt/C, but is several orders of magnitude cheaper. This further suggests that Ni–Mo/o-C composites have great potential to operate as reversible hydrogen catalysts.

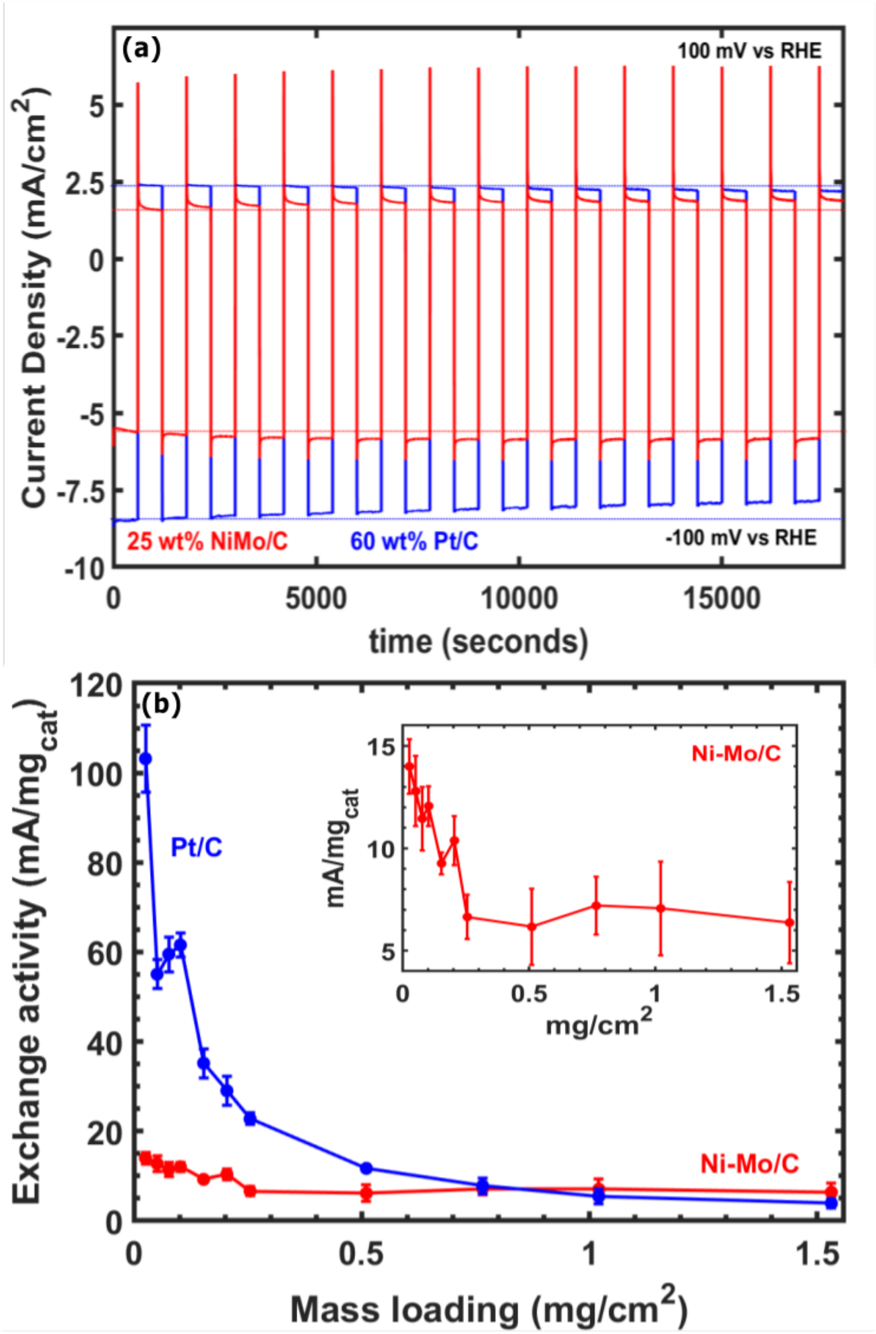

Figure 5.20: (a) Chronoamperometry data of Ni–Mo/o-C and Pt/C catalyst showing reversibility of the catalysts when held at HER and HOR overpotential of 100 mV. Mass loading of 25 wt% Ni–Mo/o-C is 1.5 mg$_{total}$/cm^2 and of 60 wt% Pt/C is 0.2 mg$_{total}$/cm^2. (b) Exchange mass specific activity of 25 wt% Ni–Mo/o-C and 60 wt% Pt/C at different mass loadings.

5.5 Summary, Impact and Recommended Future work

In summary, this chapter compiles our efforts in improving the hydrogen evolution/oxidation reaction performance of Ni–Mo composites. Owing to the low electronic conductivity of the oxide shells, the catalyst activity, which would normally be limited by reaction kinetics and solution-phase mass transfer, is also limited by interfacial resistivity (i.e., solid-state charge transfer). To mitigate this electronic resistivity concern in Ni–Mo alloys, we incorporated conductive carbon supports and observed that the HER activity of carbon-supported Ni–Mo composites improved significantly compared to unsupported alloys.

We then set out to maximize the practical HER activity of Ni–Mo composites. To do so, the dispersion of Ni–Mo alloys on carbon was improved by changing the amount and degree of oxidation on carbon support. With improved dispersion, the mass-specific HER activity increased significantly. We found that the optimized dispersion and the highest mass normalized HER activity was obtained when 25 wt% Ni–Mo is supported on oxidized-Vulcan carbon. This optimized catalyst is also active for the reverse reaction of hydrogen oxidation and that Ni–Mo/o-C catalyst enables reversible HER/HOR reactions in alkaline conditions. The stability of Ni–Mo/o-C composites under HER and HOR conditions (provided the applied potential range is maintained below 0.2 V vs. RHE) is also very promising. Accordingly, we are now continuing to evaluate catalyst performance in practical AAEM electrolyzers.

The significance of this work is that we have demonstrated that nominally metallic nonprecious catalysts can still exhibit electronic conductivity limitations, and it is crucial to address these. We are also among the only research groups to demonstrate stable, reversible HER/HOR reactions on a nonprecious catalyst. Finally, the easy and scalable synthesis approach we have developed for Ni–Mo/o-C composites strongly supports their use in practical devices.

The oxidative stability of Ni–Mo/o-C composites remains a major concern, and future work is recommended to be directed towards improving this property. The most promising avenues to pursue include incorporation of a third metal in the Ni–Mo alloy to alter the electronic state of Ni and subsequently prevent its oxidation.[279, 280, 281] Our preliminary analysis on incorporating Cu as a third metal with the existing synthesis procedure was not successful, as we were unable to produce well-mixed ternary Ni–Mo–Cu mixtures. Therefore, a novel synthetic route will likely be needed to generate solid solutions of Ni–Mo–Cu and study the influence of Cu on the oxidative stability of the catalyst.

Another route to improve the oxidative stability and the HER/HOR performance of Ni–Mo/o-C composites is to increase the Mo content of the Ni–Mo alloy. All the Ni–Mo composites studied in this work were found to comprise 10 mol% Mo in the alloy, but prior work has shown that better HER/HOR activity can be obtained with a higher level of Mo.[60, 51] However, tailoring the existing synthetic approach to increase the Mo content might not work as a complete reduction of Mo-oxides to metallic Mo requires high temperature (∼90°C) at which the catalyst sinters. Hence, new techniques are needed to facilitate more incorporation of Mo in Ni–Mo alloys.

Future aspects of this project can also focus on decreasing the inactive carbon and resdual Ni–Mo oxide content in the catalyst and decreasing the average particle size. Both of these would be expected to increase the proportion of exposed catalyst active sites per unit catalyst mass. The optimized catalyst composition that gave the highest mass-specific activity at lab scale is with 25 wt% Ni–Mo and 75 wt% oxidized Vulcan carbon, thus, at least 3/4 of the catalyst is inactive for HER/HOR. Although carbon is essential to disperse the catalyst and provide conductive pathways, the carbon content in the catalyst should be reduced to avoid employing thick catalyst layers in practical devices. One promising route to decrease the carbon content is to modify the carbon to generate more sites for nucleation of Ni–Mo oxide during the precipitation step. One way to do this might be to increase the density of heteroatom functionalities (especially oxygen) on carbon, which are expected to act as nucleation sites.

Relatively modest improvements, as detailed above, would likely be sufficient to enable practical, commercial use of our catalysts in AAEM electrolyzers and fuel cells. However, the practical implementation of AAEM electrolyzers in particular will still be limited due to the sluggish kinetics of the reactions on the oxygen side. The next chapter will focus on our efforts on Ni–Fe catalysts for oxygen evolution reaction in water electrolyzers.

6.0 Ni–Fe Composites for Oxygen Evolution Reaction

Metal oxides are usually used as catalysts under the strong oxidizing conditions of OER. However, we showed with Ni–Mo alloys that the resistivity of these oxides play a vital role in the activity of nonprecious electrocatalysts. Moreover, metal oxides are often unstable under OER reaction conditions because the driving force for lattice oxygen evolution is greater than oxygen evolution from the electrolyte. Recently, various supported and unsupported Ni–Fe catalysts have shown excellent stability over several thousands of hours.[282, 283, 284, 285, 286] Although the synthesis approaches employed for most of these catalysts ensured that they do not easily degrade under OER conditions, none of the associated procedures are likely to be usable for high-performing AAEM electrolyzers. Our work is focused on improving the activity, and especially the stability of Ni–Fe composites synthetized as nanoparticulate powders, to enable their use in current-generation devices.

Based on our work on Ni–Mo composites, we formulated a hypothesis that Ni–Fe core@shell catalysts, when synthesized on carbon supports, might yield an active and stable OER catalyst. This work was primarily performed by 2 undergraduate students, Margaret Orr and Jeffrey Hoffmann, to whom I served as a mentor and was involved in performing TEM-related measurements and analyzing experimental data. Maggie performed the initial analysis to optimize the composition of the catalyst, whereas the detailed activity and stability analysis was completed by Jeff. Dr. Stephen House was also responsible for the HAADF-TEM analysis described herein.

6.1 Core@shell structure and carbon incorporation

We synthesized metallic Ni–Fe alloy particles on oxidized Vulcan carbon black (Ni–Fe/o-C) using a wet impregnation method where a 70:30 ratio of Ni and Fe precursors were mixed with oxidized Vulcan carbon and ethanol and kept for stirring at room temperature for 2 hours (figure 6.1).[287]

After 2 hours, the reaction mixture was kept in the drying oven at 90 °C overnight and later reduced under forming gas mixture (5% H_2, 95% N_2) at 200 °C for 30 minutes and 450 °C for 1 hour. The final reduced catalyst was then analyzed using microscopy and diffraction techniques to understand its composition.

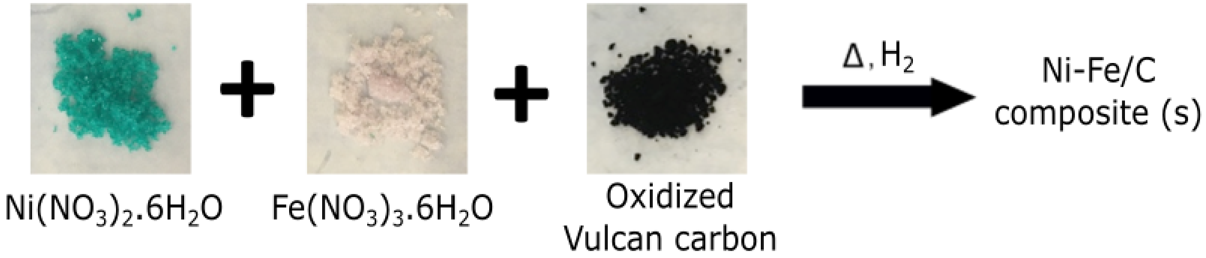

Figure 6.1: Synthesis schematic of Ni–Fe composites supported on oxidized Vulcan carbon

The metal content in the composite was varied from 35 wt% to 85 wt%. Figure 6.2 shows the corresponding SEM images and XRD patterns. The SEM images were collected with a backscatter detector that differentiates between the carbon and the Ni–Fe component based on the atomic number differences. The bright white particles in all the images correspond to metallic components whereas the grey regions represent carbon. The dispersion of Ni–Fe component on the oxidized Vulcan carbon support, demonstrated from these backscatter images indicate that Ni–Fe particles remain discrete and well dispersed at 60 wt%, but they fuse into larger aggregates at $\geq$ 84 wt%. The XRD data for all these powders showed 3 peaks that agree with the fcc Ni structure with a modest shift toward lower 2-θ values. These peak shifts translate to $\sim$7 mol% Fe incorporated in the Ni from Vegard's law.[288]

TEM analysis of 52 wt% Ni–Fe/o-C composite executed under bright and dark-field is shown in figure 6.3. The bright-field TEM image shows the dispersion of Ni–Fe nanoparticles on oxidized Vulcan carbon. The Ni–Fe particle size varies from 5 nm to 20 nm, and the inset shows its core@shell structure. The composition of the core and the shell was obtained from EDS analysis performed under the dark field. Just as with Ni–Mo composites, the core was rich in metallic Ni and Fe, whereas the shell was rich in Ni and Fe oxides. Moreover, the metallic particles are not perfectly spherical

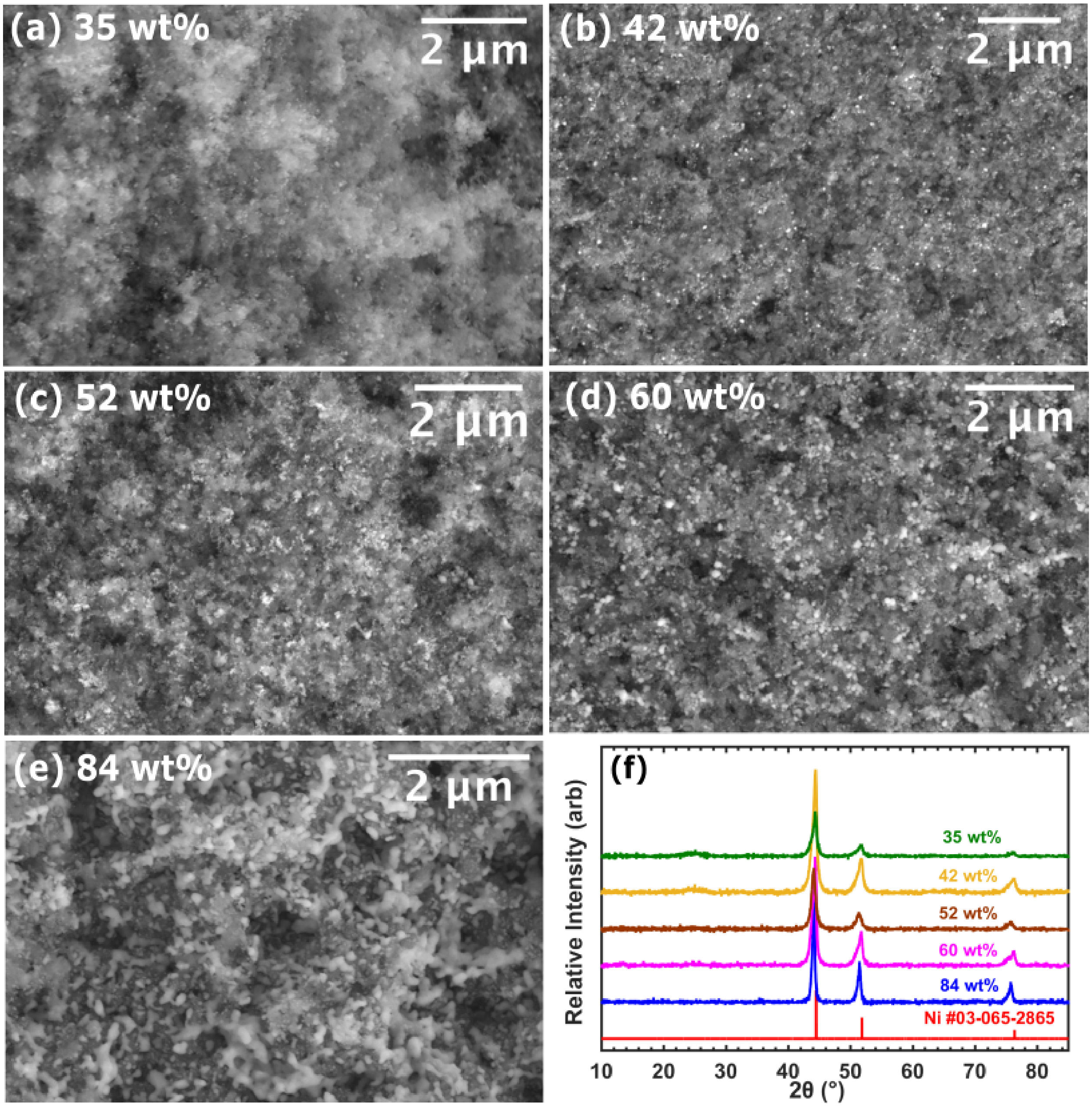

Figure 6.2: (a-e) SEM and (f) XRD data of Ni–Fe/o-C composite with different metal content. SEM images were collected with backscatter detector and the standard diffraction pattern of XRD is obtained from ICDD database. The weight percentages represent the metal content in the catalyst.

and the outer layers are relatively enriched in Fe. This observation is tentatively attributed to the Kirkendall effect, in which the composition and shape of a particle exposed to a reactive ambient environment (aerobic oxygen and/or water in this case) is influenced by the rate of diffusion of the components of the particle.[289]

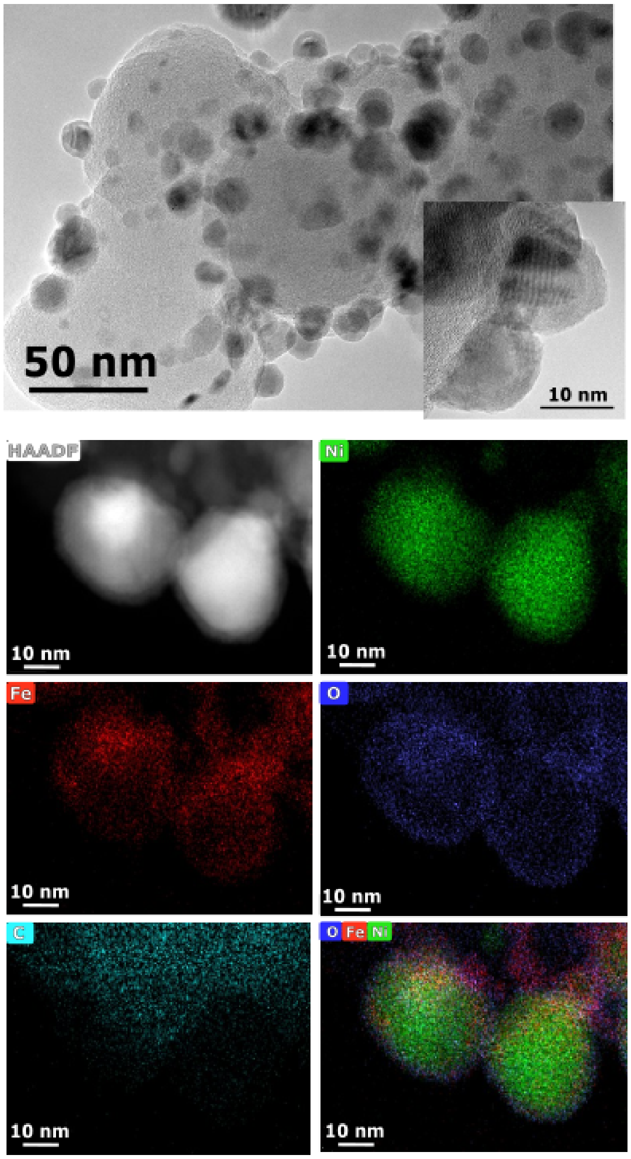

Figure 6.3: Bright and dark field TEM image of 52 wt% Ni–Fe/o-C composite with EDS maps indicating core@shell structure.

6.2 Oxygen evolution reaction performance

OER activity data for Ni–Fe/o-C composites with different metal content are shown in figure 6.4. We ultimately determined that Ni–Fe/o-C composites with ∼50 wt% carbon gave the highest OER activity – that is highest current density at lowest potential. Our best-performing catalysts yielded 10 mA/cm^2 (40 mA/mg$_{cat}$) of anodic current density at 300 mV overpotential at room temperature in 0.1 M KOH. Consistent with prior reports, we also observed improved catalytic performance with an increase in electrolyte concentration to 1 M KOH.[105, 109] In 1 M KOH, the potential required for 50 wt% Ni–Fe/o-C composite to reach 10 mA/cm^2 was reduced to 280 mV overpotential.

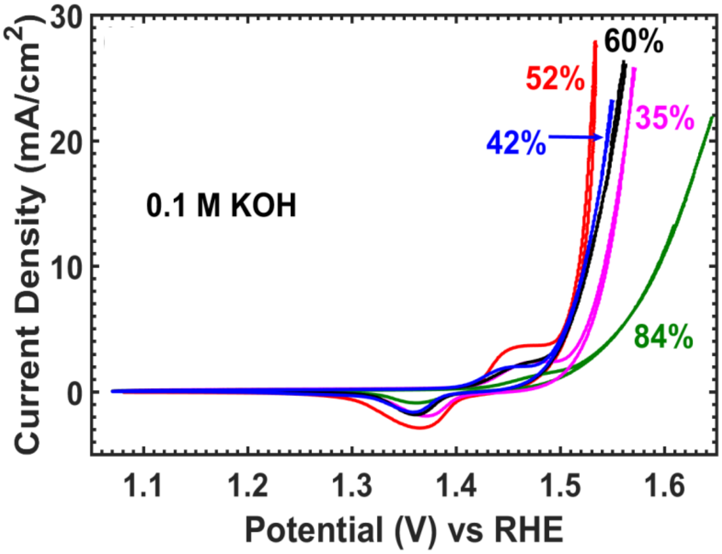

Figure 6.4: Oxygen evolution reaction activity of Ni–Fe/o-C composites with different metal content in 0.1 M KOH

Metallic catalysts are known to undergo oxidation under anodic conditions and therefore metal oxides are typically employed as catalysts for OER. Although the as-synthesized Ni–Fe/o-C composite possess an oxide shell, we employed an electrochemical activation treatment to the as-synthesized catalyst involving voltammetric cycling. The purpose of this treatment was to stabilize the oxide surface layer through sequential oxidation/reduction treatments bracketing the range of interest for OER catalysis. Despite demonstrating in Chapter 5 that the oxide shells impede the electronic conductivity, the conductivity of Ni–Fe oxide was expected to be considerably higher than Ni–Mo oxides.[258, 290, 263, 291]

The electrochemical catalyst pretreatment, referred to hereafter as catalyst activation, involved cycling in the potential range from 1.1 V vs. RHE to 1.55 V vs. RHE, which encompasses the oxidation and reductoin associated with the Ni(III/II) redox couple (figure 6.5). The current values associated with the Ni(II) oxidation (at $\sim$1.5 V vs. RHE) and Ni(III) reduction (at $\sim$1.25 V vs. RHE) of the catalyst increased and eventually attained a stable value over 400 cycles. This behavior was interpreted as indicating that the maximum amount of relatively stable Ni–Fe oxide had been generated.

Figure 6.6 compiles identical-location TEM images collected before and after the activation step. Notably, despite the fact that we generally observed increased OER activity after activation, these images clearly show a smaller number of larger particles present after activation compared to before. For those particles that remained on the carbon support, however, IL-TEM imaging did not show extensive changes in morphology. Thus, we believe that the activation step converts the $Ni(OH)_2$ component of the catalyst from its α to β phase.[108, 263] This transformation would not be apparent from TEM imaging at this length scale. It is also possible that the oxide shell thickness increased on activation, due to progressive oxidation of the metallic component. Although these images do not clearly show such a difference, their possibility cannot be eliminated. Nonetheless, this analysis serves as a good starting point to continue working with Ni–Fe/o-C composites. Further analysis on the migration or delamination effect of these materials and their stability towards OER is discussed in the next section.

6.3 Stability of Ni–Fe/o-C composites

Representative stability data for $NiFeO_x$/o-C catalyst after 3 hours of continuous potential cycling in 1 M KOH are shown in figure 6.7. Before the stability analysis, the catalyst was activated by

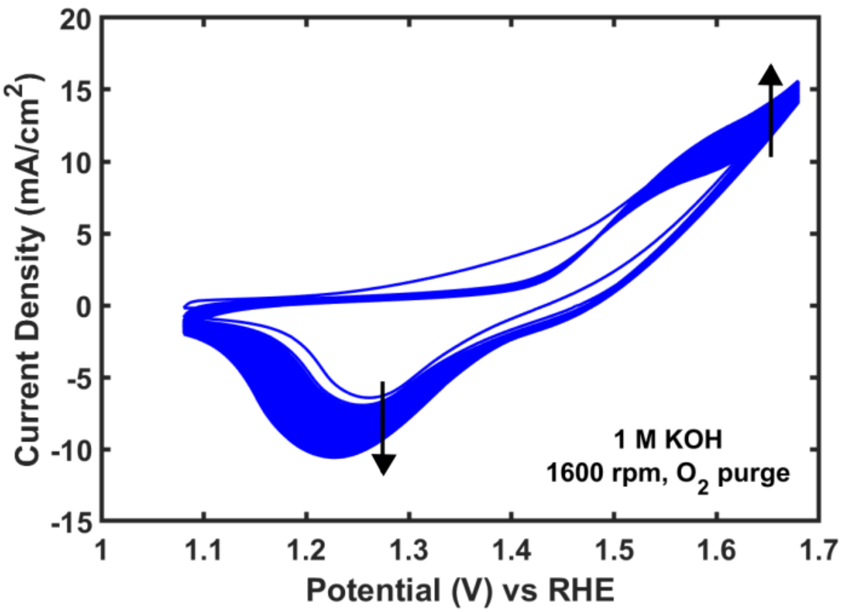

Figure 6.5: Activation of as-synthesized Ni–Fe/o-C composites to convert them in NiFeO$_x$/o-C. 400 cycles were performed during which the current density for the redox peaks increased initially and later attained a stable value.

scanning from 1 V to 1.55 V vs. RHE for 400 cycles. Specifically, the anodic current densty at modest OER overpotentials was observed to decrease to near zero after several hundred voltammetric cycles extending from 1 to ~1.7 V vs. RHE. This degradation was also coincident with the loss of the voltammeric feature associated with the Ni(III/II) redox couple.

We suspect that the instability we observed is attributable to oxidative degradation of both the carbon and the NiFeO$_x$ component of the catalyst. Indeed, carbon black and Ni–Fe both have been previously shown to degrade under OER conditions.[292, 293] Oxidation of these catalyst components lead to irreversible loss of catalyst active sites (in the case of Ni–Fe oxide) and dissolution into the electrolyte (which is possible for the transition metals and carbon).

Based on these results, we became interested in understanding better how the potential limits associated with the activation pre-treatment impacts the practical activity and stability of the catalyst. To address this question, we adopted an experimental protocol in which the potential range associated

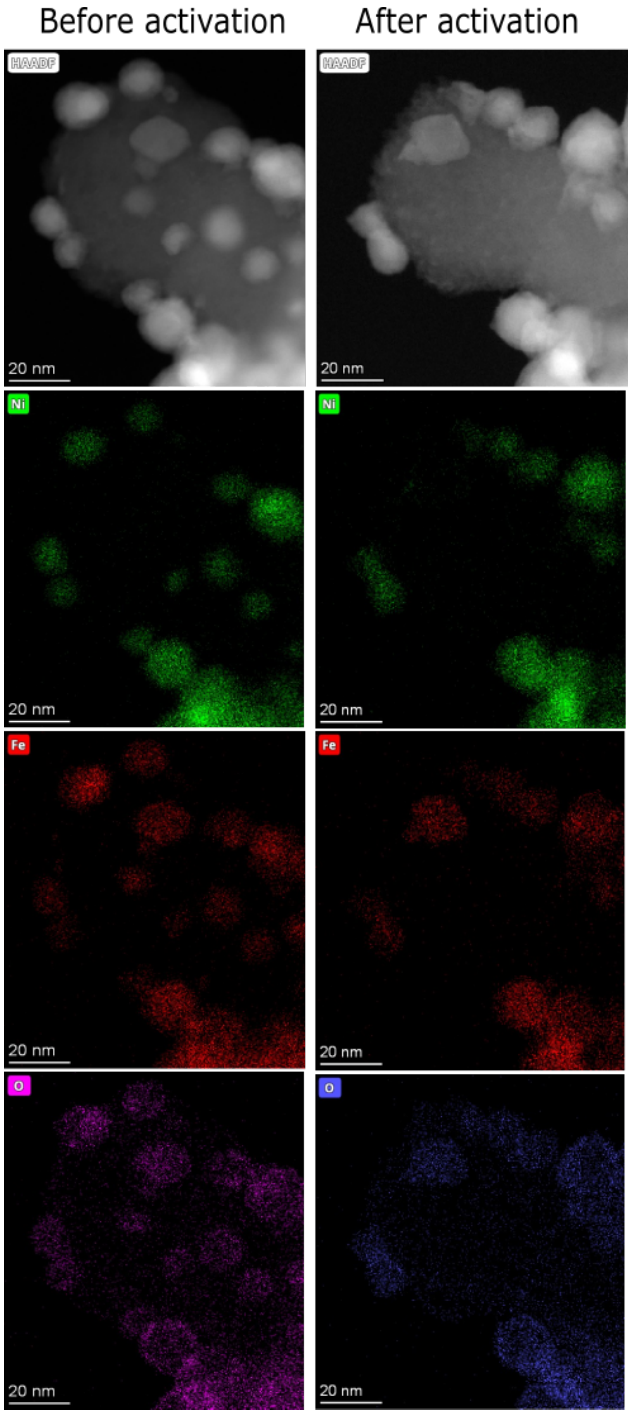

Figure 6.6: Identical location TEM analysis of Ni–Fe/o-C composites before and after the activation step

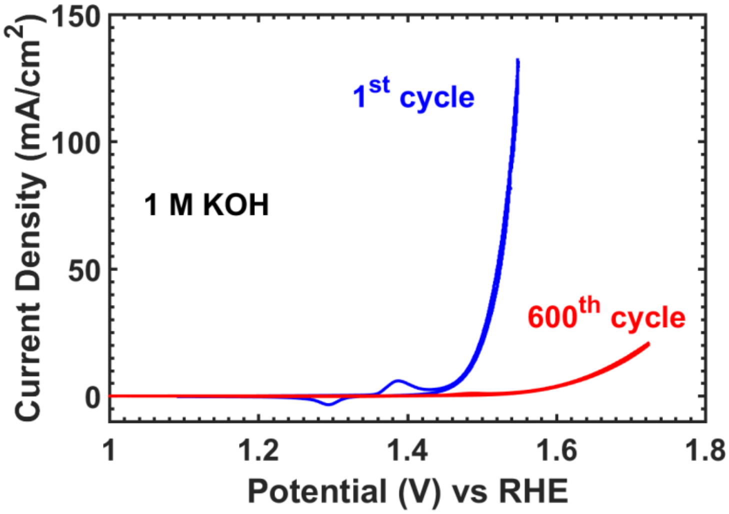

Figure 6.7: Stability of NiFeO$_x$/o-C with 52 wt% metal in 1 M KOH showing stability after 1st and 600th cycle

with the activation step was varied, followed by a period of voltammetric cycling whose conditions were held constant. Our hypothesis was that a more positive potential limit during catalyst activation would create a more oxidizing environment and lead to faster degradation of the catalyst even during the subsequent cycling treatment.

Figure 6.8 compiles data for our activation–stability sequence. The data in panels a–c generally agree with our hypothesis, where an increase in potential limit from 1.55 V vs. RHE to 1.85 vs. RHE during the activation step resulted in decreased catalyst stability when subsequently cycled 800 times. However, when we tried to repeat this experiment with an activation treatment to 1.85 V vs. RHE (figure 6.8d), we observed unexpectedly high stability. Additional review of laboratory notes indicated that this unexpectedly stable catalyst sample was derived from a parent catalyst deposition "ink" that had been left on the benchtop for several weeks. Thus, this apparent increase in stability might have had to do with as yet unknown reactions that occur in the deposition solution, which contains Ni–Fe/o-C, isopropyl alcohol, and Nafion ionomer.

To further explore the extent to which this catalyst exhibits stability properties that depend on its "shelf-life" in the deposition solution, we undertook experiments where Ni–Fe/o-C catalysts

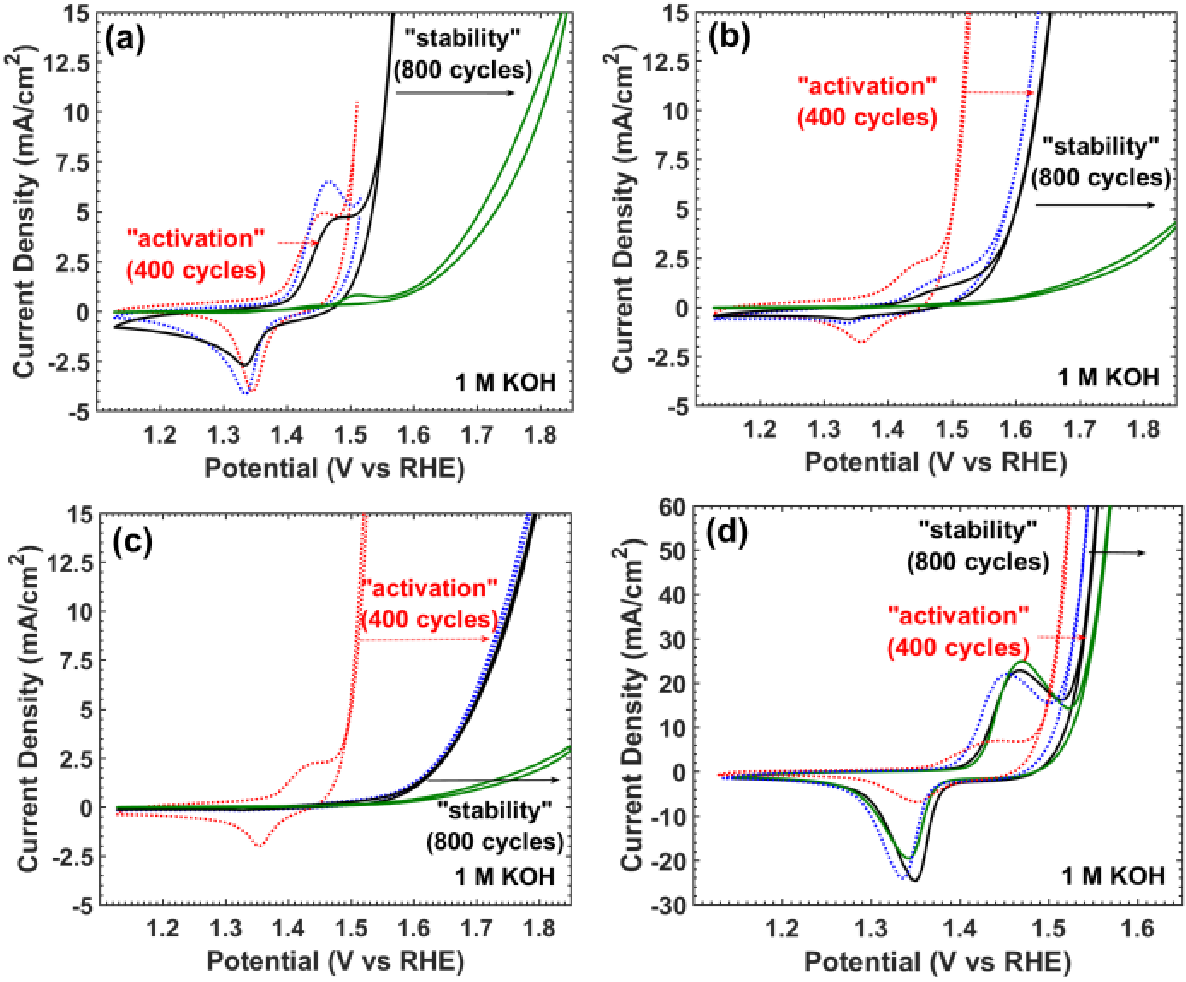

Figure 6.8: Activation and stability sequences for NiFeO$_x$/o-C catalysts as a function of oxidative potential limit (a) 1.5 V vs. RHE, (b) 1.7 V vs. RHE, (c) 1.85 V vs. RHE and (d) 1.85 V vs. RHE, where (d) was an attempt to reproduce (c) with a new film from the same parent solution . The dotted lines indicate the initial and final cycles in the “activation” phase whereas the solid lines indicate the initial and final cycles for the “stability” phase. The arrow points to the direction in which the curves shift after cycling in the activation step (denoted by red dotted arrow) and after stability step (denoted by black solid arrow).

were prepared and tested at regular intervals over several weeks. These experiments and other electrochemical measurements described below were performed using 400 activation cycles from

1.1 to 1.55 V vs. RHE and 875 stability cycles from 1.1 to 1.85 V vs. RHE. We indeed observed that the initial performance and the stability of the catalyst improved as the catalyst solution aged (figure 6.9). Aging of $Ni(OH)_2$ catalysts in KOH electrolyte has been previously attributed to the shift from α–$Ni(OH)_2$ phase to β–$Ni(OH)_2$.[108] It has also been shown that in KOH solution that has been rigorously purified of Fe contaminant, the activity of $Ni(OH)_2$ decreases with time.[99] However, the effect that we observed here was not attributable to aging the sample in the alkaline electrolyte, but rather in the deposition solution. Nonetheless, it may be reasonable to expect similar catalyst restructuring to occur in any environment in which transition metal oxides may dissolve, diffuse, and redeposit (e.g., in the presence of Nafion ionomer).

Catalyst restructuring in colloidal solution, and specifically the interactions between Nafion, isopropyl alcohol, and $NiFeO_x$/o-C can be conjectured based on several prior reports. The hydrophobic backbone of Nafion favors adsorption carbon and thus the size of carbon agglomeretes is impacted by Nafion additives.[294, 295] Another possibility is that because the Nafion ionomer is acidic in nature (i.e., it contains mobile protons), it may support transient or irreversible dissolution and/or ion exchange with the Ni–Fe catalyst components.[296, 297, 298, 299] In fact, Fe^{+2} is considered as a common contaminant in Nafion in membrane electrode assemblies and influences the proton conduction and membrane hydration.[300, 301] Upon deposition of the catalyst on an electrode and submersion in an alkaline liquid electrolyte, transition metal cations associated with the Nafion ionomer would be expected to repricipitate as hydroxides, and these compounds may be more active (or simply exhibit higher surface area) than the as-synthesized $NiFeO_x$/o-C. This explanation is consistent with the increase in the current density for the $Ni^{2+/3+}$ redox peaks in figure 6.9.

Figure 6.10 presents TEM data comparing Ni–FeO_x/o-C composites before and after stability analysis on samples with and without Nafion to monitor the effect of binder content on catalyst adhesion. In each case, the after-stability images show significant changes in the morphology of the Ni–Fe and the carbon components. However, for samples without Nafion, the samples after electrochemical treatment appear to have lost the majority of the catalyst nanoparticles, or the catalyst particles have coarsened to such an extent that their size is similar to that of the carbon. By contrast, the catalyst made with Nafion still shows clear evidence for denser Ni–Fe nanoparticles, but many of the particles have apparently grown, migrated, or detached. Moreover, there is evidence for the formation of a continuous coating surrounding all the catalyst particles, which we speculate to be

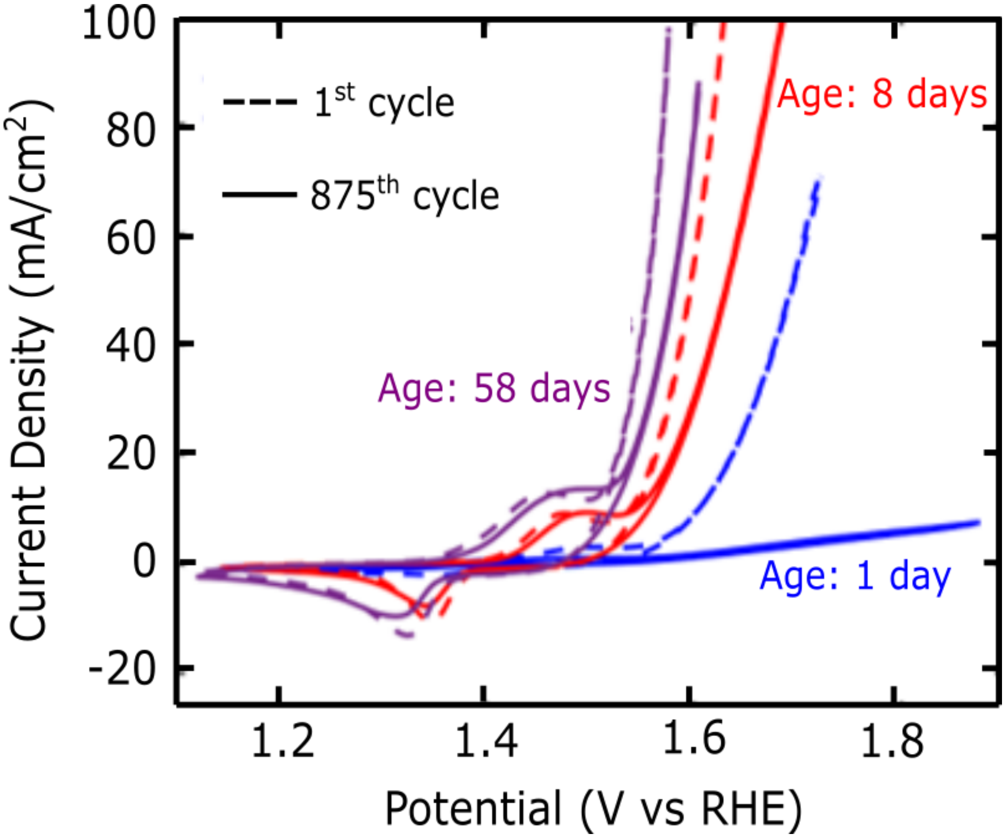

Figure 6.9: Stability of $NiFeO_x$/o-C composites after cycling for 875 cycles ($\sim$ 8 hours) at different ages of the deposition ink containing isopropyl alcohol and Nafion. The dashed lines represents curves of the 1^{st} cycle for all the solution age days and solid line indicates the 875^{th} cycle curves. The analysis was done in 1 M KOH by scanning the potential from 1.1 V vs. RHE to 1.85 V vs. RHE at 100 mV/s under O_2 gas purge and was prepared by an activation step from 1.1 V to 1.5 V vs. RHE under same conditions.

Nafion.

Our work to date on using before/after TEM analysis to understand Ni–Fe oxide stability under OER conditions has yielded indeterminate results. Based on cumulative results to date, I believe the most plausible degradation pathway involves carbon oxidation, which causes catalyst particles to physically detach from the support. Thermodynamically, carbon becomes unstable at potentials $>$ 0.207 V vs. RHE, and the mass loss associated with using pure carbon as an OER catalyst was

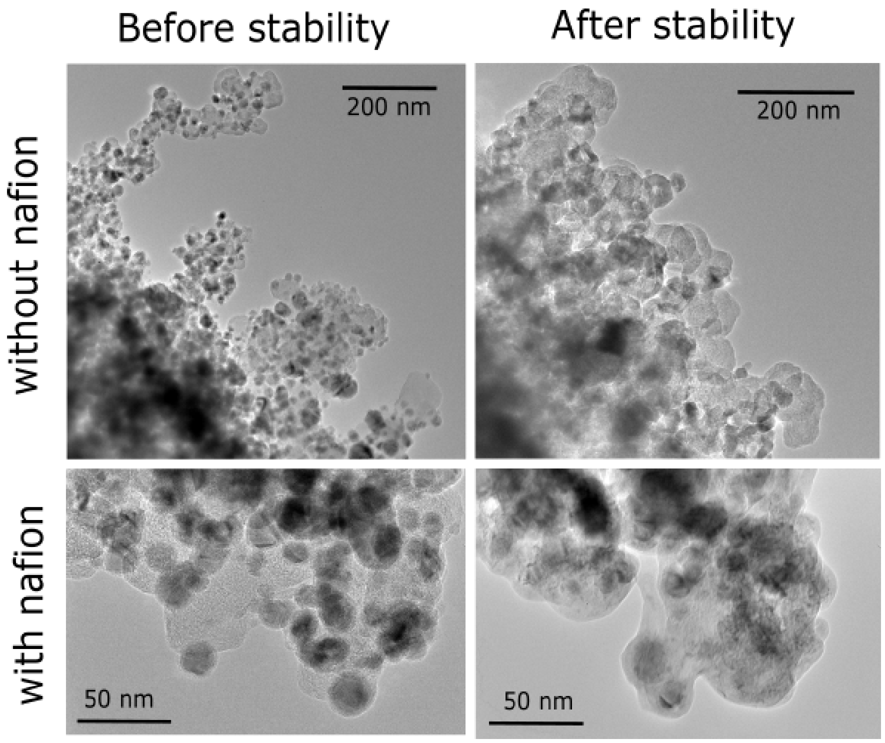

Figure 6.10: TEM images of NiFeO$_x$/o-C composites with and without Nafion depicting the composition before and after stability analysis.

previously observed to increase with an increase in applied potential. [302] Moreover, the edge plane sites of carbon were found to be predominantly responsible for corrosion, and that graphitization of carbon increased its corrosion resistance.[303] Nonetheless, a recent differential electrochemical mass spectrometry showed that carbon corrosion can be suppressed when the carbon supports a highly active OER catalyst.[304]

Based on the TEM analysis we have performed thus far, 8 hours of continuous cycling induces substantial detachment and/or migration of Ni–Fe oxides, but the composition of Ni–Fe oxide that remained did not seem to have undergone a significant change. We, therefore, performed the stability analysis under continuous OER oxidation for a longer time ($\sim$100 hours) with a goal of observing the timescale over which our NiFeO$_x$/oC undergoes a catastrophic loss in OER activity. This analysis was performed by arbitrarily depositing a dilute mass of Ni–Fe/o-C composite on hollow Au TEM grids. The stability analysis was performed by holding the current constant at about $\sim$20 mA/cm^2

(figure 6.11). The noise in the these data are again attributable to oxygen bubbles that form and detach from the electrode surface. Remarkably, the overpotential required to sustain this constant current density was found to decrease by ∼40 mV over the duration of this experiment. Even more remarkably, subsequent TEM analysis again indicated substantial loss of catalyst particles from the sample However, for those particles that remained, the core@shell structure of Ni–Fe was intact (figure 6.12 However, the EDS analysis also showed the presence of Au nanoparticles throughout the catalyst. The chemical origin of these particles has not yet been determined, but we speculate that Au atoms simply migrate via concentration-induced diffusion from the TEM grid and distribute themselves throughout the catalyst sample over timescales in the tens to hundreds of hours. Another possibility is that the oxidizing conditions of the OER experiment accelerates Au dissolution and redeposition again throghout the sample.[140] Despite this inconvenient process that precludes detailed TEM analysis, the ability of some carbon-supported Ni–Fe oxide particles, as well as the robustness of the core@shell structure to remain intact, are intriguing.

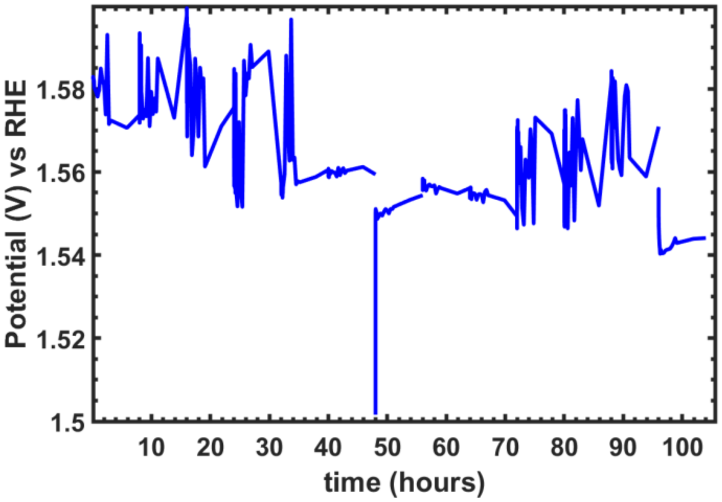

Figure 6.11: Stability of Ni–Fe/o-C composite performed at a fixed current density of 20 mA/cm^2 in 1 M KOH under O_2 gas purge. The catalyst was activated by scanning from 1.1 V to 1.55 V vs. RHE for 400 cycles under the same conditions prior to the stability measurement. An arbitrary amount of catalyst was deposited on 3 mm Au TEM grid for this analysis.

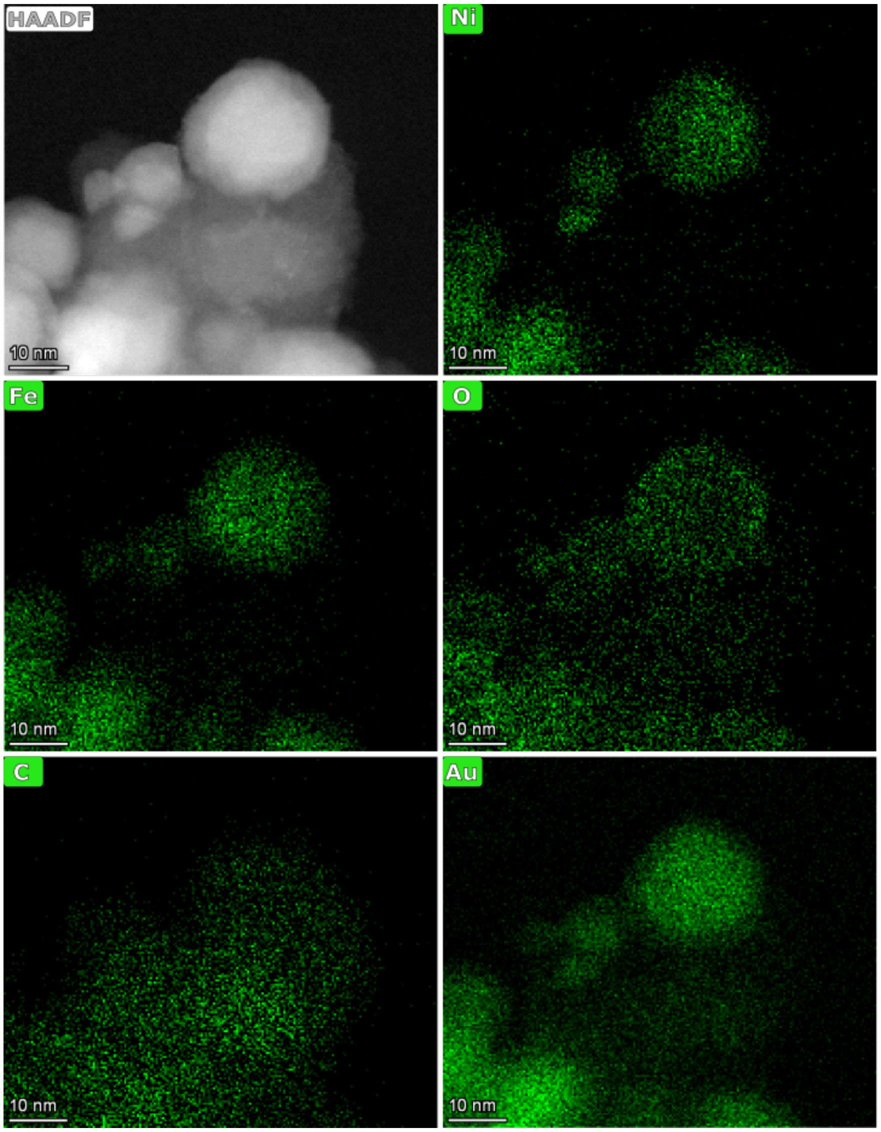

Figure 6.12: High angle annular dark field TEM image and EDS maps of Ni–Fe/o-C catalysts after being subjected to a constant current of 20 mA/cm^2 for about 100 hours.

6.4 Summary, Impact and Recommended Future work

This chapter summarized our efforts to synthesize core@shell materials for the oxygen evolution reaction. We found that the Ni–Fe/o-C composites made by the wet impregnation method yield a broad range of particle sizes and adopt a core-shell metal@oxide structures. These composites were electrochemically activated to generate surfaces that were more active toward the OER than in the as-synthesized catalyst. We also discovered an intriguing shelf-life effect where time spent in a deposition ink solution containing Ni–Fe/o-C, Nafion, and isopropyl alcohol results in increased OER activity and stability. Using identical location transmission electron microscopy (IL-TEM) techniques, we found that catalyst particles substantially migrate and/or detach from the carbon support, and we speculate that this behavior is attributable to find that oxidative degradation of carbon under OER conditions. Nonetheless, under constant-current electrolysis conditions our Ni–Fe/oC catalyst remained stable for at least 100 hours, and catalyst particles that were retained on the sample over this period retained their core@shell structure and did not undergo drastic morphological changes.

The insights about the stability of Ni–Fe composites provided from this work are crucial for designing stable catalysts. Core@shell materials were not tested before for OER, and our work suggests that they are robust. The ability to generate OER active oxides coating conductive metallic cores containing the same transition metals is attractive because it helps facilitate electron conduction and provide a reservoir of fresh catalyst if the oxide shell dissolves. Overall, this work provides a foundation to continue pursuing core@shell Ni–Fe catalysts, but a shift away from carbon supports is likely warranted.

If additional work is undertaken to better understand the stability of carbon supports under OER conditions, future experiments are recommended to quantify the catalyst mass loss. Electrochemical quartz crystal microbalance (EQCM), possibly coupled with online mass spectrometry, would be useful for these studies. To determine the robustness of the core@shell Ni–Fe component of the catalyst, I recommend that future work focus on synthesis of unsupported catalysts or identification of a more stable support material. Notably, the synthesis approach of wet impregnation that we used requires catalyst support to nucleate the particles. To create unsupported Ni–Fe catalysts, sacrificial supports like Al or Si oxides (which can be dissolved with subequent alkali treatments) could be used. However, this approach is not ideal for practical implementation. Thus, a novel synthesis approach needs to be developed using a capping agent method or a precipitation reduction approach, similar to that used for the synthesis of Ni–Mo catalysts.

Some recommendations for stable catalyst supports incude carbon nanotubes, Ni nanoparticles, magneli phase Ti oxides (e.g., Ti_4O_7), fluorine-doped tin oxide (FTO) nanoparticles, and indium tin oxide (ITO) nanoparticles. However, there are some disadvantages of using these supports. Although carbon nanotubes are shown to be good as OER catalyst supports, they are costly and may still degrade over extended periods. By contrast, pure Ni nanoparticles are expected to be stable and cost effective, but our preliminary efforts to synthesis Ni–Fe on pure Ni nanoparticles were not successful. Magneli phases are expected lose their conductivity upon extended treatment in oxidizing environments, and FTO and ITO nanoparticles may also be unstable over long periods adn are costlier than the catalyst itself. Thus, identifying conductive and stable catalyst supports for the alkaline OER clearly remains a significant challenge.

We found identical location TEM analysis to be very useful for directly observing changes in the catalyst before and after stability studies. However, the tendency for Au to migrate into the sample makes long-term studies where catalyst samples are deposited and tested on Au TEM grids less attractive. Future work should focus on identifying alternative materials for TEM grid substrates as well.

7.0 Conclusions

We have shown over the last five years that Ni–Mo and Ni–Fe composites offer promising performance for the hydrogen evolution/oxidation and the oxygen evolution reactions respectively. The synthesis procedures we employed can be easily scaled up and can be executed under safe operating conditions. The observation of core@shell structure, especially in Ni–Mo alloys, was not explicitly known before and allowed us to overcome key limitations in the practical use of these catalysts. Moreover, multiple different catalysts synthesized over these five years, all demonstrated the core@shell architecture suggesting that this type of structure can be broadly useful for electrocatalysis.

Our work on Ni–Mo composites has allowed us to demonstrate practical HER activity within one order of magnitude of that of benchmark precious metal catalysts, and stability results to date remain quite promising. This is significant improvement from prior work and positions our Ni–Mo composites, along with Ni–Fe oxides, as promising candidates for next-generation water electrolysis technology. Successful demonstration of these catalysts at industrial scale will enable its commercialization in AAEM electrolyzers and reversible fuel cells.

Another significant accomplishment of our work is the reversibility of Ni–Mo alloys for hydrogen evolution/oxidation reactions. Such a flexibility was not demonstrated before and therefore stands out as a noteworthy contribution. This finding enables the consideration of Ni–Mo composites for use in unitized regenerative fuel cells that are being considered for space applications and long-term renewable energy storage.

Despite remarkable progress in the development of Ni–Mo and Ni–Fe catalysts, challenges of oxidative stability in Ni–Mo alloys and long-term stability in Ni–Fe alloys remain. For Ni–Mo alloys, addition of ternary transition metal or increasing the Mo content in Ni are some of the future directions recommended to improve their oxidative stability. In case of Ni–Fe alloys, it is essential to identify a new catalyst support or a synthetic route that will enable unsupported Ni–Fe while retaining the core@shell morphology.

I hope this dissertation is a valuable resource for further advancements in alkaline anion exchange membrane electrolyzers and fuel cells. I wish that the significant development of Ni-based catalysts obtained from this work will motivate researchers to continue pursuing these lines of research to enable cost-effective and carbon-neutral technologies. I am very excited to see the outcomes from this field in the coming years, and I look forward to living in a near-zero carbon emission society.

Appendix A Additional details for unsupported Pt nanoparticles

A.1 Synthesis of Pt nanoparticles

Figure A.1 shows schematic of synthesis procedure for Pt nanoparticles (NPs). The color of the reaction mixture was slightly yellow to colorless initially. After 15 minutes at 90°, the color changed to black but the reaction was allowed to proceed for 60 minutes to ensure completion. After 60 minutes, the reaction mixture was allowed to cool at room temperature and 1 M NaOH was added to it. The uncapped Pt NPs settled at the bottom of the vial in 1–2 weeks. Note that some dark coloration was also observed at the meniscus of the reaction mixture, which is consistent with our observation of non-unity particle yields. The uncapped particles were recovered by centrifugation and stored in de-ionized water. For TEM analysis, a small amount of this suspension was deposited on Cu/C TEM grids. A representative particle size distribution for uncapped Pt NPs is shown in figure A.2. The particle size data were normally distributed with narrow size distribution in the range from 2–4.5 nm.

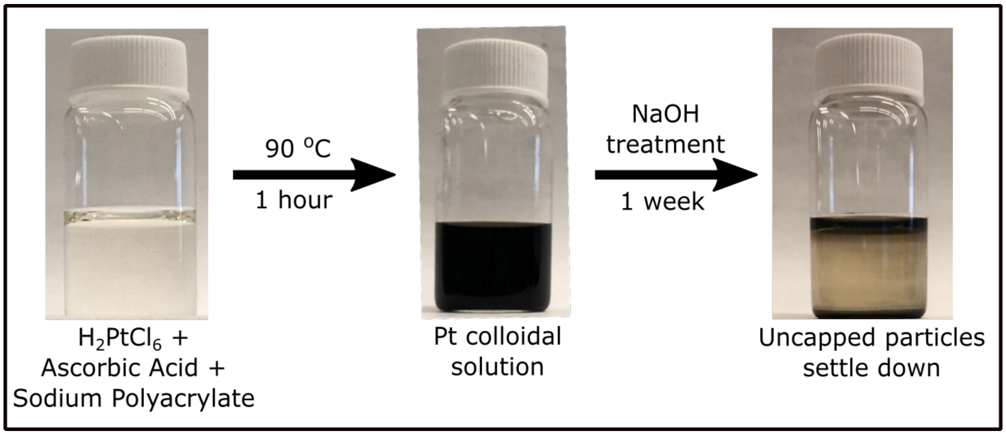

Figure A.1: Synthesis schematic of Pt NPs

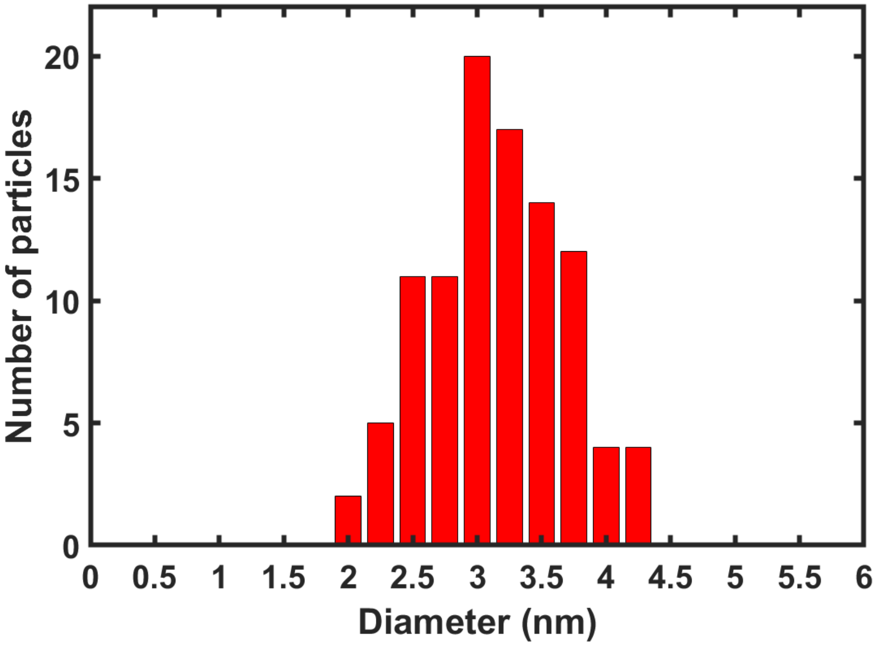

Figure A.2: Particle size distribution of uncapped Pt NPs

A.2 Cyclic voltammograms of capped and uncapped Pt NPs

Figure A.3 shows cyclic voltammetry (CV) data for capped and uncapped Pt NPs in 0.5 M H_2SO_4 and in 0.5 M KOH. Two full cycles, beginning and ending at 0.25 V vs RHE, are shown. To avoid the confounding influence of transient current flow upon initial polarization, the maintext treats the first full cycle beginning and ending at 1.5 V vs RHE as the “initial” state of the particle films. Capped Pt NPs exhibit very low current densities in the HUPD region compared to uncapped NPs, indicating that the exposed surface area of Pt in the capped particles is significantly lower than in uncapped Pt. The ECSA calculated for capped Pt is 1.67 ± 0.15 m^2/g in acid and 0.82 ± 0.35 m^2/g in base, which is only about 5–10% of that of uncapped Pt. Note also that the hydrogen desorption features in the positive-going sweep of the first cycle for uncapped NPs are similar to those in the second cycle, implying that the Pt NP surfaces are already relatively free of impurities.

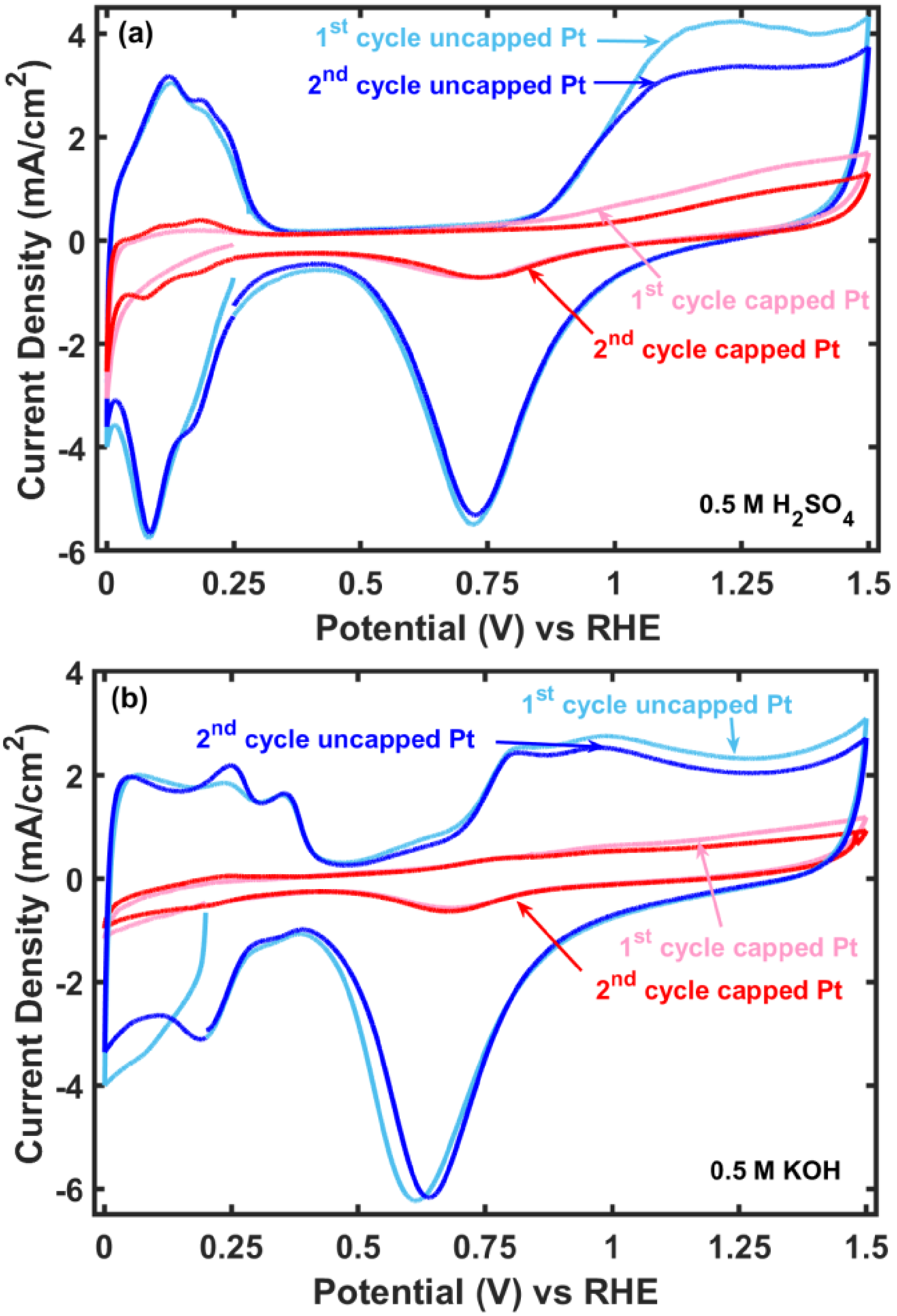

Figure A.3: Cyclic voltammograms of capped and uncapped Pt NPs depicting their first and second cycles.

Additional ECSA analysis

In alkaline solutions, we observed that the ECSA calculated from voltammetry sweeps to 1.5 V vs RHE was consistently smaller than those that swept less positive. We attribute this to a systematic deviation in the ECSA determination resulting from the fact that the oxygen desorption feature overlaps with the onset of hydrogen adsorption when the Pt electrode is swept sufficiently positive to generate a high coverage of Pt oxide (figure A.4). Specifically, this obscures the double layer capacitance in the range from 0.35–0.5 V vs RHE. Because the cathodic current flow in this region is treated as the background for ECSA calculation, this results in a systematic under-estimate of the charge associated with hydrogen adsorption.

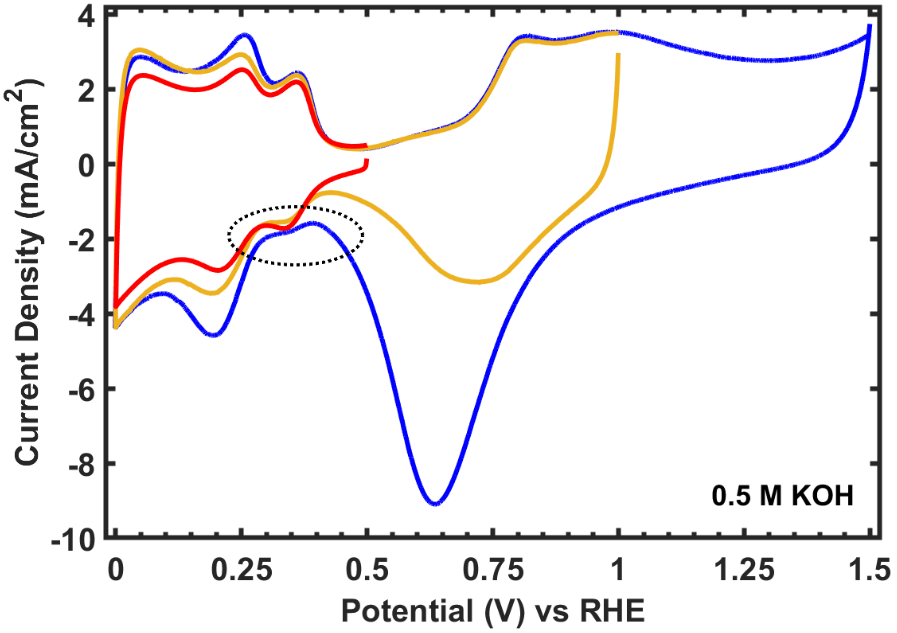

Figure A.4: Cyclic voltammograms of uncapped Pt NPs depicting second cycle at positive potential limits of 0.5 V, 1 V and 1.5 V vs RHE.

We monitored the ECSA decay as a function of positive potential limit over an extended set of 100 cycles, as shown in figure A.5. The decay rate was consistent with the observations in the main text (after considering the associated confidence intervals) up to the first 50 cycles. Scanning for 50 more cycles did not result in a drastic change in the ECSA, as it continued to decay monotonically.

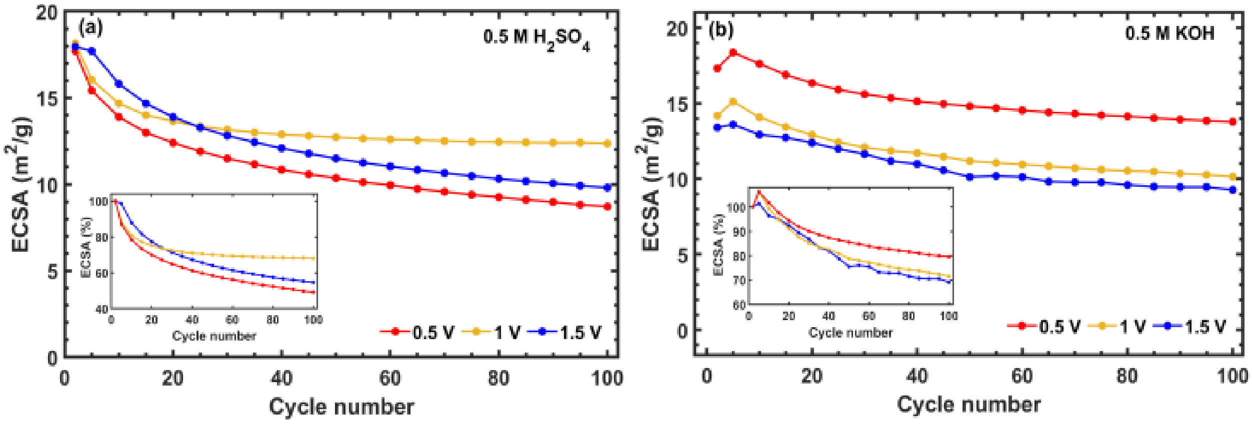

Figure A.5: ECSA variation of uncapped Pt NPs as a function of different positive potential limits for 100 cycles in (a) 0.5 M H_2SO_4 and in 0.5 M KOH under nitrogen purge.

Figure A.6 further shows ECSA analysis of uncapped Pt NPs when scanned at positive potential limits of 1.0, 1.25, and 1.5 V vs RHE in acid and base. These data were collected to attempt to observe the transition between deactivation through poisoning and particle growth mechanisms. Indeed, in acid conditions at 1.25 V vs RHE, the ECSA remains unchanged for at least 10 cycles and decays marginally slower than at 1.0 or 1.5 V when normalized to the initial value. This is evidence that cycling to 1.25 V provides a compromise involving slower particle growth than at 1.5 V at the expense of reduced oxidative cleaning effect. Indeed, we speculate that these effects are not mutually exclusive, as particle growth may result from transient dissolution resulting from Pt-oxide formation and reduction, and Pt–O intermediates are also likely to be involved in the oxidation of surface-bound impurities. In alkaline conditions, on the other hand, the relative rate of ECSA loss per cycle at 1.25 V was statistically indistinguishable (at a 95 % confidence interval) from those at 1 V or 1.5 V vs RHE, implying there exists no positive potential region in which the relative rate of deactivation per cycle can be diminished.

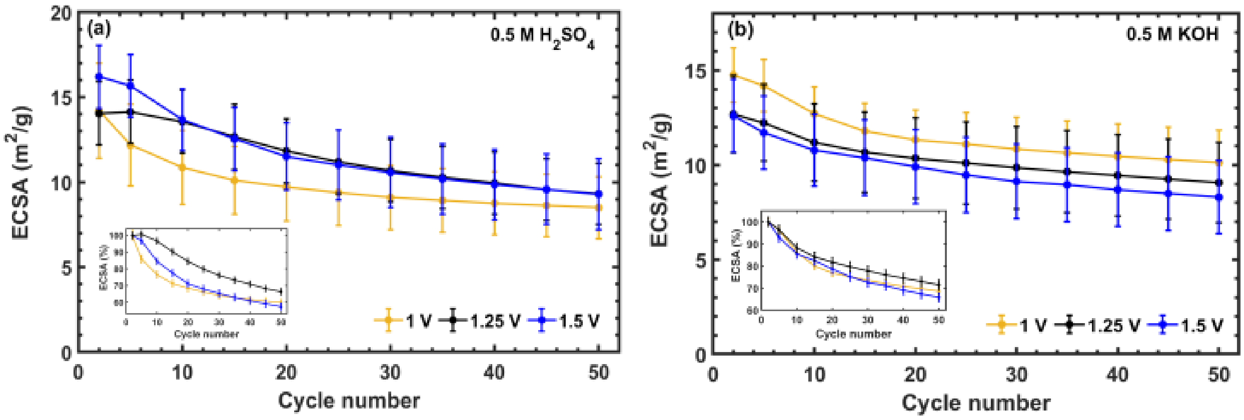

Figure A.6: ECSA variation of uncapped Pt NPs as a function of different positive potential limits for 50 cycles in (a) 0.5 M H_2SO_4 and in 0.5 M KOH under nitrogen purge.

ECSA and IL-TEM analysis on Au TEM grids: Scanning at fixed positive potential limits

Figure A.7 shows representative ECSA versus cycle number data for Pt NPs deposited on Au TEM grids in acid and base. ECSA values are reported as surface area (cm^2) rather than mass-specific surface area (m^2/g) because the experimental conditions (dropcasting small quantities of dilute NP suspensions onto porous grids, followed by drying and a brief immersion in pure water to remove poorly adhered particles) made it difficult to obtain consistent mass loadings. Nontheless, the relative rate of ECSA loss data agree well with those shown in the main text, except the final data point in Figure A.7b at 0.5 V, where ECSA decreased precipitously. We attribute this result to particle detachment, which occurred infrequently but more often in alkaline electrolyte than in acid.

IL-TEM analysis on uncapped Pt NPs in alkaline solution at different positive potential limits is shown in Figure A.8. At 0.5 V vs RHE and at 1 V vs RHE, the TEM images do not show significant changes in the particle film morphology or particle size. We therefore attribute the degradation mechanism to poisoning. An increase in particle size by approximately 30 % was observed at 1.5 V vs RHE, as discussed in the main text.

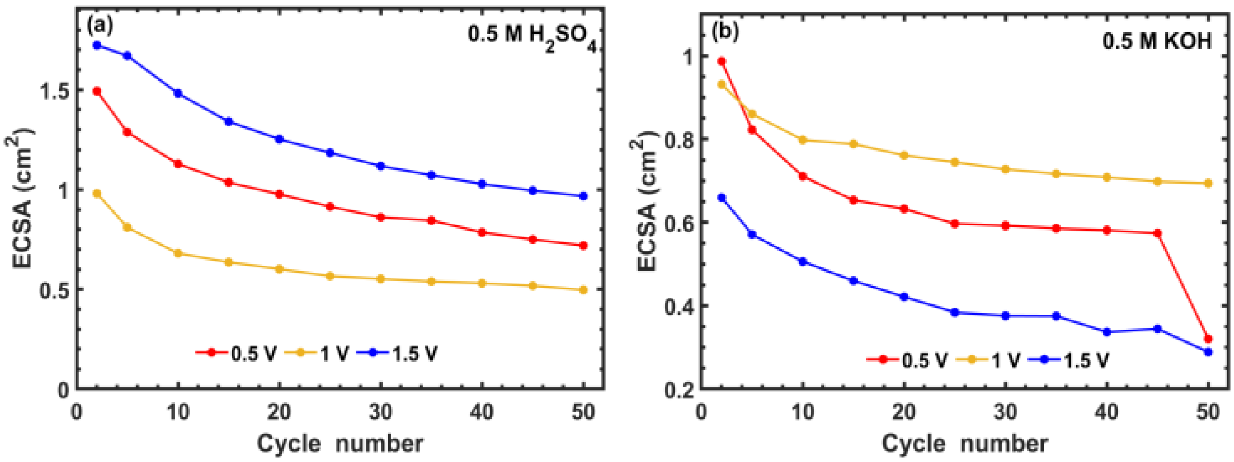

Figure A.7: ECSA variation of Pt NPs when deposited on Au TEM grid and scanned between 0 V vs RHE and the noted positive potential limits in (a) 0.5 M H_2SO_4 and (b) 0.5 M KOH under nitrogen purge.

ECSA and IL-TEM analysis on Au TEM grids: Serial change in positive potential limit

We further performed ECSA and IL-TEM analysis on Pt NPs after they were scanned at progressively more positive potential limits in acid. The ECSA analysis is shown in Figure A.9a and the corresponding IL-TEM data are compiled in Figure A.10. These data showed that cycling to 1 V vs RHE after cycling at 0.5 V vs RHE led to a modest increase in the ECSA in the initial cycles suggesting partial removal of the poison without a significant increase in particle size, which is consistent with the IL-TEM data. The ECSA then diminished again at a reduced rate and the IL-TEM data show a modest increase in the average particle size. The complete removal of the poison is possible at 1.5 v vs RHE where the ECSA recovered to near its initial value, after which ECSA diminished again rapidly and the particles coarsened to almost double their initial size.

A similar analysis was also performed in 0.5 M KOH (Figures A.9b and A.11), where progressively increasing the positive potential limit had a modest initial positive impact on ECSA, but the particles ultimately grew by ∼30 % of their initial diameter.

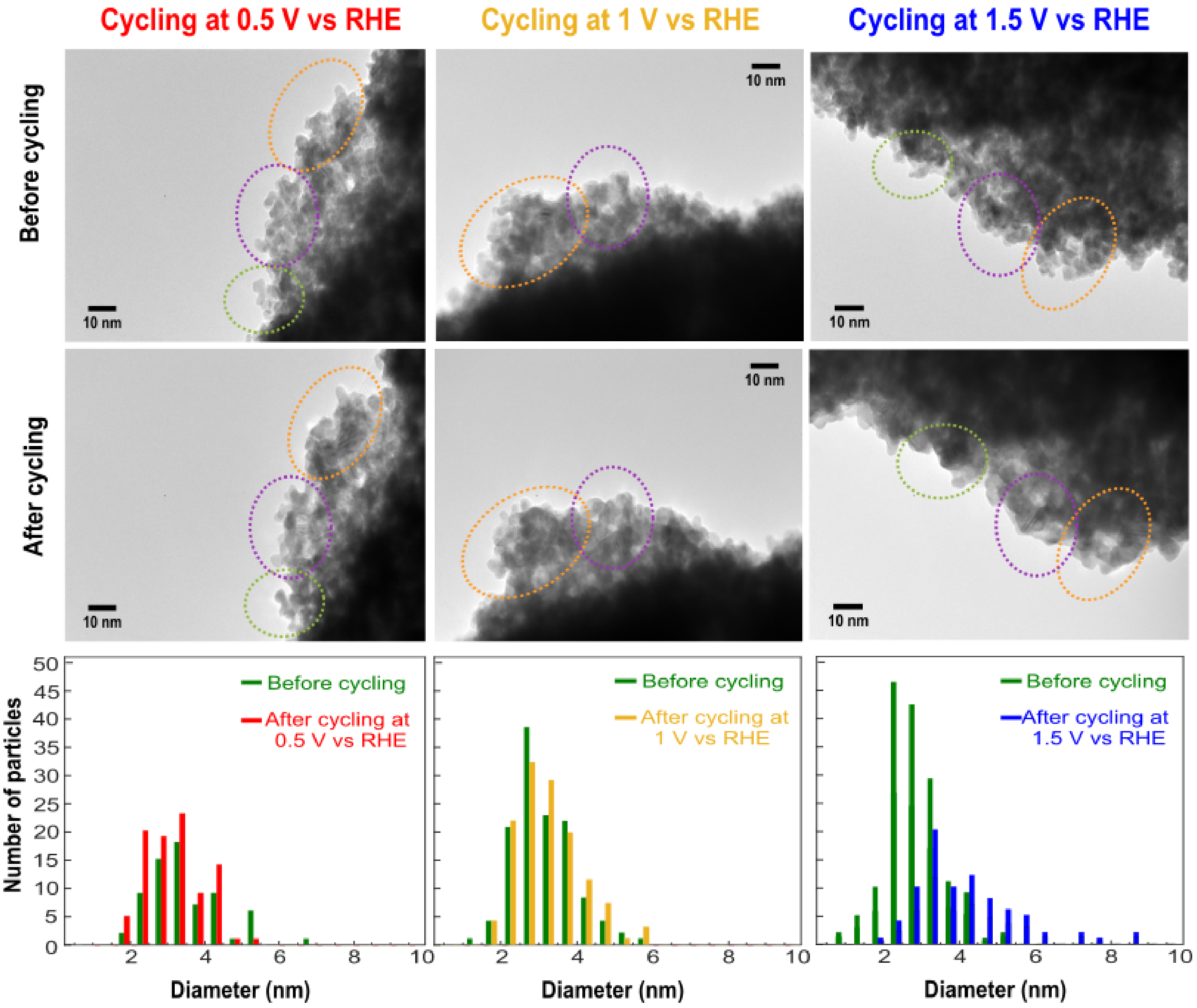

Figure A.8: Identical location TEM images and particle size analysis of Pt NPs before cycling and after cycling between 0 V vs RHE and the noted positive potential limits in 0.5 M KOH.

A.3 Concentration overpotential curve simulation details

The concentration overpotential curve shown in the maintext was simulated using the MATLAB software suite, taking as numerical inputs the electrode rotation rate, concentration, and diffusion coefficients of protons and hydrogen gas in water.[185, 125] The following equation was used for

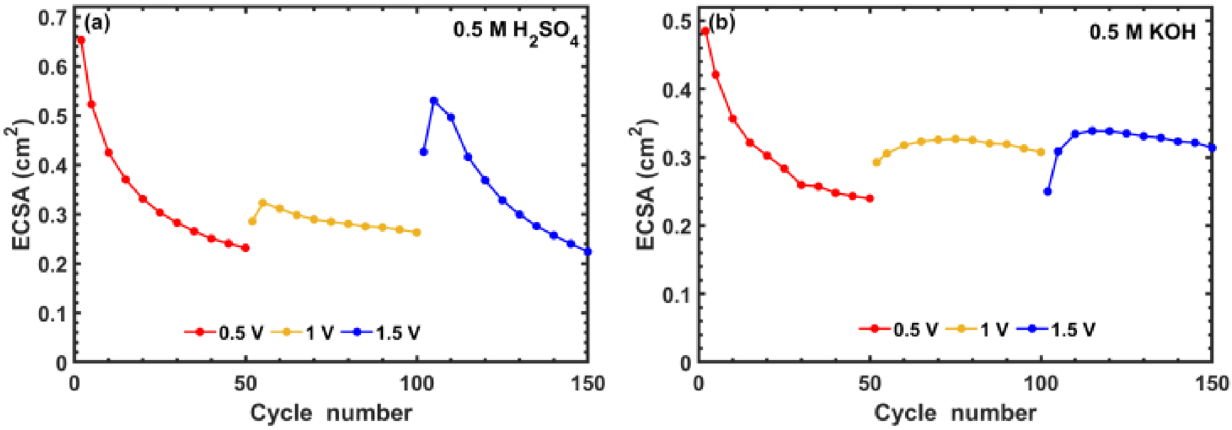

Figure A.9: ECSA variation when Pt NPs were deposited on Au TEM grids and scanned progressively between 0 V vs RHE and a series of positive potential limits increasing from 0.5 V to 1.0 V to 1.5 V vs RHE in (a) 0.5 M H_2SO_4 and (b) 0.5 M KOH under nitrogen purge.

the simulation:

$$\eta_{conc} = \frac{RT}{nF}\left[ln\left(\frac{J_{l,a}}{-J_{l,c}}\right) - ln\left(\frac{J_{l,a}-J}{J-J_{l,c}}\right)\right] \tag{A.1}$$

where R is the universal gas constant (8.314 J/mol.K); T is the Temperature (298 K); n is the number of electrons transferred (2); F is Faraday's constant (96485 C/mol). J values are current densities, where the subscript l stands for limiting, a represents anodic and c denotes cathodic. The limiting current density for anodic and cathodic sides was calculated using the following relation:

$$J_l = 0.62nFC_{bulk}D^{2/3}\omega^{1/2}\nu^{-1/6} \tag{A.2}$$

where C_{bulk} is the bulk concentration of the reactant species; D is the diffusion coefficient of protons (for HER in acid), water (for HER in base), or dissolved hydrogen (for HOR); ω is the rotation rate in rad/s; and ν denotes the kinematic viscosity of water.

Matlab code

%Mass transfer calculation

Dc = $7.62 * 10^{-5}$; % cm^2/s diffusion coefficient of ions in water: protons=7.62e-5; water for alkaline = 2.57e-5cm^2/s

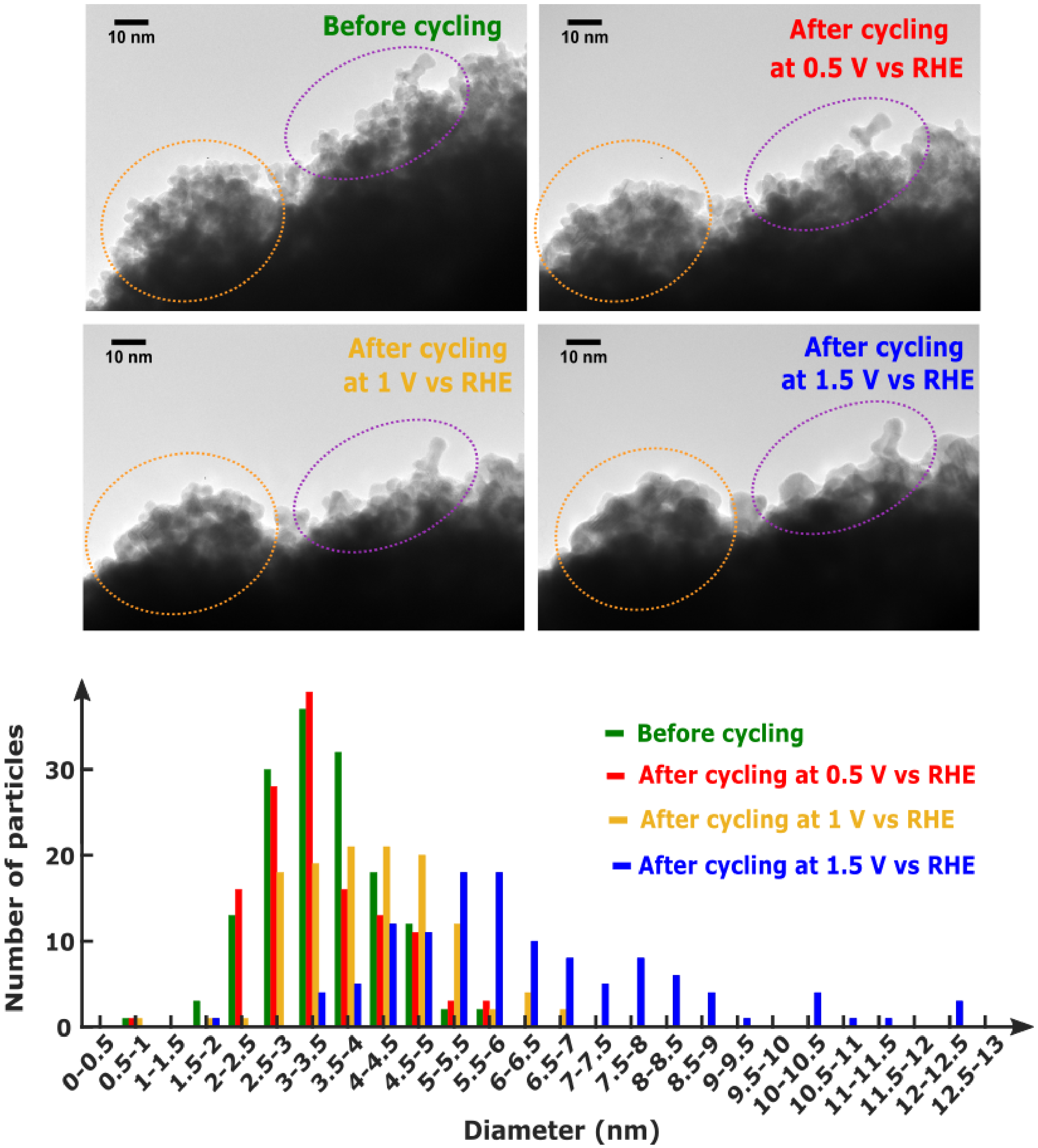

Figure A.10: Identical location TEM images and particle size analysis of Pt NPs before cycling and after cycling to the noted positive potential limits in 0.5 M H_2SO_4.

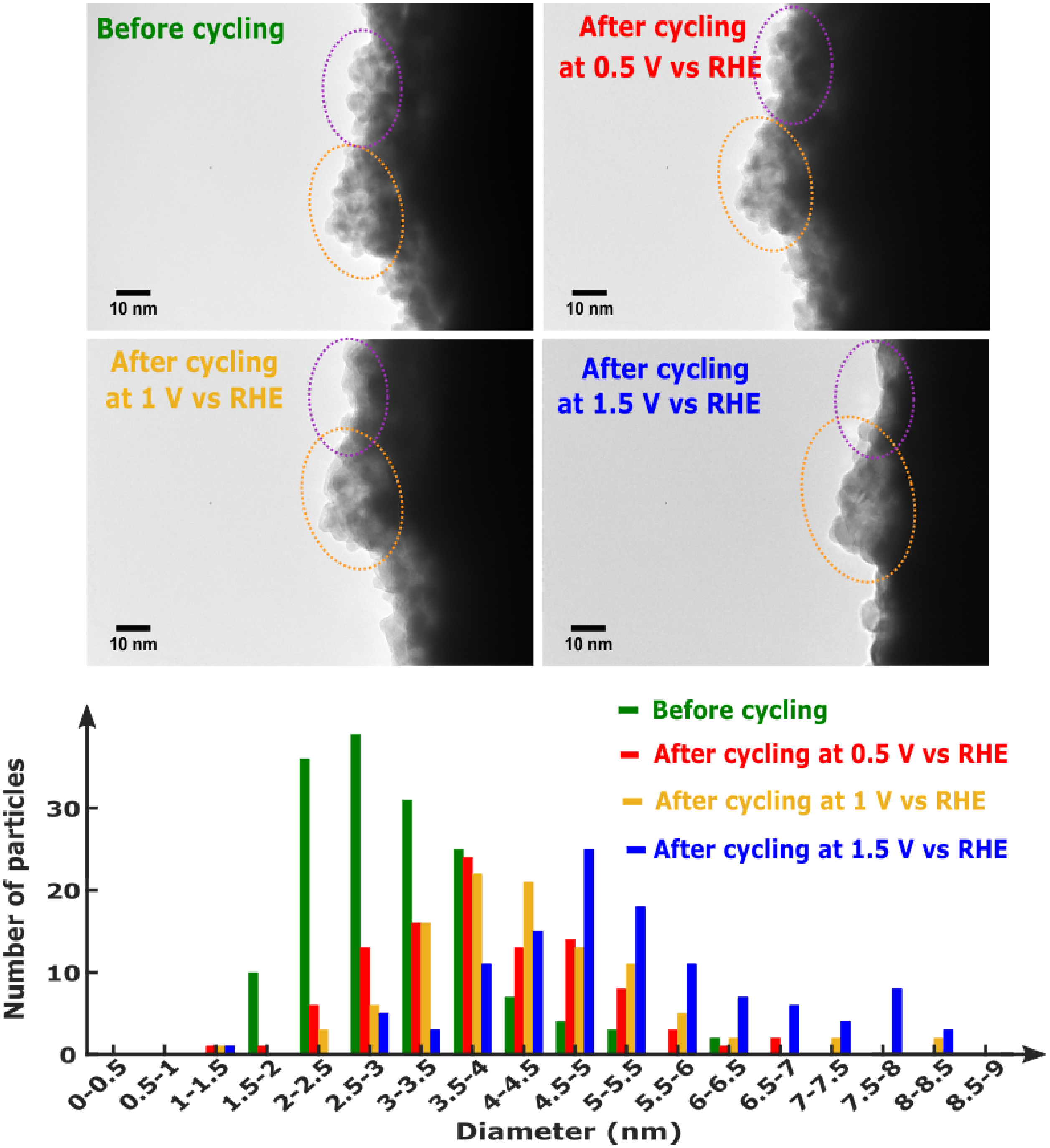

Figure A.11: Identical location TEM images and particle size analysis of Pt NPs before cycling and after cycling to the noted positive potential limits in 0.5 M KOH.

```
Da = 3 * 10^-5; %cm2/s diffusion coefficient of hydrogen gas in water
v = 0.8927*10^-2; %cm2/s kinematic viscosity of water
rpm = 1600/60; %rps
w = 2*pi*rpm; %rad/s
moc = 0.62 * Dc^(2/3) * w^(1/2) * v^( - 1/6); %cm/s
moa = 0.62 * Da^(2/3) * w^(1/2) * v^( - 1/6); %cm/s
% Limiting current calculation
n = 2;
F = 96485; %C/mol
R = 8.314; %J/mol.K
T = 298; %K
A = 0.196; %cm^2 (electrode area)
Cobulk = 0.5; %M or mol/l, concentration of protons/electrolyte concentration in acid; concentration of water in base
ilc = n*F*moc*A*Cobulk/1000; %A
jlc = ilc*1000/A; % mA/cm2
Crbulk = 0.0008; % M, concentration of H2 gas in electrolyte
ila = n*F*moa*A*Crbulk/1000; %A
jla = ila*1000/A; % mA/cm^2
j = [-60:0.01:2.6]'; %mA/cm^2
overpotential = (R*T/(n*F))*(log(jla/-jlc)-log((jla-j)/(j-jlc)));
figure
plot(overpotential,j,'r')
```

Appendix B Supporting information for Ni–Mo composition and carbon incorporation

B.1 Experimental methods

Materials and Reagents

All reagents were purchased from commercial suppliers and used as received, unless otherwise noted. Nickel(II) nitrate hexahydrate (98%), nickel(II) chloride hexahydrate (99.3%), sodium molybdate dihydrate (99.5%) and diethylene glycol (99%) were purchased from Alfa Aesar. ACROS Organics supplied ammonium molybdate tetrahydrate (ACS reagent grade). Ammonium hydroxide (28-30 w/w%, ACS reagent grade), isopropyl alocohol (99.5%), and methanol (99.5%) were purchased from Fisher Scientific. 99.5% ethanol was purchased from Decon Laboratories. Carbon black (Vulcan XC-72) was obtained from Fuel Cell Earth. Carbon-supported Pt (10 wt% Pt) was supplied by Alfa Aesar. Sigma Aldrich supplied potassium hydroxide (ACS reagent grade). Nafion ionomer solution (20 wt% dispersed in water/alcohol mixture) was supplied by Ion Power. Ni foil (0.005 in thick, $\geq$99%) and Ti foil (0.005 in thick, 99%) were supplied by Alfa Aesar. Forming gas (5% H_2 and 95% N_2) and ultrapure H_2 (99.999%) were purchased from Matheson. Deionized water was purified to $\geq$18.2 Mohm-cm resistivity and $\leq$3 ppb total organic content using a Millipore Advantage A10 system.

Ammonia-based Ni–Mo oxide precipitation

The synthetic procedure for the ammonia-based Ni–Mo was adopted from prior report by McKone et al.[60]. A representative procedure is described here. A Corning PC-420D hotplate was preheated to 400 °C for 30 minutes. 1.5 g (5.2 mmol) of nickel nitrate hexahydrate and 0.6 g (3.4 mmol) of ammonium molybdate tetrahydrate were dissolved in a mixture of 5 ml deionized water and 2 ml ammonium hydroxide in a 100 mL beaker to give a deeply blue solution. 45 ml diethylene glycol was then added to this solution. The solution was then placed on the preheated hotplate and stirred using a PTFE-coated stirbar (Fisher Scientific) at 500 rpm. An alcohol thermometer was used to monitor the temperature. The mixture was heated until the temperature reached 110 °C, which we found to require 5–7 minutes. Upon heating, a green precipitate formed; part of this precipitate remained suspended in the parent solution and part became entrained on the bottom and sidewalls of the beaker and stir bar. After reaching the target temperature, the beaker was removed from the hotplate and allowed to cool slightly. The still-warm reaction mixture was then transferred to a 50 mL polyethylene centrifugation vial and centrifuged (Thermo Scientific Sorvall ST 8) at 3000 rpm for 10 minutes. A pale blue supernatant remained and was decanted, followed by repeated washing and centrifugation steps using pure water until the supernatant became colorless. A final rinse and centrifugation step was carried out using acetone instead of water, and then the final precipitate was collected by suspending in a minimum of methanol and dried in a drying oven (Fisher Scientific Isotemp) at 60 °C for several hours. The final yield of green powder ranged from 17–21% relative to the total mass of precursors.

Carbon incorporation and electrode deposition

For Ni–Mo/C composites, Vulcan carbon black was physically mixed with either of the oxides (ammonia-based and ammonia-free) prior to thermal reduction, and the procedure was identical in each case. First, carbon was added to the Ni–Mo oxide in the desired ratio, which was determined empirically based on the observed mass loss of the neat oxide upon thermal reduction. To this mixture was added a small amount of isopropyl alcohol to produce a paste, which was ground for 10–15 minutes using a ceramic mortar and pestle (Fisher Scientific) and allowed to dry. This paste grinding process was repeated 3 times to yield a homogeneous black powder.

A Thermo-Scientific Mini Mite tube furnace was used to reduce the oxides. Carbon incorporated Ni–Mo oxides were first weighed on a microbalance (Sartorius). The oxides were then transferred to a crucible, and thermally reduced in a tube furnace under a flow of forming gas (5% H_2 and 95% N_2) at a rate of 15 sccm. The furnace temperature was first increased to 200 °C and held for 30 minutes, followed by increasing to 550 °C for 1 hour. The forming gas flow was discontinued and the furnace was allowed to cool naturally to room temperature. The product (still a black powder) was then removed and weighed again.

For electrode deposition, 20 mg of the Ni–Mo/C catalyst composite was mixed with 1 ml isopropyl alcohol and 20 mg of 20 wt% Nafion (in isopropyl alcohol-water solution) to make a $\sim$20 mg/ml Ni–Mo/C colloidal ink. Different Ni–Mo/C loadings of 1 mg/ml, 2 mg/ml, 5 mg/ml and 10 mg/ml were prepared by respectively varying the Ni–Mo/C and Nafion content in 1 ml isopropyl alcohol. The solution was homogenized in an ultrasonic bath (Branson M1800) for 30 minutes. Upon homogenization, a 5 μL volume of the catalyst suspension was dropcast onto a fully assembled glassy carbon rotating-disk electrode assembly (Pine ChangeDisk) and allowed to dry for 10 minutes under an infrared heat lamp (McMcaster Carr). A second 5 μL quantity of ink was then dropcast and allowed to dry in the same way.

We found that 20 wt% of Nafion ionomer relative to dry Ni–Mo/C mass was sufficient to give adherent catalyst films at loadings ranging from 0.05 mg/cm^2 to 1 mg/cm^2, whereas films with higher loadings sometimes exhibited observable loss of catalyst. We also found that the catalyst films were initially difficult to wet with water, presumably due to the highly fluorinated backbone of the Nafion binder. This issue was resolved by first dipping the electrode in neat ethanol, which rapidly wet the catalyst film. The electrode was then transferred to a vial containing 0.1 M aqueous KOH solution to exchange out the ethanol prior to introduction into the electrochemical cell.

Ni nanoparticle synthesis

Ni nanoparticles were synthesized by an analogous precipitation-reduction method involving Ni hydroxide formation followed by its reduction. A typical procedure for Ni hydroxide synthesis is as follows. First, 50 mL of 2M KOH(aq) was placed in a beaker and stirred. Then a solution of 1.5g nickel nitrate hexahydrate in 5 mL water was added to the KOH solution all at once. An instantaneous precipitation of green solid was observed. The product was purified by sequential water washes with centrifugation and finally suspended in methanol and dried at 60 °C for several hours. The dried hydroxides were weighed on a microbalance, transferred to a glass crucible, and reduced in a tube furnace under forming gas at 200°C for 30 minutes followed by 450°C for 1 hour. The electrode deposition procedure of Ni–Mo/C composites was then replicated for Ni nanoparticles.

High-loading catalyst deposition on Ni mesh

Ni–Mo/C loadings of greater than 1 mg/cm^2 were obtained by changing the substrate of deposition from glassy carbon to Ni mesh. Similar to pyrolysis-derived Ni–Mo synthesis, Ni mesh films of

6x6 mm were cut and weighed on an ultramicrobalance. A 40 mg/ml viscous solution of Ni–Mo/C containing 40 mg Ni–Mo/C, 40 mg of 20 wt% Nafion (in alcohol-water solution) and 1 ml isopropyl alcohol was prepared for deposition. The oven was preheated at 125 °C along with a glass petri dish. Ni mesh films were dipped in the viscous solution and placed in the preheated oven for 10 minutes. The deposition and drying process was repeated 2-3 times and the films were again weighed on an ultramicrobalance. Flag-type electrodes, similar to those made with pyrolysis-derived Ni–Mo catalyst were made with Ni–Mo/C on Ni mesh films.

Co-precipitated Ni–Mo/C composite synthesis

Co-precipitated Ni–Mo/C composites were synthesized by precipitating ammonia-based Ni–Mo oxides in the presence of carbon. 1.8 g Vulcan carbon was mixed with 1.5 g nickel nitrate and 0.6 g ammonium molybdate (targeting 90:10 ratio of carbon to Ni–Mo alloy). 5 mL water, 2 mL ammonium hydroxide and 45 mL diethylene glycol were then added to this mixture and sonicated. The precipitation-reduction reaction was carried out at 110°C and was treated in the same way as the ammonia-based Ni–Mo oxide, resulting in a black powder containing Ni–Mo oxide and carbon. The final catalyst was obtained by reducing the oxide-carbon mixture at 200 °C for 30 minutes and 450 °C for 1 hour. For coprecipitated Ni–Mo/C, carbon was added to the precursors by assuming the precipitation yield to remain the same as in the ammonia-based Ni–Mo synthesis without carbon incorporation. The exact carbon content was later found by TGA to be somewhat lower than expected. For example, 80 wt% carbon was obtained when 90 wt% was targeted, implying more complete Ni-Mo oxide precipitation occurred when carbon black was added to the reaction. The carbon contents were therefore reported as the actual values determined by TGA.

Analytical Methods

X-ray diffraction (XRD) measurements were made using a Bruker D8 system with Cu Kα radiation (λ=1.54 Å). Measurements were collected over the 2θ angle from 10 to 90° in 0.02° steps. Total data collection times were varied so as to produce XRD patterns with adequate signal-to-noise ratios for the associated analysis.

Scanning electron microscopy (SEM) analysis made use of a Zeiss Sigma 500 VP microscope. Micrographs were collected of nanopowder films drop-cast onto Ti foils using secondary electron or backscattor detectors. The accelerating voltage used for SEM was varied from 1 keV to 10 keV to maximize image contrast and minimize sample charging. SEM images were subjected to a minimum of post-processing that was limited to brightness/contrast adjustments in order to produce a similar dynamic range in all images.

Transmission electron microscopy (TEM) analysis was performed using a JEOL JEM-2100F TEM/STEM (equipped with an Oxford X-Max^N 80T energy-dispersive X-ray spectrometer) and a Hitachi H-9500 environmental TEM. High-resolution TEM (HRTEM) and selected area electron diffraction (SAED) were performed on the H-9500 and the JEM-2100F. High-angle annular dark-field scanning TEM (HAADF-STEM) and STEM energy-dispersive x-ray spectroscopy (EDS) were performed on the JEM-2100F. Specimens for TEM examination were prepared by drop-casting nanopowder samples diluted in isopropanol onto 400 mesh ultrathin carbon-coated Cu TEM grids (Ted Pella Inc.). Both instruments were predominately operated at an accelerating voltage of 200 kV for these studies, though some of the H-9500 imaging was performed at 300 kV. For STEM-EDS mapping, a spot size of 1.5 nm and pixel dwell time of 5 μs was used, with total mapping durations of 8.5 minutes per area. No appreciable changes in the specimens were observed during TEM analysis, even during the extended EDS mapping, indicating that beam-damage did not result in sample modifications under these conditions. The observed morphologies were consistent across all microscopes and imaging modes.

X-ray photoelectron spectroscopy (XPS) was performed using a Thermo Scientific ESCALAB 250Xi instrument. An initial survey scan was used to to identify the major constituents of the sample. Subsequent high-resolution scans were completed of the Ni 2p region in the range of 845–880 eV and the Mo 3d region in the 225–240 eV range. To execute peak deconvolution of the high resolution data, the data were fit to the peaks and binding energy values listed in Table 1.[305, 306].

Thermogravimetric analysis (TGA) was carried out using a SDTQ600 thermogravimetric analyzer supplied by TA instruments. Argon gas was flowing continuously throughout the experiment at a rate of 100 sccm. Samples were loaded into an alumina pan, introduced into the sample chamber, and equilibrated under 20 sccm of N_2 gas flow. Temperatures were then varied as a function of time

Compound type	Binding energy (eV)
Ni $2p_{3/2}$	852.60
$Ni(OH)_2$ $2p_{3/2}$	856.30
NiO $2p_{3/2}$	857.70
Ni^{+2} satellite $2p_{3/2}$	864
Ni^{+2} $2p_{1/2}$	874.26
Mo $3d_{5/2}$	228.00
Mo^{+4} $3d_{5/2}$	229.20
Mo^{+5} $3d_{5/2}$	231
Mo^{+6} $3d_{3/2}$	235.6

Table 1: Peak positions used to fit high-resolution XPS data

under either oxidizing (20 sccm air) or reducing (10 sccm H_2) conditions. All gases were supplied by Matheson in their ultra-pure grade.

Electrochemical measurements were carried out primarily using rotating disk electrode (RDE) voltammetry of catalyst films deposited onto glassy carbon substrates. Electrochemical data were collected using a digital potentiostat/galvanostat (Gamry Reference 600+) while rotating the working electrode using a commercial rotor (Pine MSR). We used a single-chamber glass electrochemical cell with a large-area (several cm^2) Ni foil counter electrode and a Ag/AgCl (Thermo Scientific) reference electrode. The electrolyte was 0.1 M KOH(aq) and was freshly prepared prior to each measurement. The cell was purged with hydrogen gas for at least 2-3 minutes prior to beginning measurements to maintain constant hydrogen partial pressure. The Ag/AgCl reference electrode was calibrated to the reversible hydrogen electrode (RHE) potential using commercial Pt/C composite deposited onto glassy carbon in the same way as for Ni–Mo composites. To minimize the possibility of contamination, measurements of Pt-containing films were always carried out after experimentation with nonprecious catalysts was complete. Cyclic voltammograms were collected over a range of overpotentials bracketing the equilibrium potential for the hydrogen evolution reaction at a scan rate of 10 mV/s. Solution resistance was measured via electrochemical impedance spectroscopy using a high-frequency AC waveform superimposed on a DC bias of 0 V vs. RHE. These measurements generally fell in the range from 30 to 50 Ω and were compensated by subtracting the iR drop from the observed current versus overpotential data after experiments were complete. Electrochemical impedance spectroscopy was similarly measured over the frequency range from 0.2–100 KHz using a 10 mV AC perturbation at 150 mV overpotential.

B.2 Catalyst and electrochemical characterization

Evidence of Oxides in Ammonia-based Ni–Mo

Figure B.1 shows a magnified view of the ammonia-based Ni–Mo nanopowder XRD results from Figure 1 in the main text. Broad diffraction features were observed at $2\theta = 25$, 38, and 63 suggesting the presence of NiO and MoO_2.

Carbon black quantity and activity

The mass loss of the Ni–Mo oxides on reduction and the carbon content of Ni–Mo/C composites was obtained by thermogravimetric analysis (TGA). The oxide mass loss was found to be $\sim$40% for the ammonia-based synthesis (Figure B.2a) and 30% for the ammonia-free synthesis (Figure B.2b). The carbon content of Ni–Mo/C samples was obtained by TGA in sequential oxidation and reduction steps. Representative data for 75 wt% carbon is shown in figure B.2c. First the temperature was ramped to 700 °C in the presence of air to burn off the carbon component and oxidize the Ni–Mo component back to a mixed oxide. The purge gas was then changed to pure hydrogen and the temperature ramped to 950 °C for 1 hour to re-reduce Ni and Mo to the metals. An initial 17.1 mg mass of the composite reduced to 6.5 mg upon oxidation, and decreased further to give a final mass of 4.75 mg on reduction. Thus the carbon content calculated from the difference between the initial and final mass of the powder was 72.2%, in good agreement with the 75 wt% target.

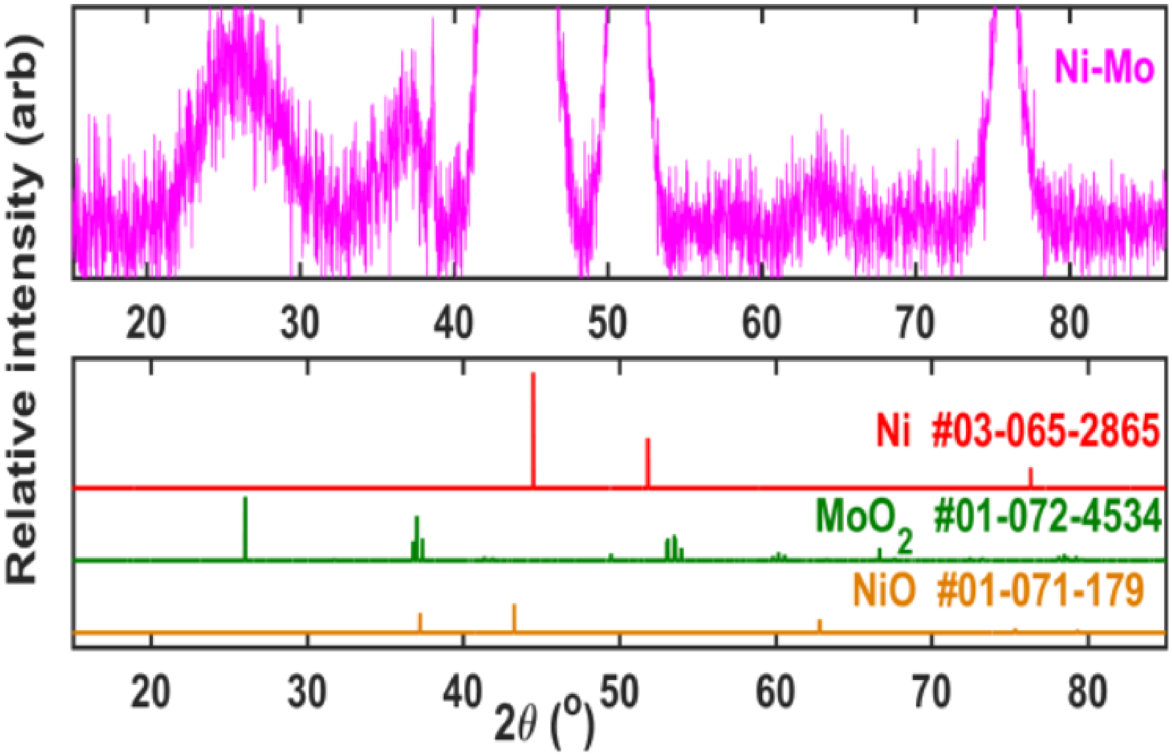

Figure B.1: Ammonia based Ni–Mo XRD image magnified to show low-intensity peaks consistent with MoO_2 and NiO.

A geometric HER activity comparison of pure vulcan carbon with Ni–Mo/C is shown in figure B.3. The samples were prepared and deposited in the same way using 1 mg/cm^2 mass loadings of each on a glassy carbon working electrode. The data show that pure vulcan carbon has negligible activity for hydrogen evolution in 0.1 M KOH electrolyte at overpotentials at least as large as 300 mV.

Tafel representation of activity data

Fig B.4 depicts representative polarization data for ammonia-based Ni–Mo/C samples as a Tafel plot. All of the films exhibited nonlinear behavior at modest overpotentials, which is consistent with

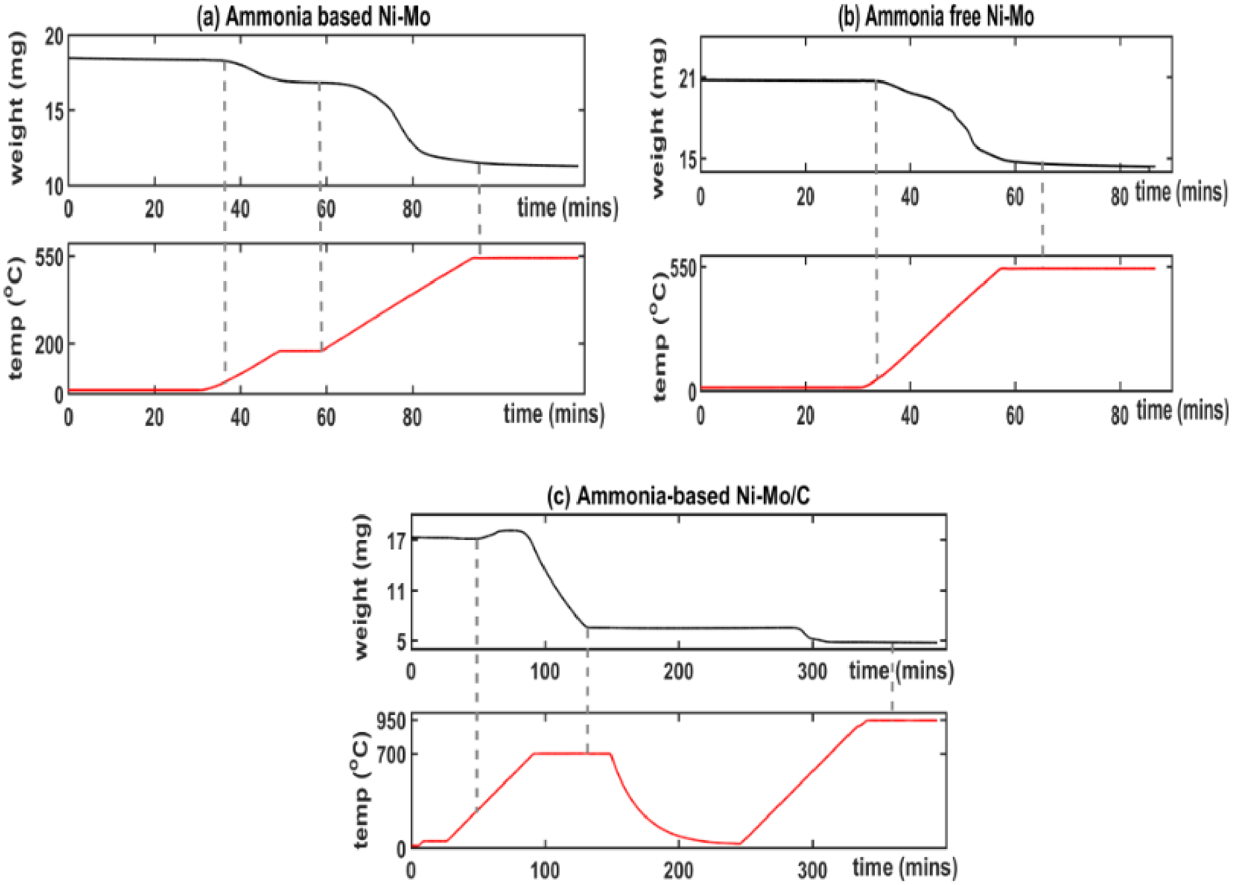

Figure B.2: Thermogravimetric analysis to determine mass loss on reduction of Ni–Mo oxide of (a) ammonia-based Ni–Mo and (b) ammonia-free Ni–Mo. (c) Thermogravimetric analysis to determine carbon content in Ni–Mo/C by an oxidation-reduction process.

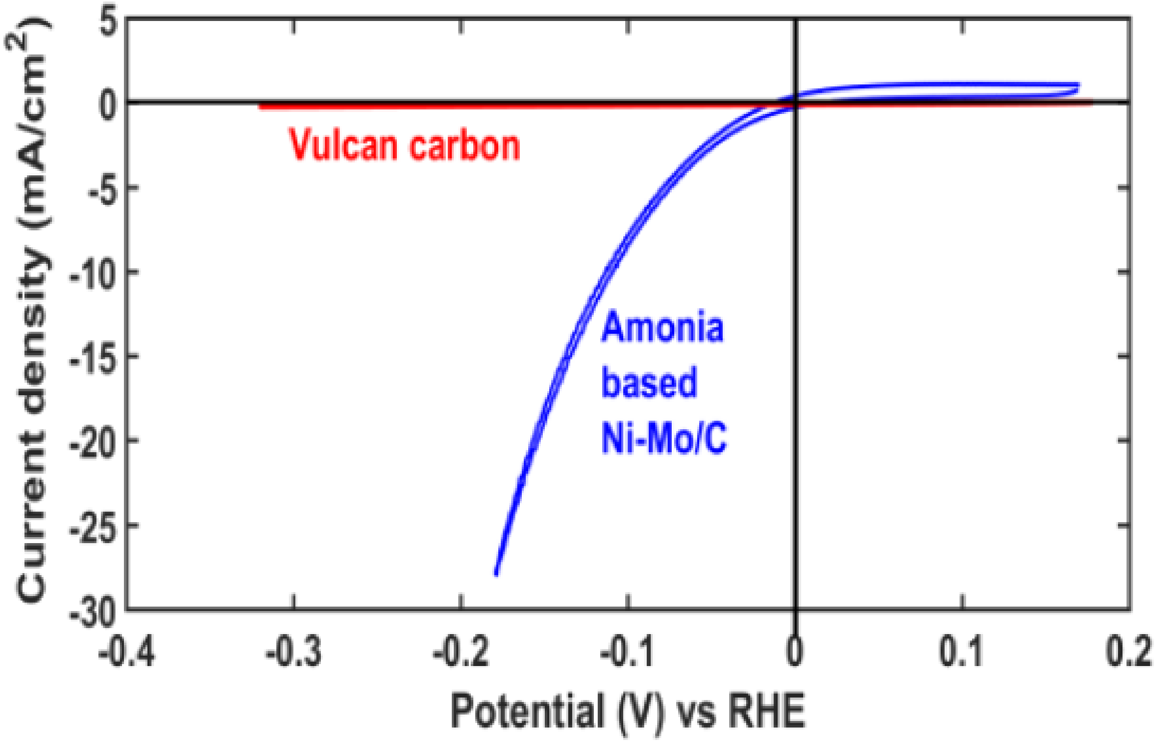

Figure B.3: Geometric activity of Vulcan carbon compared with ammonia based Ni–Mo/C.

the fact that oxidation processes compete with net hydrogen evolution near the equilibrium potential for the HER. The data at overpotentials larger than 100 mV exhibited mutually similar Tafel slopes that were all in excess of 100 mV/decade. These values are too large to attribute solely to kinetic limitations associated with the known mechanistic pathways for the HER,[307] but they may be consistent with a mixed kinetic-transport limitation.

B.3 Catalyst simulation details

As noted in the main text, we used Matlab to numerically solve maintext Equation 1 iteratively for a string of 100 oxide-coated catalyst particles comprised of a 6 nm catalyst core coated with a conformal 2 nm resistive shell. The following HER kinetic parameters corresponding to bulk

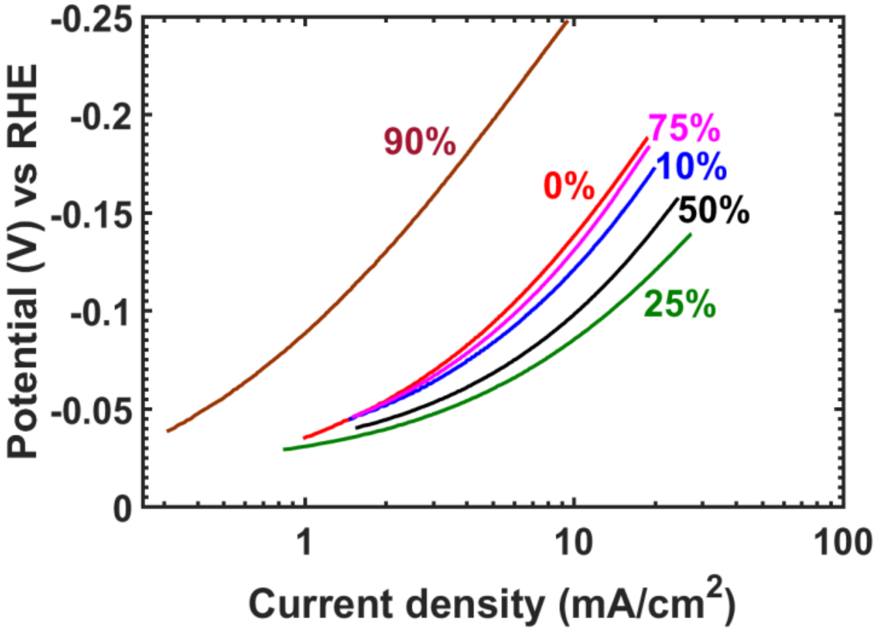

Figure B.4: Tafel plot of ammonia-based Ni–Mo/C containing the noted carbon loadings.

Ni were used in the mathematical model: exchange current density (j_o) of 10^{-6} A/cm^2 and tafel slope (b) of 120 mV/decade.[256] Kinetic constributions to overpotential were calculated based the assumption that the entire surface area of the 6 nm core was equally active, and electrolyte transport losses were not considered. The resistive interface was accounted for by calculating a value of inter-particle resistance assuming that electrons would travel between particles through a cylindrical layer of oxide 2 nm thick, 6 nm in diameter, and with a bulk resistivity that was varied between 10^5 and 10^{10} Ω-cm. The mass specific activity for each particle was then calculated as a function of overpotential. Ensemble mass activity was further calculated by summing the individual particle current contributions at each overpotential and dividing by total catalyst mass. In this case, because each catalyst particle was identical in mass, this operation was mathematically equivalent to averaging the mass activity of all the particles at each overpotential.

Matlab code %Numerical solver to calculate current vs overpotential data for a catalyst

%that accounts for kinetics via the Tafel equation and series resistance via ohms law

```
%NOTE: should be able to revise this script to calculate three different
%overpotential contributions separately - kinetic + particle resistance + electrolyte resistance (via ASR)
j0 = 1e-6; %exchange current density in A/cm^2
b = 0.12; %Tafel slope in V/decade
dia = 6e-7; %particle diameter in cm
density = 9; %mass density of catalyst in g/cm^3
pVolume = 4/3 * pi * (dia/2)^3; %volume of single particle in cm^3
pMass = pVolume * density; %mass of each particle in grams
chainlength = 5; %length of particle chain in number of particles
resistivity = 1e10; %resistivity value for resisitive interface layer in ohm-cm
layerThickness = 2e-7; %thickness of resistive interface layer in cm
layerArea = 28e-14; %contact area between particles through interface layer in cm^2
Rinterface = resistivity*layerThickness/layerArea; %inter-particle resistance in ohms
eta=[0:-.01:-.3]'; %overpotential range and simulation interval
syms q; %dummy variable for current, which we are solving for
ivectors=cell(chainlength,1); %raw current from each particle
Jvectors=cell(chainlength,1); %current density in terms of real surface area
Mvectors=cell(chainlength,1); %mass-specific current in A/g (same as mA/mg)
pArea = 4 * pi * (dia/2)^2; %area of individual particle in cm^2
i0 = pArea*j0; %exchange current for single particle
R=zeros(chainlength,1); %initialize resistance variable
R(1) = Rinterface;
for g=2:length(R);
R(g) = R(g-1)+Rinterface;
end;
%initialize figure
figure;
hold all;
for m=1:length(R);
```

```
%initialize variable for calculated current
current=zeros(length(eta),1);
%specify a for loop to step through each overpotential value and calculate
for n=1:length(eta);
clc
disp([’particle number ’,num2str(m),’/’,num2str(length(R)),’...overpotential = ’,num2str(eta(n))]);
eq=eta(n)==-(b*log10(q/i0)+q*R(m)); %writing out full overpotential expression
current(n)=-vpasolve(eq,q,i0); %numerical solver where i0 is initial guess
end
%stash the calculated current values in the appropriate cell
J=current./pArea;
M=current./pMass;
ivectorsm=current;
Jvectorsm=J;
Mvectorsm=M;
%plot the data for this resistance value
%plot(eta,Mvectorsm,’DisplayName’,[’Particle ’,num2str(m), ’ R = ’,num2str(R(m))],’LineWidth’,2);
xlabel(’overpotential (V)’)
ylabel(’particle specific current (A/g)’)
end
% plot only the first and last particle
plot(eta,Mvectors1,’–’,’LineWidth’,3); % first particle
plot(eta,Mvectorsm,’–’,’LineWidth’,3); % last particle
% find the average current value for all particles
matrix=[Mvectors:]; % convert all Mvector cells to matrix
averagecurrent=sum(matrix,2)/m; % take average by adding all columns of a row and dividing
by number of columns
plot(eta,averagecurrent,’b’,’LineWidth’,3)
```

Appendix C Supplementary data for the evolution of core@shell Ni–Mo composites

C.1 *Ex-situ* analysis

XRD data

X-ray diffraction patterns of the as-synthesized $NiMoO_4$ and the products obtained after reduction at different temperatures are shown in Figure C.1. The as-synthesized oxide is crystalline with major peaks that index well to α-$NiMoO_4$ with minor fractions of the corresponding β phase and $NaNO_3$. On heating to 200 °C under H_2(g), the composition remains unchanged. Increasing the reduction temperature to 300 °C results in a substantial loss of crystalline order in the oxide phase, with a new broad feature that corresponds to the most intense (111) reflection for fcc Ni. As the temperature is increased further, additional diffraction features emerge that are broadly indicative of a mixture of fcc alloy, Ni/Mo oxides, and one or more nitride phases. Nitrides are formed irrespective of the reduction gas mixture used (5% H_2+ 95% N_2 or Ar), which suggests that residual $NaNO_3$ from the $NiMoO_4$ precipitation reaction acts as the primary nitrogen source. In addition to diffraction lines that are attributable to nitride phases, several additional peaks appeared below 25° after annealing at $\geq$450 °C that we were unable to index to any known phase containing Ni or Mo.

A compilation of the Mo content and crystallite size of the Ni–Mo catalyst composite obtained at different reduction temperatures is given in Table 2. The Mo content in the Ni lattice was calculated using the empirical equation given by Chialvo et al.,[219] which relates the lattice parameter a to the Mo content via:

$$a[\mathrm{nm}] = 0.35242 + 4.2 \times 10^{-4} \times [\mathrm{mol\%\ Mo}] \tag{C.1}$$

The lattice parameters for each of three observable fcc reflections were extracted using Bragg's law, wherein the interplanar distance d for a given diffraction line was calculated as

$$2d \sin\theta = n\lambda, \tag{C.2}$$

where θ is the incident angle relative to the sample plane, n is positive integer, and λ is wavelength of incident radiation, which was 0.154 nm for the Cu source used in our instrument. Using the catalyst

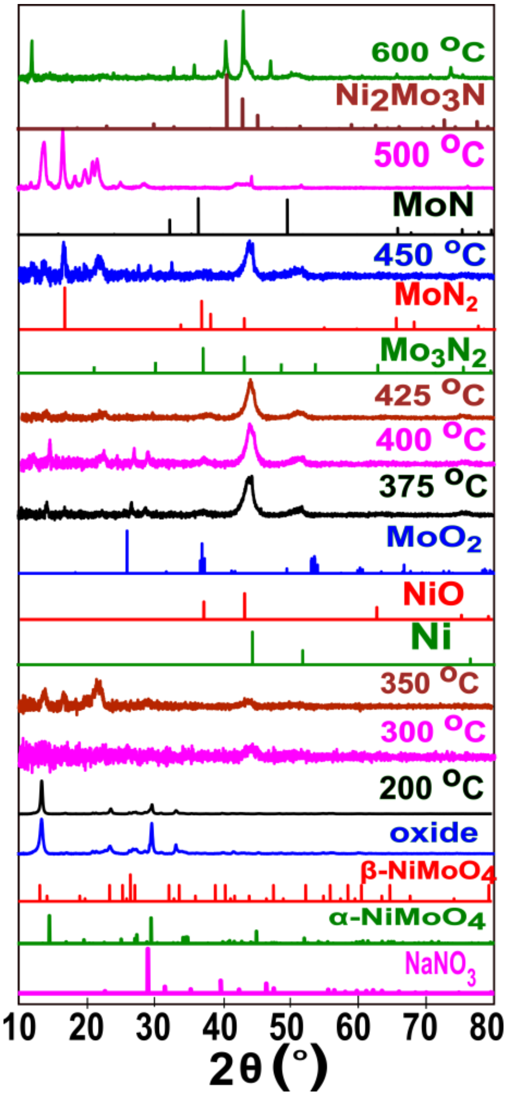

Figure C.1: XRD data for $NiMoO_4$ reduced under a gas mixture containing 5 % H_2(g) and 95 % Ar(g) at various temperatures. The standard patterns were obtained from the ICDD database.

synthesized at 400 °C as an example, the first fcc Ni peak appeared at $2\theta = 43.93°$; the interplanar distance was therefore 0.2059 nm. Bragg's law for a cubic system was again used to calculate lattice parameter a from d and the miller indices using

$$d = \frac{a}{\sqrt{h^2 + k^2 + l^2}} \tag{C.3}$$

Using the same peak noted above $(hkl) = (111)$ and the lattice parameter becomes 0.3566 nm. The Mo content was then calculated from Equation C.1 to give 9.86 at% Mo.

Using this method, the Mo content reported in the main text was taken as the mean value using each of the fcc reflections and one standard deviation as the uncertainty. Note that this analysis does not take into account systematic errors in peak position associated with the imperfect optical configuration of the XRD system. Accordingly, we consider the XRD data to indicate that the metallic component of the Ni–Mo composite contains a small but nonzero fraction of Mo^0, which is further corroborated by the XPS results shown in the main text.

Electron Microscopy

Figure C.2 shows additional SEM images of as-synthesized $NiMoO_4$. Figure C.3 shows a representative TEM image of $NiMoO_4$ after thermal reduction (in a tube furnace) at 500 °C. These data show that the morphological changes observed during *in situ* measurements coincide with the *ex situ* thermal reduction.

C.2 Electrochemical characterization

EIS Analysis

Along with the polarization data presented in the main text, electrochemical impedance spectroscopy (EIS) analysis was also performed on Ni–Mo catalyst composites generated at each reduction temperature. The EIS data were collected at 140 mV overpotential over the frequency range from 0.2 to 10^5 Hz. Results are compiled in Figure C.4. The model used to fit the EIS data consisted

reduction temperature (°C)	crystallographic index	2θ observed (°)	implied Mo content (mol%)	crystallite size (nm)
375	111	43.95	9.49	6.89
	200	51.1	11.05	5.32
	220	75.69	6.09	5.32
400	111	43.93	9.86	6.10
	200	51.02	12.29	4.36
	220	75.55	7.42	5.70
425	111	43.91	10.23	6.18
	200	51.04	11.98	4.82
	220	75.44	8.47	6.97
500	111	43.83	11.70	9.51
	200	51	12.61	5.75
	220	75.51	7.80	8.58

Table 2: Mo content and crystallite size for $NiMoO_4$ reduced at different temperatures.

of an uncompensated resistance and 2 RC circuits in series, where the capacitance elements were replaced with a constant phase element. Because $NiMoO_4$ is an electrical insulator, very high values of charge-transfer resistance were observed at 25 and 200 °C. With increasing reduction temperature, the charge transfer resistance decreased drastically and then tracked well with the observed HER activity over the range from 350 to 500 °C.

Mass Loading Dependence

We used a mass loading of 50 μg/cm^2 for the polarization measurements presented in the main text to avoid the confounding effects of electronic conductivity and mass transfer through the porous catalyst film.[227] To confirm that the observed activity was indeed kinetically limited, we performed

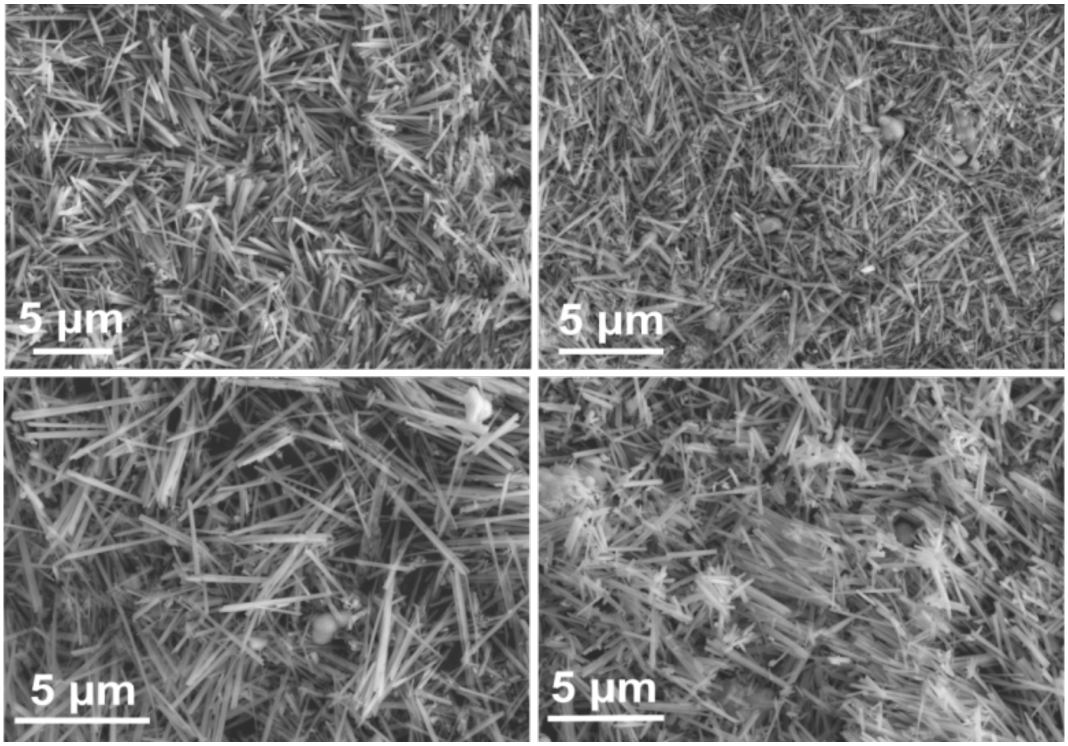

Figure C.2: SEM images across multiple areas of $NiMoO_4$, indicating the dominant nanorod morphology, albeit with a broad distribution of diameters and lengths.

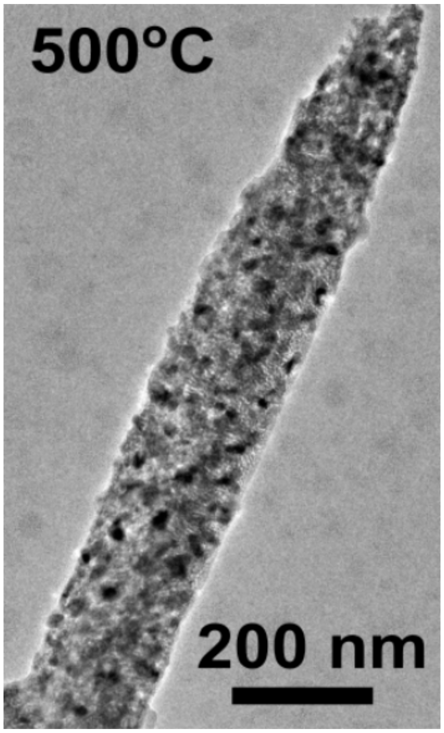

Figure C.3: Representative TEM image of $NiMoO_4$ after *ex situ* thermal reduction at 500 °C.

a mass-loading dependence of the HER activity of the best Ni–Mo catalyst (processed at 400 °C). Compiled results at 200 mV overpotential are shown in Figure C.5. These data show considerable spread: the observed cathodic current densities varied over approximately a factor of three for catalyst films at a given mass loading. We attribute this behavior to the poor catalyst dispersion that likely results from using micron-sized Ni–Mo particles, as well as the inherent uncertainty in the deposition and drying of μL volumes of dilute suspensions onto glassy carbon disks. Nonetheless, the overall trend is well described by a linear relationship, particularly at mass loadings below 0.1 mg/cm^2.

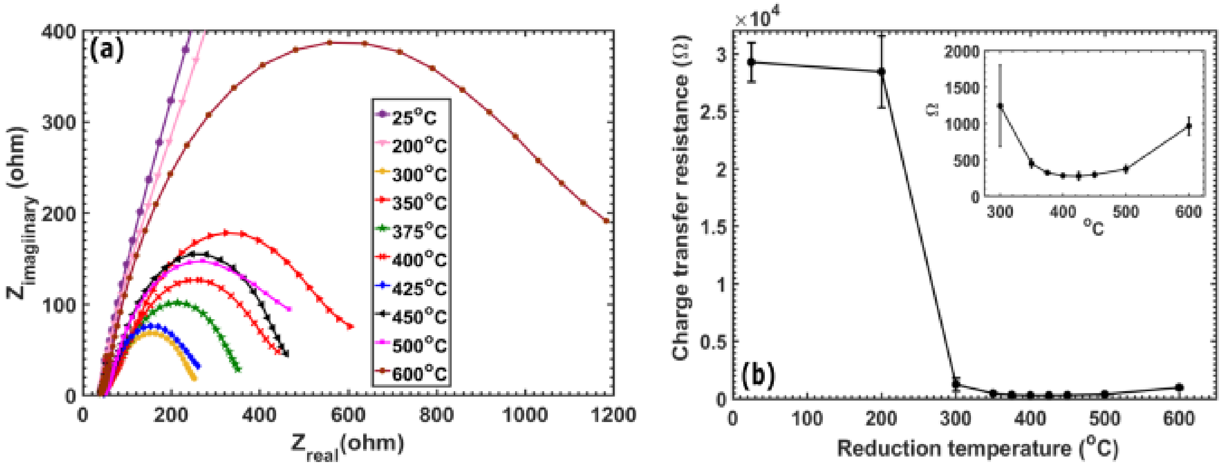

Figure C.4: (a) Compiled Nyquist plots for EIS measurements of Ni–Mo catalyst composites reduced at the noted temperatures. (b) Charge-transfer resistances values extracted from the data in (a).

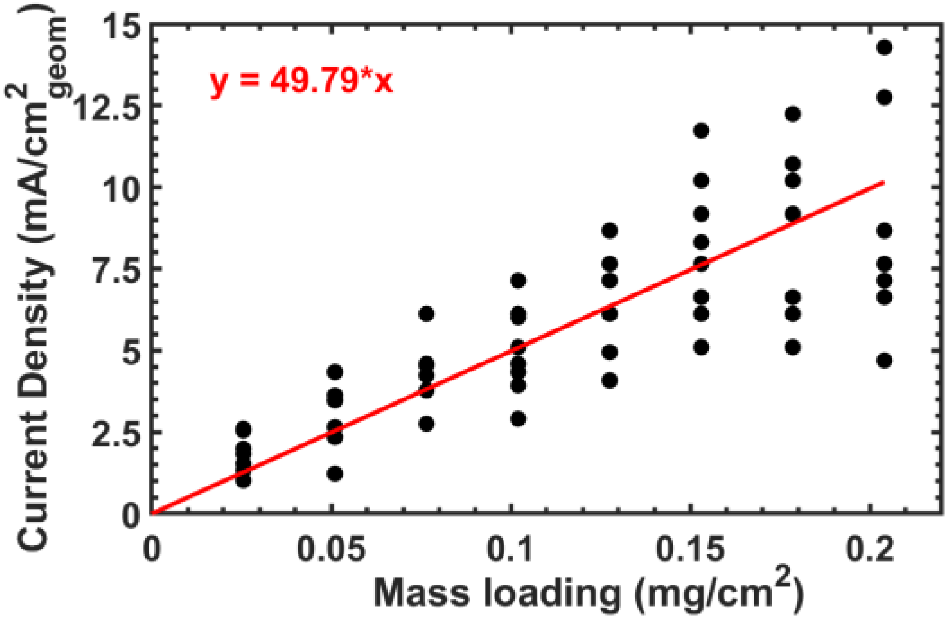

Figure C.5: Observed HER activity at 200 mV overpotential for Ni–Mo composites prepared by reducing $NiMoO_4$ nanorods at 400 °C. The dots are individual datapoints and the solid line indicates the best fit with a constrained y-intercept of zero.

Electrocatalyst Control Data

Figure C.6 shows the area-normalized HER activity of as-synthesized $NiMoO_4$, the catalyst composite reduced at 200 °C, and the bare glassy carbon substrate. These data show that the electrochemical response of both catalyst films is indistinguishable from that of glassy carbon at overpotentials up to ∼250 mV.

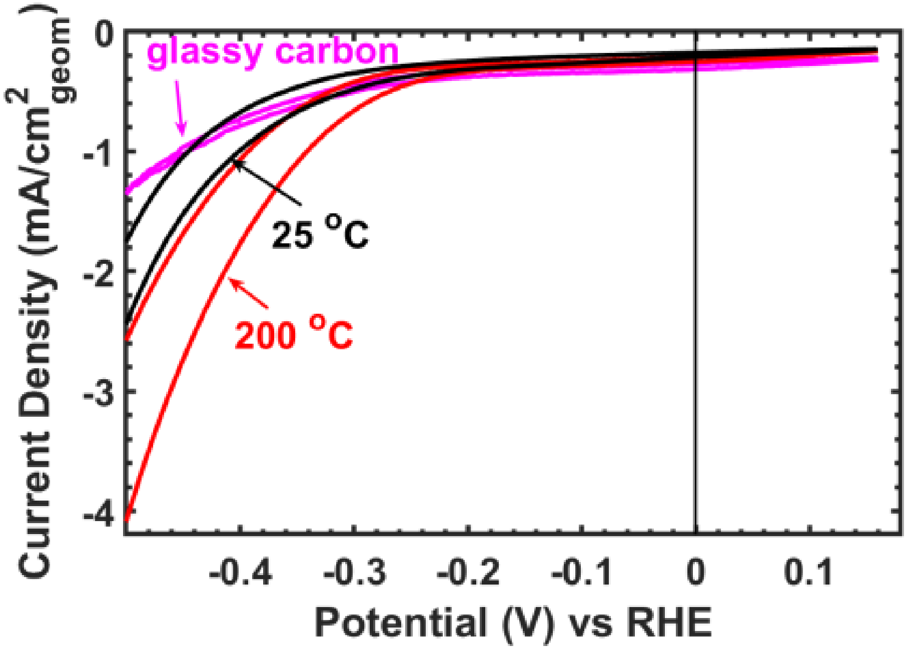

Figure C.6: Polarization data for as-synthesized $NiMoO_4$, $NiMoO_4$ reduced at 200 °C, and a glassy carbon substrate in H_2-saturated 0.1 M KOH.

Surface Area Analysis

While the catalyst mass loading was held constant for all the data shown in the main text, varying thermal treatment conditions may give rise to differences in specific surface area, which could contribute significantly to the observed differences in catalytic activity. However, accurate measurements of electrochemically active surface area are challenging, especially for nonprecious catalysts and multiphase materials. Accordingly, we semi-quantitatively assessed the surface areas of our Ni–Mo composites using two methods: double-layer capacitance from EIS and geometric analysis from HRTEM. The results of each are shown in Figure C.7 as a function of thermal reduction temperature. Double-layer capacitance values were extracted from EIS data colleced at 140 mV HER overpotential (again using 50 μg/cm^2 mass loading in all cases). The geometric analysis shown in Figure C.7b involved estimating the total surface area of the fcc alloy nanoparticles contained within a single Ni–Mo nanorod and normalizing this area to the total volume of the rod. Note that this analysis was only possible for reduction temperatures between 375 and 500 °C where the Ni-rich particles were clearly discernible.

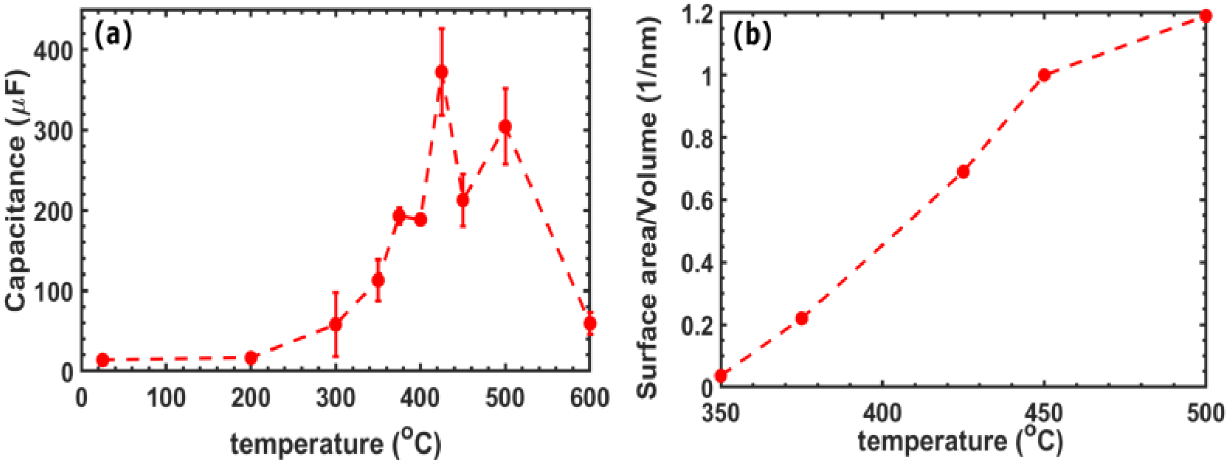

Figure C.7: (a) Capacitance of Ni–Mo composite catalyst films calculated from EIS analysis and plotted as a function of temperature. (b) Surface area to volume ratios of nanoparticles obtained from TEM analysis.

The interfacial capacitance of our Ni–Mo composites increased with thermal reduction temperature, which is consistent with an increase in the surface area of the active catalyst. However, the interfacial capacitance continued remained quite high for reduction temperatures above 400 °C before finally decreasing substantially at 600 °C, implying the electrochemically accessible surface area did not decrease substantially despite the decrease in HER activity. Similarly, the apparent surface area of the fcc alloy component of the Ni–Mo catalyst increased monotonically between 375 and 500 °C despite the clear maximum in catalytic activity at 400 °C. Accordingly, these data are not consistent with an explanation based on surface-area enhancement alone. As discussed in the main text, these data, along with the catalyst morphologies observed in ETEM and HRTEM, lead us to conclude that active sites for the HER involve metallic and oxidized sites working in tandem.

Stability Analysis

We measured the stability of the best performing Ni–Mo catalyst obtained on reduction at 400 °C under HER conditions. The “as-synthesized” catalyst, with a loading of ∼0.7 mg/cm^2 on ∼2.25 cm^2 Ni mesh, was used as a working electrode. A constant current of -20 mA (i.e., ∼9 mA/cm^2 or ∼30 mA/mg) was maintained for a duration of 21 hours. The result, compiled in Figure C.8 show that the catalyst remains stable at ∼175 mV overpotential only for several tens of minutes, after which the activity decays exponentially (linear on a log scale) over the remainder of the experimental period. Polarization data taken before and after the galvanostatic measurement confirm the significant decrease in activity as well as a decrease in the capacitive hysteresis near 0 V vs. RHE that we attribute to MoO$_x$ pseudocapacitance.

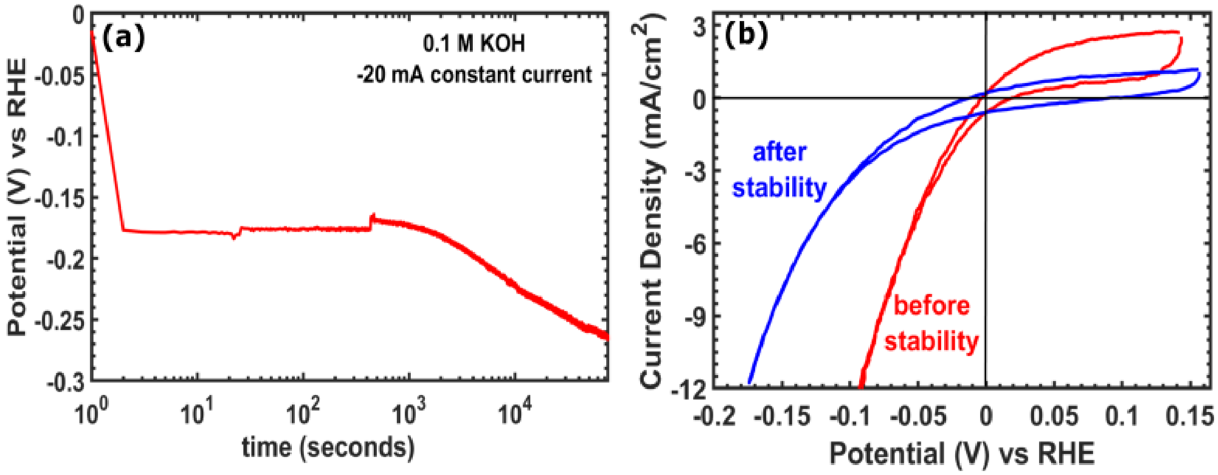

Figure C.8: (a) Chronoamperomtery analysis (not corrected for iR) of Ni–Mo catalyst reduced at 400 °C at a constant current of -20 mA over a period of 21 hours. (b) Resistance-corrected polarization data for the same Ni–Mo catalyst before and after stability measurements in H$_2$-saturated 0.1 M KOH.

We also performed TEM characterization of the Ni–Mo composite before and after stability measurements, as shown in Figures C.9– C.12. The “before” stability sample exhibited essentially the same composition and morphology as shown in the main text. The “after” stability data show that the catalyst underwent substantial restructuring from the predominantly nanorod morphology to large isotropic agglomerates, albeit without substantial coalescence of the Ni-rich fcc nanoparticles.

We speculate, then, that the Mo-rich oxide shell in the as-synthesized catalyst dissolves in the alkaline electrolyte, leading to loss of the nanorod morphology and catalyst aggregation. This is consistent with recent work showing that Ni–Mo catalyst composites are susceptible to Mo leaching under HER reaction conditions in base.[308, 309] However, the oxide in the near vicinity of the fcc alloy appears to be more stable toward dissolution, perhaps because it contains a substantial fraction of insoluble NiO_x.

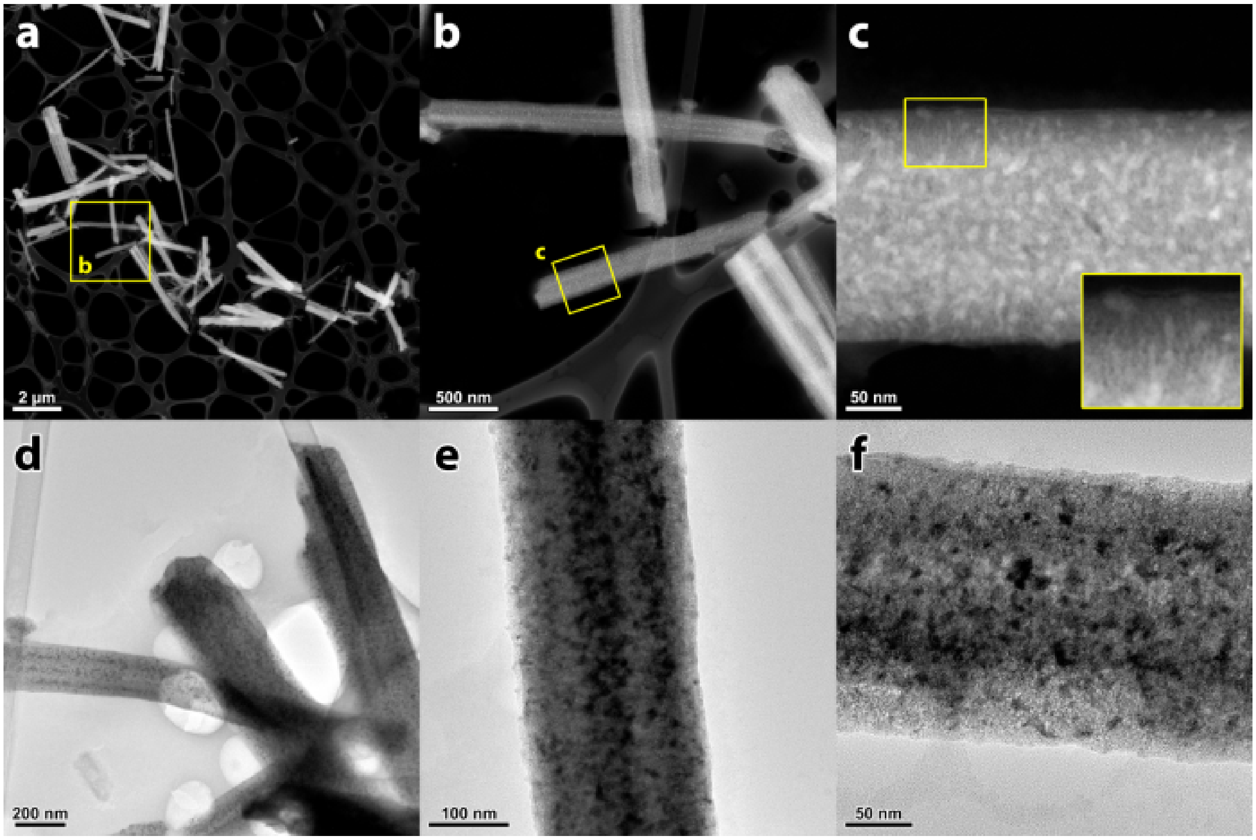

Figure C.9: (a-c) HAADF-STEM and (d-f) BF-TEM images of catalyst material before stability testing, after thermal reduction in H_2 at 400 °C. The yellow boxes indicate regions of corresponding close-up images, as labeled.

Comparison with Precipitation-Reduction Synthesis

We compared the most active Ni–Mo catalyst obtained by hydrothermal synthesis with a Ni–Mo catalyst synthesized by precipitation-reduction synthesis following a prior report.[60] Figure C.13

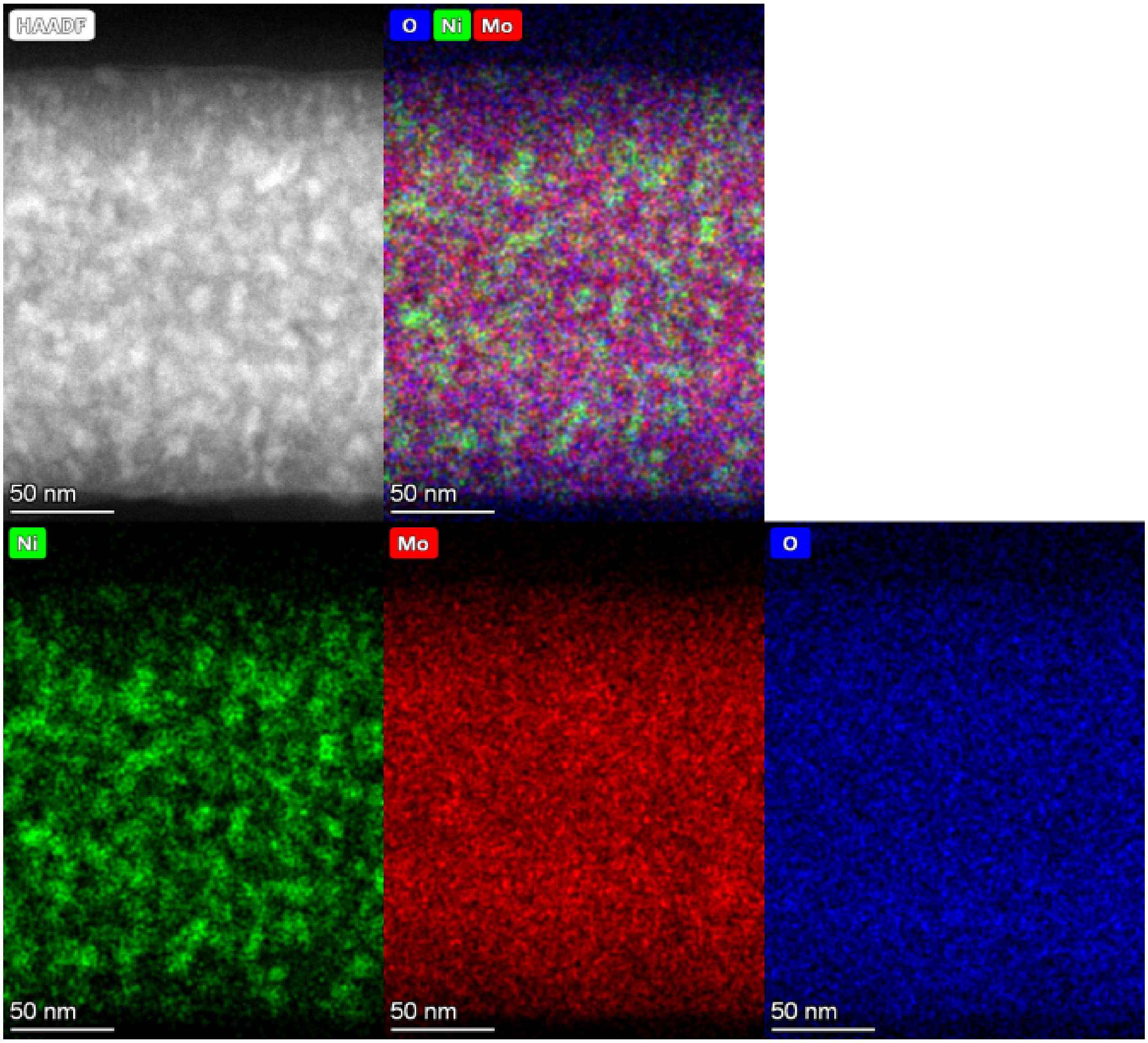

Figure C.10: EDS elemental maps from the catalyst rod shown in Figure C.9. The maps confirm that the porous rods are Mo-rich oxide while the Ni is localized to the nanoparticles. This same distribution was observed in all rods examined.

shows representative TEM images of the two catalysts along with polarization data. The isotropic catalyst prepared by precipitation-reduction shows activity similar to the catalyst obtained from hydrothermal synthesis at the same reduction temperature, but both are lower in activity than the hydrothermal catalyst reduced at 400 °C. This suggests that the core-shell catalyst formation and

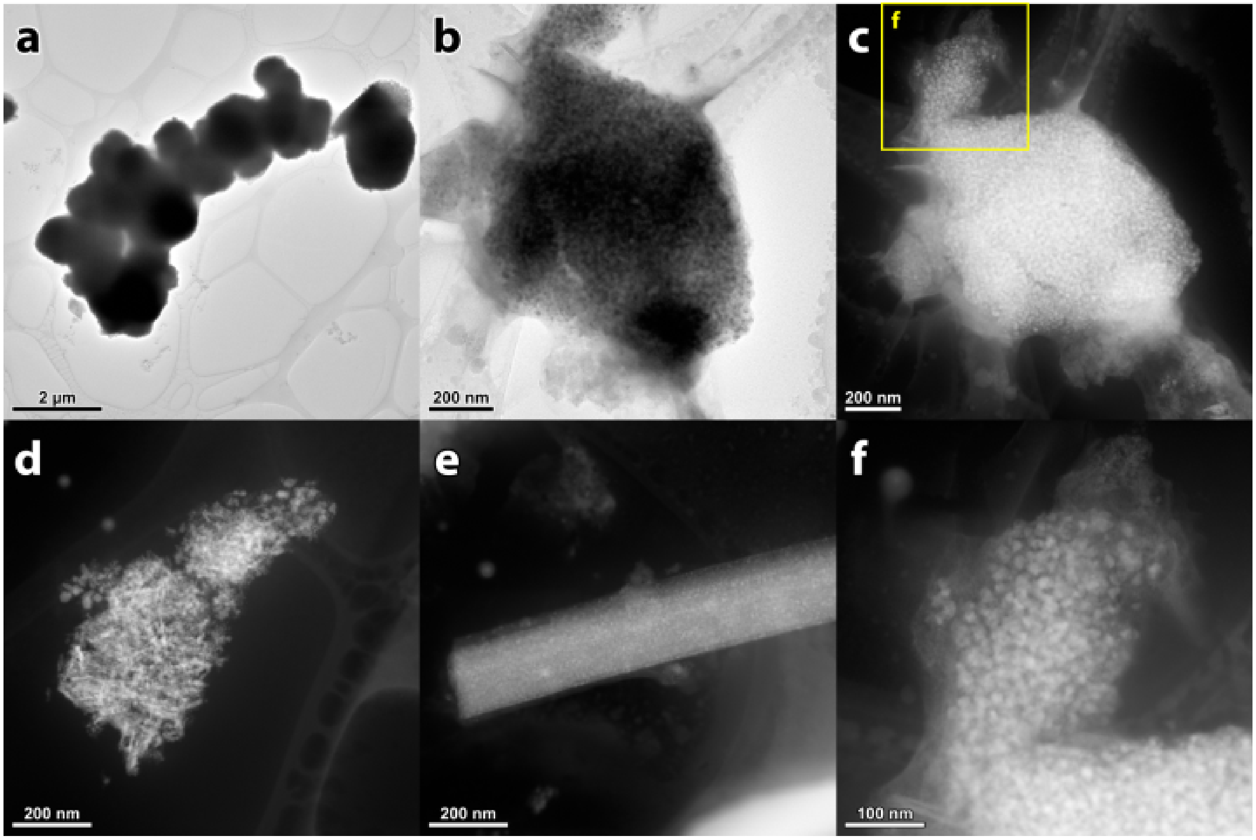

Figure C.11: (a,b) BF-TEM and (c-f) HAADF-STEM images of catalyst material after stability testing. The sample was found to be heterogeneous, consisting of (a) large, sphere/ovoid-like particles up to 1 um in diameter; (b-d) various irregularly shaped aggregates; and (e) nanorods with effectively identical morphology to the "before" sample; (f) is a close-up of the region indicated in (c).

the activity-temperature dependence is a broad characteristic of Ni–Mo composites derived from phase-pure mixed oxides.

Activity of Ni–Mo Nitride Phases

Consistent with prior observations,[213] our Ni–Mo catalyst shows evidence for nitride formation on reduction at temperatures exceeding 500°C. Ni–Mo nitride composites have also been reported to exhibit high HER activity.[310, 311, 312, 313] Figure C.14 juxtaposes XRD and polarization

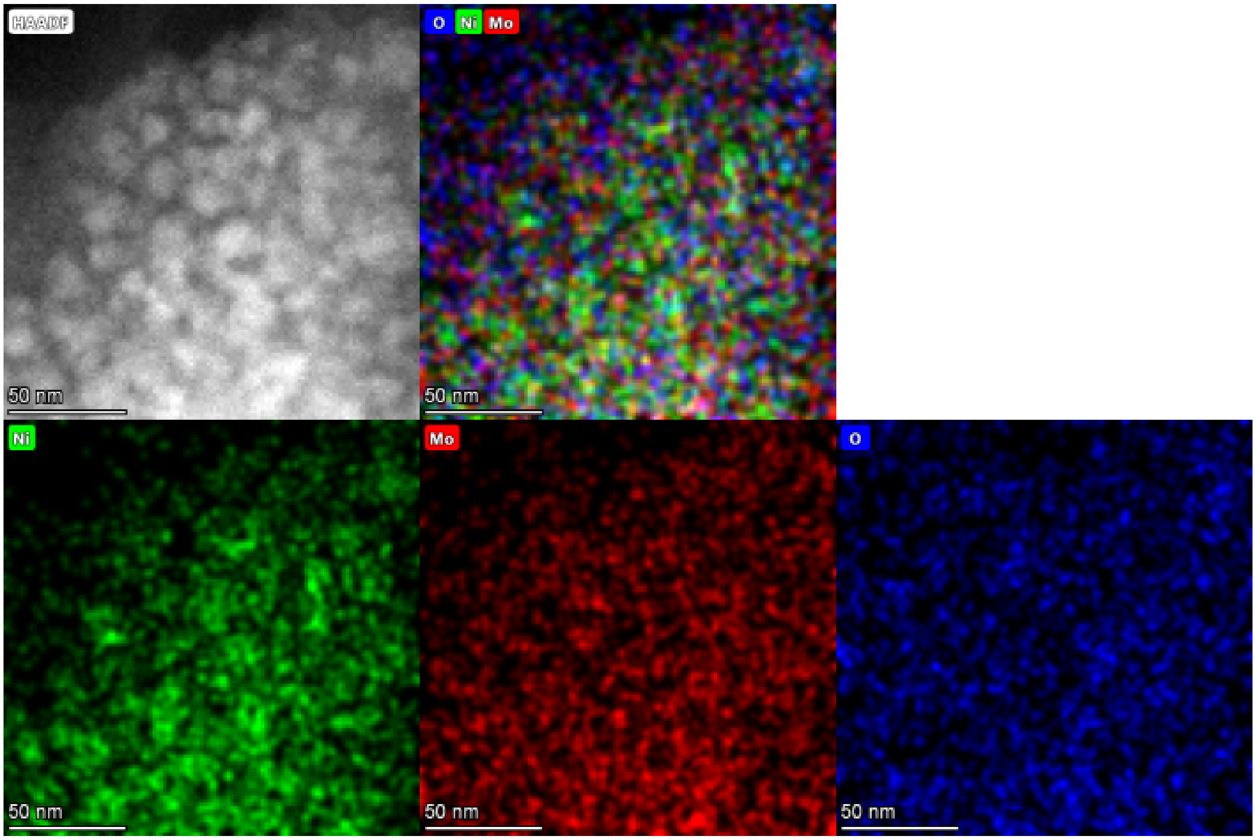

Figure C.12: EDS elemental maps from the catalyst particle shown in Figure C.11. The maps confirm that the nanoparticles are still predominantly Ni, while the matrix is Mo-rich oxide.

data for Ni–Mo composites with (600 °C reduction) and without (400 °C reduction) evidence for nitride formation. The activity of the nitride-containing catalyst was markedly lower than "pure" Ni–Mo, but the difference is attributable at least in part to a decrease in specific surface area that results from the increased thermal reduction temperature. Thus, we cannot rule out the possibility that the intrinsic activity (i.e., turnover frequency) of Ni–Mo nitride toward the HER is comparable or greater than that of the Ni–Mo metal/oxide composite obtained at 400 °C.

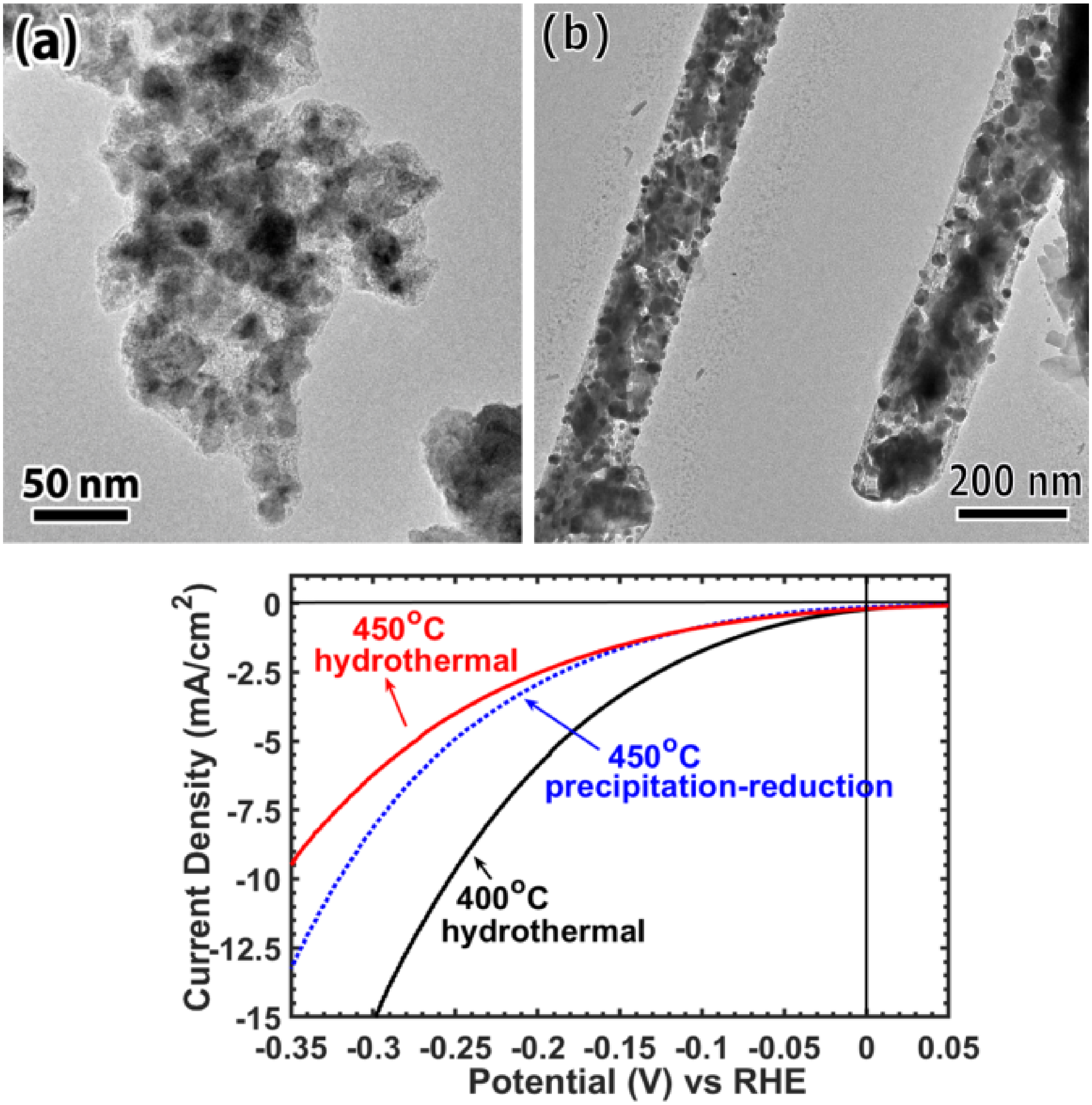

Figure C.13: TEM images of Ni–Mo catalysts synthesized by (a) co-precipitation in an open system and reduced at 450 °C and (b) hydrothermal synthesis reduced at 400 °C (as in the main text). (c) Polarization data comparing catalysts prepared by these two routes.

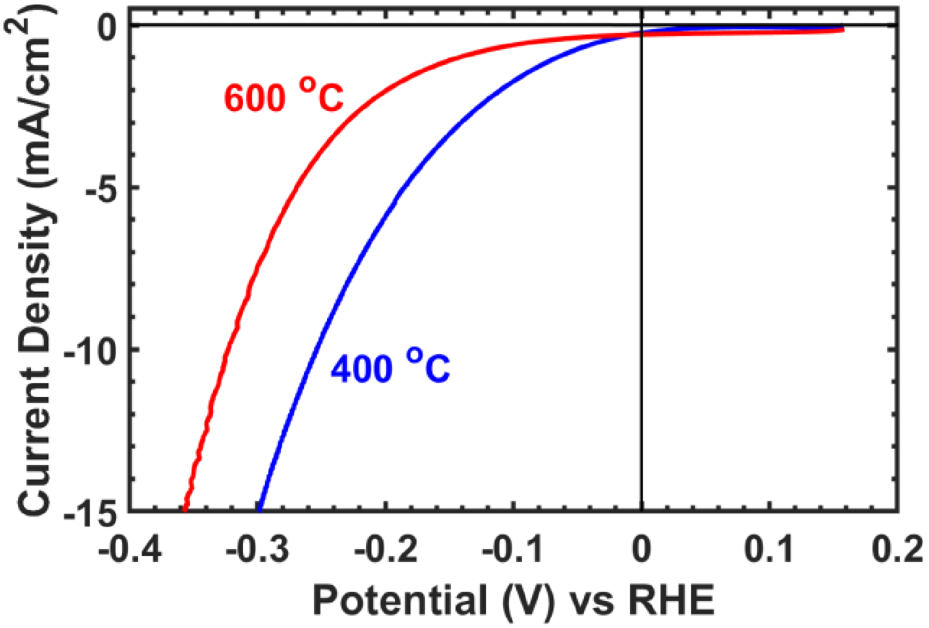

Figure C.14: (a) XRD data showing Ni–Mo catalysts that do (600°C) and do not (400°C) show evidence for crystalline metal nitride formation. (b) Polarization curve for the same catalyst materials as in (a).

C.3 *In-situ* TEM data and analysis

Figure C.15 shows TEM images and an SAED pattern from a single representative $NiMoO_4$ nanorod. Figure C.16 shows an example of the structural damage that was observed in the $NiMoO_4$ nanorods when imaged for an extended period of time (on the order of a few minutes) at operating voltages above 100 kV. Particularly at high resolutions (those sufficient to resolve lattice fringes), interactions with the electron beam would induce the formation of small voids throughout the material. In these images, the voids appear as round regions—a few nm across—with lighter intensity. The continued visibility of the crystal lattice indicates that the rods were not entirely amorphized. No void formation was observed when imaging was at an operating voltage of 100 kV for at least tens of minutes.

Figures C.17– C.18 show images and SAED patterns of several regions of the nanorod at key temperature points. These were not followed continuously, but instead imaged briefly after the continuously imaged region of the sample had equilibrated at the noted temperature. The morphological changes observed in these regions are consistent with those that occurred in the primary region, as shown in main text Figure 4.9.

Normal and lognormal quantile-quantile plots of the measured Ni-rich nanoparticle sizes following *in situ* reduction at 350, 375, and 425 °C are included in Figure C.19. The measured 350 °C and 375 °C data fit both types of distributions reasonably well. By contrast, the 425 °C measurements deviate significantly from normal, exhibiting a distinct positive skew (also easily seen in the violin plots). The nanoparticle sizes fit a lognormal distribution, however, very well. This indicates that the reduction process proceeded through Ostwald ripening, particle migration, and coalescence.

Figure C.20 shows representative HRTEM images of the nanorods after *in situ* reduction at 500 °C. The lattice fringe spacings observed are consistent with those of various Mo-rich oxides and nitrides. The continuity of the lattice fringes across each flake indicates that they are individually single-crystal. They were typically highly faceted and in many cases even atomically flat.

Figure C.21 shows a pair of TEM image montages of a single $NiMoO_4$ nanorod before any heating or exposure to H_2 and after *in situ* reduction at 425 °C. This nanorod was not actively imaged during the reduction process. It exhibits the same phase separation of Ni-rich nanoparticles and large Mo-rich crystals, as seen in the primary cluster of nanorods, but to a greater degree. This implies that while even light exposure to the electron beam can affect the specifics of the morphological change (e.g., the size, number, and/or distribution of the Ni particles nucleated), the general observations and trends hold.

Additional TEM images and elemental analysis results are shown in Figures **??**– C.22. The associated captions indicate the salient details of each. Movies M1-M3 (attached separately as video files) are portions of the *in situ* TEM reduction, during heating up to 350, 375, and 425 °C, respectively. The videos have been drift-corrected and sped up by a factor of 16. The small black spot to the right of the thin (leftmost) nanorod that appears to be moving is a dead pixel in the camera. It appears to move as a result of the motion-stabilization process.

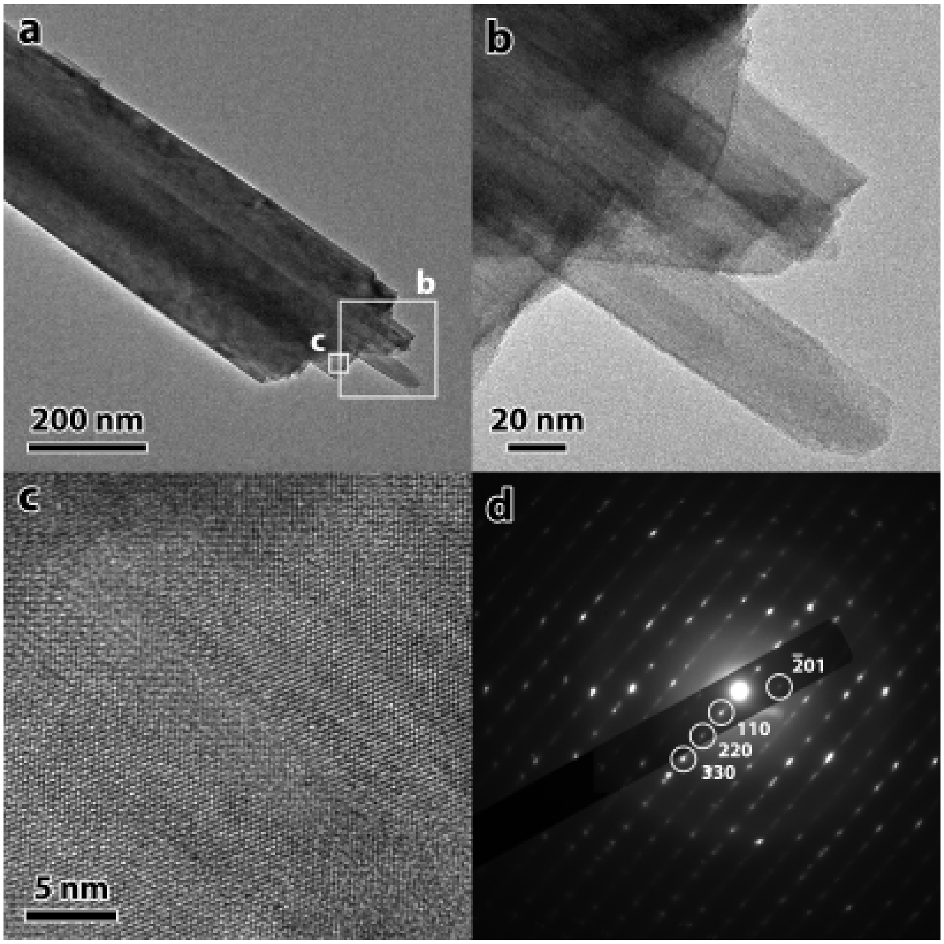

Figure C.15: TEM and electron diffraction data for a representative example of a $NiMoO_4$ nanorod. (a) TEM image of one end of a nanorod. The white boxes indicate the regions shown in the HRTEM close-ups in (b-c). (d) SAED pattern from this end of the nanorod, indexed as α-$NiMoO_4$. The planar faults running parallel to the rod axis are visible in the contrasting bands in (a-b) and more directly in (c), where the shifts in the atomic arrangement and/or visibility of the lattice fringes is seen. The streaking in the diffraction pattern (d) perpendicular to the rod axis (and thus the fault planes) is further confirmation. Panel (d) is a composite of two images: the portion of the pattern that would be obscured by the beam-blocker has been overlaid on the same pattern acquired without the beam-blocker (as well as a shorter acquisition time to minimize saturation around the transmitted spot). This allowed for the otherwise-blocked spots to be visible while not obscuring the rest of the pattern due to the significantly higher intensity of the transmitted spot.

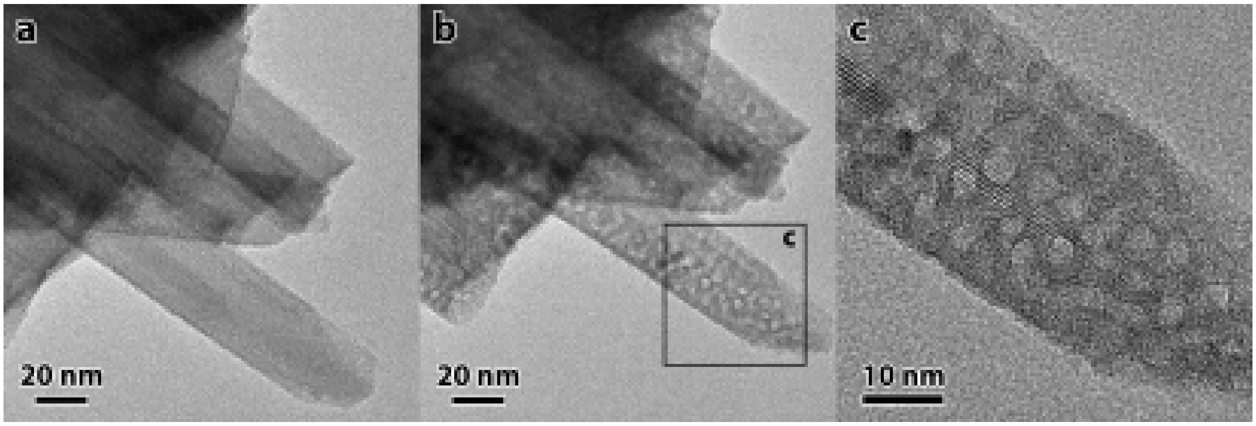

Figure C.16: HRTEM images showing the beam-induced void formation that occurred in $NiMoO_4$ nanorods at an operating voltage of 200 kV.

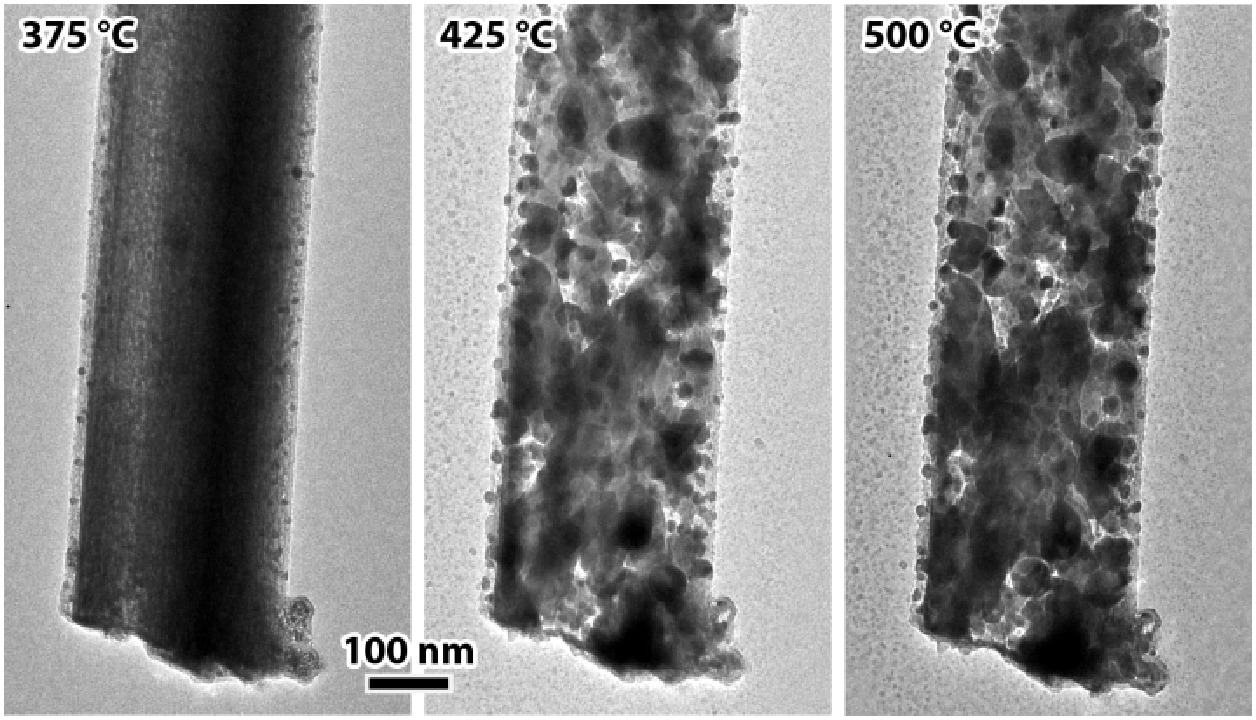

Figure C.17: TEM images at different temperatures of the nanorod that was not exposed to the beam.

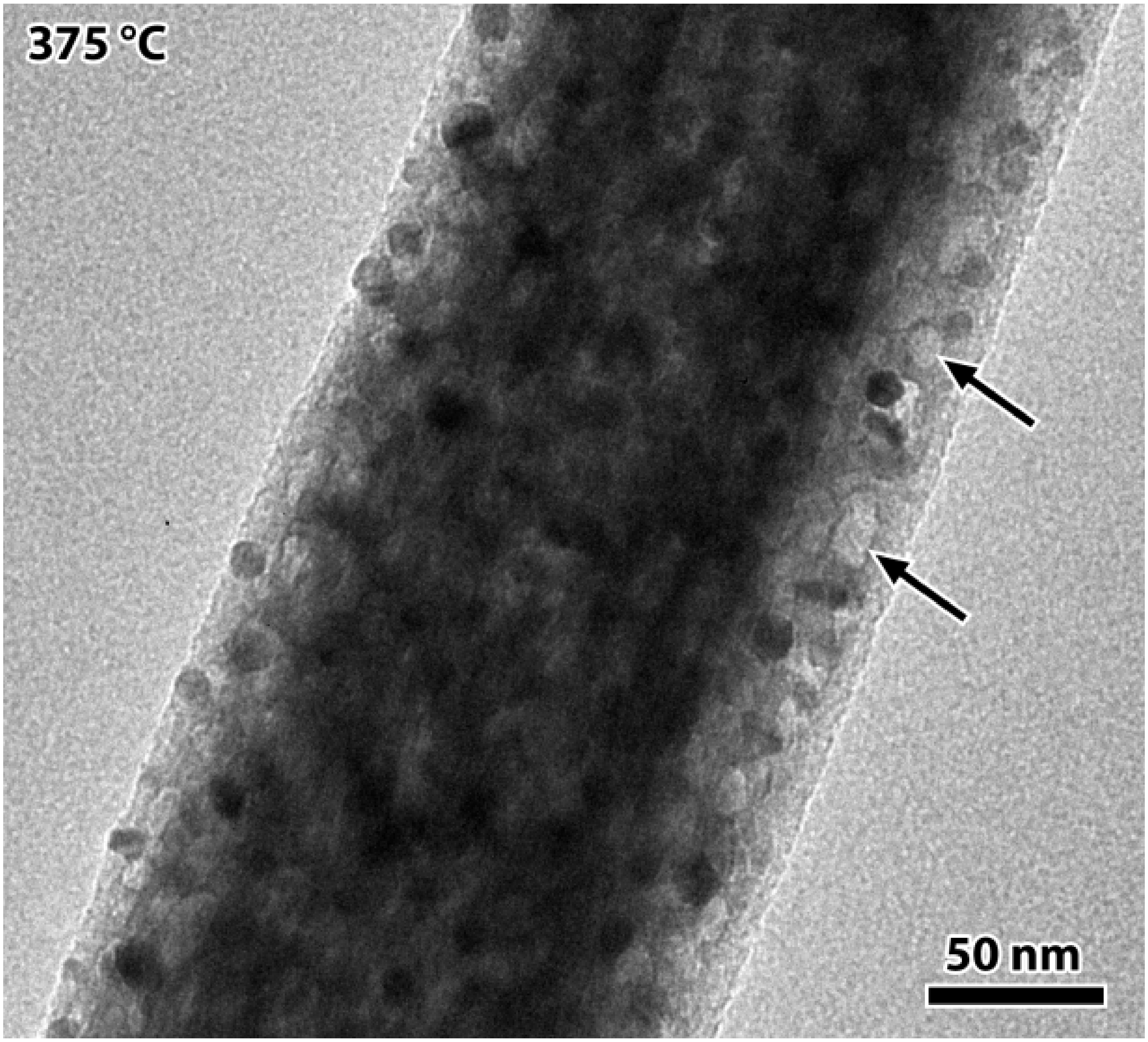

Figure C.18: Close-up of a Ni–Mo composite reduced at 375 °C clearly showing the porous nature of the outer Mo-rich layer (some example pores are indicated by arrows) with small Ni-rich nanoparticles in/on it.

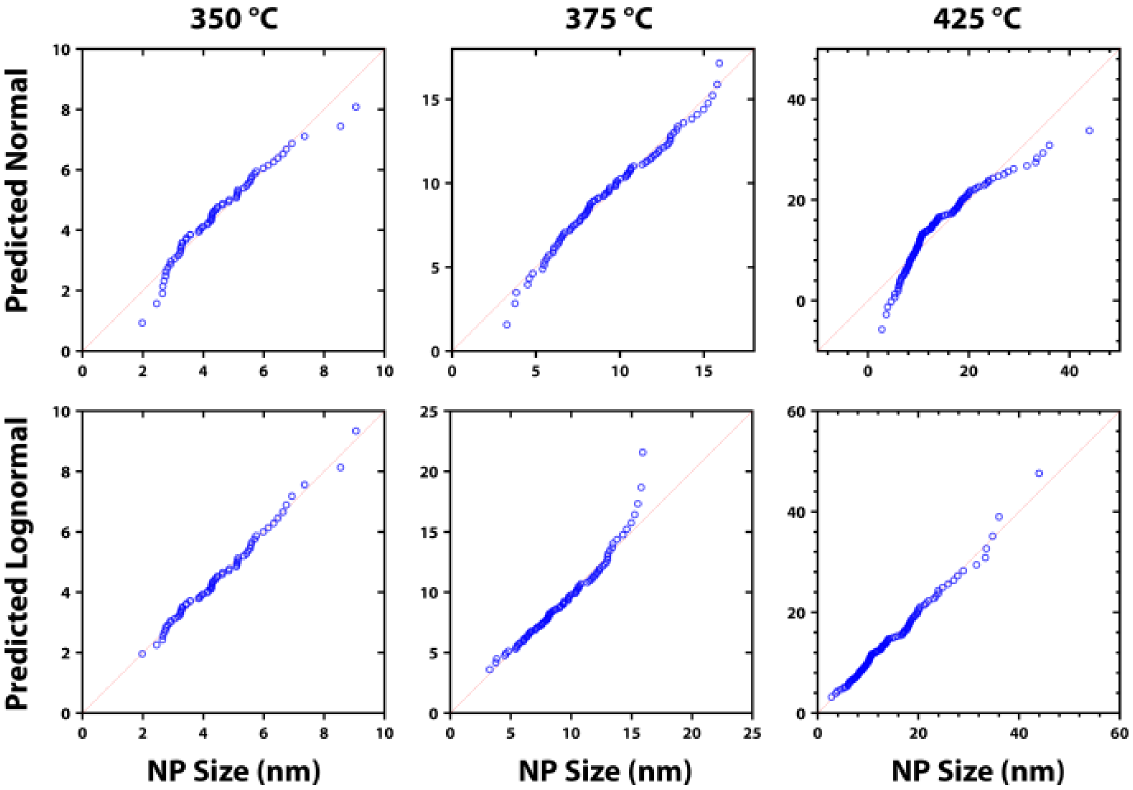

Figure C.19: Normal and lognormal quantile-quantile plots of measured Ni-rich nanoparticle size after *in situ* reduction at 350, 375, and 425 °C.

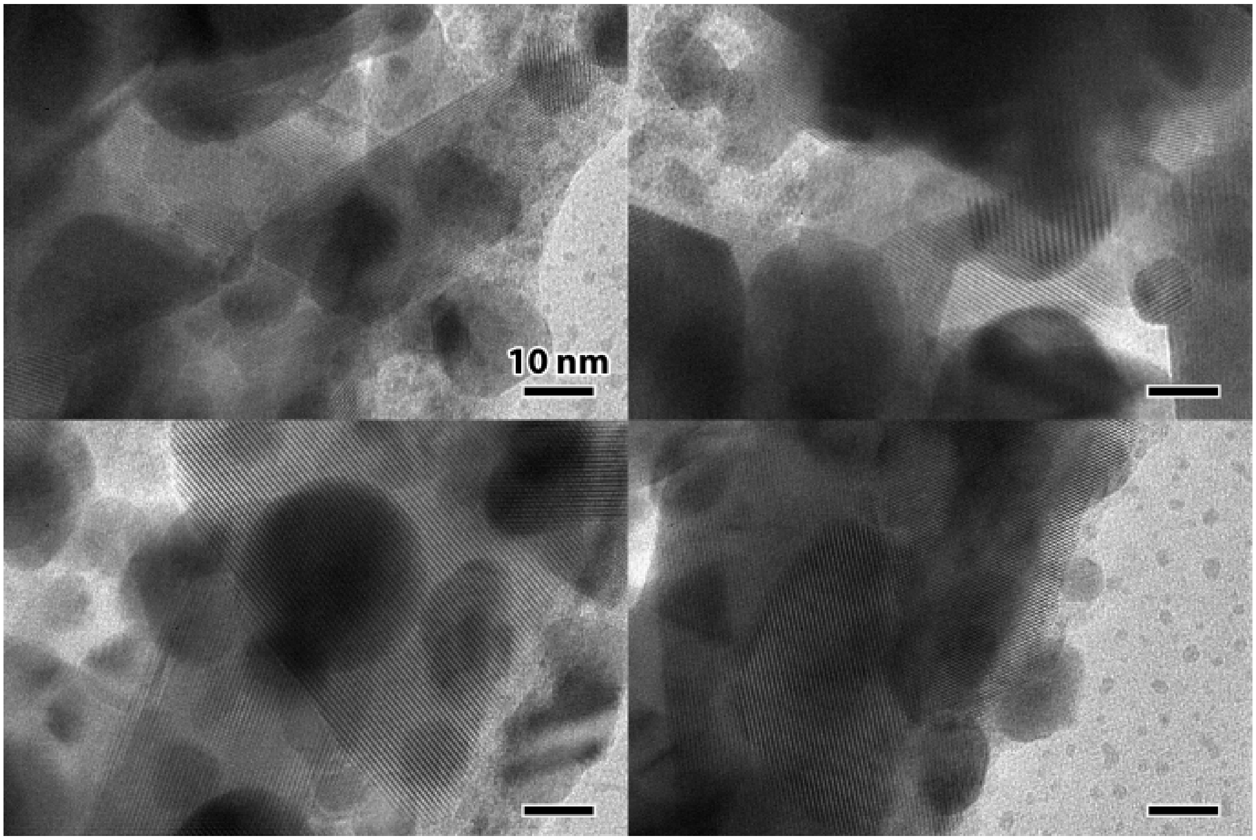

Figure C.20: HRTEM images of $NiMoO_4$ nanorods reduced at 500 °C. These images have been Fourier filtered to enhance the contrast of the lattice fringes. All scalebars are 10 nm.

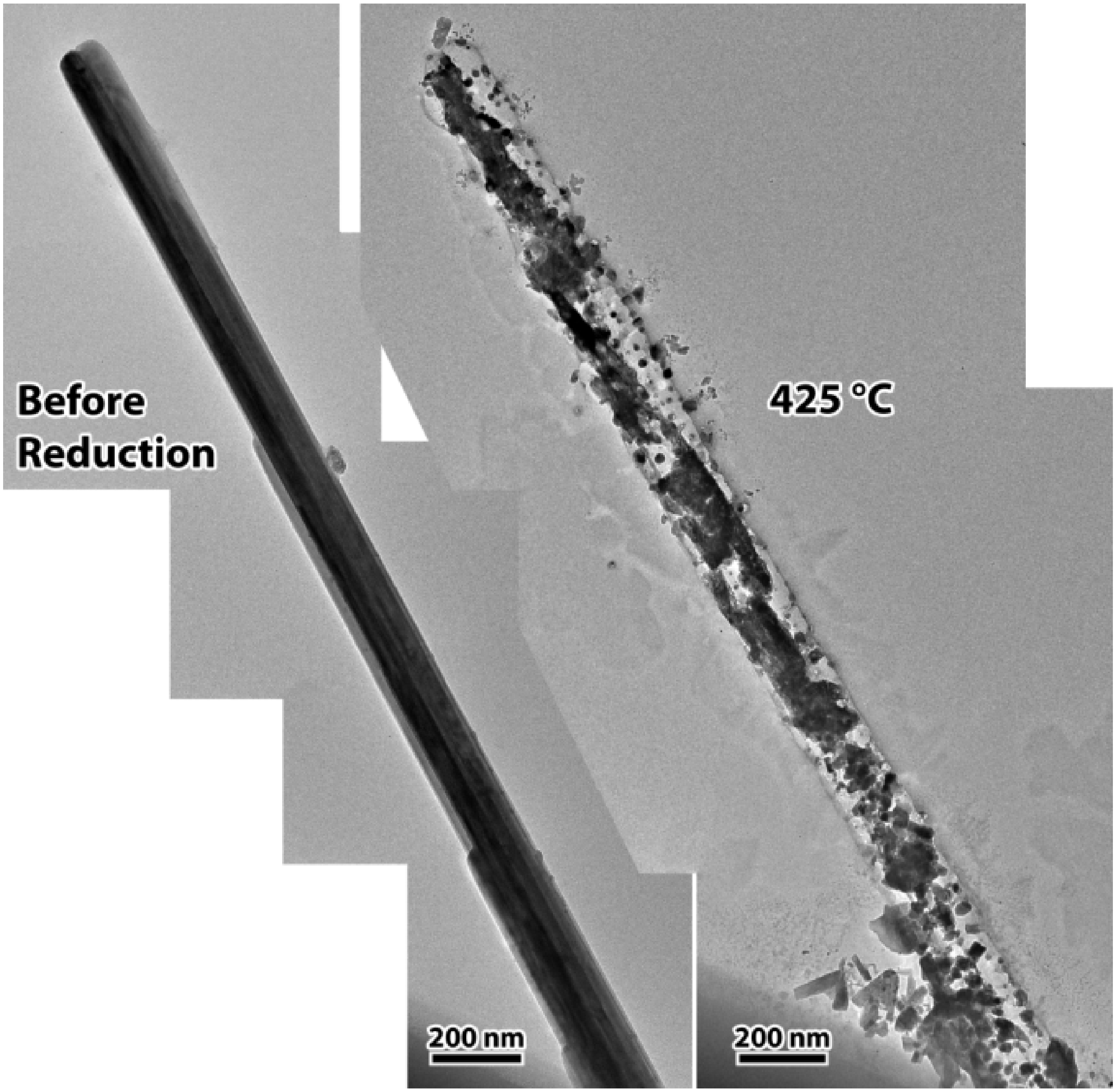

Figure C.21: TEM image montages of a $NiMoO_4$ nanorod before (left) and after (right) *in situ* reduction at 425 °C.

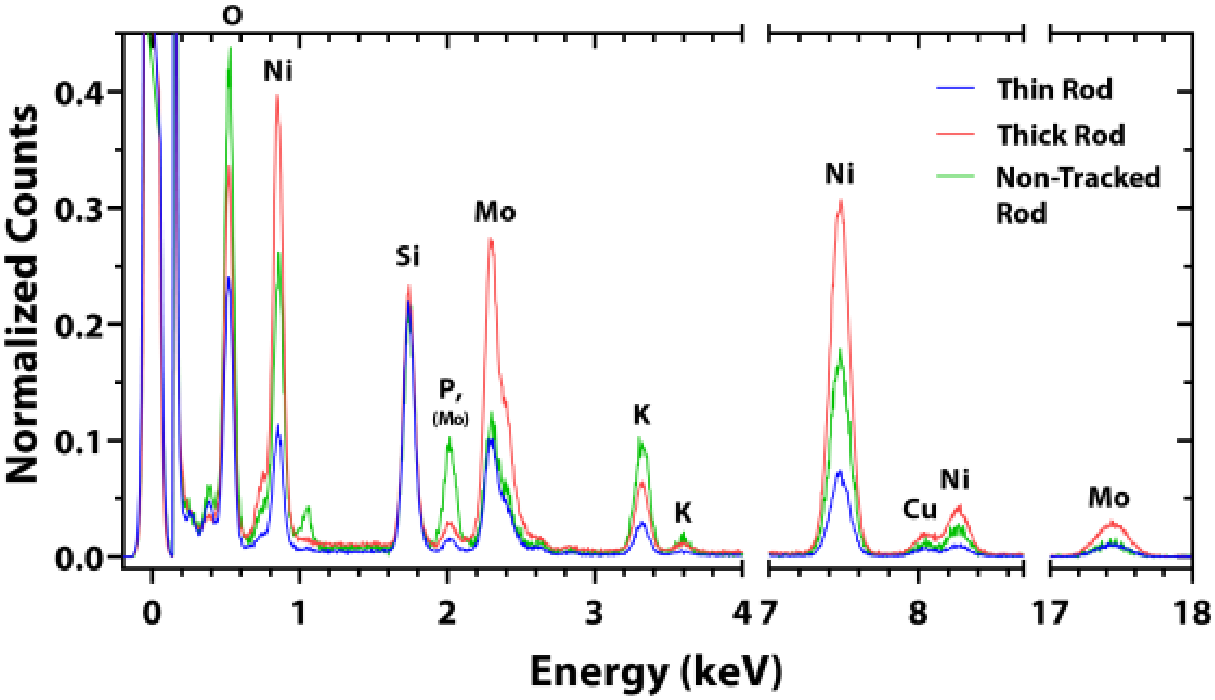

Figure C.22: EDS sum spectra from three fully reduced $NiMoO_4$ rods comprising two different diameters and one that was not tracked during the *in situ* reduction. Selected elemental peaks have been labeled. The strong Si peak is from the TEM grid membrane, which is SiN_x. The Cu peak comes from the washers of the TEM holder.

Bibliography

[1] IEA, “The Future of Hydrogen for G20,” Tech. Rep. June, 2019.

[2] N. Hunter, “Hydrogen use needs to hit 212 million mt by 2030 for net-zero: IEA,” Tech. Rep. May, 2021.

[3] J. Bartlett and A. Krupnick, “Decarbonized Hydrogen in the US Power and Industrial Sectors : Identifying and Incentivizing Opportunities to Lower Emissions,” Tech. Rep. December, 2020.

[4] R. Rajasegar, C. M. Mitsingas, E. K. Mayhew, Q. Liu, T. Lee, and J. Yoo, “Development and Characterization of Additive-Manufactured Mesoscale Combustor Array,” *Journal of Energy Engineering*, vol. 144, no. 3, p. 04018013, 2018.

[5] S. Sabihuddin, A. E. Kiprakis, and M. Mueller, “A numerical and graphical review of energy storage technologies,” *Energies*, vol. 8, no. 1, pp. 172–216, 2015.

[6] Y. Wang, D. Y. Leung, J. Xuan, and H. Wang, “A review on unitized regenerative fuel cell technologies, part-A: Unitized regenerative proton exchange membrane fuel cells,” *Renewable and Sustainable Energy Reviews*, vol. 65, pp. 961–977, 2016.

[7] T. B. Ferriday and P. H. Middleton, “Alkaline fuel cell technology - A review,” *International Journal of Hydrogen Energy*, vol. 46, no. 35, pp. 18489–18510, 2021.

[8] G. McLean, T. Niet, S. Prince-Richard, and N. Djilali, “An assessment of AFC technology,” *International Journal of Hydrogen Energy*, vol. 27, pp. 507–526, 2002.

[9] O. Schmidt, A. Gambhir, I. Staffell, A. Hawkes, J. Nelson, and S. Few, “Future cost and performance of water electrolysis: An expert elicitation study,” *International Journal of Hydrogen Energy*, vol. 42, no. 52, pp. 30470–30492, 2017.

[10] D. Ferrero, M. Gamba, A. Lanzini, and M. Santarelli, “Power-to-Gas Hydrogen: Techno-economic Assessment of Processes towards a Multi-purpose Energy Carrier,” *Energy Procedia*, vol. 101, no. September, pp. 50–57, 2016.

[11] T. Brown, “Renewable Hydrogen for Sustainable Ammonia Production,” *Chemical Engineering Progress*, vol. 115, no. 8, pp. 47–53, 2019.

[12] S. Hicks and P. Gross, "U.E. Energy Information Administration: Hydrogen for refineries is increasingly provided by industrial suppliers," tech. rep., 2016.

[13] H. Ritchie, "How long before we run out of fossil fuels? - Our World in Data," 2017.

[14] G. Kuo, "When will fossil fuels run out?, What Then? MAHB," 2019.

[15] J. Delbeke, A. Runge-Metzger, Y. Slingenberg, and J. Werksman, "The paris agreement," *Towards a Climate-Neutral Europe: Curbing the Trend*, pp. 24–45, 2019.

[16] US Department of Energy, "Technical Targets for Hydrogen Production from Electrolysis," 2020.

[17] Our World in Data, "Electricity production by source, World, based on BP Statistical Review of World Energy & Ember," 2020.

[18] H. Chen, T. N. Cong, W. Yang, C. Tan, Y. Li, and Y. Ding, "Progress in electrical energy storage system: A critical review," *Progress in Natural Science*, vol. 19, no. 3, pp. 291–312, 2009.

[19] H. Kobayashi, A. Hayakawa, K. D. A. Somarathne, and E. C. Okafor, "Science and technology of ammonia combustion," *Proceedings of the Combustion Institute*, vol. 37, no. 1, pp. 109–133, 2019.

[20] M. Warshay and P. R. Prokopius, "The fuel cell in space: yesterday, today and tomorrow," *Journal of Power Sources*, vol. 29, no. 1-2, pp. 193–200, 1990.

[21] G. Llewellyn, "Hydrogen fuel cells, explained - Innovation - Airbus," 2020.

[22] City of Lancaster, "Lancaster , CA Becomes the First Hydrogen City in the United States," 2020.

[23] C. Newport Coast, "Toyota Introduces Second-Generation Mirai Fuel Cell Electric Vehicle as Design and Technology Flagship Sedan - Toyota USA Newsroom," 2020.

[24] M. Burgess, "Hyundai Nexo breeak worl record for longest distance travlled in a FCEV," 2021.

[25] C. E. Thomas, “Fuel cell and battery electric vehicles compared,” *International Journal of Hydrogen Energy*, vol. 34, no. 15, pp. 6005–6020, 2009.

[26] Hydrogen Council, McKinsey &, and Company, “Hydrogen Insights: A Perspective on Hydrogen Investment, Market Development and Cost Competitivenes,” no. February, p. 58, 2021.

[27] A. Schneemann, J. L. White, S. Kang, S. Jeong, L. F. Wan, E. S. Cho, T. W. Heo, D. Prendergast, J. J. Urban, B. C. Wood, M. D. Allendorf, and V. Stavila, “Nanostructured Metal Hydrides for Hydrogen Storage,” *Chemical Reviews*, vol. 118, no. 22, pp. 10775–10839, 2018.

[28] P. Preuster, A. Alekseev, and P. Wasserscheid, “Hydrogen storage technologies for future energy systems,” *Annual Review of Chemical and Biomolecular Engineering*, vol. 8, pp. 445–471, 2017.

[29] R. Moradi and K. M. Groth, “Hydrogen storage and delivery: Review of the state of the art technologies and risk and reliability analysis,” *International Journal of Hydrogen Energy*, vol. 44, no. 23, pp. 12254–12269, 2019.

[30] J. Andersson and S. Grönkvist, “Large-scale storage of hydrogen,” *International Journal of Hydrogen Energy*, vol. 44, no. 23, pp. 11901–11919, 2019.

[31] Y. Huang, Y. Cheng, and J. Zhang, “A review of high density solid hydrogen storage materials by pyrolysis for promising mobile applications,” *Industrial and Engineering Chemistry Research*, vol. 60, no. 7, pp. 2737–2771, 2021.

[32] G. L. Soloveichik, “Regenerative fuel cells for energy storage,” *Proceedings of the IEEE*, vol. 102, no. 6, pp. 964–975, 2014.

[33] F. Barbir, T. Molter, and L. Dalton, “Efficiency and weight trade-off analysis of regenerative fuel cells as energy storage for aerospace applications,” *International Journal of Hydrogen Energy*, vol. 30, no. 4, pp. 351–357, 2005.

[34] J. Bone, S. Gilman, L. Niedrach, and M. Read, “Ion-exchnage regenerative fuel cells,” in *Proc. 15th Annual Power Source Conference, Ft. Monmouth, NJ, USA*, pp. 47–49, 1961.

[35] H. A. Miller, K. Bouzek, J. Hnat, S. Loos, C. I. Bernäcker, T. Weißgärber, L. Röntzsch, and J. Meier-Haack, “Green hydrogen from anion exchange membrane water electrolysis: A

review of recent developments in critical materials and operating conditions," *Sustainable Energy and Fuels*, vol. 4, no. 5, pp. 2114–2133, 2020.

[36] R. Phillips and C. W. Dunnill, "Zero gap alkaline electrolysis cell design for renewable energy storage as hydrogen gas," *RSC Advances*, vol. 6, no. 102, pp. 100643–100651, 2016.

[37] S. Marini, P. Salvi, P. Nelli, R. Pesenti, M. Villa, M. Berrettoni, G. Zangari, and Y. Kiros, "Advanced alkaline water electrolysis," *Electrochimica Acta*, vol. 82, pp. 384–391, 2012.

[38] B. D. James, D. A. Desantis, J. M. Huya-Kouadio, C. Houchins, and G. Saur, "Analysis of Advanced H 2 Production Pathways from Strategic Analysis," tech. rep., 2020.

[39] T. Nguyen, Z. Abdin, T. Holm, and W. Mérida, "Grid-connected hydrogen production via large-scale water electrolysis," *Energy Conversion and Management*, vol. 200, no. October, p. 112108, 2019.

[40] O. Toussi, "White Paper: Hydrogen Production Cost by AEM Water Electrolysis," tech. rep., 2020.

[41] J. R. Varcoe, P. Atanassov, D. R. Dekel, A. M. Herring, M. A. Hickner, P. A. Kohl, A. R. Kucernak, W. E. Mustain, K. Nijmeijer, K. Scott, T. Xu, and L. Zhuang, "Anion-exchange membranes in electrochemical energy systems," *Energy and Environmental Science*, vol. 7, no. 10, pp. 3135–3191, 2014.

[42] G. Merle, M. Wessling, and K. Nijmeijer, "Anion exchange membranes for alkaline fuel cells: A review," *Journal of Membrane Science*, vol. 377, no. 1-2, pp. 1–35, 2011.

[43] K. F. Hagesteijn, S. Jiang, and B. P. Ladewig, "A review of the synthesis and characterization of anion exchange membranes," *Journal of Materials Science*, vol. 53, no. 16, pp. 11131–11150, 2018.

[44] J. Pan, C. Chen, L. Zhuang, and J. Lu, "Designing advanced alkaline polymer electrolytes for fuel cell applications," *Accounts of Chemical Research*, vol. 45, no. 3, pp. 473–481, 2012.

[45] K. A. Mauritz and R. B. Moore, "State of understanding of Nafion," *Chemical Reviews*, vol. 104, no. 10, pp. 4535–4586, 2004.

[46] N. Li and M. D. Guiver, "Ion transport by nanochannels in ion-containing aromatic copolymers," *Macromolecules*, vol. 47, no. 7, pp. 2175–2198, 2014.

[47] J. Ran, L. Wu, and T. Xu, “Enhancement of hydroxide conduction by self-assembly in anion conductive comb-shaped copolymers,” *Polymer Chemistry*, vol. 4, no. 17, pp. 4612–4620, 2013.

[48] D. Henkensmeier, M. Najibah, C. Harms, J. Žitka, J. Hnát, and K. Bouzek, “Overview: State-of-the Art Commercial Membranes for Anion Exchange Membrane Water Electrolysis,” *Journal of Electrochemical Energy Conversion and Storage*, vol. 18, no. 2, 2021.

[49] B. V. Tilak and B. E. Conway, “High performance electrode materials for the hydrogen evolution reaction from alkaline media,” *Proc. Indian Acad. Sci. (Chem. Sci.)*, vol. 97, no. 4, pp. 359–393, 1986.

[50] C. González-Buch, I. Herraiz-Cardona, E. M. Ortega, J. García-Antón, and V. Pérez-Herranz, “Development of Ni-Mo, Ni-W and Ni-Co Macroporous Materials for Hydrogen Evolution Reaction,” *Chemical Engineering Science*, vol. 32, 2013.

[51] D. E. Brown, M. N. Mahmood, M. C. M. Man, and A. K. Turner, “Preparation and characterization of low overvoltage transition metal alloy electrocatalysts for hydrogen evolution in alkaline solutions,” *Electrochimica Acta*, vol. 29, no. 11, pp. 1551–1556, 1984.

[52] I. A. Raj, “Nickel-based, binary-composite electrocatalysts for the cathodes in the energy-efficient industrial production of hydrogen from alkaline-water electrolytic cells,” *Journal of Materials Science*, vol. 28, no. 16, pp. 4375–4382, 1993.

[53] I. A. Raj and K. I. Vasu, “Transition metal-based hydrogen electrodes in alkaline solution - electrocatalysis on nickel based binary alloy coatings,” *Journal of Applied Electrochemistry*, 1990.

[54] I. S. McKay, J. A. Schwalbe, E. D. Goodman, J. J. Willis, A. Majumdar, and M. Cargnello, “Elucidating the synergistic mechanism of nickel-molybdenum electrocatalysts for the hydrogen evolution reaction,” *MRS Communications*, vol. 6, no. 3, pp. 241–246, 2016.

[55] P. Quaino, F. Juarez, E. Santos, and W. Schmickler, “Volcano plots in hydrogen electrocatalysis-uses and abuses,” *Beilstein Journal of Nanotechnology*, vol. 5, no. 1, pp. 846–854, 2014.

[56] N. V. Krstajić, L. Gajić-Krstajić, U. Lačnjevac, B. M. Jović, S. Mora, and V. D. Jović, “Non-noble metal composite cathodes for hydrogen evolution. Part I: The Ni-MoOxcoatings electrodeposited from Watt’s type bath containing MoO3powder particles,” *International Journal of Hydrogen Energy*, vol. 36, no. 11, pp. 6441–6449, 2011.

[57] J. K. Nørskov, T. Bligaard, A. Logadottir, J. R. Kitchin, J. G. Chen, S. Pandelov, and U. Stimming, "Trends in the Exchange Current for Hydrogen Evolution," *Journal of The Electrochemical Society*, vol. 152, no. 3, p. J23, 2005.

[58] J. R. McKone, S. C. Marinescu, B. S. Brunschwig, J. R. Winkler, and H. B. Gray, "Earth-abundant hydrogen evolution electrocatalysts," *Chemical Science*, vol. 5, no. 3, pp. 865–878, 2014.

[59] M. M. Jakšić, "Brewer intermetallic phases as synergetic electrocatalysts for hydrogen evolution," *Materials Chemistry and Physics*, vol. 22, no. 1-2, pp. 1–26, 1989.

[60] J. R. McKone, B. F. Sadtler, C. A. Werlang, N. S. Lewis, and H. B. Gray, "Ni-Mo nanopowders for efficient electrochemical hydrogen evolution," *ACS Catalysis*, vol. 3, no. 2, pp. 166–169, 2013.

[61] V. D. Jović, B. M. Jović, U. Lačnjevac, G. Branković, S. Bernik, and A. Rečnik, "An attempt to predict the mechanism of Mo-Ni-O powders electrodeposition from the results of their TEM analysis," *Electrochimica Acta*, vol. 55, no. 13, pp. 4188–4193, 2010.

[62] L. S. Sanches, S. H. Domingues, C. E. B. Marino, and L. H. Mascaro, "Characterisation of electrochemically deposited Ni–Mo alloy coatings," *Electrochemistry Communications*, vol. 6, pp. 543–548, 6 2004.

[63] Z. Liang, H. S. Ahn, and A. J. Bard, "A Study of the Mechanism of the Hydrogen Evolution Reaction on Nickel by Surface Interrogation Scanning Electrochemical Microscopy," *Journal of the American Chemical Society*, vol. 139, no. 13, pp. 4854–4858, 2017.

[64] R. Subbaraman, D. Tripkovic, K. C. Chang, D. Strmcnik, A. P. Paulikas, P. Hirunsit, M. Chan, J. Greeley, V. Stamenkovic, and N. M. Markovic, "Trends in activity for the water electrolyser reactions on 3d M(Ni,Co,Fe,Mn) hydr(oxy)oxide catalysts," *Nature Materials*, vol. 11, no. 6, pp. 550–557, 2012.

[65] N. Danilovic, R. Subbaraman, D. Strmcnik, K. C. Chang, A. P. Paulikas, V. R. Stamenkovic, and N. M. Markovic, "Enhancing the alkaline hydrogen evolution reaction activity through the bifunctionality of Ni(OH)2/metal catalysts," *Angewandte Chemie - International Edition*, vol. 51, no. 50, pp. 12495–12498, 2012.

[66] M. Pourbaix, "Atlas of electrochemical equilibria in aqueous solutions," 1966.

[67] A. G. Oshchepkov, G. Braesch, A. Bonnefont, E. R. Savinova, and M. Chatenet, “Recent Advances in the Understanding of Nickel-Based Catalysts for the Oxidation of Hydrogen-Containing Fuels in Alkaline Media,” *ACS Catalysis*, vol. 10, no. 13, pp. 7043–7068, 2020.

[68] E. S. Davydova, F. D. Speck, M. T. Y. Paul, D. R. Dekel, and S. Cherevko, “Stability Limits of Ni-Based Hydrogen Oxidation Electrocatalysts for Anion Exchange Membrane Fuel Cells,” *ACS Catalysis*, vol. 9, no. 8, pp. 6837–6845, 2019.

[69] P. Mars, T. V. D. Mono, and J. J. F. Scholten, “Storage stability of nickel catalysts decrease in activity of nickel catalysts under liquids, with special reference to raney nickel,” *Industrial and Engineering Chemistry Product Research and Development*, vol. 1, no. 3, pp. 161–164, 1962.

[70] T. Kenjo, “Chromium-Doped Raney Nickel Hydrogen Electrodes in Alkaline Fuel Cells,” *Journal of Electrochemical Science and Technology*, vol. 132, no. 2, pp. 383–386, 1985.

[71] T. Tomida and I. Nakabayashi, “Spongy Raney Nickel Hydrogen Electrodes for Alkaline Fuel Cells,” *Journal of The Electrochemical Society*, vol. 136, no. 11, pp. 3296–3298, 1989.

[72] W. Jenseit, A. Khalil, and H. Wendt, “Material properties and processing in the production of fuel cell components: I. Hydrogen anodes from Raney nickel for lightweight alkaline fuel cells,” *Journal of Applied Electrochemistry*, vol. 20, no. 6, pp. 893–900, 1990.

[73] H. K. Lee, E. E. Jung, and J. S. Lee, “Enhancement of catalytic activity of Raney nickel by cobalt addition,” *Materials Chemistry and Physics*, vol. 55, no. 2, pp. 89–93, 1998.

[74] J. P. Shim, Y. S. Park, H. K. Lee, and J. S. Lee, “Hydrogen oxidation characteristics of Raney nickel electrodes with carbon black in an alkaline fuel cell,” *Journal of Power Sources*, vol. 74, no. 1, pp. 151–154, 1998.

[75] J. A. Linnekoski, A. O. I. Krause, J. Keskinen, J. Lamminen, and T. Anttila, “Processing of Raney-Nickel Catalysts for Alkaline Fuel Cell Applications,” *Journal of Fuel Cell Science and Technology*, vol. 4, no. 1, p. 45, 2007.

[76] Y. Kiros and S. Schwartz, “Long-term hydrogen oxidation catalysts in alkaline fuel cells,” *Journal of Power Sources*, vol. 87, no. 1, pp. 101–105, 2000.

[77] K. Mund, “Titanium-Containing Raney Nickel Catalyst for Hydrogen Electrodes in Alkaline Fuel Cell Systems,” *Journal of The Electrochemical Society*, vol. 124, no. 1, p. 1, 1977.

[78] S. Lu, J. Pan, A. Huang, L. Zhuang, and J. Lu, "Alkaline polymer electrolyte fuel cells completely free from noble metal catalysts," *Proceedings of the National Academy of Sciences of the United States of America*, vol. 105, no. 52, pp. 20611–20614, 2008.

[79] A. Serov and P. I. A. Serov, "Development of PGM-free Catalysts for Hydrogen Oxidation Reaction in Alkaline Media," tech. rep., 2016.

[80] A. G. Oshchepkov, P. A. Simonov, O. V. Cherstiouk, R. R. Nazmutdinov, D. V. Glukhov, V. I. Zaikovskii, T. Y. Kardash, R. I. Kvon, A. Bonnefont, A. N. Simonov, V. N. Parmon, and E. R. Savinova, "On the effect of Cu on the activity of carbon supported Ni nanoparticles for hydrogen electrode reactions in alkaline medium," *Topics in Catalysis*, vol. 58, no. 18-20, pp. 1181–1192, 2015.

[81] O. V. Cherstiouk, P. A. Simonov, A. G. Oshchepkov, V. I. Zaikovskii, T. Y. Kardash, A. Bonnefont, V. N. Parmon, and E. R. Savinova, "Electrocatalysis of the hydrogen oxidation reaction on carbon-supported bimetallic NiCu particles prepared by an improved wet chemical synthesis," *Journal of Electroanalytical Chemistry*, vol. 783, pp. 146–151, 2016.

[82] S. Kabir, K. Lemire, K. Artyushkova, A. Roy, M. Odgaard, D. Schlueter, A. Oshchepkov, A. Bonnefont, E. Savinova, D. C. Sabarirajan, P. Mandal, E. J. Crumlin, I. V. Zenyuk, P. Atanassov, and A. Serov, "Platinum group metal-free NiMo hydrogen oxidation catalysts: High performance and durability in alkaline exchange membrane fuel cells," *Journal of Materials Chemistry A*, vol. 5, no. 46, pp. 24433–24443, 2017.

[83] E. S. Davydova, J. Zaffran, K. Dhaka, M. C. Toroker, and D. R. Dekel, "Hydrogen oxidation on Ni-based electrocatalysts: The effect of metal doping," *Catalysts*, vol. 8, no. 10, p. 454, 2018.

[84] A. Roy, M. R. Talarposhti, S. J. Normile, I. V. Zenyuk, V. De Andrade, K. Artyushkova, A. Serov, and P. Atanassov, "Nickel-copper supported on a carbon black hydrogen oxidation catalyst integrated into an anion-exchange membrane fuel cell," *Sustainable Energy and Fuels*, vol. 2, no. 10, pp. 2268–2275, 2018.

[85] Y. Cong, B. Yi, and Y. Song, "Hydrogen oxidation reaction in alkaline media: From mechanism to recent electrocatalysts," 2018.

[86] E. S. Davydova, S. Mukerjee, F. Jaouen, and D. R. Dekel, "Electrocatalysts for Hydrogen Oxidation Reaction in Alkaline Electrolytes," *ACS Catalysis*, vol. 8, no. 7, pp. 6665–6690, 2018.

[87] G. Wang, W. Li, B. Huang, L. Xiao, J. Lu, and L. Zhuang, "Exploring the Composition-Activity Relation of Ni-Cu Binary Alloy Electrocatalysts for Hydrogen Oxidation Reaction in Alkaline Media," *ACS Applied Energy Materials*, vol. 2, no. 5, pp. 3160–3165, 2019.

[88] Y. Duan, Z. Y. Yu, L. Yang, L. R. Zheng, C. T. Zhang, X. T. Yang, F. Y. Gao, X. L. Zhang, X. Yu, R. Liu, H. H. Ding, C. Gu, X. S. Zheng, L. Shi, J. Jiang, J. F. Zhu, M. R. Gao, and S. H. Yu, "Bimetallic nickel-molybdenum/tungsten nanoalloys for high-efficiency hydrogen oxidation catalysis in alkaline electrolytes," *Nature Communications*, vol. 11, no. 1, pp. 1–10, 2020.

[89] W. Sheng, A. P. Bivens, M. Myint, Z. Zhuang, R. V. Forest, Q. Fang, J. G. Chen, and Y. Yan, "Non-precious metal electrocatalysts with high activity for hydrogen oxidation reaction in alkaline electrolytes," *Energy and Environmental Science*, vol. 7, no. 5, pp. 1719–1724, 2014.

[90] Z. Zhuang, S. A. Giles, J. Zheng, G. R. Jenness, S. Caratzoulas, D. G. Vlachos, and Y. Yan, "Nickel supported on nitrogen-doped carbon nanotubes as hydrogen oxidation reaction catalyst in alkaline electrolyte," *Nature Communications*, vol. 7, pp. 1–8, 2016.

[91] A. G. Oshchepkov, A. Bonnefont, S. N. Pronkin, O. V. Cherstiouk, C. Ulhaq-Bouillet, V. Papaefthimiou, V. N. Parmon, and E. R. Savinova, "Nanostructured nickel nanoparticles supported on vulcan carbon as a highly active catalyst for the hydrogen oxidation reaction in alkaline media," *Journal of Power Sources*, vol. 402, no. September, pp. 447–452, 2018.

[92] F. Yang, X. Bao, Y. Zhao, X. Wang, G. Cheng, and W. Luo, "Enhanced HOR catalytic activity of PGM-free catalysts in alkaline media: The electronic effect induced by different heteroatom doped carbon supports," *Journal of Materials Chemistry A*, vol. 7, no. 18, pp. 10936–10941, 2019.

[93] W. Sheng, A. P. Bivens, M. Myint, Z. Zhuang, R. V. Forest, Q. Fang, J. G. Chen, and Y. Yan, "Non-precious metal electrocatalysts with high activity for hydrogen oxidation reaction in alkaline electrolytes," *Energy and Environmental Science*, vol. 7, no. 5, pp. 1719–1724, 2014.

[94] N. T. Suen, S. F. Hung, Q. Quan, N. Zhang, Y. J. Xu, and H. M. Chen, "Electrocatalysis for the oxygen evolution reaction: Recent development and future perspectives," *Chemical Society Reviews*, vol. 46, no. 2, pp. 337–365, 2017.

[95] E. Fabbri, A. Habereder, K. Waltar, R. Kötz, and T. J. Schmidt, "Developments and perspectives of oxide-based catalysts for the oxygen evolution reaction," *Catal. Sci. Technol.*, vol. 4, no. 11, pp. 3800–3821, 2014.

[96] F. Song, L. Bai, A. Moysiadou, S. Lee, C. Hu, L. Liardet, and X. Hu, "Transition Metal Oxides as Electrocatalysts for the Oxygen Evolution Reaction in Alkaline Solutions: An Application-Inspired Renaissance," *Journal of the American Chemical Society*, vol. 140, no. 25, pp. 7748–7759, 2018.

[97] T. Binninger, R. Mohamed, K. Waltar, E. Fabbri, P. Levecque, R. Kötz, and T. J. Schmidt, "Thermodynamic explanation of the universal correlation between oxygen evolution activity and corrosion of oxide catalysts," *Scientific Reports*, vol. 5, no. February, pp. 1–7, 2015.

[98] C. C. L. McCrory, S. Jung, I. M. Ferrer, S. M. Chatman, J. C. Peters, and T. F. Jaramillo, "Benchmarking Hydrogen Evolving Reaction and Oxygen Evolving Reaction Electrocatalysts for Solar Water Splitting Devices," *Journal of the American Chemical Society*, vol. 137, no. 13, pp. 4347–4357, 2015.

[99] L. Trotochaud and S. W. Boettcher, "Precise oxygen evolution catalysts: Status and opportunities," *Scripta Materialia*, vol. 74, pp. 25–32, 2014.

[100] D. A. Corrigan, "The Catalysis of the Oxygen Evolution Reaction by Iron Impurities in Thin Film Nickel Oxide Electrodes," *Journal of The Electrochemical Society*, vol. 134, no. 2, p. 377, 1987.

[101] M. Gong and H. Dai, "A mini review of NiFe-based materials as highly active oxygen evolution reaction electrocatalysts," *Nano Research*, vol. 8, no. 1, pp. 23–39, 2015.

[102] M. S. Burke, S. Zou, L. J. Enman, J. E. Kellon, C. A. Gabor, E. Pledger, and S. W. Boettcher, "Revised Oxygen Evolution Reaction Activity Trends for First-Row Transition-Metal (Oxy)hydroxides in Alkaline Media," *Journal of Physical Chemistry Letters*, vol. 6, no. 18, pp. 3737–3742, 2015.

[103] Z. Lu, W. Xu, W. Zhu, Q. Yang, X. Lei, J. Liu, Y. Li, X. Sun, and X. Duan, "Three-Dimensional NiFe Layered Double Hydroxide Film for High-efficiency Oxygen Evolution Reaction," *RSC Chem Communication*, 2012.

[104] M. Gong, Y. Li, H. Wang, Y. Liang, J. Z. Wu, J. Zhou, J. Wang, T. Regier, F. Wei, and H. Dai, "An advanced Ni-Fe layered double hydroxide electrocatalyst for water oxidation," *Journal of the American Chemical Society*, vol. 135, no. 23, pp. 8452–8455, 2013.

[105] Y. Li, H. Wang, L. Xie, Y. Liang, G. Hong, and H. Dai, "MoS2 nanoparticles grown on graphene: An advanced catalyst for the hydrogen evolution reaction," *Journal of the American Chemical Society*, vol. 133, no. 19, pp. 7296–7299, 2011.

[106] Y. Feng, H. Zhang, Y. Zhang, X. Li, and Y. Wang, "Ultrathin two-dimensional free-standing sandwiched NiFe/C for high-efficiency oxygen evolution reaction," *ACS Applied Materials and Interfaces*, vol. 7, no. 17, pp. 9203–9210, 2015.

[107] Y. H. Chung, I. Jang, J. H. Jang, H. S. Park, H. C. Ham, J. H. Jang, Y. K. Lee, and S. J. Yoo, "Anomalous in situ Activation of Carbon-Supported Ni2P Nanoparticles for Oxygen Evolving Electrocatalysis in Alkaline Media," *Scientific Reports*, vol. 7, no. 1, pp. 1–8, 2017.

[108] S. Klaus, Y. Cai, M. W. Louie, L. Trotochaud, and A. T. Bell, "Effects of Fe electrolyte impurities on Ni(OH)2/NiOOH structure and oxygen evolution activity," *Journal of Physical Chemistry C*, vol. 119, no. 13, pp. 7243–7254, 2015.

[109] M. W. Louie and A. T. Bell, "An investigation of thin-film Ni-Fe oxide catalysts for the electrochemical evolution of oxygen," *Journal of the American Chemical Society*, vol. 135, no. 33, pp. 12329–12337, 2013.

[110] J. Chaston, "The growing industrial use of the platinum metals," *Platinum Metals Review*, vol. 26, no. 1, pp. 3–9, 1982.

[111] J. Matthey, "About PGM - PMM," pp. 2–3, 2015.

[112] T. Bell, "The Properties and Applications of Platinum," 2020.

[113] World Platinum Investment Council, "Platinum Industrial Demand," 2020.

[114] C. Shaffer, "Platinum Group Metals at Work : Industrial Applications Chemical processing Nitric acid," *Accelerating Science*, pp. 1–4, 2015.

[115] M. V. Twigg, "Progress and future challenges in controlling automotive exhaust gas emissions," *Applied Catalysis B: Environmental*, vol. 70, no. 1-4, pp. 2–15, 2007.

[116] M. S. Paraskevas, K. Papoutsi, and M. Ochsenkühn-Petropoulou, "A Novel Way of Sampling Particles Containing Platinum Group Elements from Automobile Catalysts," *Analytical Letters*, vol. 45, no. 5-6, pp. 539–550, 2012.

[117] M. Moldovan, M. M. Gömez, and M. A. Palacios, "Determination of platinum, rhodium and palladium in car exhaust fumes," *Journal of analytical atomic spectrometry*, vol. 14, no. 8, pp. 1163–1169, 1999.

[118] S. E. Golunski, "Why use platinum in catalytic converters?," *Platinum Metals Review*, vol. 51, no. 3, p. 162, 2007.

[119] A. u. R. Salman, B. C. Enger, X. Auvray, R. Lødeng, M. Menon, D. Waller, and M. Rønning, "Catalytic oxidation of NO to NO2 for nitric acid production over a Pt/Al2O3 catalyst," *Applied Catalysis A: General*, vol. 564, no. 2, pp. 142–146, 2018.

[120] C. A. Grande, K. A. Andreassen, J. H. Cavka, D. Waller, O. A. Lorentsen, H. Øien, H. J. Zander, S. Poulston, S. García, and D. Modeshia, "Process Intensification in Nitric Acid Plants by Catalytic Oxidation of Nitric Oxide," *Industrial and Engineering Chemistry Research*, vol. 57, no. 31, pp. 10180–10186, 2018.

[121] L. N. Lewis, J. Stein, Y. Gao, R. E. Colborn, and G. Hutchins, "Platinum catalysts used in the silicone industry," *Platinum Matals Reviews*, vol. 41, no. 2, pp. 66–75, 1997.

[122] R. Y. Lukin, A. M. Kuchkaev, A. V. Sukhov, G. E. Bekmukhamedov, and D. G. Yakhvarov, "Platinum-catalyzed hydrosilylation in polymer chemistry," *Polymers*, vol. 12, no. 10, pp. 1–22, 2020.

[123] J. Pellegrino, S. Brueske, T. Carole, S. Richlen, and B. Valentine, "Energy and Environmental Profile of the U.S. Petroleum Refining Industry," tech. rep., 2007.

[124] V. Kapustin, E. Chernysheva, A. Maximova, and Y. Zinchenko, "Development of new catalytic processes for processing petroleum feedstock," *Pure and Applied Chemistry*, vol. 89, no. 10, pp. 1579–1585, 2017.

[125] S. M. Alia and B. S. Pivovar, "Evaluating Hydrogen Evolution and Oxidation in Alkaline Media to Establish Baselines," *Journal of The Electrochemical Society*, vol. 165, no. 7, pp. F441–F455, 2018.

[126] J. Zheng, W. Sheng, Z. Zhuang, B. Xu, and Y. Yan, "Universal dependence of hydrogen oxidation and evolution reaction activity of platinum-group metals on pH and hydrogen binding energy," *Science Advances*, vol. 2, no. 3, pp. 1–9, 2016.

[127] A. Zadick, L. Dubau, N. Sergent, G. Berthomé, and M. Chatenet, "Huge Instability of Pt/C Catalysts in Alkaline Medium," *ACS Catalysis*, vol. 5, no. 8, pp. 4819–4824, 2015.

[128] W. Sheng, H. A. Gasteiger, and Y. Shao-Horn, "Hydrogen Oxidation and Evolution Reaction Kinetics on Platinum: Acid vs Alkaline Electrolytes," *Journal of The Electrochemical Society*, vol. 157, no. 11, p. B1529, 2010.

[129] D. J. Weber, C. Dosche, and M. Oezaslan, “Fundamental Aspects of Contamination during the Hydrogen Evolution/Oxidation Reaction in Alkaline Media,” *Journal of The Electrochemical Society*, vol. 167, no. 2, p. 024506, 2020.

[130] D. J. Weber, M. Janssen, and M. Oezaslan, “Effect of Monovalent Cations on the HOR/HER Activity for Pt in Alkaline Environment,” *Journal of The Electrochemical Society*, vol. 166, no. 2, pp. F66–F73, 2019.

[131] J. N. Hansen, H. Prats, K. K. Toudahl, N. Mørch Secher, K. Chan, J. Kibsgaard, and I. Chorkendorff, “Is There Anything Better than Pt for HER?,” *ACS Energy Letters*, pp. 1175–1180, 2021.

[132] K. G. Chandler, D. J. Genders, and D. Pletcher, “Electrodes Based on Noble Metals,” *Platinum Metals Rev.*, vol. 41, no. 2, pp. 54–63, 1997.

[133] P. Hayfield, “Development of the Noble Metal / Oxide Coated Titanium Electrode,” *Platinum Metals Review*, vol. 42, no. 1, pp. 27–33, 1998.

[134] A. Kongkanand, W. Gu, and M. F. Mathias, “Fuel Cells and Hydrogen Production,” *Fuel Cells and Hydrogen Production*, 2019.

[135] P. J. Ferreira, G. J. la O’, Y. Shao-Horn, D. Morgan, R. Makharia, S. Kocha, and H. A. Gasteiger, “Instability of PtC Electrocatalysts in Proton Exchange Membrane Fuel Cells,” *Journal of The Electrochemical Society*, vol. 152, no. 11, p. A2256, 2005.

[136] R. Mom, L. Frevel, J. J. Velasco-Vélez, M. Plodinec, A. Knop-Gericke, and R. Schlögl, “The Oxidation of Platinum under Wet Conditions Observed by Electrochemical X-ray Photoelectron Spectroscopy,” *Journal of the American Chemical Society*, vol. 141, no. 16, pp. 6537–6544, 2019.

[137] L. Tang, B. Han, K. Persson, C. Friesen, T. He, K. Sieradzki, and G. Ceder, “Electrochemical stability of nanometer-scale Pt particles in acidic environments,” *Journal of the American Chemical Society*, vol. 132, no. 2, pp. 596–600, 2010.

[138] L. Jacobse, M. J. Rost, and M. T. Koper, “Atomic-Scale Identification of the Electrochemical Roughening of Platinum,” *ACS Central Science*, vol. 5, no. 12, pp. 1920–1928, 2019.

[139] H. Yang, Y. Tang, and S. Zou, “Electrochemical removal of surfactants from Pt nanocubes,” *Electrochemistry Communications*, vol. 38, pp. 134–137, 2014.

[140] S. Cherevko, A. R. Zeradjanin, G. P. Keeley, and K. J. J. Mayrhofer, “A Comparative Study on Gold and Platinum Dissolution in Acidic and Alkaline Media,” *Journal of The Electrochemical Society*, vol. 161, no. 12, pp. H822–H830, 2014.

[141] C. Wei, R. R. Rao, J. Peng, B. Huang, I. E. Stephens, M. Risch, Z. J. Xu, and Y. Shao-Horn, “Recommended Practices and Benchmark Activity for Hydrogen and Oxygen Electrocatalysis in Water Splitting and Fuel Cells,” *Advanced Materials*, vol. 31, no. 31, 2019.

[142] X. Deng, F. Galli, and M. T. Koper, “In Situ Electrochemical AFM Imaging of a Pt Electrode in Sulfuric Acid under Potential Cycling Conditions,” *Journal of the American Chemical Society*, vol. 140, no. 41, pp. 13285–13291, 2018.

[143] A. A. Topalov, I. Katsounaros, M. Auinger, S. Cherevko, J. C. Meier, S. O. Klemm, and K. J. Mayrhofer, “Dissolution of platinum: Limits for the deployment of electrochemical energy conversion?,” *Angewandte Chemie - International Edition*, vol. 51, no. 50, pp. 12613–12615, 2012.

[144] J. Solla-Gullón, V. Montiel, A. Aldaz, and J. Clavilier, “Electrochemical characterization of platinum nanoparticles prepared by microemulsion: How to clean them without loss of crystalline surface structure,” *Journal of Electroanalytical Chemistry*, vol. 491, no. 1-2, pp. 69–77, 2000.

[145] V. Climent and J. M. Feliu, “Thirty years of platinum single crystal electrochemistry,” *Journal of Solid State Electrochemistry*, vol. 15, no. 7-8, pp. 1297–1315, 2011.

[146] M. Mundschau and R. Vanselow, “Difficulties in the detection of surface impurities on platinum using Auger electron spectroscopy,” *Surface Science*, vol. 157, no. 1, pp. 87–98, 1985.

[147] M. Salmeron, L. Brewer, and G. Somorjai, “The Structure and Stability of Surface Platinum Oxide and of Oxides of Other Noble Metals,” *Surface Science*, vol. 112, pp. 207–228, 1981.

[148] N. Hodnik and S. Cherevko, “Spot the difference at the nanoscale: identical location electron microscopy in electrocatalysis,” *Current Opinion in Electrochemistry*, vol. 15, pp. 73–82, 2019.

[149] C. Lafforgue, M. Chatenet, L. Dubau, and D. R. Dekel, “Accelerated Stress Test of Pt/C Nanoparticles in an Interface with an Anion-Exchange Membrane - An Identical-Location Transmission Electron Microscopy Study,” *ACS Catalysis*, vol. 8, no. 2, pp. 1278–1286, 2018.

[150] T. S. Ahmadi, Z. L. Wang, T. C. Green, A. Henglein, and M. A. El-sayed, “Shape-Controlled Synthesis of Colloidal Platinum Nanoparticles,” *Science*, vol. 272, no. June 1996, pp. 1924–1926, 1996.

[151] U. S. Mehrotra, M. C. Agrawal, and S. P. Mushran, “Reduction of hexachloroplatinate by ascorbic acid,” *Journal of Inorganic and Nuclear Chemistry*, vol. 32, no. 7, pp. 2325–2329, 1970.

[152] F. J. Vidal-Iglesias, R. M. Arán-Ais, J. Solla-Gullón, E. Herrero, and J. M. Feliu, “Electrochemical characterization of shape-controlled Pt nanoparticles in different supporting electrolytes,” *ACS Catalysis*, vol. 2, no. 5, pp. 901–910, 2012.

[153] R. Y. Parapat, M. Wijaya, M. Schwarze, S. Selve, M. Willinger, and R. Schomäcker, “Particle shape optimization by changing from an isotropic to an anisotropic nanostructure: Preparation of highly active and stable supported Pt catalysts in microemulsions,” *Nanoscale*, vol. 5, no. 2, pp. 796–805, 2013.

[154] M. Yang and J. J. Xia, “Preparation and characterization of platinum nanorods using ascorbic acid as the reducing agent,” *Advanced Materials Research*, vol. 774-776, pp. 577–580, 2013.

[155] S. Senapati, S. P. Das, and A. K. Patnaik, “Kinetics and mechanism of oxidation of L-Ascorbic acid by Pt(IV)(aq) in aqueous hydrochloric acid medium,” *Advances in Physical Chemistry*, vol. 2012, pp. 2–7, 2012.

[156] J. D. Hoefelmeyer, K. Niesz, G. A. Somorjai, and T. D. Tilley, “Radial anisotropic growth of rhodium nanoparticles,” *Nano Letters*, vol. 5, no. 3, pp. 435–438, 2005.

[157] Y. Song, Y. Yang, C. J. Medforth, E. Pereira, A. K. Singh, H. Xu, Y. Jiang, C. J. Brinker, F. Van Swol, and J. A. Shelnutt, “Controlled Synthesis of 2-D and 3-D Dendritic Platinum Nanostructures,” *Journal of the American Chemical Society*, vol. 126, no. 2, pp. 635–645, 2004.

[158] F. Si, L. Ma, C. Liu, X. Zhang, and W. Xing, “The role of anisotropic structure and its aspect ratio: High-loading carbon nanospheres supported Pt nanowires with high performance toward methanol electrooxidation,” *RSC Advances*, vol. 2, no. 2, pp. 401–403, 2012.

[159] T. H. Yang, Y. Shi, A. Janssen, and Y. Xia, “Surface Capping Agents and Their Roles in Shape-Controlled Synthesis of Colloidal Metal Nanocrystals,” *Angewandte Chemie - International Edition*, vol. 59, no. 36, pp. 15378–15401, 2020.

[160] J. M. Petroski, Z. L. Wang, T. C. Green, and M. A. El-Sayed, “Kinetically controlled growth and shape formation mechanism of platinum nanoparticles,” *Journal of Physical Chemistry B*, vol. 102, no. 18, pp. 3316–3320, 1998.

[161] Y. Shiraishi and N. Toshima, “Oxidation of ethylene catalyzed by colloidal dispersions of poly(sodium acrylate)-protected silver nanoclusters,” *Colloids and Surfaces A: Physicochemical and Engineering Aspects*, vol. 169, no. 1-3, pp. 59–66, 2000.

[162] J. Solla-Gullón, F. J. Vidal-Iglesias, P. Rodríguez, E. Herrero, J. M. Feliu, J. Clavilier, and A. Aldaz, “In situ surface characterization of preferentially oriented platinum nanoparticles by using electrochemical structure sensitive adsorption reactions,” *Journal of Physical Chemistry B*, vol. 108, no. 36, pp. 13573–13575, 2004.

[163] J. Solla-Gullón, P. Rodríguez, E. Herrero, A. Aldaz, and J. M. Feliu, “Surface characterization of platinum electrodes,” *Phys. Chem. Chem. Phys.*, vol. 10, no. 10, pp. 1359–1373, 2008.

[164] A. Henglein, B. G. Ershov, and M. Malow, “Absorption spectrum and some chemical reactions of colloidal platinum in aqueous solution,” *Journal of Physical Chemistry*, vol. 99, no. 38, pp. 14129–14136, 1995.

[165] A. E. Russell, “Electrocatalysis: Theory and experiment at the interface,” *Physical Chemistry Chemical Physics*, vol. 10, no. 25, pp. 3607–3608, 2008.

[166] E. Herrero, J. M. Feliu, and A. Aldaz, “CO monolayer oxidation on semi-spherical and preferentially oriented (1 0 0) and (1 1 1) platinum nanoparticles,” vol. 8, pp. 189–194, 2006.

[167] K. Tong, X. Song, G. Xiao, and J. Yu, “Colloidal processing of Mg(OH)2 aqueous suspensions using sodium polyacrylate as dispersant,” *Industrial and Engineering Chemistry Research*, vol. 53, no. 12, pp. 4755–4762, 2014.

[168] K. Buyse, M. D. Gernon, R. Matton, and E. Van de Woestijne, “The benefits of alkanolamines over caustic: For pH neutralization of latex paint,” *PCI-Paint and Coatings Industry*, vol. 29, no. 5, 2013.

[169] L. J. Kirwan, P. D. Fawell, and W. Van Bronswijk, “An in situ FTIR-ATR study of polyacrylate adsorbed onto hematite at high pH and high ionic strength,” *Langmuir*, vol. 20, no. 10, pp. 4093–4100, 2004.

[170] J. J. Taylor and W. M. Sigmund, "Adsorption of sodium polyacrylate in high solids loading calcium carbonate slurries," *Journal of Colloid and Interface Science*, vol. 341, no. 2, pp. 298–302, 2010.

[171] B. Grabowska and M. Holtzer, "Structural examination of the cross-linking reaction mechanism of polyacrylate binding agents," *Archives of Metallurgy and Materials*, vol. 54, no. 2, pp. 427–437, 2009.

[172] W. Sheng, Z. Zhuang, M. Gao, J. Zheng, J. G. Chen, and Y. Yan, "Correlating hydrogen oxidation and evolution activity on platinum at different pH with measured hydrogen binding energy," *Nature Communications*, vol. 6, 2015.

[173] A. P. Yadav, T. Okayasu, Y. Sugawara, A. Nishikata, and T. Tsuru, "Effects of pH on Dissolution and Surface Area Loss of Platinum Due to Potential Cycling," vol. 159, no. 4, pp. 190–194, 2012.

[174] V. Komanicky, K. C. Chang, A. Menzel, N. M. Markovic, H. You, X. Wang, and D. Myers, "Stability and Dissolution of Platinum Surfaces in Perchloric Acid," *Journal of The Electrochemical Society*, vol. 153, no. 10, p. B446, 2006.

[175] P. P. Lopes, D. Tripkovic, P. F. Martins, D. Strmcnik, E. A. Ticianelli, V. R. Stamenkovic, and N. M. Markovic, "Dynamics of electrochemical Pt dissolution at atomic and molecular levels," *Journal of Electroanalytical Chemistry*, vol. 819, no. September, pp. 123–129, 2018.

[176] K. I. Ota, S. Nishigori, and N. Kamiya, "Dissolution of platinum anodes in sulfuric acid solution," *Journal of Electroanalytical Chemistry*, vol. 257, no. 1-2, pp. 205–215, 1988.

[177] P. P. Lopes, D. Li, H. Lv, C. Wang, D. Tripkovic, Y. Zhu, R. Schimmenti, H. Daimon, Y. Kang, J. Snyder, N. Becknell, K. L. More, D. Strmcnik, N. M. Markovic, M. Mavrikakis, and V. R. Stamenkovic, "Eliminating dissolution of platinum-based electrocatalysts at the atomic scale," *Nature Materials*, vol. 19, no. 11, pp. 1207–1214, 2020.

[178] V. I. Pavlov, E. V. Gerasimova, E. V. Zolotukhina, G. M. Don, Y. A. Dobrovolsky, and A. B. Yaroslavtsev, "Degradation of Pt/C electrocatalysts having different morphology in low-temperature PEM fuel cells," *Nanotechnologies in Russia*, vol. 11, no. 11-12, pp. 743–750, 2016.

[179] S. Rasouli, D. Myers, N. Kariuki, K. Higashida, N. Nakashima, and P. Ferreira, "Electrochemical Degradation of Pt-Ni Nanocatalysts: An Identical Location Aberration-Corrected

Scanning Transmission Electron Microscopy Study," *Nano Letters*, vol. 19, no. 1, pp. 46–53, 2019.

[180] A. Pavlišič, P. Jovanovič, V. S. Šelih, M. Šala, N. Hodnik, and M. Gaberšček, "Platinum Dissolution and Redeposition from Pt/C Fuel Cell Electrocatalyst at Potential Cycling," *Journal of The Electrochemical Society*, vol. 165, no. 6, pp. F3161–F3165, 2018.

[181] F. J. Scheijen, G. L. Beltramo, S. Hoeppener, T. H. Housmans, and M. T. Koper, "The electrooxidation of small organic molecules on platinum nanoparticles supported on gold: Influence of platinum deposition procedure," *Journal of Solid State Electrochemistry*, vol. 12, no. 5, pp. 483–495, 2008.

[182] D. E. Ramaker, D. Gatewood, A. Korovina, Y. Garsany, and K. E. Swider-Lyons, "Resolving sulfur oxidation and removal from Pt and Pt3Co electrocatalysts using in situ X-ray absorption spectroscopy," *Journal of Physical Chemistry C*, vol. 114, no. 27, pp. 11886–11897, 2010.

[183] C. Quijada, A. Rodes, J. L. Vázquez, J. M. Pérez, and A. Aldaz, "Electrochemical behaviour of aqueous SO2 at Pt electrodes in acidic medium. A voltammetric and in situ Fourier transform IR study Part I. Oxidation of SO2 on Pt electrodes with sulphur-oxygen adsorbed species," *Journal of Electroanalytical Chemistry*, vol. 394, no. 1-2, pp. 217–227, 1995.

[184] J. Durst, C. Simon, F. Hasché, and H. A. Gasteiger, "Hydrogen Oxidation and Evolution Reaction Kinetics on Carbon Supported Pt, Ir, Rh, and Pd Electrocatalysts in Acidic Media," *Journal of The Electrochemical Society*, vol. 162, no. 1, pp. F190–F203, 2015.

[185] J. Zheng, Y. Yan, and B. Xu, "Correcting the Hydrogen Diffusion Limitation in Rotating Disk Electrode Measurements of Hydrogen Evolution Reaction Kinetics," *Journal of The Electrochemical Society*, vol. 162, no. 14, pp. F1470–F1481, 2015.

[186] H. Wang and H. D. Abruña, "Rh and Rh Alloy Nanoparticles as Highly Active H2 Oxidation Catalysts for Alkaline Fuel Cells," *ACS Catalysis*, vol. 9, no. 6, pp. 5057–5062, 2019.

[187] H. Wang and H. D. Abruña, "Designing Synergistic Electrocatalysts for H2Oxidation and Evolution Reactions in Alkaline Media," *Journal of Physical Chemistry C*, vol. 125, no. 13, pp. 7188–7203, 2021.

[188] R. Subbaraman, D. Tripkovic, D. Strmcnik, K. C. Chang, M. Uchimura, a. P. Paulikas, V. Stamenkovic, and N. M. Markovic, "|vac ⟩) given an expected mean number of events m 0 = d 2 Np," *Science*, vol. 334, no. December, pp. 1256–1260, 2011.

[189] T. Hagyard and J. R. Williams, “Potential of aluminium in aqueous chloride solutions. Part 1,” *Transactions of the Faraday Society*, vol. 57, pp. 2288–2294, 1961.

[190] M. Nagai, A. M. Zahidul, and K. Matsuda, “Nano-structured nickel-molybdenum carbide catalyst for low-temperature water-gas shift reaction,” *Applied Catalysis A: General*, vol. 313, pp. 137–145, 2006.

[191] D. Li, H. Xu, and G. D. Guthrie, “Zeolite-supported Ni and Mo catalysts for hydrotreatments: II. HRTEM observations,” *Journal of Catalysis*, vol. 189, no. 2, pp. 281–296, 2000.

[192] A. E. Aksoylu, Z. Mõsõrlõ, and Z. I. Ç Lsen, “Interaction between nickel and molybdenum in Ni±Mo/Al2O3 catalysts: I. CO2 methanation and SEM-TEM studies,” *Applied Catalysis A: General*, vol. 168, pp. 385–397, 1998.

[193] Y. Peng, K. Jiang, W. Hill, Z. Lu, H. Yao, and H. Wang, “Large-Scale, Low-Cost, and High-Efficiency Water-Splitting System for Clean H2 Generation,” *ACS Applied Materials and Interfaces*, vol. 11, no. 4, pp. 3971–3977, 2019.

[194] J. Hou, Y. Wu, S. Cao, Y. Sun, and L. Sun, “Active Sites Intercalated Ultrathin Carbon Sheath on Nanowire Arrays as Integrated Core–Shell Architecture: Highly Efficient and Durable Electrocatalysts for Overall Water Splitting,” *Small*, vol. 13, no. 46, pp. 1–9, 2017.

[195] X. Tang, L. Xiao, C. Yang, J. Lu, and L. Zhuang, “Noble fabrication of Ni-Mo cathode for alkaline water electrolysis and alkaline polymer electrolyte water electrolysis,” *International Journal of Hydrogen Energy*, vol. 39, no. 7, pp. 3055–3060, 2014.

[196] M. Fang, W. Gao, G. Dong, Z. Xia, S. P. Yip, Y. Qin, Y. Qu, and J. C. Ho, “Hierarchical NiMo-based 3D electrocatalysts for highly-efficient hydrogen evolution in alkaline conditions,” *Nano Energy*, vol. 27, pp. 247–254, 2016.

[197] S. Peng, L. Li, H. B. Wu, S. Madhavi, and X. W. Lou, “Controlled growth of NiMoO4 nanosheet and nanorod arrays on various conductive substrates as advanced electrodes for asymmetric supercapacitors,” *Advanced Energy Materials*, vol. 5, no. 2, pp. 1–7, 2015.

[198] J. R. McKone, E. L. Warren, M. J. Bierman, S. W. Boettcher, B. S. Brunschwig, N. S. Lewis, and H. B. Gray, “Evaluation of Pt, Ni, and Ni-Mo electrocatalysts for hydrogen evolution on crystalline Si electrodes,” *Energy and Environmental Science*, vol. 4, no. 9, pp. 3573–3583, 2011.

[199] J. L. Brito, J. Laine, and K. C. Pratt, “Temperature-programmed reduction of Ni-Mo oxides,” *Journal of Materials Science*, vol. 24, no. 2, pp. 425–431, 1989.

[200] J. L. Brito, A. L. Barbosa, A. Albornoz, F. Severino, and J. Laine, “Nickel molybdate as precursor of HDS catalysts: Effect of phase composition,” *Catalysis Letters*, vol. 26, no. 3-4, pp. 329–337, 1994.

[201] R. Burch and A. Collins, “Temperature Programmed Reduction of Ni/Mo Hydrotreating Catalysts,” *Applied Catalysis*, vol. 18, pp. 389–400, 1985.

[202] S. Baoyi, X. Aiju, and W. Jiang, “The impact of preparation methods on the structure and catalytic performance of NiMoO4 for oxidative dehydrogenation of propane,” *Integrated Ferroelectrics*, vol. 171, no. 1, pp. 16–22, 2016.

[203] L. M. Madeira, M. F. Portela, and C. Mazzocchia, “Nickel molybdate catalysts and their use in the selective oxidation of hydrocarbons,” 2004.

[204] C. Mazzocchia, R. Anouchinsky, A. Kaddouri, M. Sautel, G. Thomas, D. I. Chimica, I. E. Ingegneria, and P. Di, “Thermal activation of typical oxidative catalyst preparation,” *Journal of Thermal Analysis*, vol. 40, pp. 1253–1265, 1993.

[205] C. Mazzocchia, C. Aboumrad, C. Diagne, E. Tempesti, J. M. Herrmann, and G. Thomas, “On the NiMoO4 oxidative dehydrogenation of propane to propene: some physical correlations with the catalytic activity,” *Catalysis Letters*, vol. 10, no. 3-4, pp. 181–191, 1991.

[206] A. I. Vagin, N. V. Burmistrova, and V. I. Erofeev, “Reduction kinetics of NiO-MoO3 catalysts,” *React. Kinet. Catal. Lett.*, vol. 28, no. 1, pp. 47–52, 1985.

[207] Y. Wang, G. Zhang, W. Xu, P. Wan, Z. Lu, Y. Li, and X. Sun, “A 3D Nanoporous Ni-Mo Electrocatalyst with Negligible Overpotential for Alkaline Hydrogen Evolution,” *ChemElectroChem*, vol. 1, no. 7, pp. 1138–1144, 2014.

[208] J. Zhang, T. Wang, P. Liu, Z. Liao, S. Liu, X. Zhuang, M. Chen, E. Zschech, and X. Feng, “Efficient hydrogen production on MoNi4 electrocatalysts with fast water dissociation kinetics,” *Nature Communications*, vol. 8, p. 15437, 2017.

[209] S. Zhao, J. Huang, Y. Liu, J. Shen, H. Wang, X. Yang, Y. Zhu, and C. Li, “Multimetallic Ni–Mo/Cu nanowires as nonprecious and efficient full water splitting catalyst,” *J. Mater. Chem. A*, vol. 5, no. 8, pp. 4207–4214, 2017.

[210] S. Shetty, M. Mohamed Jaffer Sadiq, D. K. Bhat, and A. C. Hegde, "Electrodeposition and characterization of Ni-Mo alloy as an electrocatalyst for alkaline water electrolysis," *Journal of Electroanalytical Chemistry*, vol. 796, pp. 57–65, 2017.

[211] M. Schalenbach, F. D. Speck, M. Ledendecker, O. Kasian, D. Goehl, A. M. Mingers, B. Breitbach, H. Springer, S. Cherevko, and K. J. Mayrhofer, "Nickel-molybdenum alloy catalysts for the hydrogen evolution reaction: Activity and stability revised," *Electrochimica Acta*, vol. 259, pp. 1154–1161, 2017.

[212] Y. Jin, X. Yue, C. Shu, S. Huang, and P. K. Shen, "Three-dimensional porous MoNi4 networks constructed by nanosheets as bifunctional electrocatalysts for overall water splitting," *J. Mater. Chem. A*, vol. 5, no. 6, pp. 2508–2513, 2017.

[213] P. M. Csernica, J. R. McKone, C. R. Mulzer, W. R. Dichtel, H. D. Abruña, and F. J. DiSalvo, "Electrochemical Hydrogen Evolution at Ordered Mo7Ni7," *ACS Catalysis*, vol. 7, no. 5, pp. 3375–3383, 2017.

[214] C. Xu, J. b. Zhou, M. Zeng, X. l. Fu, X. j. Liu, and J. m. Li, "Electrodeposition mechanism and characterization of Ni–Mo alloy and its electrocatalytic performance for hydrogen evolution," *International Journal of Hydrogen Energy*, vol. 41, no. 31, pp. 13341–13349, 2016.

[215] L. Zhang, K. Xiong, Y. Nie, X. Wang, J. Liao, and Z. Wei, "Sputtering nickel-molybdenum nanorods as an excellent hydrogen evolution reaction catalyst," *Journal of Power Sources*, vol. 297, pp. 413–418, 2015.

[216] J. Tian, N. Cheng, Q. Liu, X. Sun, Y. He, and A. M. Asiri, "Self-supported NiMo hollow nanorod array: an efficient 3D bifunctional catalytic electrode for overall water splitting," *J. Mater. Chem. A*, vol. 3, no. 40, pp. 20056–20059, 2015.

[217] Q. Han, S. Cui, N. Pu, J. Chen, K. Liu, and X. Wei, "A study on pulse plating amorphous Ni–Mo alloy coating used as HER cathode in alkaline medium," *International Journal of Hydrogen Energy*, vol. 35, no. 11, pp. 5194–5201, 2010.

[218] N. V. Krstajić, V. D. Jović, L. Gajić-Krstajić, B. M. Jović, A. L. Antozzi, and G. N. Martelli, "Electrodeposition of Ni-Mo alloy coatings and their characterization as cathodes for hydrogen evolution in sodium hydroxide solution," *International Journal of Hydrogen Energy*, vol. 33, no. 14, pp. 3676–3687, 2008.

[219] M. R. de Chialvo and A. C. Chialvo, "Hydrogen evolution reaction on smooth Ni(1x)+Mo(x) alloys (0x0.25)," *Journal of Electroanalytical Chemistry*, vol. 448, no. 1, pp. 87–93, 1998.

[220] A. Kawashima, E. Akiyama, H. Habazaki, and K. Hashimoto, "Characterization of sputter-deposited Ni-Mo and Ni-W alloy electrocatalysts for hydrogen evolution in alkaline solution," *Materials Science and Engineering: A*, vol. 226-228, pp. 905–909, 1997.

[221] W. Hu, X. Cao, F. Wang, and Y. Zhang, "A novel cathode for alkaline water electrolysis," *International Journal of Hydrogen Energy*, vol. 22, no. 6, pp. 621–623, 1997.

[222] C. Fan, "Study of Electrodeposited Nickel-Molybdenum, Nickel-Tungsten, Cobalt-Molybdenum, and Cobalt-Tungsten as Hydrogen Electrodes in Alkaline Water Electrolysis," *Journal of The Electrochemical Society*, vol. 141, no. 2, p. 382, 1994.

[223] J. Y. Huot, M. L. Trudeau, and R. Schulz, "Low Hydrogen Overpotential Nanocrystalline Ni-Mo Cathodes for Alkaline Water Electrolysis," *Journal of The Electrochemical Society*, vol. 138, no. 5, pp. 1316–1321, 1991.

[224] J. Divisek, H. Schmitz, and J. Balej, "Ni and Mo coatings as hydrogen cathodes," *Journal of Applied Electrochemistry*, vol. 19, no. 4, pp. 519–530, 1989.

[225] D. Stachurski, G. Pouli, G. Pokrzyk, and J. Ripas, "Low overvoltage hydrogen cathodes. U.S. Patent 4,354,915, October 19, 1982."

[226] A. Mantri, "Towards Scalable Synthesis Methods for Nickel-Molybdenum Alkaline Hydrogen Evolution Catalysts. Master's Thesis, University of Pittsburgh, Pittsburgh, PA, 2018 (Unpublished)," 2018.

[227] R. B. Patil, A. Mantri, S. D. House, J. C. Yang, and J. R. Mckone, "Enhancing the Performance of Ni-Mo Alkaline Hydrogen Evolution Electrocatalysts with Carbon Supports," *ACS Applied Energy Materials*, vol. 2, no. 4, pp. 2524–2533, 2019.

[228] D. Cai, D. Wang, B. Liu, Y. Wang, Y. Liu, L. Wang, H. Li, H. Huang, Q. Li, and T. Wang, "Comparison of the electrochemical performance of nimoo4 nanorods and hierarchical nanospheres for supercapacitor applications," *ACS Applied Materials & Interfaces*, vol. 5, no. 24, pp. 12905–12910, 2013.

[229] D. Guo, P. Zhang, H. Zhang, X. Yu, J. Zhu, Q. Li, and T. Wang, "NiMoO4 nanowires supported on Ni foam as novel advanced electrodes for supercapacitors," *Journal of Materials Chemistry A*, vol. 1, no. 32, pp. 9024–9027, 2013.

[230] P. R. Jothi, K. Shanthi, R. R. Salunkhe, M. Pramanik, V. Malgras, S. M. Alshehri, and Y. Yamauchi, "Synthesis and Characterization of {\$$\alpha$\$}-NiMoO4 Nanorods for Supercapacitor

Application," *European Journal of Inorganic Chemistry*, vol. 2015, no. 22, pp. 3694–3699, 2015.

[231] L. Lin, T. Liu, J. Liu, R. Sun, J. Hao, K. Ji, and Z. Wang, "Facile synthesis of groove-like NiMoO4 hollow nanorods for high-performance supercapacitors," *Applied Surface Science*, vol. 360, pp. 234–239, 2016.

[232] E. R. Ezeigwe, P. S. Khiew, C. W. Siong, I. Kong, and M. T. T. Tan, "Synthesis of NiMoO4 nanorods on graphene and superior electrochemical performance of the resulting ternary based composites," *Ceramics International*, vol. 43, no. 16, pp. 13772–13780, 2017.

[233] Z. Wang, G. Wei, K. Du, X. Zhao, M. Liu, S. Wang, Y. Zhou, C. An, and J. Zhang, "Ni Foam-Supported Carbon-Sheathed NiMoO4 Nanowires as Integrated Electrode for High-Performance Hybrid Supercapacitors," *ACS Sustainable Chemistry and Engineering*, vol. 5, no. 7, pp. 5964–5971, 2017.

[234] K. Hu, S. Jeong, M. Wakisaka, J.-i. Fujita, and Y. Ito, "Bottom-up Synthesis of Porous NiMo Alloy for Hydrogen Evolution Reaction," *Metals*, vol. 8, no. 2, p. 83, 2018.

[235] F. Nti, D. A. Anang, and J. I. Han, "Facilely synthesized NiMoO4/CoMoO4 nanorods as electrode material for high performance supercapacitor," *Journal of Alloys and Compounds*, vol. 742, pp. 342–350, 2018.

[236] Y. Zhang, H. Gao, X. Jia, S. Wang, J. Yan, H. Luo, K. Gao, H. Fang, A. Zhang, and L. Wang, "NiMoO4 nanorods supported on nickel foam for high-performance supercapacitor electrode materials," *Journal of Renewable and Sustainable Energy*, vol. 10, no. 5, p. 54101, 2018.

[237] C. Mazzocchia, F. Di Renzo, C. Aboumrad, and G. Thomas, "Stability of {\$$\beta$\$}-nickel molybdate," *Solid State Ionics*, vol. 32-33, no. PART 1, pp. 228–233, 1989.

[238] F. Di Renzo, C. Mazzocchia, G. Thomas, and A. M. Vernay, "Formation and properties of the solid solution of NiO in NiMoO4," *Reactivity of Solids*, vol. 6, no. 2-3, pp. 145–155, 1988.

[239] D. T. Hawkins and W. L. Worrell, "Hydrogen reduction of MoO3 at temperatures between 300 C and 450 C," *Metallurgical Transactions*, vol. 1, no. 1, pp. 271–273, 1970.

[240] E. Lalik, W. I. F. David, P. Barnes, and J. F. C. Turner, "Mechanisms of reduction of MoO3 to MoO2 reconciled?," *Journal of Physical Chemistry B*, vol. 105, no. 38, pp. 9153–9156, 2001.

[241] W. V. Schulmeyer and H. M. Ortner, “Mechanisms of the Hydrogen Reduction of Molybdenum Oxides,” in *15’ International Plansee Seminar*, vol. 3, pp. 129–146, 2001.

[242] M. Gong, W. Zhou, M. C. Tsai, J. Zhou, M. Guan, M. C. Lin, B. Zhang, Y. Hu, D. Y. Wang, J. Yang, S. J. Pennycook, B. J. Hwang, and H. Dai, “Nanoscale nickel oxide/nickel heterostructures for active hydrogen evolution electrocatalysis,” *Nature Communications*, vol. 5, pp. 1–6, 2014.

[243] X. Yu, J. Zhao, L. R. Zheng, Y. Tong, M. Zhang, G. Xu, C. Li, J. Ma, and G. Shi, “Hydrogen Evolution Reaction in Alkaline Media: Alpha- or Beta-Nickel Hydroxide on the Surface of Platinum?,” *ACS Energy Letters*, vol. 3, no. 1, pp. 237–244, 2018.

[244] W. Yuhong, L. Wei, Z. Minghui, G. Naijia, and T. Keyi, “Characterization and catalytic properties of supported nickel molybdenum nitrides for hydrodenitrogenation,” *Applied Catalysis A: General*, no. 215, pp. 39–45, 2001.

[245] C. Suresh, D. Santhanaraj, M. Gurulakshmi, G. Deepa, M. Selvaraj, N. R. S. Rekha, and K. Shanthi, “Mo-Ni/Al-SBA-15 (Sulfide) catalysts for hydrodenitrogenation: Effect of Si/Al ratio on catalytic activity,” *ACS Catalysis*, vol. 2, pp. 127–134, 2012.

[246] J. L. Brito, F. Severino, N. N. Delgado, and J. Laine, “HDS activity of carbon-supported Ni-Mo catalysts derived from thiomolybdate complexes,” *Applied Catalysis A: General*, vol. 173, pp. 193–199, 1998.

[247] T. Klimova, D. A. Solís-Casados, and J. Ramírez, “New selective Mo and NiMo HDS catalysts supported on Al2O3-MgO(x) mixed oxides,” *Catalysis Today*, vol. 43, no. 1-2, pp. 135–146, 1998.

[248] D. Li, A. Nishijima, and D. E. Morris, “Zeolite-supported Ni and Mo catalysts for hydrotreatments: I. Catalytic Activity and Spectroscopy,” *Journal of Catalysis*, vol. 182, pp. 339–348, 1999.

[249] V. E. Borisenko and P. J. Hesketh, *Rapid Thermal Processing of Semiconductors*. Plenum Press, New York, 1997.

[250] R. B. Fair, *Rapid Thermal Processing: Science and Technology*. Academic Press Inc., 1st ed., 1993.

[251] T. Iwasita, H. Hoster, A. John-Anacker, W. F. Lin, and W. Vielstich, “Methanol oxidation on PtRu electrodes. Influence of surface structure and Pt-Ru atom distribution,” *Langmuir*, vol. 16, no. 2, pp. 522–529, 2000.

[252] W. Chrzanowski, H. Kim, and A. Wieckowski, “Enhancement in methanol oxidation by spontaneously deposited ruthenium on low-index platinum electrodes,” *Catalysis Letters*, vol. 50, no. 3-4, pp. 69–75, 1998.

[253] D. S. Hall, D. J. Lockwood, C. Bock, and B. R. MacDougall, “Nickel hydroxides and related materials: A review of their structures, synthesis and properties,” *Proceedings of the Royal Society A: Mathematical, Physical and Engineering Sciences*, vol. 471, no. 2174, 2015.

[254] Wolfram and Research, “Electrical Conductivity of the Elements.”

[255] H. Chen, D. Wang, Y. Yu, K. A. Newton, D. A. Muller, H. Abruña, and F. J. Disalvo, “A surfactant-free strategy for synthesizing and processing intermetallic platinum-based nanoparticle catalysts,” *Journal of the American Chemical Society*, vol. 134, no. 44, pp. 18453–18459, 2012.

[256] N.Krstajić, M.Popović, B.Grgur, M.Vojnović, and D.Šepa, “On the kinetics of the hydrogen evolution reaction on nikel in alkaline solution. Part I. The mechanism,” *Journal of Electroanalytical Chemistry*, vol. 512, no. 1, pp. 16–26, 2001.

[257] F. J. Morin, “Electrical properties of NiO,” *Physical Review*, vol. 93, no. 6, pp. 1199–1204, 1954.

[258] S. K. Deb and J. A. Chopoorian, “Optical properties and color-center formation in thin films of molybdenum trioxide,” *Journal of Applied Physics*, vol. 37, no. 13, pp. 4818–4825, 1966.

[259] Z. Chen, D. Cummins, B. N. Reinecke, E. Clark, M. K. Sunkara, and T. F. Jaramillo, “Core-shell MoO3-MoS2 Nanowires for Hydrogen Evolution: A Functional Design for Electrocatalytic Materials,” *Nano Letters*, vol. 11, no. 10, pp. 4168–4175, 2011.

[260] M. A. Lukowski, A. S. Daniel, F. Meng, A. Forticaux, L. Li, and S. Jin, “Enhanced hydrogen evolution catalysis from chemically exfoliated metallic MoS2 nanosheets,” *Journal of the American Chemical Society*, vol. 135, no. 28, pp. 10274–10277, 2013.

[261] A. B. Laursen, K. R. Patraju, M. J. Whitaker, M. Retuerto, T. Sarkar, N. Yao, K. V. Ramanujachary, M. Greenblatt, and G. C. Dismukes, “Nanocrystalline Ni5P4: A hydrogen

evolution electrocatalyst of exceptional efficiency in both alkaline and acidic media," *Energy and Environmental Science*, vol. 8, no. 3, pp. 1027–1034, 2015.

[262] M. S. Burke, L. J. Enman, A. S. Batchellor, S. Zou, and S. W. Boettcher, "Oxygen Evolution Reaction Electrocatalysis on Transition Metal Oxides and (Oxy)hydroxides: Activity Trends and Design Principles," *Chemistry of Materials*, vol. 27, no. 22, pp. 7549–7558, 2015.

[263] L. Trotochaud, S. L. Young, J. K. Ranney, and S. W. Boettcher, "Nickel-Iron oxyhydroxide oxygen-evolution electrocatalysts: The role of intentional and incidental iron incorporation," *Journal of the American Chemical Society*, vol. 136, no. 18, pp. 6744–6753, 2014.

[264] W. Sheng, H. A. Gasteiger, and Y. Shao-Horn, "Hydrogen Oxidation and Evolution Reaction Kinetics on Platinum: Acid vs Alkaline Electrolytes," *Journal of The Electrochemical Society*, vol. 157, no. 11, p. B1529, 2010.

[265] K. Shinozaki, J. W. Zack, R. M. Richards, B. S. Pivovar, and S. S. Kocha, "Oxygen Reduction Reaction Measurements on Platinum Electrocatalysts Utilizing Rotating Disk Electrode Technique," *Journal of The Electrochemical Society*, vol. 162, no. 10, pp. F1144–F1158, 2015.

[266] I. Takahashi and S. S. Kocha, "Examination of the activity and durability of PEMFC catalysts in liquid electrolytes," *Journal of Power Sources*, vol. 195, no. 19, pp. 6312–6322, 2010.

[267] Y. Garsany, O. A. Baturina, S. S. Kocha, and K. E. Swider-lyons, "Experimental methods for quantifying the activity of Pt electrocatalysts for the oxygen reduction reaction," *Fuel Cell*, vol. 82, no. 15, pp. 1–29, 1825.

[268] M. E. Orazem and T. Bernard, *Electrochemical Impedance Spectroscopy*. John Wiley and Sons Inc., New York, 2008.

[269] P. Marcel, *Atlas of electrochemical equilibria in aqueous solutions*. Houston, Tex.: National Association of Corrosion Engineers, second ed., 1974.

[270] S. Pérez-Rodríguez, E. Pastor, and M. J. Lázaro, "Electrochemical behavior of the carbon black Vulcan XC-72R: Influence of the surface chemistry," *International Journal of Hydrogen Energy*, vol. 43, no. 16, pp. 7911–7922, 2018.

[271] J. L. de la Fuente, S. Rojas, M. V. Martínez-Huerta, P. Terreros, M. A. Peña, and J. L. Fierro, "Functionalization of carbon support and its influence on the electrocatalytic behaviour of Pt/C in H2 and CO electrooxidation," *Carbon*, vol. 44, no. 10, pp. 1919–1929, 2006.

[272] C. Prado-Burguete, A. Linares-Solano, F. Rodríguez-Reinoso, and C. S. M. de Lecea, "The effect of oxygen surface groups of the support on platinum dispersion in Pt/carbon catalysts," *Journal of Catalysis*, vol. 115, no. 1, pp. 98–106, 1989.

[273] J. L. Figueiredo, M. F. Pereira, M. M. Freitas, and J. J. Órfão, "Modification of the surface chemistry of activated carbons," *Carbon*, vol. 37, no. 9, pp. 1379–1389, 1999.

[274] M. Lázaro, L. Calvillo, V. Celorrio, J. I. Pardo, S. Perathoner, and R. Moliner, "Study and application of Carbon Black Vulcan XC-72R in Polymeric Electrolyte Fuel Cells," *Carbon Black: Production, Properties and Uses*, no. May 2014, pp. 1–28, 2011.

[275] Metalary, "Metal Prices."

[276] S. Flandrois and B. Simon, "Carbon materials for lithium-ion rechargeable batteries," *Carbon*, vol. 37, no. 2, pp. 165–180, 1999.

[277] D. Li, E. J. Park, W. Zhu, Q. Shi, Y. Zhou, H. Tian, Y. Lin, A. Serov, B. Zulevi, E. D. Baca, C. Fujimoto, H. T. Chung, and Y. S. Kim, "Highly quaternized polystyrene ionomers for high performance anion exchange membrane water electrolysers," *Nature Energy*, vol. 5, no. 5, pp. 378–385, 2020.

[278] A. Roy, "Anodic Catalysts for Anion Exchange Membrane Fuel Cells.," p. 101 pp., 2017.

[279] M. Gong, D. Y. Wang, C. C. Chen, B. J. Hwang, and H. Dai, "A mini review on nickel-based electrocatalysts for alkaline hydrogen evolution reaction," *Nano Research*, vol. 9, no. 1, pp. 28–46, 2016.

[280] M. Xia, T. Lei, N. Lv, and N. Li, "Synthesis and electrocatalytic hydrogen evolution performance of Ni-Mo-Cu alloy coating electrode," *International Journal of Hydrogen Energy*, vol. 39, no. 10, pp. 4794–4802, 2014.

[281] D. Goranova, E. Lefterova, and R. Rashkov, "Electrocatalytic activity of Ni-Mo-Cu and Ni-Co-Cu alloys for hydrogen evolution reaction in alkaline medium," *International Journal of Hydrogen Energy*, vol. 42, no. 48, pp. 28777–28785, 2017.

[282] Y. Liu, X. Liang, L. Gu, Y. Zhang, G. D. Li, X. Zou, and J. S. Chen, "Corrosion engineering towards efficient oxygen evolution electrodes with stable catalytic activity for over 6000 hours," *Nature Communications*, vol. 9, no. 1, pp. 1–10, 2018.

[283] X. Zhao, S. C. Abbas, Y. Huang, J. Lv, M. Wu, and Y. Wang, “Robust and Highly Active FeNi@NCNT Nanowire Arrays as Integrated Air Electrode for Flexible Solid-State Rechargeable Zn-Air Batteries,” *Advanced Materials Interfaces*, vol. 5, no. 9, pp. 1–7, 2018.

[284] S. Kim, C. Ahn, Y. Cho, G. Hyun, S. Jeon, and J. H. Park, “Suppressing buoyant force: New avenue for long-term durability of oxygen evolution catalysts,” *Nano Energy*, vol. 54, no. October, pp. 184–191, 2018.

[285] J. Shen, M. Wang, L. Zhao, P. Zhang, J. Jiang, and J. Liu, “Amorphous Ni(Fe)OxHy-coated nanocone arrays self-supported on stainless steel mesh as a promising oxygen-evolving anode for large scale water splitting,” *Journal of Power Sources*, vol. 389, no. February, pp. 160–168, 2018.

[286] P. Liu, D. Gao, W. Xiao, L. Ma, K. Sun, P. Xi, D. Xue, and J. Wang, “Self-Powered Water-Splitting Devices by Core–Shell NiFe@N-Graphite-Based Zn–Air Batteries,” *Advanced Functional Materials*, vol. 28, no. 14, pp. 1–8, 2018.

[287] A. More, S. Bhavsar, and G. Veser, “Iron–Nickel Alloys for Carbon Dioxide Activation by Chemical Looping Dry Reforming of Methane,” *Energy Technology*, vol. 4, no. 10, pp. 1147–1157, 2016.

[288] S. M. Kim, P. M. Abdala, T. Margossian, D. Hosseini, L. Foppa, A. Armutlulu, W. Van Beek, A. Comas-Vives, C. Copéret, and C. Müller, “Cooperativity and dynamics increase the performance of NiFe dry reforming catalysts,” *Journal of the American Chemical Society*, vol. 139, no. 5, pp. 1937–1949, 2017.

[289] A. A. El Mel, R. Nakamura, and C. Bittencourt, “The Kirkendall effect and nanoscience: Hollow nanospheres and nanotubes,” *Beilstein Journal of Nanotechnology*, vol. 6, no. 1, pp. 1348–1361, 2015.

[290] D. S. Tannhauser, “Conductivity in iron oxides,” *Journal of Physics and Chemistry of Solids*, vol. 23, no. 1-2, pp. 25–34, 1962.

[291] D. Xu, M. B. Stevens, M. R. Cosby, S. Z. Oener, A. M. Smith, L. J. Enman, K. E. Ayers, C. B. Capuano, J. N. Renner, N. Danilovic, Y. Li, H. Wang, Q. Zhang, and S. W. Boettcher, “Earth-Abundant Oxygen Electrocatalysts for Alkaline Anion-Exchange-Membrane Water Electrolysis: Effects of Catalyst Conductivity and Comparison with Performance in Three-Electrode Cells,” *ACS Catalysis*, vol. 9, no. 1, pp. 7–15, 2019.

[292] Yi Youngmi, *Study on the degradation of carbon materials for electrocatalytic applications*. PhD thesis, 2014.

[293] S. Lee, H. S. Cho, W. C. Cho, S. K. Kim, Y. Cho, and C. H. Kim, "Operational durability of three-dimensional Ni-Fe layered double hydroxide electrocatalyst for water oxidation," *Electrochimica Acta*, vol. 315, pp. 94–101, 2019.

[294] J. H. Lee, U. Paik, J. Y. Choi, K. K. Kim, S. M. Yoon, J. Lee, B. K. Kim, J. M. Kim, M. H. Park, C. W. Yang, K. H. An, and Y. H. Lee, "Dispersion stability of single-walled carbon nanotubes using nafion in bisolvent," *Journal of Physical Chemistry C*, vol. 111, no. 6, pp. 2477–2483, 2007.

[295] J. Xie, F. Xu, D. L. Wood, K. L. More, T. A. Zawodzinski, and W. H. Smith, "Influence of ionomer content on the structure and performance of PEFC membrane electrode assemblies," *Electrochimica Acta*, vol. 55, no. 24, pp. 7404–7412, 2010.

[296] K. Artyushkova, M. J. Workman, I. Matanovic, M. J. Dzara, C. Ngo, S. Pylypenko, A. Serov, and P. Atanassov, "Role of Surface Chemistry on Catalyst/Ionomer Interactions for Transition Metal-Nitrogen-Carbon Electrocatalysts," *ACS Applied Energy Materials*, vol. 1, no. 1, pp. 68–77, 2018.

[297] S. J. Sondheimer, N. J. Bunce, M. E. Lemke, and C. A. Fyfe, "Acidity and Catalytic Activity of Nafion-H," *Macromolecules*, vol. 19, no. 2, pp. 339–343, 1986.

[298] A. Han, C. Fu, X. Yan, J. Chen, X. Cheng, C. Ke, J. Hou, S. Shen, and J. Zhang, "Effect of cobalt ion contamination on proton conduction of ultrathin Nafion film," *International Journal of Hydrogen Energy*, vol. 45, no. 46, pp. 25276–25285, 2020.

[299] M. M. Nasef and A. H. Yahaya, "Adsorption of some heavy metal ions from aqueous solutions on Nafion 117 membrane," *Desalination*, vol. 249, no. 2, pp. 677–681, 2009.

[300] A. Pozio, R. F. Silva, M. De Francesco, and L. Giorgi, "Nafion degradation in PEFCs from end plate iron contamination," *Electrochimica Acta*, vol. 48, no. 11, pp. 1543–1549, 2003.

[301] K. Kawai, T. Mabuchi, and T. Tokumasu, "Molecular Dynamics Analysis of Proton Diffusivity in Hydrated Nafion Membranes Contaminated with Ferrous Ions," *Macromolecular Theory and Simulations*, vol. 29, no. 1, pp. 1–8, 2020.

[302] P. N. Ross and H. Sokol, “Corrosion of Carbon Black Anodes in Alkaline Electrolyte: I. Acetylene Black and the Effect of Cobalt Catalyzation.,” *Proceedings - The Electrochemical Society*, vol. 131, p. 1742, 1984.

[303] P. N. Ross and M. Sattler, “The Corrosion of Carbon Black Anodes in Alkaline Electrolyte: III . The Effect of Graphitization on the Corrosion Resistance of Furnace Blacks,” *Journal of The Electrochemical Society*, vol. 135, p. 1464, 1988.

[304] S. Möller, S. Barwe, J. Masa, D. Wintrich, S. Seisel, H. Baltruschat, and W. Schuhmann, “Online Monitoring of Electrochemical Carbon Corrosion in Alkaline Electrolytes by Differential Electrochemical Mass Spectrometry,” *Angewandte Chemie - International Edition*, vol. 59, no. 4, pp. 1585–1589, 2020.

[305] “NIST X-ray Photoelectron Spectroscopy Database, NIST Standard Reference Database Number 20, National Institute of Standards and Technology, Gaithersburg MD, 20899 (2000), doi:10.18434/T4T88K, (retrieved 26th November, 2018)..”

[306] D. Briggs, “X: X-Ray Photoelectron Spectroscopy,” *Handbook of Adhesion: Second Edition*, pp. 621–622, 2005.

[307] B. E. Conway and M. Salomon, “Electrochemical reaction orders: Applications to the hydrogen- and oxygen-evolution reactions,” *Electrochimica Acta*, vol. 9, no. 12, pp. 1599–1615, 1964.

[308] M. Schalenbach, F. D. Speck, M. Ledendecker, O. Kasian, D. Goehl, A. M. Mingers, B. Breitbach, H. Springer, S. Cherevko, and K. J. J. Mayrhofer, “Nickel-molybdenum alloy catalysts for the hydrogen evolution reaction: Activity and stability revised,” *Electrochimica Acta*, vol. 259, pp. 1154–1161, 2018.

[309] F. Safizadeh, E. Ghali, and G. Houlachi, “Electrocatalysis developments for hydrogen evolution reaction in alkaline solutions - A Review,” *International Journal of Hydrogen Energy*, vol. 40, no. 1, pp. 256–274, 2015.

[310] S. Xue, W. Zhang, Q. Zhang, J. Du, H. M. Cheng, and W. Ren, “Heterostructured Ni–Mo–N nanoparticles decorated on reduced graphene oxide as efficient and robust electrocatalyst for hydrogen evolution reaction,” *Carbon*, vol. 165, pp. 122–128, 2020.

[311] Y. Li, X. Wei, L. Chen, J. Shi, and M. He, “Nickel-molybdenum nitride nanoplate electrocatalysts for concurrent electrolytic hydrogen and formate productions,” *Nature Communications*, vol. 10, no. 1, pp. 1–12, 2019.

[312] T. Wang, X. Wang, Y. Liu, J. Zheng, and X. Li, “A highly efficient and stable biphasic nanocrystalline Ni-Mo-N catalyst for hydrogen evolution in both acidic and alkaline electrolytes,” *Nano Energy*, vol. 22, pp. 111–119, 2016.

[313] W.-F. Chen, K. Sasaki, C. Ma, A. I. Frenkel, N. Marinkovic, J. T. Muckerman, Y. Zhu, and R. R. Adzic, “Hydrogen-Evolution Catalysts Based on Non-Noble Metal Nickel–Molybdenum Nitride Nanosheets,” *Angewandte Chemie International Edition*, vol. 51, no. 25, pp. 6131–6135, 2012.